PROBING STRUCTURAL AND ORBITAL PROPERTIES OF BINARY PULSARS

By

DHRUV PATHAK

Enrollment No.: PHYS10201305009

The Institute of Mathematical Sciences, Chennai

A thesis submitted to the

Board of Studies in Physical Sciences

In partial fulfillment of requirements
For the Degree of
DOCTOR OF PHILOSOPHY

of

HOMI BHABHA NATIONAL INSTITUTE

August, 2021

Homi Bhabha National Institute

Recommendations of the Viva Voce Board

As members of the Viva Voce Board, we certify that we have read the dissertation prepared by Dhruv Pathak entitled “Probing Structural and Orbital Properties of Binary Pulsars" and recommend that it maybe accepted as fulfilling the dissertation requirement for the Degree of Doctor of Philosophy.

D. Indumathi

Date: 07/03/2022

Chair - Prof. D. Indumathi

Manjari Bagchi

Date: 07/03/2022

Guide/Convener - Prof. Manjari Bagchi

Date: 07/03/2022

Examiner - Prof. Dipankar Bhattacharya

Date: 07/03/2022

Member - Prof. Shrihari Gopalakrishna

Date: 07/03/2022

Member - Prof. Sitabhra Sinha

Sanatan Digal

Date: 07/03/2022

Member - Prof. Sanatan Digal

Final approval and acceptance of this dissertation is contingent upon the candidate’s submission of the final copies of the dissertation to HBNI.

I hereby certify that I have read this dissertation prepared under my direction and recommend that it may be accepted as fulfilling the dissertation requirement.

Date: 07/03/2022

Manjari Bagchi

Place: Chennai

Guide Prof. Manjari Bagchi

STATEMENT BY AUTHOR

This dissertation has been submitted in partial fulfillment of requirements for an advanced degree at Homi Bhabha National Institute (HBNI) and is deposited in the Library to be made available to borrowers under rules of the HBNI.

Brief quotations from this dissertation are allowable without special permission, provided that accurate acknowledgement of source is made. Requests for permission for extended quotation from or reproduction of this manuscript in whole or in part may be granted by the Competent Authority of HBNI when in his or her judgement the proposed use of the material is in the interests of scholarship. In all other instances, however, permission must be obtained from the author.

Dhruv Pathak

DECLARATION

I, hereby declare that the investigation presented in the thesis has been carried out by me. The work is original and has not been submitted earlier as a whole or in part for a degree / diploma at this or any other Institution / University.

Dhruv Pathak

DEDICATIONS

Dedicated to my parents, my grandparents, and my brother Tarkshay

ACKNOWLEDGEMENTS

I would like to begin by expressing my sincere gratitude for my guide Prof. Manjari Bagchi. Working under the excellent guidance of my esteemed supervisor has been a privilege and honour. I was fortunate to get an opportunity to work with a guide who always wants the best for her student, who always stands by the student, and whose sincerity, dedication and zeal towards the field are inspirational. She has always motivated me to better myself at every stage. Today, if my thesis has come to fruition, it is only because of the constant unflinching support of my guide.

I am extremely grateful to the members of my Doctoral committee- Prof. D. Indumathi, Prof. Shreehari Gopalakrishna, Prof. Sanatan Diggal, and Prof. Sitabhra Sinha, for their encouragement, insightful questions, and suggestions that helped improve my work. They have always been extremely considerate and supportive of me.

I would also like to express my gratitude towards the administrative staff at IMSc, especially, Ms. R. Indra, Ms. Prema, and Mr. R Baskaran. With their help, any administrative issue that I faced during my stay was swiftly resolved without any hassles. I am also extremely grateful to the technical staff at IMSc, especially, Mr. G. Srinivasan for their timely technical support.

I am especially thankful to the housekeeping and the security staff for their interactions with me that made my stay at IMSc comfortable. Special mention to Mahalakshmi aunty for always being so caring.

I am also thankful to the reviewers of my publications for their constructive suggestions.

My time at HRI during my Int.-PhD coursework was one of my most enriching experiences. Be it the amazing lectures of coursework at HRI or even the experimental projects at IGCAR, Kalpakkam as well as at NISER, Bhubaneswar, I enjoyed every moment of them. I would like to thank the esteemed faculty at HRI, especially, Prof. Ashoke Sen, Prof. Jayant Kumar Bhattacharya, Prof. S. K. Naik, Prof. Tapas Kumar Das for always letting me barge into their offices and patiently clearing my doubts. I would like to thank Prof. Pinaki Majumdar for hosting me for my first reading project during my undergrad and inviting me to HRI in 2011.

By the end of my school life, I was already passionate about physics. However, during my B.Tech years in IIT Delhi, my love for the subject grew by leaps and bounds. Although my main degree was in Textile technology, thanks to IIT's system of open electives, I did all of my elective courses in Physics. I would like to thank all the faculty that taught me at IIT Delhi, especially, Prof. Mangala Joshi (my B.Tech. project supervisor), Dr. Dilip Ranganathan, Prof. Samrat Mukhopadhyay, Prof. Bhanu Nandan, Prof. Rajiv Srivastava, and Prof. Sankalp Ghosh. They have always encouraged me.

Thanks to PhD, I came in contact with some colleagues who are now like family. I would like to thank Dr. Ritika Sharma, Dr. Nafisa Aftab, Dr. Arpita Choudhary, and Dr. Neelam Dhanda Batra, for their constant support and care. I would especially like to thank Tamanna Jain, my soul sister, who has been one of my greatest support systems.

I would also like to thank my friends - Varun, Sudhakar, Akanksha, Ayushi, Ridhima, Parvez, Priyanka, Deepika, Pradyumn and others for their support.

Finally, I thank my parents- Dr. Ashok Pathak, Dr. Renu Pathak, my grandparents- Shri R. C. Pathak, Smt. Kalawati Pathak and Prof. R. A. Sharma, Smt. Pragya Sharma, and my brother Tarkshay ... my lifelines.

In the end, I thank the omnificent universal life force.

Dhruv Pathak

List of publications arising from the thesis

1. Pathak, D., Bagchi, M., 2021. A study of dynamical effects in the observed second time-derivative of the spin or orbital frequencies of pulsars. New Astronomy. 85, 101549, https://doi.org/10.1016/j.newast.2020.101549.

2. Pathak, D., Bagchi, M., 2018. Dynamical Effects in the Observed Rate of Change of the Orbital and the Spin Periods of Radio Pulsars: Improvement in the Method of Estimation and Its Implications. ApJ. 868, 123-136. https://doi.org/10.3847/1538-4357/aae9d9.

List of presentations and participations at Conferences/Workshops

Presentations

1. European Pulsar Timing Array (EPTA)-COMO Meeting 2020, virtual meeting organized by European Pulsar Timing Array group (2nd-4th December 2020) - Talk titled “Dynamical effects in second derivative of spin and orbital frequency of radio pulsars".

2. International Pulsar Timing Array (IPTA) Catch-up Meeting 2020, virtual meeting organized by Australian National Telescope Facility (22nd-23rd September 2020) - Slides titled “Dynamical effects in second derivative of spin and orbital frequency of radio pulsars".

3. 10th International Pulsar Timing Array (IPTA) Workshop, Pune, India (10th-21st June 2019) - Talk titled “Dynamical contributions in the rate of change of the periods of radio pulsars".

4. 30th meeting of the Indian Association for General Relativity and Gravitation (IAGRG), BITS Pilani, Hyderabad Campus, India (3rd-5th January 2019) - Talk titled

"Dynamical contributions in the rate of change of the periods of radio pulsars".

5. Multi Wavelength Neutron Star Workshop, BITS Pilani, Hyderabad Campus, India (7th-8th January 2018) - Talk titled "Dynamical contributions in the rate of change of the period of radio pulsars".
6. 35th Annual Meeting of the Astronomical Society of India (ASI), Birla Institute of Scientific Research (BISR), Jaipur, India (6th-10th March 2017) - Poster titled "Probing orbital properties of wide binary pulsars".

Participations

1. SLAC Summer Institute 2020 (SSI 2020), online Summer School by SLAC National Accelerator Laboratory, US (10th-21st August 2020).
2. Online Workshop on Testing General Relativity using Gravitational Waves, jointly by Indian Association for the Cultivation Of Science (IACS) and Indian Institute of Technology, Gandhinagar (IITGN), India (13th-14th August 2020).
3. Kavli-RISE Summer School on Gravitational Waves, Centre for Theoretical Cosmology, Cambridge, UK (23rd-27th Sep. 2019).
4. Summer School on Gravitational-Wave Astronomy, International Centre for Theoretical Sciences (ICTS), Bengaluru, India (17th-28th Jul. 2017).
5. Pulsar Astronomy with uGMRT Boot-Camp, BITS Pilani, Hyderabad Campus, India (3th-6th Jan. 2018) - Tutor.
6. First ASIONS (Asia SKA Initiative On NS) Conference, Goa, India (4th-5th Nov. 2016) - Local Organizing Committee member.
7. Neutron Star School and Workshop, NCRA, Pune, India (5th-15th Jan. 2016).

Dhruv Pathak

Contents

1 Introduction **31**

Summary

The timing analysis of radio pulsars gives many interesting results and is expected to contribute further in many areas of fundamental physics in the future. In this connection, it is important to understand the external factors affecting the values of the parameters estimated in the timing analysis. Among all these timing parameters, the measured values of the time-derivatives of the frequencies (both the spin and the orbital) are affected by the velocity, the acceleration, the jerk, etc. of the pulsar. These effects are known as 'dynamical contributions'. In this thesis, we explore these dynamical effects in the first as well as the second time-derivatives of the frequency (both the spin and the orbital).

The previous studies on estimation of the dynamical terms contributing to the first and the second derivatives of the frequency (or the period) resorted to approximate methods which fail to provide accurate values of these parameters for all the pulsars spread across the Galaxy. We point out the limitations of existing methods to calculate the dynamical effects in the first and the second derivatives of the frequency and argue the need for improved methods to extract these effects. We present improved methods to do so and emphasize the fact that these methods should be used for pulsars located away from the solar system, especially when precise values of the first and the second derivatives of the frequency are needed.

We provide analytical expressions for all the dynamical terms contributing to the first and the second derivatives of the frequency without resorting to any numerical fitting. These analytical expressions are derived in terms of the Galactic coordinates, the proper motion, the distance, the radial velocity, and the observed values of the frequency and its derivatives, with the assumption that the gravitational potential of the Galaxy is the only cause of the acceleration and the jerk of the pulsar.

We introduce a package, 'GalDynPsr', that evaluates these different dynamical effects in the first derivative of the period (both the spin and the orbital), following the traditional

as well as improved methods based on a well-known model of the Galactic potential. We also demonstrate the differences between the results returned by the improved methods from those obtained using the traditional ones.

We then introduce another python package ‘GalDynPsrFreq’ that estimates the dynamical terms in the measured values of the first and the second time derivatives of the frequency (both the spin and the orbital). We demonstrate the usage of GalDynPsrFreq in the study of the effect of the dynamics on the measured values of the second derivative of the frequency for real as well as simulated pulsars. We establish the fact that all dynamical terms affecting the measured values of the second derivative of the frequency are equally important. With the help of simulated pulsars, we demonstrate that the effects of the dynamics would be much larger for pulsars near the Galactic centre than those for the pulsars in the Galactic field. We also show how dynamics can affect values of the braking index and the second derivative of the orbital frequency.

List of Figures

List of Tables

Chapter 1

Introduction

1.1 Overview

On August 6, 1967, a young graduate student at Cambridge, Jocelyn Bell, found something strange in her data from the radio telescope she helped build to detect quasars. These were a series of radio pulses recorded, with each being a little more than a second apart, something that was unprecedented. As we now know, Bell had stumbled upon the very first discovery of a pulsar. It has been more than 50 years since the discovery of pulsars and yet they continue to be the source of intrigue.

But, what are pulsars? Pulsars are the radio-observable subsets of neutron stars. When a star of mass in the range of $8-25$ $M_\odot$[1] undergoes gravitational collapse as it advances in its life cycle, it results in a supernova explosion (Vidaña, 2018). The brief mechanism of such an explosion is outlined below. The final stage in burning of the fuel inside a star is the formation of an iron core, as iron has the maximum binding energy per nucleon. This iron core starts growing by silica shell burning, which makes the core cross the Chandrashekhar limit of 1.44 $M_\odot$. At this stage, the electron degeneracy pressure can no longer counter the self-gravity, and consequently, the core collapses. This causes an

---

[1] $M_\odot$ is the unit of mass in terms of the mass of the Sun, i.e., 1.989×10^{30} kg.

explosion in which the outer shells and the heavy elements from the core are released in the interstellar medium. This event is called the core-collapse supernova (Couch, 2017). The resulting core-collapsed star has a neutron-rich inner crust and a core of superfluid neutrons (Lorimer and Kramer, 2005). So, quite fittingly, this collapsed star is called a neutron star. It should be noted that some theoretical studies expect exotic particles, e.g., hyperons inside such stars (Balberg et al., 1999; Vidaña, 2016). If the progenitor star had a mass greater than 25 $M_\odot$, the eventual collapse of the star would have resulted in the formation of a black hole (Fryer, 1999).

Neutron stars are extremely dense. The masses of the known neutron stars are in the range of $1-2$ $M_\odot$ while their radii are around 10 km. Because of such a high density, neutron stars have very strong gravitational fields. They also have very high magnetic fields, lying in the range of $10^8 - 10^{15}$ G.

A neutron star emits beamed electromagnetic waves along its magnetic axis, which may not coincide with the spin axis. This radiation covers a wide spectrum of electromagnetic waves, most of which are blocked by the earth's atmosphere. The part of the radiation in the radio wavelengths reaches the earth's surface unattenuated. During a rotation of the neutron star, it may happen that the beam of the electromagnetic radiation sweeps across an observatory (radio telescope) on the earth. This repeats with consecutive rotations. At the observatory, it appears that radio pulses are being received at regular intervals. Such neutron stars which appear to emit radio pulses are referred to as radio pulsars[2]. In the present thesis, radio pulsars are called pulsars for the sake of simplicity. The regular intervals at which the pulses are received are the approximate measures of the spin period of the pulsar.

So far, more than 2800 pulsars have been discovered. These are located in the Galactic disk and the field, in globular clusters, in the Large Magellanic Cloud, and in the Small Magellanic Cloud. No pulsars have been yet discovered in any other galaxy. In-

---

[2] There are other types of pulsars like γ-ray pulsars, X-ray pulsars, etc., whose emission mechanisms are different and are observed with space-based detectors. We do not study such pulsars in the present thesis.

dividual pulsars are denoted by their coordinates, e.g., PSR J2145−0750 is a pulsar with the value of the right ascension (RA) as 21hh45mm50.46s and the declination (DEC) as −07dd50mm18.59ss in the J2000 coordinate system; PSR B1913+16 is a pulsar with RA 19hh15mm28ss and DEC +16dd06mm27.40s in the B1950 coordinate system. In both of the cases, 'PSR' stands for pulsar. A little over 11% of these occur in a binary system with another star (or a heavy planet in some cases). Such pulsars are called binary pulsars. Some examples of binary pulsars are PSR J0437−4715, PSR J1012+5307, and PSR J1713+0747 (Manchester et al., 2005). The pulsars with no companion are called isolated pulsars, e.g., PSR J0002+6216, PSR J1044−5737, and PSR J1821−1432 (Manchester et al., 2005). Out of the known pulsars, only two have been found to occur in triple systems, PSR B1620−26 (a system of a pulsar, a white dwarf, and a planetary-mass object; (Sigurdsson et al., 2003)), and PSR J0337+1715 (a system of a pulsar, and two white dwarfs; Ransom et al. (2014)). Fig. 1.1 shows the Aitoff projection plot in the Galactic longitude and the Galactic latitude (in degrees) in subplot 1.1(a) and in the right ascension and declination (in degrees) in subplot 1.1(b) for all known pulsars using the data from the version 1.64 of the ATNF (Australian Telescope National Facility) pulsar catalogue (Manchester et al., 2005).

In the following sections, we discuss various characteristic features and parameters of pulsars, as well as their use to explore various aspects of fundamental physics. In section 1.2, we discuss the electromagnetics and the emission mechanism of pulsars. In section 1.3, we discuss the high magnetic field strength of pulsars. In section 1.4, we discuss the binary system formation and the resulting orbital dynamics. In section 1.5, we talk briefly about the technique of pulsar timing analysis. In section 1.6, we discuss various parameters of pulsars and methods to measure those. In section 1.7, we talk about a few applications of pulsars as tools to study physics. In section 1.8, we briefly discuss the application of a pulsar parameter, namely, the braking index, in the study of the structure of pulsars. In section 1.9, we discuss the dynamical effects that influence measured pulsar parameters. In section 1.10, we present the structure of this thesis.

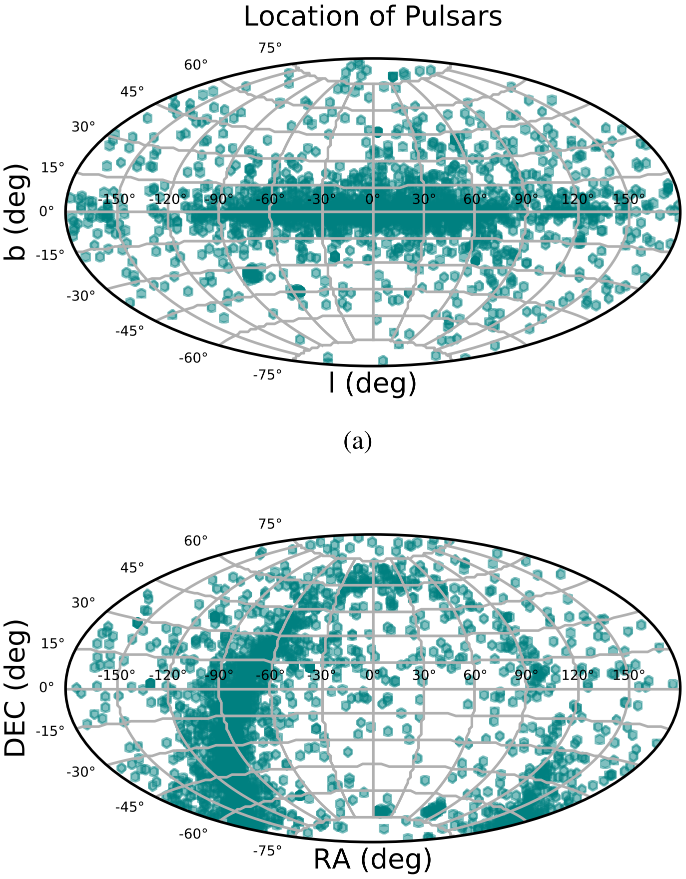

(a)

(b)

Figure 1.1: a) Aitoff projection diagram of all known pulsars in the Galactic longitude and the Galactic latitude (in degrees). b) Aitoff projection diagram of all known pulsars in the right ascension and declination (in degrees). Data are taken from the version 1.64 of the ATNF pulsar catalogue (Manchester et al., 2005).

1.2 Rotation Powered Emission Mechanism

The electromagnetic energy emitted from the pulsar comes at the expense of its rotational kinetic energy. That is why these pulsars are called 'rotation powered pulsars'. Hence, with time, the rotational kinetic energy decreases and the pulsar slows down, i.e., the spin period increases. The rate of loss of the kinetic energy ($\dot{E}_{\rm rot}$) is given by[3]:

$$\dot{E}_{\rm rot} = -\frac{d}{dt}\left(\frac{1}{2}\,I\omega_{\rm s}^2\right) = -I\,\omega_{\rm s}\,\dot{\omega}_{\rm s} = 4\pi^2 I\dot{P}_{\rm s}P_{\rm s}^{-3}\ , \tag{1.1}$$

where I is the moment of inertia of the pulsar about its spin axis, $P_{\rm s}$ is the spin period, and $\omega_{\rm s}$ ($= 2\pi/P_{\rm s}$) is the angular frequency of the rotation. $\dot{E}_{\rm rot}$ is also called the spin down luminosity and indicates the total power output of the pulsar (Lorimer and Kramer, 2005).

Pulsars act as rotating magnetic dipoles. Generally, the magnetic axis is not aligned with the spin axis of the pulsar. This misalignment between the two axes results in a time-varying magnetic moment from the spinning magnetic dipole. This time-varying magnetic moment, in turn, is responsible for the emission of the electromagnetic radiation along the magnetic axis of the pulsar, which we eventually receive as radio signals. The electromagnetic power generated from the rotating magnetic dipole is given as (Lorimer and Kramer, 2005):

$$\dot{E}_{\rm dipole} = \frac{2}{3c^3}|\mathbf{m}|^2\omega_{\rm s}^4\sin^2\,\alpha\ , \tag{1.2}$$

where $|\mathbf{m}|$ is the magnitude of the magnetic moment, α is the angle between the magnetic moment and the spin axis, and c is the speed of light in vacuum.

Assuming that the loss of the rotational kinetic energy is used entirely in the generation of the electromagnetic power, we can equate $\dot{E}_{\rm rot}$ to $\dot{E}_{\rm dipole}$. Therefore, from eqs. (1.1) and (1.2), we get:

$$\dot{\omega}_{\rm s} = -\left(\frac{2|\mathbf{m}|^2\sin^2\alpha}{3Ic^3}\right)\omega_{\rm s}^3\ . \tag{1.3}$$

Extending the idea put forth in eq. (1.3), to a more general power law expression of $\dot{f}_{\rm s}$ in

---

[3] The dot on any parameter, henceforth, represents the time-derivative of that parameter.

terms of the power of f_s, where $f_\mathrm{s} = \omega_\mathrm{s}/(2\pi)$, we can write:

$$\dot{f}_\mathrm{s} = -K f_\mathrm{s}^{n} \,, \tag{1.4a}$$

and taking the time derivative of eq. (1.4a),

$$\ddot{f}_\mathrm{s} = -n\, K\, f_\mathrm{s}^{n-1}\, \dot{f}_\mathrm{s} \,, \tag{1.4b}$$

where $K = \left(\frac{|\mathbf{m}|^2 \sin^2\alpha}{6\pi^2 I c^3}\right)$ is the proportionality constant, and n is called the braking index. The braking index can be calculated from the measured values of f_s, $\dot{f}_\mathrm{s}$, and $\ddot{f}_\mathrm{s}$ using the following equation:

$$n = \frac{f_\mathrm{s}\ddot{f}_\mathrm{s}}{\dot{f}_\mathrm{s}^2} \,. \tag{1.5}$$

For an ideal magnetic dipole, $n = 3$, as seen in eq. (1.3). However, in reality, the rotational kinetic energy might be dissipated through processes other than electromagnetic radiation as well, such as the pulsar wind, the gravitational radiation, etc. Hence, the value of n might differ from three.

The magnetic moment is related to the magnetic field strength (B) at a distance r as $B(r) \approx |\mathbf{m}|/r^3$. Using this expression in eq. (1.3), and replacing ω_s and $\dot{\omega}_\mathrm{s}$ by $2\pi/P_\mathrm{s}$ and $-(2\pi\dot{P}_\mathrm{s})/P_\mathrm{s}^2$ respectively, we get the expression for the magnetic field strength at the surface of the neutron star, B_surface as:

$$B_\mathrm{surface} = \sqrt{\frac{3c^3}{8\pi^2}\frac{I}{R^6\sin^2\alpha}P_\mathrm{s}\dot{P}_\mathrm{s}} \,, \tag{1.6}$$

where r in the expression of $B(r)$ has been substituted by R, the radius of the neutron star.

Using canonical values of $I = 10^{45}$ gm cm^2, $R = 10$ km, and the maximum value of the $\sin\alpha$, i.e., 1, one gets the minimum value of the surface magnetic field as:

$$B_\mathrm{surface,min} = 3.2 \times 10^{19}\,\sqrt{P_\mathrm{s}\dot{P}_\mathrm{s}}\ \mathrm{G} \,. \tag{1.7}$$

The values of $B_\mathrm{surface,min}$ obtained for pulsars using the measured values of P_s and $\dot{P}_\mathrm{s}$ in the above equation match closely with the values of the magnetic field at the surface of neutron stars measured by other methods (Konar, 2017).

In terms of $P_{\rm s}$ and $\dot{P}_{\rm s}$, eq. (1.4a) can be written as $\dot{P}_{\rm s} = K\,P_{\rm s}^{2-n}$. This differential equation can be integrated from $t = 0$ to $t = T$ to give

$$T = \frac{P_{\rm s}}{(n-1)\,\dot{P}_{\rm s}} \left[1 - \left(\frac{P_{\rm s,0}}{P_{\rm s}} \right)^{n-1} \right] , \tag{1.8}$$

where $P_{\rm s,0}$ is the spin period at the time of the birth of the pulsar. Assuming the spin down being caused only by the magnetic dipole radiation, i.e., $n = 3$, and $P_{\rm s,0} << P_{\rm s}$, we define the characteristic age (τ_c) from eq. (1.8) as,

$$\tau_c = \frac{P_{\rm s}}{2\,\dot{P}_{\rm s}} \approx 15.8 \times 10^6\,{\rm yr} \left(\frac{P_{\rm s}}{s} \right) \left(\frac{\dot{P}_{\rm s}}{10^{-15}} \right)^{-1} . \tag{1.9}$$

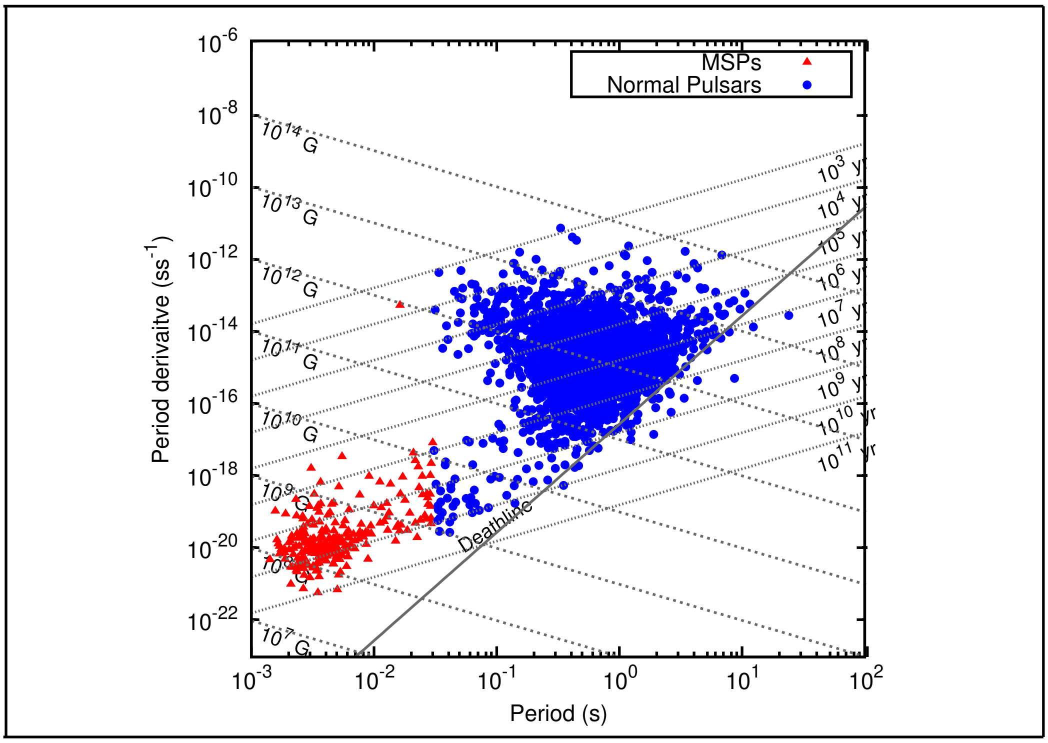

Figure 1.2: The values of $P_{\rm s}$ are plotted along the abscissa and the values of $\dot{P}_{\rm s}$ along the ordinate in the logarithmic scale for all known pulsars. The red triangles denote the millisecond pulsars and the blue circles denote the normal pulsars (see the text for definitions). Constant $B_{\rm surface,min}$ and constant τ_c lines as defined, respectively, in eqs. (1.7) and (1.9), are also plotted. We also plot the ‘deathline’ that represents the equality of the condition (1.10).

In Fig. 1.2, we plot $P_{\rm s}$ along the abscissa and $\dot{P}_{\rm s}$ along the ordinate for all known rotation powered pulsars. We also draw constant $B_{\rm surface,min}$ and constant τ_c lines as defined in eqs. (1.7) and (1.9). In the figure, we see some pulsars (denoted by red triangles) at the bottom-left part of the figure with $B_{\text{surface,min}}$ in the range of $0.5 \times 10^8 - 0.5 \times 10^{10}$ G, τ_c in the range of $10^8 - 10^{11}$ yr, and P_s in the range of $1.3 - 30$ ms. These pulsars are known as 'millisecond pulsars (MSPs)' or 'recycled pulsars'. Pulsars with $P_\text{s} > 30$ ms are called 'normal pulsars'. This nomenclature is explained in subsection 1.4.1.

Fig. 1.2 also shows the 'deathline', which represents the condition that needs to be satisfied by the neutron star to be classified as radio-observable. This condition is given by (Bhattacharya et al., 1992)

$$\frac{B_{\text{surface,min}}}{P_\text{s}^2} \geq 0.17 \times 10^{12}\ \text{G/s}^2\ , \tag{1.10}$$

where the equality represents the 'deathline'. As expected, in Fig. 1.2, we see that most of the pulsars lie above the 'deathline', i.e., satisfy the above condition. However, there exist a handful of pulsars below the 'deathline' that indicate the need for more rigorous models for the emission mechanism than the simple rotating dipole model described here.

Most of the models explaining the radio emission mechanism require the presence of acceleration gaps in the magnetosphere of the pulsar. In these gaps, there exist residual electric fields. These gaps occur in the regions of depleted plasma. In the acceleration gaps near the magnetic polar caps, the residual electric field pulls the charged particles from parts of the magnetosphere close to the surface of the neutron star. These charged particles get accelerated along the magnetic field lines. This accelerated motion of the charged particles produces γ-ray photons due to the curvature emission or inverse Compton scattering (Lorimer and Kramer, 2005). These photons further create electron-positron pairs in the presence of the strong magnetic field. These new generation particles further create photons and more charged particles, causing a cascading effect called the secondary plasma production. This secondary plasma is considered to be responsible for the observed radio emission (Lorimer and Kramer, 2005).

1.3 The High Magnetic Field

As shown in Fig. 1.2, pulsars have large values of the magnetic field at their surfaces. The same is true for other types of neutron stars too (Konar, 2017). In Table 1.1, we compare the values of the surface magnetic fields of pulsars with various terrestrial objects.

Table 1.1: Comparison of orders of magnitude of magnetic field strength of various objects.

Order of magnitude (CGS)	Object	Reference
6×10^{-4} G to 0.007 G	Electric toaster (measured at a distance of 30 cm)	Gauger (1985)
0.013 G to 0.027 G	High power (500 kV) transmission lines (measured at a distance of 30 m)	EPA (1992)
0.040 G to 0.080 G	Microwave oven (measured at a distance of 30 cm)	Gauger (1985)
0.580 G	Earth (at 50° latitude)	Matzka et al. (2010)
100 G	Typical refrigerator magnet	Slocum (1992)
1.5×10^{4} G to 3×10^{4} G	Typical MRI	Nowogrodzki (2018)
10^{8} G to 10^{14} G	Pulsar (surface)	Fig. 1.2 and Lorimer and Kramer (2005).

The question that arises at this point is how neutron stars get such high magnetic field strengths. The most popular hypothesis for the origin of these high magnetic fields is the flux conservation during the core-collapse. This would lead to amplification of the progenitor star's magnetic field as the radius decreases during the gravitational collapse. Spruit (2008) discusses three scenarios for the origin of magnetic fields in neutron stars:

- The fossil field: It is hypothesized here that the final magnetic field of the neutron star is the remnant of the already existing magnetic field of the original main sequence star. This field gets amplified due to the flux conservation during the core-collapse. Spruit (2008) argues that this process is not statistically viable and unsuitable to explain extremely high magnetic fields of magnetars, which are magnetically powered neutron stars having the surface magnetic field strength in the range of about $10^{14} - 10^{15}$ G.

- Fields generated internally in the supernova progenitor: In this scenario, it is hypothesized that the magnetic field is somehow internally generated in the progenitor star during the pre-supernova phase. This field eventually gets amplified, again due to the flux conservation. Here too, Spruit (2008) argues that the fields produced after amplification would still be lower in strength than that observed for pulsars and magnetars.

- Field generation during the core collapse: Spruit (2008) mentions that, in terms of energetics, if the rise of the magnetic energy is driven only by the gravitational collapse, it increases as $\sim 1/$(radius). This is insufficient to produce dynamically significant fields. The differential rotation is a major driving force for the magnetic field generation during the collapse, as the rotational kinetic energy increases as $\sim 1/$(radius)^2, which is sufficient to produce the high values of the magnetic fields possessed by pulsars (Spruit, 2008).

There are a few additional hypotheses to explain the high magnetic field of neutron stars. One such hypothesis is the generation of the magnetic field caused by thermal effects in their outer crust (Blandford et al., 1983). However, according to this model, the growing magnetic field saturates when the surface value reaches around 10^{12} G and then starts decreasing.

So this model is inadequate to explain the magnetic fields of not only the magnetars, even of the slow pulsars of magnetic field strength in the range of 10^{13} to 10^{14} G. The version 1.64 of the ATNF pulsar catalogue lists 75 such pulsars.

1.4 The Binary Pulsars

1.4.1 Formation of Binary Pulsars

Out of the total 2872 pulsars presently known, 11.21% are in binary systems. Out of all these binaries, 80.61% contain millisecond pulsars, 10.27% contain pulsars with the values of P_s in the range of $30-100$ ms, and the rest 9.12% contain pulsars with $P_s > 100$ ms (normal pulsars). There are total 32 pulsars in the second category (i.e., with P_s in the range of $30-100$ ms), and 9 of them are neutron star − neutron star binaries or double neutron star binaries. In other words, out of total 322 binary pulsars, 189 are neutron star - white dwarf binaries, 20 are neutron star - neutron star binaries, 23 are neutron star - main sequence binaries and 58 are neutron star - sub-stellar systems (spider pulsars). It should be noted that out of all double neutron star binaries, for only one, both neutron stars are pulsars, and this is the double pulsar PSR J0737−3039A/B.

These facts can be understood from the evolution and formation of binary pulsars. Below we describe a brief outline of the most common evolutionary channel of binary neutron stars.

In a binary stellar system, the more massive star evolves faster and becomes a neutron star first after going through a core-collapse supernova. If the binary survives the explosion, a neutron star binary is born.

This neutron star, if it is a pulsar, slows down as the constant emission of the electromagnetic waves takes place at the expense of its rotational kinetic energy. So, the older pulsars are supposed to be slower. These are the normal pulsar population. If the pulsar slows down significantly, it might go below the deathline and cannot emit electromagnetic waves anymore.

However, with time, the companion star also advances in its life cycle and becomes a giant before starting to undergo gravitational collapse. During its red giant phase, the outer layers of the companion star expand and become more loosely bound to its core. At this point, depending on the separation between the neutron star and the companion, the strong gravitational field of the neutron star might attract matter from the outer layers of the companion. This accretion of matter forms an accretion disk around the neutron star and is responsible for the transfer of the orbital angular momentum to the neutron star. This causes the neutron star to spin up and its spin period decreases. Such a neutron star, when observable as a pulsar, is called a recycled pulsar. Note that during the accretion process, the neutron star does not emit radio pulses, it rather emits X-ray pulses. When the accretion process stops, the neutron star again can emit radio pulses. After a sufficient amount of accretion, the spin period of this recycled pulsar becomes in the order of milliseconds, and hence, its called a millisecond pulsar (Alpar et al., 1982; Radhakrishnan & Srinivasan, 1982; Lorimer, 2009). If the companion star is massive enough and evolves very fast so that the duration of the mass-transfer phase is short, i.e., there is not enough transfer of angular momentum, a mildly-recycled pulsar is born with $P_{\rm s}$ in the range of 30 – 100 ms (Keith et al., 2009; Lazarus et al., 2014). This explains why most of the pulsars in double neutron star binaries are mildly recycled (Martinez et al., 2017). It is obvious that the second-born neutron star in a double neutron star system will not be recycled, i.e., if it is a pulsar, it will be a normal pulsar.

There are some millisecond pulsars that are found to exist without any orbiting companion, mostly inside globular clusters, but a few in the Galactic field as well. The ones in globular clusters can be explained by the knocking away of the companion by stars passing by very closely. For the ones in the Galactic field, it is hypothesized that during the course of time, the pulsars, originally in the binary system, might have completely ablated their companions with strong pulsar winds (Lorimer, 2008).

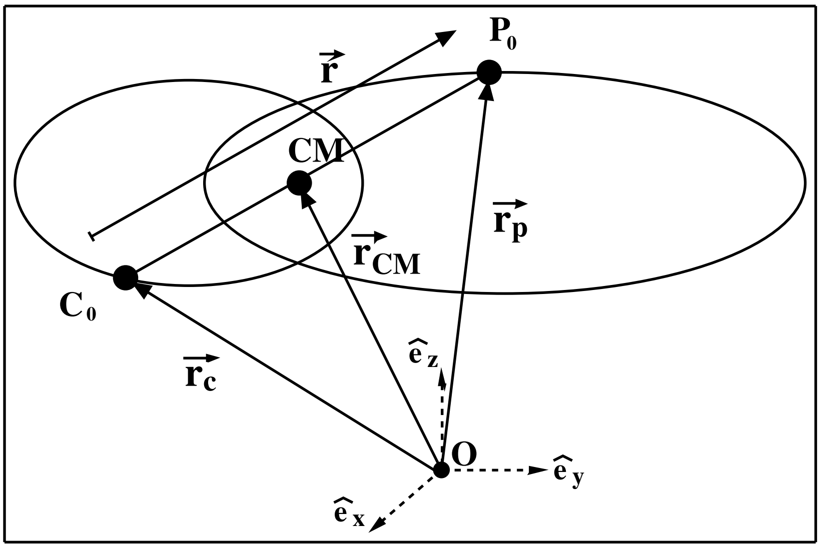

Figure 1.3: The schematic diagram of a binary pulsar system. P_0 denotes the pulsar, C_0 denotes the companion star, CM denotes the centre of mass of the binary system, O denotes the origin of a reference coordinate frame (denoted by the orthonormal unit vectors $\widehat{e_x}$, $\widehat{e_y}$ and $\widehat{e_z}$). $\vec{r}_p$ is the position vector of the pulsar, $\vec{r}_c$ is the position vector of the companion, $\vec{r}_{CM}$ is the position vector of the centre of mass of the binary system, and $\vec{r}$ is defined as $\vec{r}_p - \vec{r}_c$.

1.4.2 The Binary Orbit: A Central Force Problem

A schematic diagram of a binary pulsar system is shown in Fig. 1.3. In this figure, P_0 denotes the pulsar, C_0 denotes the companion star, CM denotes the centre of mass of the binary system, and O denotes the origin of a reference coordinate frame. $\vec{r}_p$ is the position vector of the pulsar, $\vec{r}_c$ is the position vector of the companion, $\vec{r}_{CM}$ is the position vector of the centre of mass of the binary system, and $\vec{r}$ is defined as $\vec{r}_p - \vec{r}_c$. We can study the two-body binary pulsar system as a one-body central force problem as discussed below.

The Lagrangian for the binary system is given by:

$$L = \frac{1}{2} m_p \dot{\vec{r}_p}^2 + \frac{1}{2} m_c \dot{\vec{r}_c}^2 + \frac{G m_p m_c}{|\vec{r}_p - \vec{r}_c|}, \tag{1.11}$$

where the pulsar and the companion masses are denoted by m_p and m_c respectively, and G is the gravitational constant.

From Fig. 1.3 and the definition of the centre of mass, we can write $\vec{r}_p = \vec{r}_{CM} + \frac{m_c}{M}\vec{r}$, and $\vec{r}_c = \vec{r}_{CM} - \frac{m_p}{M}\vec{r}$ where $M = m_p + m_c$ is the total mass. In case of a binary system free from any external influence, the centre of mass can be taken as stationary, i.e., $\dot{\vec{r}}_{CM} = 0$.

With these expressions, we can rewrite eq. (1.11) in terms of the separation $r = |\vec{r}|$, the total mass M, and the reduced mass $\mu = \frac{m_p m_c}{M}$, as,

$$\begin{aligned}
L =& \frac{1}{2} m_p \dot{\vec{r}}_p^{\,2} + \frac{1}{2} m_c \dot{\vec{r}}_c^{\,2} + \frac{G m_p m_c}{|\vec{r}_p - \vec{r}_c|} \\
=& \frac{1}{2} m_p \left(\frac{m_c}{M} \dot{\vec{r}} \right)^2 + \frac{1}{2} m_c \left(\frac{m_p}{M} \dot{\vec{r}} \right)^2 + \frac{G m_p m_c}{r} \\
=& \frac{1}{2} m_p m_c \left(\frac{m_p + m_c}{M^2} \right) \dot{\vec{r}}^2 + \frac{G m_p m_c M}{M r} \\
=& \frac{1}{2} \mu \dot{\vec{r}}^2 + \frac{G \mu M}{r}, \qquad (1.12)
\end{aligned}$$

which represents the Lagrangian of a fiducial body of mass μ in an orbit around the central force generating source of the effective mass M. The semi-major axis of the orbit of this fiducial body is related to the orbital period as:

$$P_{\mathrm{b}}^2 = \frac{4\pi^2}{GM} a^3 \ , \qquad (1.13)$$

which is the generalised form of the Kepler's third law. The semi-major axes of the pulsar's orbit (a_p) and the companion's orbit (a_c) are related by the expressions:

$$\begin{aligned}
a =& a_p + a_c \ , && (1.14) \\
a_p =& a \, \frac{m_c}{M} \ , \text{ and} && (1.15) \\
a_c =& a \, \frac{m_p}{M} \ . && (1.16)
\end{aligned}$$

It should be noted that, in reality, we observe the signal from the pulsar, not from the fiducial body of mass μ. Hence, we need to study the parameters for the orbit of the pulsar. The orbit of the pulsars is characterised by some geometrical parameters that will be discussed next.

A schematic diagram of a pulsar in an elliptical orbit in a binary system is shown in Fig. 1.4. Here, i is the angle of inclination of the orbital plane to the sky plane. A_T represents the true anomaly, which is the angle between the pulsar (P) and the periastron (L) at the

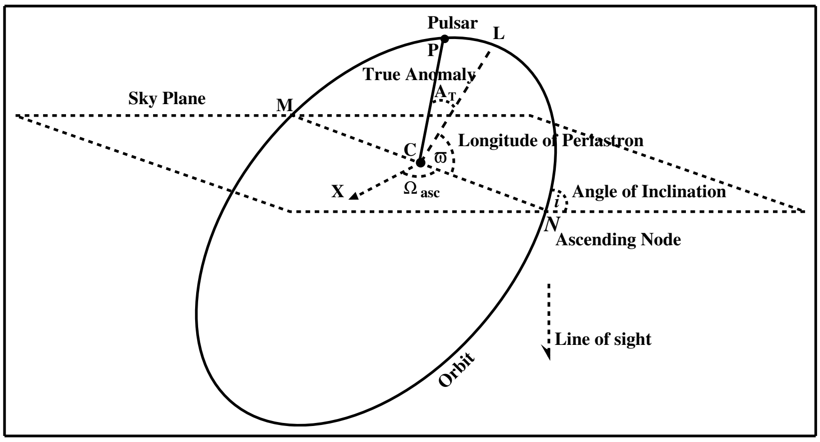

Figure 1.4: The schematic diagram of a pulsar (P) in an elliptical orbit with the centre of mass (C) as one of the focii. Here, i is the angle of inclination of the orbital plane to the sky plane. A_T represents the true anomaly, which is the angle between the pulsar (P) and the periastron (L) at the centre of mass (C). The ascending node (N) is the point on the orbit where the sky plane passing through the centre of mass appears to cut the orbital plane and the orbit appears to rise above at this point. The longitude of the ascending node, $\Omega_{\rm asc}$, represents the angle between the reference direction (X) and the ascending node (N) subtended at C in the sky plane. The longitude of the periastron, ϖ, is the angle between the semi-major axis and the line joining the ascending node to the centre of mass. The line of sight is perpendicular to the sky plane.

centre of mass (C). C is located at one of the focii of the orbital ellipse. The ascending node (N) is the point on the orbit where the sky plane passing through the centre of mass appears to cut the orbital plane and the orbit appears to rise above at this point with respect to the observer. The longitude of the periastron, ϖ, is the angle between the semi-major axis and the line joining the ascending node to the centre of mass. The line of sight is perpendicular to the sky plane. Fig. 1.4 also shows the longitude of the ascending node, $\Omega_{\rm asc}$, which represents the angle between the reference direction (X) and the ascending node (N) subtended at C in the sky plane. The reference direction is generally taken to be the perpendicular projection of the line joining the celestial north pole and the observer, on the sky plane.

As the pulsar moves in its orbit, it has orbital velocity, acceleration, jerk, etc. It is the line-of-sight components of these parameters that affect observable parameters. Hence, we first study the expressions for these higher time derivatives of the line-of-sight velocity (v_l), i.e., the line-of-sight acceleration ($a_l = dv_l/dt$), the line-of-sight jerk ($j_l = da_l/dt$), the line-of-sight jounce ($Jo_l = dj_l/dt$), the line-of-sight crackle ($Ck_l = dJo_l/dt$) and the line-of-sight pop ($Pop_l = dCk_l/dt$).

The equation for an elliptical orbit is known as:

$$r = a_p\left(1 - e^2\right)(1 + e\cos\,A_T)^{-1}\ , \tag{1.17}$$

where r is the magnitude of the radius vector, e is the eccentricity of the orbit, A_T is the true anomaly and a_p is the semi-major axis of the orbit. Here, the subscript 'p' stands for pulsar, although the analytical expressions derived in this section are valid for binary systems in general. The line-of-sight component of r is given by:

$$r_l = a'_p\left(1 - e^2\right)(1 + e\cos\,A_T)^{-1}\ \sin\left(A_T + \varpi\right), \tag{1.18}$$

where $a'_p = a_p\ \sin\,i$ is the projection of the semi-major axis to the plane containing the line of sight. Differentiating r_l with respect to time, we get,

$$v_l = a'_p\left(1 - e^2\right)[\cos\left(A_T + \varpi\right) + e\ \sin\ \varpi]\frac{\dot{A}_T}{(1 + e\cos\,A_T)^2}\ . \tag{1.19}$$

We further obtain an expression of $\dot{A}_T$ in terms of A_T and e by simultaneously solving the following Kepler's equations,

$$A_M = \frac{2\pi}{P_b}(t - T_o)\,, \tag{1.20a}$$

$$A_E - e\cos A_E = A_M\ ,\ \text{and} \tag{1.20b}$$

$$\tan\frac{A_T}{2} = \sqrt{\frac{1 + e}{1 - e}}\tan\frac{A_E}{2}\ , \tag{1.20c}$$

where A_M is the mean anomaly, P_b is the orbital period, A_E is the eccentric anomaly, T_o is the epoch of the periastron passage, and t is the time. Using the eqs. (1.20a), (1.20b), and (1.20c), we get,

$$\dot{A}_T = \frac{(1 + e\cos\,A_T)^2}{(1 - e^2)^{3/2}}\frac{2\pi}{P_b}\ . \tag{1.21}$$

Substituting the expression for $\dot{A}_T$ in eq. (1.19), we get,

$$v_l = \frac{2\pi}{P_b}\frac{a'_p}{\sqrt{1-e^2}}\left[\cos\left(A_T+\varpi\right)+e\,\sin\,\varpi\right] . \tag{1.22}$$

It should be noted that, here we take $\dot{e} = 0$, $\dot{\varpi} = 0$, and $\dot{P}_b = 0$. This is so because currently, we are considering a non-relativistic description of binary systems. Non-zero values of $\dot{e}$, $\dot{\varpi}$, and $\dot{P}_b$ are consequences of general relativity and are added separately as Post-Keplerian parameters that will be discussed later. These parameters are so small that they can be ignored over a few orbital cycles.

Continuing the time-differentiation, we get the higher order parameters as follows:

$$a_l = \dot{v}_l = -\left(\frac{2\pi}{P_b}\right)^2 \frac{a'_p}{\left(1-e^2\right)^2}\,\sin\left(A_T+\varpi\right)\left(1+e\,\cos\,A_T\right)^2 , \tag{1.23}$$

$$\begin{aligned} j_l = \dot{a}_l = -\left(\frac{2\pi}{P_b}\right)^3 \frac{a'_p}{\left(1-e^2\right)^{7/2}}\left(1+e\,\cos\,A_T\right)^3 &\left[\cos\left(A_T+\varpi\right)+e\,\cos\,\varpi\right. \\ &\left.-3e\,\sin\left(A_T+\varpi\right)\,\sin\,A_T\right] , \end{aligned} \tag{1.24}$$

$$\begin{aligned} Jo_l = \frac{dj_l}{dt} = \left(\frac{2\pi}{P_b}\right)^4 \frac{a'_p}{\left(1-e^2\right)^5}\left(1+e\,\cos\,A_T\right)^4 &\left[2e\sin\,A_T\,\cos\left(A_T+\varpi\right)+4e\sin\left(2A_T+\varpi\right)\right. \\ +\left(1-3e^2\right)\,\sin\left(A_T+\varpi\right)+\frac{3}{2}e^2\,\sin\left(3A_T+\varpi\right)&\left.+\frac{9}{2}e^2\,\cos\,2A_T\,\sin\left(2A_T+\varpi\right)\right] , \end{aligned} \tag{1.25}$$

$$\begin{aligned} Ck_l = \frac{dJo_l}{dt} = \left(\frac{2\pi}{P_b}\right)^5 \frac{a'_p}{\left(1-e^2\right)^{13/2}}\left(\frac{1}{8}\right)\left(1+e\,\cos\,A_T\right)^5 &\left[3e^2\left(9e^2-4\right)\cos\,\varpi\right. \\ -15e^3\cos\left(2A_T-\varpi\right)+10e^2\cos\left(A_T-\varpi\right)+\left(8-68e^2\right)\cos\left(A_T+\varpi\right)& \\ +\left(100e-45e^3\right)\cos\left(2A_T+\varpi\right)+210e^2\cos\left(3A_T+\varpi\right)+105e^3\cos\left(4A_T+\varpi\right)&\left.\right] , \end{aligned} \tag{1.26}$$

and

$$
\begin{aligned}
Pop_l = \frac{dCk_l}{dt} = \left(\frac{2\pi}{P_b}\right)^6 \frac{a'_p}{(1-e^2)^8} \left(\frac{1}{16}\right)(1 + e\cos A_T)^6 \Big[75e^4 \sin(3A_T - \varpi) \\
+(40e^2 - 210e^4)\sin(A_T - \varpi) + (32e - 272e^3)\sin\varpi \\
-(16 - 496e^2 + 270e^4)\sin(A_T + \varpi) - (448e - 1050e^2 + 42e^3)\sin(2A_T + \varpi) \\
-(1960e^2 - 420e^4)\sin(3A_T + \varpi) - (1050e^2 + 1470e^3)\sin(4A_T + \varpi) \\
-945e^4 \sin(5A_T + \varpi)\Big] \, . \quad (1.27)
\end{aligned}
$$

Although the expressions for v_l, a_l, j_l, Jo_l, and Ck_l were already known in the literature (Bassa et al., 2016), the expression for Pop_l is given for the first time.

1.5 Pulsar Timing Analysis

Pulsar timing is a powerful tool to study a wide range of physics, e.g., dense matter equations of state (Bagchi, 2018), properties of interstellar medium (Keith et al., 2013), alternative theories of gravity (Freire et al., 2012a; Bagchi and Torres, 2014), and even low-frequency gravitational waves (Detweiler, 1979). In this technique, pulse time of arrivals (ToAs) are measured and are compared with the pulse arrival times calculated from a pulsar timing model. The differences in these two times are called the timing residuals. The set of parameters that leads to a good fit between the expected pulse time of arrivals and the observed time of arrivals is called a timing solution. The timing solutions of radio pulsars contain various measured parameters such as the coordinates of the pulsar, the proper motion, the spin frequency and its derivatives, the dispersion measure, the parallax (not always), etc. In case of binary pulsars, timing solutions give Keplerian parameters like the orbital period, the orbital eccentricity, the longitude of periastron, the projected semi-major axis of the orbit, and the epoch of periastron passage as well as Post-Keplerian parameters like the time-derivative of the orbital period, the advance of the periastron, the shape the Shapiro delay, the range of the Shapiro delay, and the Einstein delay. Sometimes, even the higher-order time-derivatives of the spin and/or the orbital frequency are fitted.

1.6 Pulsar Parameters

Pulsars are characterized by various parameters. These include the spin period P_{s}, the spin period derivative $\dot{P}_{\mathrm{s}}$, the mass m_p, the radius R, the minimum dipolar magnetic field strength at the surface $B_{\mathrm{surface,min}}$, the braking index n, etc. The values of these parameters unveil intrinsic properties of the pulsar. Among these parameters, only P_{s} and $\dot{P}_{\mathrm{s}}$ are directly measurable through timing analysis, others can be inferred indirectly and will be discussed later. There are additional parameters that are not so inherent to pulsars. These include the location of the pulsar in the Galaxy, the parallax, the proper motion of the pulsar, the dispersion measure, etc. Pulsar timing analysis can measure either the equatorial coordinates (right ascension and declination) or the ecliptic coordinates (ecliptic longitude and latitude). These can be converted to the Galactic longitude and latitude, and even can pinpoint the location of the pulsar in the Galaxy if, in addition to those, the distance of the pulsar from the solar system is also known. The proper motion is the change in the location of the pulsar in the sky plane and is a result of the motion of the pulsar in the Galaxy. On the other hand, the parallax is the apparent change in the location of the pulsar due to the change in the line of sight (mainly caused by the earth's orbital motion). The dispersion measure is the column density of electrons of the interstellar medium, integrated along the line of sight and causes a differential arrival time of the same pulse at different frequencies.

As already mentioned, in the case of binary pulsars, there are additional parameters that can be categorized into i) Keplerian and ii) Post-Keplerian (PK). Keplerian parameters include the orbital period (P_b), the eccentricity (e), the longitude of the periastron (ϖ), the projection of the semi-major axis perpendicular to the sky plane (a'_p), the epoch of the periastron passage (T_o), and the longitude of the ascending node (Ω_{asc}). The PK parameters describe the relativistic effects on the orbit and cause deviations from the Keplerian picture. These include the rate of change of the orbital period ($\dot{P}_b$), the advance of the periastron ($\dot{\varpi}$), Einstein delay factor (γ), the range of Shapiro delay ($r_{\rm sh}$), and the shape of Shapiro delay ($s_{\rm sh}$).

The PK parameters can be written as (Lorimer and Kramer, 2005):

$$\dot{P}_{\rm b} = \dot{P}^{Q}_{\rm b,GW} = -\frac{192\pi}{5}\left(\frac{G\,M_{\odot}}{c^3}\right)^{5/3}\left(\frac{P_{\rm b}}{2\pi}\right)^{-5/3}\left(\frac{(1+(73/24)e^2+(37/96)e^4)}{(1-e^2)^{7/2}}\right)\left(\frac{m_{\rm p}\,m_{\rm c}}{(m_{\rm p}+m_{\rm c})^{1/3}}\right), \tag{1.28}$$

$$\dot{\varpi} = 3\left(\frac{G\,M_{\odot}}{c^3}\right)^{2/3}\left(\frac{P_{\rm b}}{2\pi}\right)^{-5/3}\frac{1}{1-e^2}(m_{\rm p}+m_{\rm c})^{2/3}\,, \tag{1.29}$$

$$\gamma = \left(\frac{G\,M_{\odot}}{c^3}\right)^{2/3}\left(\frac{P_{\rm b}}{2\pi}\right)^{1/3} e\frac{m_{\rm c}(m_{\rm p}+m_{\rm c})}{(m_{\rm p}+m_{\rm c})^{4/3}}\,, \tag{1.30}$$

$$r_{\rm sh} = \left(\frac{G\,M_{\odot}}{c^3}\right) m_{\rm c}\,, \tag{1.31}$$

and

$$s_{\rm sh} = \sin\,i = \left(\frac{G\,M_{\odot}}{c^3}\right)^{-1/3}\left(\frac{P_{\rm b}}{2\pi}\right)^{-2/3} a'_p\,\frac{(m_{\rm p}+m_{\rm c})^{2/3}}{m_{\rm c}}\,. \tag{1.32}$$

In eqs. (1.28), (1.29), (1.30), (1.31), and (1.32), $m_{\rm p}$ and $m_{\rm c}$ are the masses of the pulsar and the companion respectively, both in the unit of the solar mass, and $a'_p = a_p \sin i$. The value of $G\,M_{\odot}/c^3$ is $4.925490947\,\mu$s where G is the gravitational constant.

All these expressions were derived using the post-Newtonian approximation (to the lowest order) of general relativity. For some parameters, depending on the characteristics of the system, there might be additional classical or relativistic effects (Lorimer and Kramer, 2005). The expression for the rate of change of the orbital period as shown in eq. (1.28) has been derived with the assumption that it is caused solely due to the emission of quadrupolar gravitational waves (the only type of gravitational waves allowed by general relativity), and hence we could write $\dot{P}_{\mathrm{b}} = \dot{P}^{Q}_{\mathrm{b,GW}}$.

1.6.1 Estimation of Pulsar Parameters

Here, we briefly discuss methods to measure values of some of the parameters of pulsars.

- Astrometric parameters, spin parameters, and binary parameters: Astrometric parameters include positional coordinates of the pulsar, e.g., the right ascension (RA) and the declination (DEC) (or Ecliptic latitude and longitude), the proper motion (either in RA and DEC or in the ecliptic latitude and longitude), and the parallax. The spin parameters include the spin frequency and its derivatives. The binary parameters are the Keplerian as well as the PK parameters. In order to measure these parameters, we use pulsar timing which is a technique used for measurements of various pulsar parameters from the observational data of the time of arrival of pulses (see section 1.5).

- Distance: If the parallax is measured either through the timing analysis or by the very-long-baseline interferometry (VLBI) technique (Deller et al. (2019) and references therein), then the inverse of the parallax gives the distance of the pulsar (Lorimer and Kramer, 2005). Otherwise, the dispersion measure along with a model of the electron density of the interstellar medium can give an estimate of the distance (Lorimer and Kramer, 2005). Presently, two such models of the electron density are in use, one is the NE2001 model (Cordes and Lazio, 2002, 2003), and the other is the YMW16 model (Yao et al., 2017).

- Magnetic field strength: Cyclotron radiation spectra from accreting neutron stars forming X-ray binaries can lead to measurements of the surface magnetic field (B_{surface}). However, for radio pulsars no technique for direct measurement of the magnetic field is available. However, we can have an indirect estimation of the minimum value of the dipolar magnetic field at the surface of the pulsar using the relation given in eq. (1.7).

- Mass: The PK parameters (left hand sides of equations (1.28), (1.29), (1.30), (1.31), and (1.32)) are the functions of Keplerian parameters P_b, e, and a'_p, as well as m_p and m_c. Both Keplerian and PK parameters are measured in a timing analysis (might not be all PK parameters for every binary pulsar), but not m_p and m_c. However, here we have five equations with only these two unknowns (m_p and m_c). So, whenever we have measurements of at least two PK parameters, we can solve the equations for those PK parameters simultaneously to obtain the values of m_p and m_c. Therefore, the mass of the pulsars can be estimated only in case of binary pulsars (Lorimer and Kramer, 2005).

- Radius: Conventionally, luminosity observations were used to estimate the size of the emitting region. Observations carried out in the optical and X-ray regime of the spectrum were considered useful in estimating the radius of the neutron star (Lorimer and Kramer, 2005). Recently, X-ray timing analysis of the pulsed thermal X-ray emission from several millisecond pulsars using the data taken by NICER satellite provided measurements of the radius of several neutron stars (Bogdanov et al., 2019).

1.7 Pulsars As Tools To Study Gravitational Physics

Pulsars can be used as laboratories to study various aspects of fundamental physics such as the detection of gravitational waves and tests of general relativity (GR), as well as alternative theories of gravity.

1.7.1 Detection of Gravitational Waves

Pulsars can be used for the detection of different types of gravitational waves (GWs) like the continuous GWs from spinning pulsars (due to pulsars being deformed spheres), the short burst of GWs emitted during individual cases of inspiral and merger of binary pulsars, the isotropic stochastic gravitational waves background, GWs from individual supermassive black hole Binaries, and the GW memory from GW burst sources. For the first two types of sources, interferometric gravitational wave detectors like LIGO (Laser Interferometer Gravitational-Wave Observatory) and Virgo are used, whereas, for the last three types of sources, Pulsar Timing Arrays can be used (Lommen, 2015).

Pulsar Timing Array (PTA) is the experiment that carries out observations, using radio telescopes, of an ensemble of millisecond pulsars scattered across the observable Galactic coordinates for the detection of the above-mentioned GW signals. There are three main established PTA consortia- the European Pulsar Timing Array (EPTA), the North American Nanohertz Observatory for Gravitational Waves (NANOGrav), and the Parkes Pulsar Timing Array (PPTA). These three PTAs and additionally a comparatively new Indian Pulsar Timing Array (InPTA) together form a consortium of consortia called the International Pulsar Timing Array (IPTA) (Perera et al., 2019; Joshi et al., 2018). There are two more emerging PTAs, the South African PTA (SPTA) and the Chinese PTA (CPTA) that are associated members of IPTA.

GWs cause perturbations in the space-time fabric, which is then manifested as small perturbations in the time of arrival (ToA) measurements of pulses from pulsars. The resulting redshift ($z(t)$) due to the fractional change in the pulse frequency is given by,

$$z(t) = \frac{\nu_0 - \nu(t)}{\nu_0} = \frac{1}{2}\frac{\alpha^2 - \beta^2}{1+\gamma}\Delta h_+ + \frac{\alpha\beta}{1+\gamma}\Delta h_\times \, , \tag{1.33}$$

where ν_0 is the initial pulse frequency, $\nu(t)$ is the pulse frequency at time t, (α, β, γ) are the direction cosines of the GW propagating in the z-direction. $\Delta h_{(+,\times)} = h^{\mathrm{P}}_{(+,\times)} - h^{\mathrm{E}}_{(+,\times)}$, where $(+, \times)$ are the polarizations of the GW, and $h^{\mathrm{P}}_{(+,\times)}(t - d/c)$ and $h^{\mathrm{E}}_{(+,\times)}(t)$ are gravitational wave strain values at the pulsar (at a distance d) and the earth, respectively (Manchester, 2015). $h^{\mathrm{P}}_{(+,\times)}$ signals remain uncorrelated from pulsar to pulsar, whereas $h^{\mathrm{E}}_{(+,\times)}$ signals are correlated over a pair of pulsars due to the presence of GWs. PTAs aim to detect this correlation over an ensemble of pulsars for the detection of GWs. PTAs can detect the stochastic gravitational waves background in nanohertz regime and the corresponding GW amplitude is represented in the form of a dimensionless 'characteristic strain' given as a function of frequency of the GWs (f_{gw}) by,

$$h_c(f_{\mathrm{gw}}) \approx 10^{-15} \left(\frac{f_{\mathrm{gw}}}{\mathrm{yr}^{-1}} \right)^{-2/3} . \tag{1.34}$$

1.7.2 Tests of gravity theories

Pulsar timing is also used for tests of various theories of gravity. The tests of gravity theories can be divided into tests of GR and tests of alternative theories of gravity. Tests of GR can further be categorized as being about i) matching the measured values of PK parameters from pulsar timing with those predicted using GR (also called the Strong field gravity tests), or ii) putting constraints on the parameters that denote the violation of GR, especially, the Strong Equivalence Principle (SEP) (Stairs, 2003). The parametrized post-Newtonian (PPN) formalism was developed to facilitate the comparison among various gravity theories by Will and Nordtvedt (1972). The constraints on PPN parameters serve as constraints on various GR violation effects too. We briefly discuss some of these tests below.

1.7.2.1 Test of GR: Strong field gravity tests

As already mentioned, for binary pulsars, PK parameters can be measured through timing analysis of the pulsars. Using eqs. (1.28), (1.29), (1.30), (1.31), and (1.32), the measured values of PK parameters are plotted as curves in the $m_p - m_c$ phase space as values of P_{b}, e and a'_p are also measured. If the post-Newtonian approximation of GR is correct, then all such curves should intersect at a particular point representing the true mass of the pulsar and the companion. Fig. 1.5 shows one such example of a mass-mass diagram of PSR J0737−3039A/B, where the PK parameters agree with GR predictions within an uncertainty of 0.05% (Kramer et al., 2006). However, an important point to consider here is the fact that the measured values of $\dot{P}_b$, one of the best measured PK parameters, is generally contaminated by the dynamics of the pulsar. These dynamical effects need to be subtracted from the measured values of $\dot{P}_b$ before using PK parameters for the measurement of masses and the strong field tests of gravity.

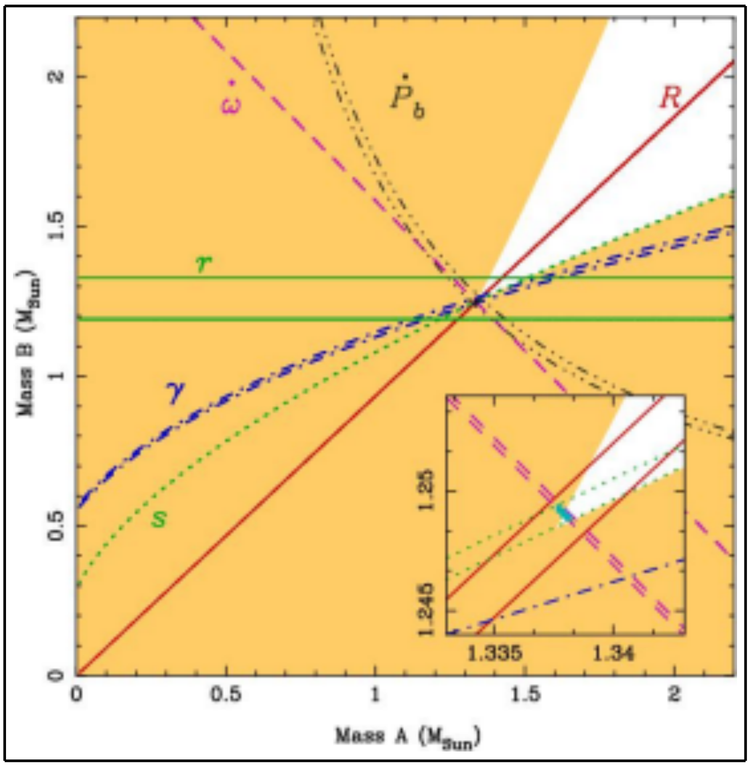

Figure 1.5: Mass-mass diagram of PSR J0737−3039A/B (Kramer et al., 2006). This diagram shows the measured values of PK parameters plotted as functions of masses. The PK parameters shown are the derivative of the orbital period $\dot{P}_b$, Einstein delay factor γ, the advance of the periastron $\dot{\varpi}$, the Shapiro delay parameters- the range r_{sh} and the shape s_{sh}. The last three parameters are denoted by '$\dot{\omega}$', 'r', and 's', respectively in the plot. As for this system, both members of the binary are pulsars, one additional parameter R that represents the mass ratio obtained from the ratio of the projected semi-major axes of the orbits of the two members of the binary, was measured and plotted. The separation of parallel lines corresponding to a parameter represents the measurement uncertainty in that parameter. The small turquoise region residing in the intersection of pairs of lines denotes the measurement precision of the masses of the components of the binary system.

1.7.2.2 Test of GR: Violation of SEP

The two equivalence principles are the two main components of GR. The Weak Equivalence Principle (WEP) states that objects of different compositions and masses experience the same acceleration in an external gravitational field (also interpreted as the universality of free fall or UFF). The Strong Equivalence Principle (SEP) incorporates the WEP and adds to it the existence of a local Lorentz frame (where laws of special relativity are valid) in an external gravitational field. SEP also includes the local Lorentz invariance, i.e., the outcome of any local experiment is independent of the velocity of the freely falling frame, and the local position invariance, i.e., the outcome of any local experiment is independent of where and when it is performed. We mention here some of the tests on violation of SEP and its consequences.

- Test of Strong field extension of Nordtvedt effect: In a binary system, if SEP is violated, then the two members of the system would experience different acceleration from the external gravitational field of the Galaxy and consequently the orbit will be polarized. This is known as the Nordtvedt effect (Nordvedt, 1968). In the case of SEP violation, there is also a difference in the gravitational mass of a body and its inertial mass. Damour & Schäfer (1991) considered the strong field extension of the Nordtvedt effect and suggested that this would lead to a forced eccentricity in the direction of the gravitational force from the Galaxy. The expression for this forced eccentricity ($e_{\rm F}$) induced in the orbit of the pulsar is given by:

  $$\vec{e}_{\rm F} = \frac{3}{2}\frac{\vec{g}_{\perp}\,\Delta}{\dot{\varpi}\,a_p\,(2\pi/P_{\rm b})}\,, \tag{1.35}$$

  where the projection of the gravitational field of the Galaxy onto the orbital plane of the pulsar is denoted by $\vec{g}_{\perp}$. We also define $\Delta = \Delta_{pulsar} - \Delta_{companion}$, such that for the i^{th} body, Δ_i represents the fractional difference between the gravitational mass (m_g) and the inertial mass (m_{in}) of the body (which is zero if SEP is valid). The expression for Δ_i is,

$$\Delta_i = \left(\frac{m_g}{m_{in}}\right)_i - 1 = \eta \left(\frac{E_{grav}}{m_{in}\, c^2}\right)_i + \eta' \left(\frac{E_{grav}}{m_{in}\, c^2}\right)_i^2 \dots \ . \tag{1.36}$$

Here, η is the Nordtvedt parameter and is a combination of PPN parameters, η' is another dimensionless parameter that denotes the strong field extension of the Nordtvedt effect and its expression depends on the 2PN theory-specific framework (Freire et al., 2012b). E_{grav} is the gravitational self-energy of the body. Timing analysis of pulsars in binary systems can sometimes put constraints on the Nordtvedt parameter (Manchester, 2015).

- Test of violation of the Local Lorentz Invariance (LLI): LLI violations also produce forced eccentricity whose expression is analogous to the one produced in the Nordtvedt effect. This forced eccentricity also depends on the PPN parameters, which can be constrained through the timing analysis of binary pulsars (Manchester, 2015).

- Test of constancy of the gravitational constant: Gravity theories that violate SEP can also cause the gravitational constant G to vary with time. A time-varying G will contribute to the orbital period decay as,

$$\frac{\dot{P}_{\mathrm{b}}}{P_{\mathrm{b}}} = -2\frac{\dot{G}}{G} \ . \tag{1.37}$$

  Timing solutions of binary pulsars can provide measured P_{b} and $\dot{P}_{\mathrm{b}}$ values that can put constraint on the ratio of $\frac{\dot{G}}{G}$ (Stairs, 2003). It should be noted that here one should use the corrected value of $\dot{P}_{\mathrm{b}}$ obtained after eliminating the dynamical effects from the measured value.

1.7.2.3 Test of scalar-tensor and scalar-vector-tensor theories of gravity

In the case of scalar-tensor theories of gravity, scalar fields couple to the metric tensor fields through a coupling function. Similarly, in the case of scalar-vector-tensor theories of gravity, additional vector fields couple to the metric tensor fields through a coupling function. The coupling constants, defined from the coupling functions in terms of the asymptotic values of the coupled fields, appear in the expressions of some PPN parameters as well as PK parameters derived from those theories of gravity. Constraints from observations on those PPN and PK parameters, help us put constraints on the coupling constants. These theories may violate SEP and may also lead to other effects like the time-variation of G and emission of dipolar gravitational waves (Damour, 2009).

1.8 Braking Index as a Probe to Structural Properties of Pulsars

The braking index (n) of a pulsar acts as an indicator of the kind of spin-down mechanism followed by the pulsar. As mentioned earlier, if we consider a pulsar to be an ideal rotating magnetic dipole, its braking index turns out to be three. However, in reality, pulsars exhibit braking indices, calculated based on the measured values of the first and the second derivatives of the spin frequency in eq. (1.5), in a wide range. Various people have tried to find the physical reason for the deviation of n from three (Hobbs et al., 2004; Ho and Andersson, 2012; Dang et al., 2020). Hobbs et al. (2004) reported measurements of n for 374 pulsars. They found that the reported values of n for a number of pulsars lie in the range of -2.6×10^8 to 2.5×10^8. These large deviations from the expected value of three cannot be due to the timing noise as they had taken care of it by whitening the timing residuals. Dang et al. (2020) suggested that the measured values of the braking index are affected by the glitch[4] recovery in the case of pulsars with $\tau_c < 10^5$ yrs, while for pulsars with $\tau_c \gtrsim 10^5$ yrs, the measured values of the braking index are contaminated by the red timing noise. A red noise is a noise with more power at lower frequencies in the power spectrum of the timing residual. The possible reasons for this red timing

---

[4] Glitches are the sudden increase in the spin frequency of pulsars owing to the rotational instabilities whose origin lie in the structural properties of pulsars.

noise, as suggested by Dang et al. (2020), can be due to fluctuations in the magnetic inclination angle, in the magnetosphere of the pulsar, or in the rate of transfer of the angular momentum from the superfluid in the interior of the neutron star to its crust. The study of these fluctuations can give an insight into the structure of pulsars, for which knowing the correct value of the braking index is essential. The first step to obtain a correct value of the braking index is to use the correct values of the spin frequency and its derivatives in eq. (1.5).

1.9 The Dynamical Effects

We have seen that the accurate knowledge of the values of the spin frequency and its derivatives is important in some studies of structural properties of pulsars, e.g., studies that involve the braking index, etc. Furthermore, accurate knowledge of the values of the orbital period and its derivatives is essential to study gravitational physics. However, the values of the derivatives of the spin frequency and the orbital frequency (in the case of a binary pulsar) measured in a timing analysis do not represent the values intrinsic to the pulsar system. To establish this fact, we will present some extreme examples in the next paragraph. It is noteworthy to mention here the fact that through the process of timing analysis, one fits values of the spin frequency and its derivatives, while in the case of orbital parameters, fits the values of the orbital period and its first derivative. However, for some cases, especially when higher derivatives are needed to obtain a good timing solution, the orbital frequency and its derivatives are fitted (Crawford et al., 2013; Deneva et al., 2016; Shaifullah et al., 2016; Ridolfi et al., 2016; Freire et al., 2017). That is why in the present thesis, we worked both in the period and frequency domain. In particular, when we investigate the effect of the dynamics on the second derivatives, we work in the frequency domain, as, whether the spin or the orbital, it is the frequency whose second derivatives are fitted in a timing analysis. So, results of the timing analysis can be used directly in our expressions without the need of the conversion from the period domain to the frequency domain or vice versa using the relations: $P_{\rm s} = 1/f_{\rm s}$, $\dot{P}_{\rm s} = -\dot{f}_{\rm s}/f_{\rm s}^2$, $\ddot{P}_{\rm s} = 2\dot{f}_{\rm s}^2/f_{\rm s}^3 - \ddot{f}_{\rm s}/f_{\rm s}^2$, and $\dot{P}_{\rm b} = -\dot{f}_{\rm b}/f_{\rm b}^2$, $\dot{P}_{\rm b} = -\dot{f}_{\rm b}/f_{\rm b}^2$, $\ddot{P}_{\rm b} = 2\dot{f}_{\rm b}^2/f_{\rm b}^3 - \ddot{f}_{\rm b}/f_{\rm b}^2$.

We have already mentioned that the emission of the electromagnetic waves causes the pulsar to slow down, i.e., $P_{\rm s}$ to increase with time (see eq. 1.1). In reality, there might be additional forms of energy losses from pulsars, e.g., the emission of continuous gravitational waves from the rotationally deformed pulsars, the loss of charged particles from the magnetosphere of the pulsar in the form of winds, etc. All of these would make $P_{\rm s}$ to increase with time, i.e., the value of $\dot{P}_{\rm s}$ would be positive for non-accreting rotation powered pulsars[5].

Similarly, we have seen that the emission of the gravitational waves causes the orbital period to decrease with time, i.e., $\dot{P}_{\rm b}$ is negative. Note that, there might be other phenomena that can cause $P_{\rm b}$ of a binary to change differently. Some examples of such phenomena are the mass transfer from one member to another, the tidal interaction between the members of the binary, etc. However, most of the known radio pulsars are in binaries where these processes do not take place. Hence, for binary radio pulsars $\dot{P}_{\rm b}$ is expected to be negative.

The signs of the measured values of $\dot{P}_{\rm s}$ and $\dot{P}_{\rm b}$ usually comply with these expectations. There are, however, some pulsars with the measured values of the rate of change of the spin period as negative quantities, e.g., PSRs J1144-6146 and J1801-3210 (Manchester et al., 2005). Likewise, there are some pulsars with the measured values of the rate of change of the orbital period being positive, e.g., PSRs J0613-0200 and J1012+5307 (Manchester et al., 2005).

It is known that the observed values of the rate of change of the orbital and the spin frequencies of pulsars are affected by dynamical parameters of the pulsars, e.g., the relative velocity, acceleration, jerk, etc. of the pulsar with respect to the Solar system barycentre

---

[5] When a neutron star accretes matter from its binary companion, it gets spun-up due to the transfer of the angular momentum, i.e., $\dot{P}_{\rm s}$ becomes negative. However, such pulsars emit X-ray pulses instead of radio pulses and are not being studied in the present thesis.

along the line of sight. The gravitational potential of the Galaxy plays a significant role in imparting the acceleration and jerk to pulsars (Damour & Taylor (1991); Nice & Taylor (1995) and references therein).

This thesis studies these dynamical effects in the first and the second time-derivatives of the frequencies or periods (both the spin and the orbital). It also presents accurate methods to eliminate these dynamical terms facilitating estimation of the true values of these derivatives that would enable people to probe fundamental physics with pulsars.

1.10 Structure of the Thesis

In the second chapter, we present analytical derivations of the dynamical terms contributing to the measured values of the derivatives of the frequency, in terms of the observable parameters like the Galactic longitude, the Galactic latitude, the distance, the proper motion in the Galactic longitude and latitude, the relative radial velocity of the pulsar with respect to the solar system barycentre, and the observed (measured) values of the frequency and its derivatives.

In the third chapter, we present the numerical works done to eliminate the dynamical effects in the first derivative of the period (either the spin or the orbital). We describe a python-based package 'GalDynPsr' that we created for this purpose in this chapter. GalDynPsr has several methods to compute the dynamical contribution in the derivative of the period due to the relative acceleration. Some of the methods involve traditional approximate methods and some are new methods based on a realistic model of the gravitational potential of the Galaxy. There are some mixed models too. These methods are discussed in detail and the results obtained by various methods are compared. The new method is superior to older ones.

In chapter four, we describe the numerical works done in order to eliminate the dynamical effects in the second derivative of the frequency (either the spin or the orbital). We introduce ‘GalDynPsrFreq’, a python package to estimate the dynamical terms in the first and the second time-derivative of the frequency (both spin and orbital). In this chapter, we also investigate how dynamical terms can affect the measured values of the braking index and we also explore the contributions from the dynamical terms to the second derivative of orbital frequencies.

In chapter five, we present the conclusions of this PhD work.

Bibliography

Alpar, M. A., Cheng, A. F., Ruderman, M. A., Shaham, J., 1982. A new class of radio pulsars. Nature, 300, 728. https://doi.org/10.1038/300728a0.

Bagchi, M. and Torres, D., 2014. In what sense a neutron star-black hole binary is the holy grail for testing gravity? JCAP. 08, 055. https://doi.org/10.1088/1475-7516/2014/08/055.

Bagchi, M., 2018. Prospects of Constraining the Dense Matter Equation of State from Timing Analysis of Pulsars in Double Neutron Star Binaries: The Cases of PSR J0737−3039A and PSR J1757−1854. Universe. 4, 36. https://doi.org/10.3390/universe4020036.

Balberg, S., Lichtenstadt, I., Cook, G.B., 1999. Roles of Hyperons in Neutron Stars. ApJS. 121, 515. https://doi.org/10.1086/313196.

Bassa, C. G., Janssen, G. H., Stappers, B. W., Tauris, T. M., & Wevers, T., 2016. A millisecond pulsar in an extremely wide binary system. MNRAS. 460, 2207-2222. https://doi.org/10.1093/mnras/stw1134.

Bhattacharya, D., Wijers, R. A. M. J., Hartman, J. W., Verbunt, F., 1992. On the decay of the magnetic fields of single radio pulsars. A&A. 254, 198. https://ui.adsabs.harvard.edu/abs/1992A%26A...254..198B/abstract.

Blandford, R. D., Applegate, J. H., & Hernquist, L., 1983. Thermal origin of neutron star magnetic fields. MNRAS. 204, 1025-1048. https://doi.org/10.1093/mnras/204.4.1025.

Bogdanov, S., Guillot, S., Ray, P. S., Wolff, M. T., Chakrabarty, D. et. al., 2019. Constraining the Neutron Star Mass-Radius Relation and Dense Matter Equation of State with NICER. I. The Millisecond Pulsar X-Ray Data Set. ApJ. 887, L25. https://doi.org/10.3847/2041-8213/ab53eb.

Cordes, J. M., Lazio, T. J. W., 2002. NE2001.I. A New Model for the Galactic Distribution of Free Electrons and its Fluctuations. preprint(arXiv:astro-ph/0207156).

Cordes, J. M., Lazio, T. J. W., 2003. NE2001. II. Using Radio Propagation Data to Construct a Model for the Galactic Distribution of Free Electrons. preprint(arXiv:astro-ph/0301598).

Crawford, F. et al., 2013. PSR J1723−2837: An Eclipsing Binary Radio Millisecond Pulsar. ApJ. 776, 20-31. https://doi.org/10.1088/0004-637X/776/1/20.

Couch, S. M., 2017. The mechanism(s) of core-collapse supernovae. Phil. Trans. R. Soc. A, 375, 20160271. http://dx.doi.org/10.1098/rsta.2016.0271

Damour, T., 2009. Binary Systems as Test-Beds of Gravity Theories. In: Colpi M., Casella P., Gorini V., Moschella U., Possenti A. (eds) Physics of Relativistic Objects in Compact Binaries: From Birth to Coalescence. Astrophysics and Space Science Library, 359. Springer, Dordrecht. https://doi.org/10.1007/978-1-4020-9264-0_1.

Damour, T., & Schäfer , G., 1991. New tests of the strong equivalence principle using binary-pulsar data . Phys Rev Lett. 66, 2549. https://doi.org/10.1103/PhysRevLett.66.2549.

Damour, T., & Taylor, J. H., 1991. On the Orbital Period Change of the Binary Pulsar PSR 1913+16. ApJ. 366, 501. https://doi.org/10.1086/169585.

Dang, S. J. et al., 2020. Results of 12 Years of Pulsar Timing at Nanshan . I. ApJ. 896, 140-160. https://doi.org/10.3847/1538-4357/ab9082.

Deneva, J. S. et al., 2016. Multiwavelength Observations of the Redback Millisecond Pulsar J1048+2339. ApJ. 823, 105-118. https://doi.org/10.3847/0004-637X/823/2/105.

Deller, A. T. et al., 2019. Microarcsecond VLBI Pulsar Astrometry with PSRΠ II. Parallax Distances for 57 Pulsars. ApJ, 875, 100. https://doi.org/10.3847/1538-4357/ab11c7.

Detweiler, S., 1979. Pulsar timing measurements and the search for gravitational waves. ApJ. 234, 1100. https://doi.org/10.1086/157593.

EMF in your Environment- Magnetic Field Measurements of Everyday Electrical Devices. EPA. 1992, ISBN 9780160362828. https://nepis.epa.gov/Exe/ZyPDF.cgi/000005EP.PDF?Dockey=000005EP.PDF.

Fryer, C. L., 1999. Mass Limits For Black Hole Formation. ApJ. 522, 413. https://doi.org/10.1086/307647.

Freire, P. C. C. et al., 2012a. The relativistic pulsar-white dwarf binary PSR J1738+0333 – II. The most stringent test of scalar-tensor gravity. MNRAS. 423, 3328-3343. https://doi.org/10.1111/j.1365-2966.2012.21253.x.

Freire, P. C. C., Kramer, M., & Wex, N., 2012b. Tests of the universality of free fall for strongly self-gravitating bodies with radio pulsars. Classical and Quantum Gravity. 29, 184007. https://doi.org/10.1088/0264-9381/29/18/184007.

Freire, P. C. C., Ridolfi, A., Kramer, M., Jordan, C., Manchester, R. N. et al., 2017. Long-term observations of the pulsars in 47 Tucanae - II. Proper motions, accelerations and jerks. MNRAS. 471, 857-876. https://doi.org/10.1093/mnras/stx1533.

Gauger, J. R., 1985. Household Appliance Magnetic Field Survey. IEEE Transactions on Power Apparatus and Systems. PAS-104, 2435. https://doi.org/10.1109/TPAS.1985.318988.

Ho, W. C. G., Andersson, N., 2012. Rotational evolution of young pulsars due to superfluid decoupling. NatPh. 8, 787-789. https://doi.org/10.1038/nphys2424.

Hobbs, G., Lyne, A. G., Kramer, M., Martin, C. E., Jordan, C., 2004. Long-term timing observations of 374 pulsars. MNRAS 353, 1311-1344. https://doi.org/10.1111/j.1365-2966.2004.08157.x.

Joshi, B. C., Aramugasamy, P., Bagchi, M., Bandopadhyay, D., Basu, A. et al., 2018. Precision pulsar timing with the ORT and the GMRT and its applications in pulsar astrophysics. J Astrophys Astron. 39, 51. https://doi.org/10.1007/s12036-018-9549-y.

Keith, M. J., Kramer, M., Lyne, A. G., Eatough, R. P., Stairs, I. H. et al., 2009. PSR J1753-2240: a mildly recycled pulsar in an eccentric binary system. MNRAS. 393, 623. https://doi.org/10.1111/j.1365-2966.2008.14234.x.

Keith, M. J. et al., 2013. Measurement and correction of variations in interstellar dispersion in high-precision pulsar timing. MNRAS. 429, 2161-2174. https://doi.org/10.1093/mnras/sts486.

Konar, S., 2017. Magnetic Fields of Neutron Stars. JoAA. 38, 47. https://doi.org/10.1007/s12036-017-9467-4.

Kramer, M., Stairs, I. H., Manchester, R. N., McLaughlin, M. A., Lyne, A. G. et al., 2006. Tests of General Relativity from Timing the Double Pulsar. Science. 314, 97. https://doi.org/10.1126/science.1132305.

Lazarus, P., Tauris, T. M., Knispel, B., Freire, P. C. C., Deneva, J. S. et al., 2014. Timing of a young mildly recycled pulsar with a massive white dwarf companion. MNRAS. 437, 1485. https://doi.org/10.1093/mnras/stt1996.

Lommen, A. N., 2015. Pulsar timing arrays: the promise of gravitational wave detection. RPPh, 78, 124901. https://doi.org/10.1088/0034-4885/78/12/124901.

Lorimer, D. R., 2008. Binary and Millisecond Pulsars. Living Rev. Relativ. 11, 8. https://doi.org/10.12942/lrr-2008-8.

Lorimer, D., Kramer, M., 2005. Handbook of Pulsar Astronomy, Cambridge Observing Handbooks for Research Astronomers. Cambridge Univ. Press, Cambridge, UK.

Lorimer, D., 2009. Radio Pulsar Statistic. In Neutron Stars and Pulsars, Astrophysics and Space Science Library, 357, Editor Becker, W. Springer. https://doi.org/10.1007/978-3-540-76965-1.

Manchester, R. N., 2015. Pulsars and Gravity. IJMPD. 24, 1530018. https://doi.org/10.1142/S0218271815300189.

Manchester, R. N., Hobbs, G. B., Teoh, A., Hobbs, M., 2005. The Australia Telescope National Facility Pulsar Catalogue. AJ. 129, 1993-2006. Online version http://www.atnf.csiro.au/people/pulsar/psrcat/. https://doi.org/10.1086/428488.

Martinez, J. G., Stovall, K., Freire, P. C. C., Deneva, J. S., Tauris, T. M. et al., 2017. Pulsar J1411+2551: A Low-mass Double Neutron Star System. ApJ. 851, L29. https://doi.org/10.3847/2041-8213/aa9d87.

Matzka, J., Chulliat, A., Mandea, M., Finlay, C. C., Qamili, E., 2010. Geomagnetic Observations for Main Field Studies: From Ground to Space. Space Sci Rev. 155, 29. https://doi.org/10.1007/s11214-010-9693-4.

Nice, D. J., & Taylor, J. H., 1995. PSR J2019+2425 and PSR J2322+2057 and the Proper Motions of Millisecond Pulsars. ApJ. 441, 429. https://doi.org/10.1086/175367.

Nordvedt, K., 1968. Equivalence Principle for Massive Bodies. I. Phenomenology. Phys Rev. 169, 1014. https://doi.org/10.1103/PhysRev.169.1014.

Nowogrodzki, A., 2018. The world's strongest MRI machines are pushing human imaging to new limits. Nature. 563, 24. https://doi.org/10.1038/d41586-018-07182-7.

Perera, B. B. P., DeCesar, M. E., Demorest, P. B., Kerr, M., Lentati, L. et al., 2019. The International Pulsar Timing Array: second data release. MNRAS. 490, 4666. https://doi.org/10.1093/mnras/stz2857.

Radhakrishnan, V., Srinivasan, G., 1982. On the origin of the recently discovered ultra-rapid pulsar. Current Science, 51, 1096-1099. https://www.jstor.org/stable/24087904.

Ransom, S. M., Stairs, I. H., Archibald, A. M., Hessels, J. W. T., Kaplan, D. L. et al. 2014. A millisecond pulsar in a stellar triple system. Nature. 505, 520. https://doi.org/10.1038/nature12917.

Ridolfi, A. et al., 2016. Long-term observations of the pulsars in 47 Tucanae - I. A study of four elusive binary systems. MNRAS. 462, 2918-2933. https://doi.org/10.1093/mnras/stw1850.

Shaifullah, G. et al., 2016. 21 year timing of the black-widow pulsar J2051−0827. MNRAS. 462, 1029-1038. https://doi.org/10.1093/mnras/stw1737.

Sigurdsson, S., Richer, H. B., Hansen, B. M., Stairs, I. H., Thorsett, S. E., 2003, A Young White Dwarf Companion to Pulsar B1620-26: Evidence for Early Planet Formation. Science. 301, 193. https://doi.org/10.1126/science.1086326.

Slocum, A. H., 1992. Precision Machine Design. Society of Manufacturing. ISBN: 0872634922,9780872634923.

Spruit, H. C., 2008. The source of magnetic fields in (neutron-) stars. Cosmic Magnetic Fields: From Planets, to Stars and Galaxies, Proceedings of the International Astronomical Union, IAU Symposium. 4, 61. https://doi.org/10.1017/S1743921309030075.

Stairs, I.H., 2003. Testing General Relativity with Pulsar Timing. Living Rev. Relativity, 6, 5. [Online Article]: cited on 15/01/2021, http://www.livingreviews.org/lrr-2003-5/.

Vidaña, I., 2016. Hyperons in Neutron Stars. J. Phys.: Conf. Ser. 668, 012031. https://doi.org/10.1088/1742-6596/668/1/012031.

Vidaña, I., 2018. A short walk through the physics of neutron stars. EPJP. 133, 445. https://doi.org/10.1140/epjp/i2018-12329-x.

Will, C. M., Nordtvedt, K. J., 1972. Conservation Laws and Preferred Frames in Relativistic Gravity. I. Preferred-Frame Theories and an Extended PPN Formalism. ApJ. 177, 757. https://doi.org/10.1086/151754.

Yao, J. M., Manchester, R. N., Wang, N., 2017. A New Electron-density Model for Estimation of Pulsar and FRB Distances. ApJ. 835, 29-60. https://doi.org/10.3847/1538-4357/835/1/29.

Chapter 2

Dynamical Effects in Frequency Derivatives (Spin and Orbital): Analytical Description

2.1 Introduction

In Chapter 1 of the present thesis, we have discussed how various parameters can be measured through the timing analysis of a pulsar. Among all these parameters, the measured values of the time-derivatives of the frequency or the period (both the spin and the orbital) play crucial roles in revealing properties of pulsars and their evolutionary histories, and, assist in testing postulates of fundamental physics. However, to achieve these goals, it is essential to estimate the ‘true’ or ‘intrinsic’ values of these parameters precisely by understanding and eliminating external factors as accurately as possible. In the process of pulsar timing analysis, although one fits the values of the spin frequency and its derivatives, it is the period and its derivative that are generally fitted when it comes to the orbital parameters. However, for some cases, especially when higher derivatives are needed to obtain a good timing solution, orbital frequency and its derivatives are fitted. So, we aim to devise formalisms to estimate the intrinsic values of the first derivative of the period and the first and the second derivatives of frequencies so that our formalisms can be used directly without the need for conversion of the period to the frequency or vice versa.

We know that for a clean binary system, i.e., where gravity is the only interaction between the pulsar and its companion and both of them can be treated as point-like objects, it is believed that the orbital period decreases due to the emission of gravitational waves[1], and hence the rate of change of the orbital period must be negative. On the other hand, the existence of various forms of energy loss from pulsars, e.g., the emission of electromagnetic waves, the emission of winds of charged particles, the expected emission of continuous gravitational waves due to the rotational deformation of the pulsar, etc., lead to the expectation of the rate of change of the spin-periods of the non-accreting rotation powered radio pulsars to be positive. The signs of the measured rate of change of the orbital and the spin periods usually comply with these expectations, although there are a few exceptions for both of the parameters. These exceptions are explained as results of external effects, some of which will be discussed in this thesis. The values of the rate of change of the spin frequency and the orbital periods are very small, still, these can be measured accurately if a timing campaign is pursued long enough. For instance, 15-years of data of PSR J0437−4715 by the Parkes Pulsar Timing Array enabled the measurements of both of the derivatives very accurately, e.g., the rate of change of the spin frequency as $-1.728361(5) \times 10^{-15}$ s^{-2} and the rate of change of the orbital period as $3.728(6) \times 10^{-12}$ ss^{-1}(Reardon et al., 2016). Such accurate measurements would be useless if the knowledge of the external factors is not accurate enough. The Doppler shift is one of these external factors. Like other periodic functions, both the spin and the orbital periods (or the frequencies) experience the Doppler shift due to the relative motion between the pul-

---

[1] Otherwise, various other phenomena might cause the orbital period to change, e.g., the mass loss from the binary, tidal interactions between the members of the binary, etc. The changes of the orbital period due to such processes would be different from those caused by the emission of the gravitational waves. So, knowledge of the exact nature and amount of the change of the orbital period would help us understand physical processes happening in the system. Identification and elimination of external dynamical causes from such intrinsic change of the orbital period would be the first step to achieve this goal. This thesis is aimed to facilitate this first step.

sar (the source) and the observer. As a result, the first and the second derivatives of the periods (or the frequencies) depend on the dynamical parameters of the pulsars, e.g., their velocities, accelerations, and jerk with respect to the observer.

In this chapter, we derive analytical expressions for the dynamical terms contributing to the first and the second time derivative of the frequency (both the spin and the orbital), as well as to the first derivative of the period. Additionally, we also provide ways to evaluate those dynamical terms.

We start the chapter with a discussion of earlier works to set the preamble of our work in section 2.2. In section 2.3, we describe unit vectors and their derivatives used in our subsequent derivations. In section 2.4, we describe the components of the velocity and the acceleration of the Sun and the pulsar. In section 2.5, we derive the analytical expressions for the dynamical terms contributing to the first time-derivative of the frequency and consequently present the expression for the intrinsic first derivative of the frequency. In section 2.6, we derive analytical expressions for the dynamical terms contributing to the second time-derivative of the frequency and consequently present the expression for the intrinsic second derivative of the frequency. In section 2.7, we give the expressions for the dynamical terms contributing to the first derivative of the period and consequently present the expression for the intrinsic first derivative of the period. In section 2.8, we describe the methods of obtaining values of the components of the relative acceleration between the pulsar and the Sun, both parallel and perpendicular to the Galactic plane. In section 2.9, we describe the methods of obtaining the components of the relative jerk between the pulsar and the Sun, both parallel and perpendicular to the Galactic plane. The expressions derived in 2.8 appear in sections 2.5, 2.6, and 2.7, while the expressions derived in section 2.9 appear only in section 2.6. In sections 2.10 and 2.11, we briefly discuss additional dynamical effects that might arise in specific cases but are not the subject of study of the present thesis. We summarize the results of this chapter in section 2.12.

2.2 Preamble to our work: earlier studies

As already mentioned, the first and the higher-order time derivatives of the spin and the orbital frequencies are affected by dynamics. In one of the seminal works on this topic, Joshi and Rasio (1997) discussed how the higher derivatives of the spin frequency bear the imprints of unmodeled orbital motion. More specifically, they expressed the spin frequency derivative as the line of sight acceleration, the spin frequency second derivative as the line of sight jerk, and so on. However, they ignored a few effects, e.g., the intrinsic values of the frequency derivatives, the acceleration and jerk of the pulsar due to the gravitational potential of the Galaxy, and the change in the direction of the line of sight due to the motion of the pulsar.

In reality, the line of sight acceleration, jerk, jounce, etc., might arise due to the motion of the pulsar in the gravitational potential of the Galaxy as well as due to the orbital motion (if any). The contribution of the gravitational potential of the Galaxy to the line of sight jerk and higher-order terms are usually small. However, these can be non-negligible if they are due to the orbital motion of an unmodeled binary and can eventually help constrain the parameters of the binary (Joshi and Rasio, 1997; Bassa et al., 2016; Perera et al., 2017). It is noteworthy to mention here the fact that the higher derivatives of the spin frequency in the timing solution might arise due to the intrinsic 'timing noise' too. Careful analysis and the use of good noise models (Shannon & Cordes , 2010; Coles et al., 2011) can help us overcome such ambiguities.

The expressions for the line of sight acceleration, jerk, jounce, and crackle, due to the orbital motion are given in Bagchi et al. (2013) and Bassa et al. (2016). The expression for the line of sight pop due to the orbital motion has been given for the first time in Chapter-1 of this thesis.

A few years ago, Liu et al. (2018) provided a semi-analytical derivation for the dynamical effects in the first and the second derivatives of the pulsar spin frequency. However, the expressions they provided were in the frame where the motion of the Sun is taken to be negligible. Additionally, instead of deriving and using analytical expressions for the terms involving the acceleration, jerk, etc., they used a model of the gravitational potential of the Galaxy and an orbit integrator to integrate the motion of the pulsars and numerically obtained the acceleration and jerk terms by a polynomial fitting.

In the present thesis, we derive complete analytical expressions for the dynamical effects in the first and the second derivatives of the frequency as well as in the first derivative of the period. We also devise methods to compute these terms if they are caused by the gravitational potential of the Galaxy. In the next few sections, we present our formalism.

2.3 Geometrical Understanding: unit vectors, their derivatives, and proper motion

During the procedure of pulsar timing analysis, the site arrival times are translated to the barycentric arrival times, i.e., the solar system barycentre plays the role of the observer in the Doppler shift equation, which is the origin of the dynamical effects we are studying. The barycenter of the Solar system lies very close to the surface of the Sun, specifically, within 0.008 AU from the centre of the Sun (Perryman and Schulze-Hartung, 2011). So, the word 'Sun' is used in this thesis in the place of the 'solar system barycenter'.

To obtain expressions for unit vectors and their derivatives that will be used later, we use a Sun centred spherical coordinate system as well as a Sun centred cartesian coordinate system as shown in Fig. 2.1. In this figure, the Sun is denoted by 'S', the pulsar by 'P', and the Galactic centre by 'C'. Additionally, θ is the angle, which, the radius vector ($\overrightarrow{SP}$) makes with the positive Z-axis, ϕ is the angle that the projection of the radius vector on the XY-plane ($\overrightarrow{SP'}$) makes with the positive X-axis, b is the Galactic latitude, l is the Galactic longitude, and the distance of the pulsar from the Sun, $SP = d$, is equivalent to

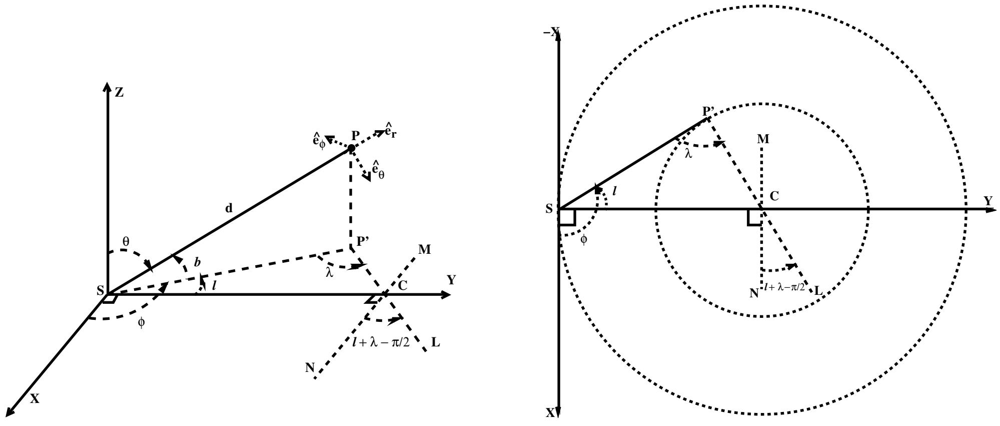

(a) (b)

Figure 2.1: a) A schematic 3D-diagram describing the position of a pulsar P. b) The top view of the Galactic plane shown in the left panel. See the text in section 2.3 for the description of the figure.

its radial coordinate r, i.e., the spherical coordinates (r, θ, ϕ) are equivalent to $(d, 90^\circ - b, 90^\circ + l)$. Here, the Sun centred cartesian coordinate system is chosen in such a way that the Galactic centre 'C' is along the Y-axis having the (x, y, z) coordinates as $(0, R_\mathrm{s}, 0)$, where R_s is the Galactocentric distance of the Sun. SP is projected on the Galactic plane as $\mathrm{SP}' = d\cos b$, i.e., P′ is the projected location of the pulsar on the Galactic plane. The value of P′C is denoted by $R_{\mathrm{p}'}$, which is the Galactocentric distance of the pulsar projection on the Galactic plane. Fig. 2.1 shows that,

$$z = d\sin b\ , \tag{2.1}$$

where z (P′P) is the vertical height of the pulsar from the Galactic plane. z is positive for positive values of b (above the Galactic plane) and negative for negative values of b (below the Galactic plane).

Using the properties of spherical coordinates, we can write:

$$\widehat{e_r} = \sin\theta\,\cos\phi\,\widehat{e_x} + \sin\theta\,\sin\phi\,\widehat{e_y} + \cos\theta\,\widehat{e_z}, \tag{2.2}$$

$$\widehat{e_\theta} = \cos\theta\,\cos\phi\,\widehat{e_x} + \cos\theta\,\sin\phi\,\widehat{e_y} - \sin\theta\,\widehat{e_z}, \tag{2.3}$$

$$\widehat{e_\phi} = -\sin\phi\,\widehat{e_x} + \cos\phi\,\widehat{e_y}\ , \tag{2.4}$$

where $\widehat{e}_x$, $\widehat{e}_y$, $\widehat{e}_z$ are the Cartesian unit vectors and $\widehat{e}_r$, $\widehat{e}_\theta$, $\widehat{e}_\phi$ are the unit vectors of the spherical coordinate system as mentioned above. Also, $\theta = 90^\circ - b$ gives $\sin\theta = \cos b$, $\cos\theta = \sin b$, $\dot{\theta} = -\dot{b}$, and $\phi = 90^\circ + l$ gives $\sin\phi = \cos l$, $\cos\phi = -\sin l$, $\dot{\phi} = \dot{l}$.

The well-known expressions for the time-derivatives of $\widehat{e}_r$, $\widehat{e}_\theta$, and $\widehat{e}_\phi$ are:

$$\dot{\widehat{e}}_r = \dot{\theta}\widehat{e}_\theta + \dot{\phi}\,\sin\theta\widehat{e}_\phi, \tag{2.5}$$

$$\dot{\widehat{e}}_\theta = -\dot{\theta}\widehat{e}_r + \dot{\phi}\,\cos\theta\widehat{e}_\phi, \tag{2.6}$$

$$\dot{\widehat{e}}_\phi = -\dot{\phi}\,(\sin\theta\widehat{e}_r + \cos\theta\widehat{e}_\theta) = -\dot{\phi}\left(\cos\phi\widehat{e}_x + \sin\phi\widehat{e}_y\right) \tag{2.7}$$

The second expression of $\dot{\widehat{e}}_\phi$ came from eq. (2.4).

From Fig. 2.1(a), we can see that the unit vector from the Sun to the pulsar $\widehat{n}_{\rm sp}$ is the radial unit vector $\widehat{e}_r$. Hence, $\widehat{n}_{\rm sp} = \widehat{e}_r$ gives $\dot{\widehat{n}}_{\rm sp} = \dot{\widehat{e}}_r$ and $\ddot{\widehat{n}}_{\rm sp} = \ddot{\widehat{e}}_r$, which can be written as:

$$\begin{aligned}
\ddot{\widehat{n}}_{\rm sp} &= \ddot{\widehat{e}}_r \\
&= \ddot{\theta}\widehat{e}_\theta + \dot{\theta}\dot{\widehat{e}}_\theta + \ddot{\phi}\,\sin\theta\widehat{e}_\phi + \dot{\phi}\,\dot{\theta}\,\cos\theta\widehat{e}_\phi + \dot{\phi}\,\sin\theta\dot{\widehat{e}}_\phi \quad \text{[Used eq. (2.5)]} \\
&= \ddot{\theta}\widehat{e}_\theta + \dot{\theta}\left(-\dot{\theta}\widehat{e}_r + \dot{\phi}\,\cos\theta\widehat{e}_\phi\right) + \ddot{\phi}\,\sin\theta\widehat{e}_\phi + \dot{\phi}\,\dot{\theta}\,\cos\theta\widehat{e}_\phi + \dot{\phi}\,\sin\theta\left(-\dot{\phi}\,(\sin\theta\widehat{e}_r + \cos\theta\widehat{e}_\theta)\right) \\
&\qquad\qquad\qquad\qquad\qquad\qquad\qquad\qquad \text{[Used eq. (2.6) and (2.7)]} \\
&= \left(\ddot{\theta} - \dot{\phi}^2\,\sin\theta\,\cos\theta\right)\widehat{e}_\theta - \left(\dot{\theta}^2 + \dot{\phi}^2\,\sin^2\theta\right)\widehat{e}_r + \left(2\,\dot{\theta}\dot{\phi}\,\cos\theta + \ddot{\phi}\,\sin\theta\right)\widehat{e}_\phi\,. \qquad (2.8)
\end{aligned}$$

The total proper motion of a star is defined as the angular velocity across the sky exhibited by it, i.e., $\mu_T = v_T/d$ where v_T is the transverse velocity (the velocity in the sky plane perpendicular to the line of sight $\widehat{e}_r$) and d is the distance of the star (here pulsar). There are different conventions to measure components of proper motions. These can be measured in terms of the components in the equatorial coordinates, i.e., the proper motion in the right ascension (μ_α where α is the right ascension) and the proper motion in the declination (μ_δ where δ is the declination) giving $\mu_T = \sqrt{\mu_\alpha^2 + \mu_\delta^2}$ or in terms of its ecliptic coordinates, i.e., the proper motion in the ecliptic longitude ($\mu_{e\lambda}$ where $e\lambda$ is the the ecliptic longitude) and the proper motion in the ecliptic latitude ($\mu_{e\beta}$ where $e\beta$ is the ecliptic latitude) giving $\mu_T = \sqrt{\mu_{e\lambda}^2 + \mu_{e\beta}^2}$, or the proper motion in the Galactic latitude (μ_b) and the proper motion in the Galactic longitude (μ_l) giving $\mu_T = \sqrt{\mu_b^2 + \mu_l^2}$. We prefer the last convention where we can use $\mu_b = -\dot{\theta} = \dot{b}$, $\mu_l = \dot{\phi}\,\sin\theta = \dot{\phi}\,\cos b = \dot{l}\,\cos b$.

The unit vector in the direction of the transverse velocity is denoted by $\widehat{e_{\rm T,v}}$ so that the transverse velocity is $\vec{v}_{\rm T} = v_{\rm T}\,\widehat{e_{\rm T,v}}$. To understand how the time derivatives of $\widehat{e_r}$ and $\widehat{e_{\rm T,v}}$ can be expressed in terms of the total proper motion, let us consider a 2-dimensional Cartesian plane (X′ Y') containing the orthonormal unit vectors $\widehat{e_r}$ and $\widehat{e_{\rm T,v}}$ as shown in Fig. 2.2, such that $\widehat{e_r}$ makes an angle γ with $\widehat{e_{x'}}$ and so $\widehat{e_{\rm T,v}}$ makes an angle $\gamma + 90°$ with $\widehat{e_{x'}}$. As a result, $\dot{\gamma} = \mu_{\rm T}$ is the total transverse proper motion. Additionally,

$$\widehat{e_r} = \cos\gamma\widehat{e_{x'}} + \sin\gamma\widehat{e_{y'}}\ , \tag{2.9a}$$

and

$$\widehat{e_{\rm T,v}} = -\sin\gamma\widehat{e_{x'}} + \cos\gamma\widehat{e_{y'}}\ . \tag{2.9b}$$

Taking time-derivatives of above equations, we get,

$$\begin{aligned}\dot{\widehat{e_r}} &= \dot{\gamma}(-\sin\gamma\widehat{e_{x'}} + \cos\gamma\widehat{e_{y'}}) \\ &= \mu_{\rm T}\,\widehat{e_{\rm T,v}} \qquad [\text{used } \dot{\gamma} = \mu_{\rm T} \text{ and eq. (2.9b)}] \\ &= \frac{v_{\rm T}}{d}\widehat{e_{\rm T,v}} \qquad [\text{as } \mu_T = v_T/d\,]\ ,\end{aligned} \tag{2.10a}$$

and

$$\begin{aligned}\dot{\widehat{e_{\rm T,v}}} &= -\dot{\gamma}(\cos\gamma\widehat{e_{x'}} + \sin\gamma\widehat{e_{y'}}) \\ &= -\mu_{\rm T}\,\widehat{e_r} \qquad [\text{used } \dot{\gamma} = \mu_{\rm T} \text{ and eq. (2.9a)}] \\ &= -\frac{v_{\rm T}}{d}\widehat{e_r} \qquad [\text{as } \mu_T = v_T/d\,]\ .\end{aligned} \tag{2.10b}$$

From Fig. 2.1, it is clear that in a Galactocentric cylindrical coordinate system, the coordinates of the Sun and the pulsar are $(R_s, 0, 0)$ and (R_p, ζ, z) where the azimuthal angle ζ

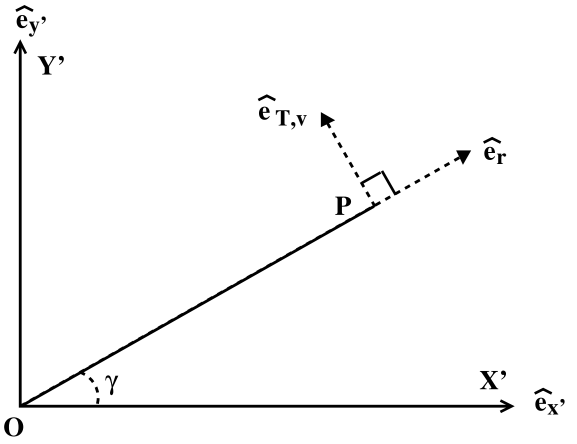

Figure 2.2: A schematic 3D-diagram showing unit vectors $\widehat{e_r}$ and $\widehat{e}_{\mathrm{T,v}}$ at point P in the Cartesian plane (X′Y′) centred at a point O.

is taken with respect to the line CS. We also see that $R_p = R_{p'}$.

2.4 Components of velocities and accelerations

The stars in the Galaxy move with different values of velocity, acceleration, jerk etc. The gradient of the gravitational potential of the Galaxy is the main source of accelerations of the objects in it. There can be additional sources like local potentials, orbital motions, etc. In the present thesis, we mainly concentrate on the first source of acceleration.

In this section, we demonstrate the directions and magnitudes of the velocities of the Sun and the pulsar ($\vec{v}_{\mathrm{s}}$ and $\vec{v}_{\mathrm{p}}$ respectively) as well as their accelerations ($\vec{a}_{\mathrm{s}}$ and $\vec{a}_{\mathrm{p}}$). Like any other vector, these vectors can also be decomposed into two mutually perpendicular components, and we take one component parallel and the other perpendicular to the Galactic plane. So, $\vec{v}_{\mathrm{s}} = \vec{v}_{\mathrm{s,pl}} + \vec{v}_{\mathrm{s,z}}$, $\vec{v}_{\mathrm{p}} = \vec{v}_{\mathrm{p,pl}} + \vec{v}_{\mathrm{p,z}}$, $\vec{a}_{\mathrm{s}} = \vec{a}_{\mathrm{s,pl}} + \vec{a}_{\mathrm{s,z}}$, and $\vec{a}_{\mathrm{p}} = \vec{a}_{\mathrm{p,pl}} + \vec{a}_{\mathrm{p,z}}$. Here subscripts ‘pl’ stands for parallel to the Galactic disc and the subscript ‘z’ stands for the ‘z-direction’ or perpendicular to the Galactic disc. The magnitudes of these vectors are denoted by the same symbols without the arrow over them. In fact, as the Sun is orbiting around the Galactic centre, at any instant, $v_{\mathrm{s,pl}}$ is along the X-axis and $a_{\mathrm{s,pl}}$ is along the

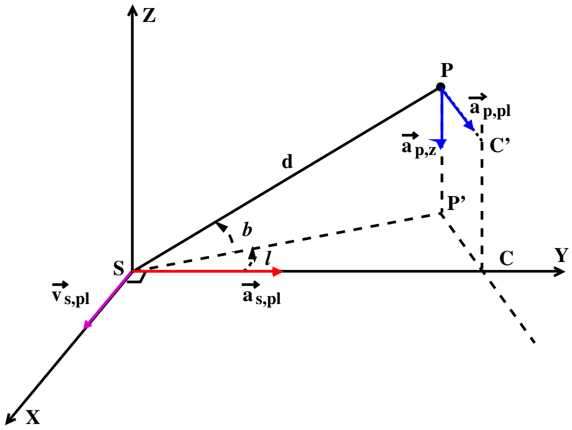

Figure 2.3: A schematic 3D diagram describing the accelerations experienced by the Sun (in red) and the Pulsar (in blue) due to the gravitational potential of the Galaxy. Here, S is the location of the Sun, P is the location of the pulsar, P′ is the projection of P on the Galactic plane, C is the Galactic centre, and C′ is the projection of C on the plane parallel to the Galactic plane passing through the pulsar. Additionally, the velocity of the Sun has also been shown with a purple arrow. In the text, we have used R_p as the value of PC′ and $R_{p'}$ as the value of P′C. It is obvious that $R_p = R'_p$.

Y-axis, in the coordinate system shown in Fig. 2.1(a).

The vertical velocity of stars in the Galaxy with respect to the local standard of rest is defined as $v_z = W = \dot{d}\sin b + \mu_b\, d\, \cos b$ (Bovy, 2011). The first term contains the radial velocity $v_r = \dot{d}$ which is difficult to measure. For five binary pulsars, optical spectroscopy of their binary companions made it possible to measure v_r (Liu et al., 2018)), whose absolute value lie in the range of $42-185$ km s^{-1}, and in their simulation, they vary v_r from -200 km s^{-1} to 200 km s^{-1}. The second term in the expression of W is usually smaller, as for the 106 pulsars in the Galactic field with reported values of μ_b and dispersion measure independent measurements of distances, we find that the values of this term can be fitted with a Gaussian of mean -12.49 km s^{-1} and standard deviation 172 km s^{-1}. These two terms in the expression of W can add up if they have the same sign. On the other hand, for the Sun, the latest measurement of W is only $7.25^{+0.37}_{-0.36}$ km s^{-1} (Schönrich et al., 2010). This means that the value of W for the Sun is usually negligible in comparison to the value of W of pulsars, i.e., $v_{\rm s,z} << v_{\rm p,z}$.

Additionally, Schönrich et al. (2010) also reported other two components of the motion of the Sun with respect to the local standard of rest. These are the radial (U) and along the Galactic rotation (V) velocities, values being $11.1^{+0.69}_{-0.75}$ km s^{-1} and $12.24^{+0.47}_{-0.47}$ km s^{-1} respectively. These values would contribute to the net velocity of the Sun parallel to the disc $v_{\rm s,pl} = \sqrt{(\Theta_S + V)^2 + U^2}$ where Θ_S is the Galactic rotation at the location of the Sun, whose value (240 ± 8 km s^{-1} according to Reid et al. (2014)) is much larger than the values of U and V.

As the Sun is located in the Galactic plane with a vertical height zero, the value of the z-gradient of the gravitational potential of the Galaxy, which causes the vertical acceleration of the stars, is zero at this location (Pathak and Bagchi, 2018). Although, the measured value of the vertical acceleration of the Sun is non-zero, 3.95 ± 0.47 mm s^{-1} yr^{-1} (Xu et al., 2017) which translates (dividing by c) into 4.17×10^{-19} s^{-1}. The cause of this acceleration is not yet understood, but surely something in addition to the acceleration due to the standard Galactic gravitational potential. However, this value is much smaller than the z-component of the Galactic acceleration at most of the places in the Galaxy, as shown in Fig. 2.8(b), and hence can be ignored, i.e., $a_{\rm s,z} = 0$. The non-zero components of the accelerations of the Sun and the pulsar are shown with thick coloured arrows in Fig. 2.3. In this figure, the velocity of the Sun has been shown too. Note that, although the pulsar has been shown located above the Galactic plane (XY plane), in reality, there are pulsars below the Galactic plane too. As $\vec{a}_{\rm p,z}$ is always directed towards the Galactic plane, we can write,

$$\vec{a}_{\rm p,z} = \begin{cases} -a_{\rm p,z}\,\widehat{e_z} & \text{if } b > 0\,, \\ a_{\rm p,z}\,\widehat{e_z} & \text{if } b < 0\,. \end{cases} \tag{2.11}$$

Similarly, the parallel components of the accelerations can be written as:

$$\vec{a}_{\rm p,pl} = -a_{\rm p,pl}\,\widehat{e_{R_p}}\,, \tag{2.12}$$

$$\vec{a}_{\rm s,pl} = -a_{\rm s,pl}\,\widehat{e_{R_s}}\,, \tag{2.13}$$

where $\widehat{e_{R_p}}$ and $\widehat{e_{R_s}}$ are the unit vectors in the Galactocentric cylindrical coordinate R at the location of the pulsar and the Sun respectively. Note that $\widehat{e_{R_p}}$ and $\widehat{e_{R_s}}$ are directed outwards while $\vec{a}_{\mathrm{p,pl}}$ and $\vec{a}_{\mathrm{p,pl}}$ are directed inwards. The positive, negative signs of the above three equations ensures that $a_{\mathrm{p,z}}$, $a_{\mathrm{p,pl}}$, $a_{\mathrm{s,pl}}$ are all positive quantities, which help us use trigonometric relations in the next few sections.

2.5 Analytical expression for the intrinsic first derivative of the frequency

The Doppler shift of the frequency (either the spin or the orbital) of the pulsar can be written as:

$$f_{\mathrm{int}} = (c + \vec{v}_{\mathrm{p}}.\widehat{n}_{\mathrm{sp}})(c + \vec{v}_{\mathrm{s}}.\widehat{n}_{\mathrm{sp}})^{-1} f_{\mathrm{obs}} \,, \tag{2.14}$$

where c is the speed of light in vacuum, $\vec{v}_{\mathrm{p}}$ is the velocity of the pulsar, $\vec{v}_{\mathrm{s}}$ is the velocity of the Sun, $\widehat{n}_{\mathrm{sp}}$ is the unit vector from the Sun to the pulsar and is taken to be the radial direction ($\widehat{e_r}$ in Fig. 2.1(a)), f_{obs} is the observed (measured) frequency, and f_{int} is the intrinsic frequency. As the pulse arrival times on the earth are first translated to the Solar system barycentre before doing any timing analysis, the Solar system barycentre plays the role of the receiver in the Doppler shift eq. (2.14), and due to the proximity of the barycentre to the Sun, we simply write it as 'the Sun'. Differentiating eq. (2.14) with respect to time, we get,

$$\dot{f}_{\mathrm{int}} = \frac{\left(\vec{a}_{\mathrm{p}} \cdot \widehat{n}_{\mathrm{sp}} + \vec{v}_{\mathrm{p}} \cdot \dot{\widehat{n}}_{\mathrm{sp}}\right)}{(c + \vec{v}_{\mathrm{s}} \cdot \widehat{n}_{\mathrm{sp}})} f_{\mathrm{obs}} - \frac{(c + \vec{v}_{\mathrm{p}} \cdot \widehat{n}_{\mathrm{sp}})}{(c + \vec{v}_{\mathrm{s}} \cdot \widehat{n}_{\mathrm{sp}})^2} \left(\vec{a}_{\mathrm{s}} \cdot \widehat{n}_{\mathrm{sp}} + \vec{v}_{\mathrm{s}} \cdot \dot{\widehat{n}}_{\mathrm{sp}}\right) f_{\mathrm{obs}} + \frac{(c + \vec{v}_{\mathrm{p}} \cdot \widehat{n}_{\mathrm{sp}})}{(c + \vec{v}_{\mathrm{s}} \cdot \widehat{n}_{\mathrm{sp}})} \dot{f}_{\mathrm{obs}} \,. \tag{2.15}$$

In eq. (2.15), $\vec{a}_{\mathrm{p}} = \dot{\vec{v}}_{\mathrm{p}}$ is the acceleration of the pulsar, $\vec{a}_{\mathrm{s}} = \dot{\vec{v}}_{\mathrm{s}}$ is the acceleration of the Sun, the dot over any parameter corresponds to the time derivative of that parameter, and the double dot represents the second time derivative. Dividing of eq. (2.15) by eq. (2.14) and assuming $1 + \frac{\vec{v}_{\rm s}.\widehat{n}_{\rm sp}}{c} \simeq 1$ and $1 + \frac{\vec{v}_{\rm p}.\widehat{n}_{\rm sp}}{c} \simeq 1$, we get,

$$\frac{\dot{f}_{\rm int}}{f_{\rm int}} = \frac{(\vec{a}_{\rm p} - \vec{a}_{\rm s}) \cdot \widehat{n}_{\rm sp}}{c} + \frac{1}{c}(\vec{v}_{\rm p} - \vec{v}_{\rm s}) \cdot \frac{d}{dt}(\widehat{n}_{\rm sp}) + \frac{\dot{f}_{\rm obs}}{f_{\rm obs}} . \tag{2.16}$$

The above assumptions just before eq. (2.16) also enable us to write $f_{\rm int} \simeq f_{\rm obs} = f$, $\frac{\dot{f}_{\rm obs}}{f_{\rm obs}} = \frac{\dot{f}_{\rm obs}}{f} = \left(\frac{\dot{f}}{f}\right)_{\rm obs}$, and $\frac{\dot{f}_{\rm int}}{f_{\rm int}} = \frac{\dot{f}_{\rm int}}{f} = \left(\frac{\dot{f}}{f}\right)_{\rm int}$. (2.16) is then simplified as:

$$\left(\frac{\dot{f}}{f}\right)_{\rm ex} = \left(\frac{\dot{f}}{f}\right)_{\rm obs} - \left(\frac{\dot{f}}{f}\right)_{\rm int} = -\left[\frac{(\vec{a}_{\rm p} - \vec{a}_{\rm s}) \cdot \widehat{n}_{\rm sp}}{c} + \frac{1}{c}(\vec{v}_{\rm p} - \vec{v}_{\rm s}) \cdot \frac{d}{dt}(\widehat{n}_{\rm sp})\right] . \tag{2.17}$$

The subscript ‘ex’ means the ‘excess’ term. The first term in the right hand side of eq. (2.17) depends on the acceleration of the pulsar relative to the Sun. As we are considering the gradient of the gravitational potential of the Galaxy to be the only source of acceleration of objects, the first term can be written as $\left(\frac{\dot{f}}{f}\right)_{\rm ex,Gal} = -\frac{(\vec{a}_{\rm p} - \vec{a}_{\rm s}) \cdot \widehat{n}_{\rm sp}}{c}$.

We have seen in section 2.4, that both of the acceleration vectors in the above term can be decomposed into two components, one is parallel to the Galactic plane and the other is perpendicular to the Galactic plane. The contribution from these parallel components is denoted by $\left(\frac{\dot{f}}{f}\right)_{\rm ex,Galpl} = -\frac{\left(\vec{a}_{\rm p,pl} - \vec{a}_{\rm s,pl}\right) \cdot \widehat{n}_{\rm sp}}{c}$, while the contribution of the perpendicular terms is $\left(\frac{\dot{f}}{f}\right)_{\rm ex,Galz} = -\frac{\left(\vec{a}_{\rm p,z} - \vec{a}_{\rm s,z}\right) \cdot \widehat{n}_{\rm sp}}{c}$, i.e., $\left(\frac{\dot{f}}{f}\right)_{\rm ex,Gal} = \left(\frac{\dot{f}}{f}\right)_{\rm ex,Galpl} + \left(\frac{\dot{f}}{f}\right)_{\rm ex,Galz}$.

The second term in the right hand side of eq. (2.17), which involves the relative velocity and the change of the location of the pulsar, is the well-known ‘Shklovskii term’ (Shklovskii , 1970) and is denoted by $\left(\frac{\dot{f}}{f}\right)_{\rm ex,Shk}$. So, we can write,

$$\left(\frac{\dot{f}}{f}\right)_{\rm ex} = \left(\frac{\dot{f}}{f}\right)_{\rm ex,Gal} + \left(\frac{\dot{f}}{f}\right)_{\rm ex,Shk} = \left(\frac{\dot{f}}{f}\right)_{\rm ex,Galpl} + \left(\frac{\dot{f}}{f}\right)_{\rm ex,Galz} + \left(\frac{\dot{f}}{f}\right)_{\rm ex,Shk} . \tag{2.18}$$

The terms in the right hand side of eq. (2.18) can be calculated using a model of the gravitational potential of the Galaxy and the measured values of the locations and the motions of the pulsars. The expressions for these terms have been derived in sections 2.5.1 and 2.5.2. Using expressions derived in those sections, we can write,

$$\left(\frac{\dot{f}}{f}\right)_{\rm ex} = \frac{\cos b}{c} \left\{ a_{\rm p,pl} \frac{R_{\rm s}}{R_{\rm p'}} \left(\frac{d \cos b}{R_{\rm s}} - \cos l \right) + a_{\rm s,pl} \cos l \right\} + \frac{1}{c}(a_{\rm p,z} \sin b) - \frac{1}{c} \frac{v_T^2}{d} , \tag{2.19}$$

where the meaning of various parameters are the same as in section 2.3.

After computing $\left(\frac{\dot{f}}{f}\right)_{\text{ex}}$ using eq. (2.19), one can estimate the value of $\dot{f}_{\text{int}}$ using the relation:

$$\dot{f}_{\text{int}} = f\left[\left(\frac{\dot{f}}{f}\right)_{\text{obs}} - \left(\frac{\dot{f}}{f}\right)_{\text{ex}}\right] = \dot{f}_{\text{obs}} - f\left(\frac{\dot{f}}{f}\right)_{\text{ex}} , \tag{2.20}$$

if f and $\dot{f}_{\text{obs}}$ are known.

Sometimes, it might be useful to work with the absolute dynamical terms instead of the fractional dynamical terms shown in eq. (2.18). The absolute dynamical terms can be written as:

$$\dot{f}_{\text{Galpl}} = f\left(\frac{\dot{f}}{f}\right)_{\text{ex,Galpl}} , \tag{2.21a}$$

$$\dot{f}_{\text{Galz}} = f\left(\frac{\dot{f}}{f}\right)_{\text{ex,Galz}} , \tag{2.21b}$$

$$\dot{f}_{\text{Gal}} = f\left(\frac{\dot{f}}{f}\right)_{\text{ex,Gal}} = \dot{f}_{\text{Galpl}} + \dot{f}_{\text{Galz}} , \tag{2.21c}$$

$$\dot{f}_{\text{Shk}} = f\left(\frac{\dot{f}}{f}\right)_{\text{ex,Shk}} , \tag{2.21d}$$

and

$$\dot{f}_{\text{int}} = \dot{f}_{\text{obs}} - \dot{f}_{\text{Gal}} - \dot{f}_{\text{Shk}} . \tag{2.21e}$$

All these equations will remain the same regardless of whether we use the spin frequency and its derivatives or the orbital frequency and its derivatives.

However, if the pulsar is in an unmodeled binary, the expression for $\left(\frac{\dot{f}_{\text{s}}}{f_{\text{s}}}\right)_{\text{ex}}$ will have an extra term caused by the line-of-sight component of the orbital acceleration. There will be additional terms in both $\left(\frac{\dot{f}_{\text{b}}}{f_{\text{b}}}\right)_{\text{ex}}$ and $\left(\frac{\dot{f}_{\text{s}}}{f_{\text{s}}}\right)_{\text{ex}}$ if the pulsar is in a globular cluster. We do not explore these effects in the present thesis.

Next, we describe the derivation of each of the terms on the right-hand side of eq. (2.17).

2.5.1 Simplifying the first term of eq. (2.17), i.e., $\frac{(\vec{a}_{\mathrm{p}}-\vec{a}_{\mathrm{s}})\cdot\widehat{n}_{\mathrm{sp}}}{c}$

The first term in right hand side of eq. (2.17) can be simplified as:

$$
\begin{aligned}
\left(\frac{\dot{f}}{f}\right)_{\mathrm{ex,Gal}} = -\frac{(\vec{a}_{\mathrm{p}} - \vec{a}_{\mathrm{s}}) \cdot \widehat{n}_{\mathrm{sp}}}{c} &= -\frac{\Big((\vec{a}_{\mathrm{p,pl}} + \vec{a}_{\mathrm{p,z}}) - (\vec{a}_{\mathrm{s,pl}} + \vec{a}_{\mathrm{s,z}})\Big) \cdot \widehat{n}_{\mathrm{sp}}}{c} \\
&= -\frac{\Big(\vec{a}_{\mathrm{p,pl}} - \vec{a}_{\mathrm{s,pl}} + \vec{a}_{\mathrm{p,z}} - \vec{a}_{\mathrm{s,z}}\Big) \cdot \widehat{n}_{\mathrm{sp}}}{c} \\
&= -\frac{\Big(\vec{a}_{\mathrm{p,pl}} - \vec{a}_{\mathrm{s,pl}}\Big) \cdot \widehat{n}_{\mathrm{sp}}}{c} - \frac{\Big(\vec{a}_{\mathrm{p,z}} - \vec{a}_{\mathrm{s,z}}\Big) \cdot \widehat{n}_{\mathrm{sp}}}{c} \\
&= \left(\frac{\dot{f}}{f}\right)_{\mathrm{ex,Galpl}} + \left(\frac{\dot{f}}{f}\right)_{\mathrm{ex,Galz}} , \qquad (2.22)
\end{aligned}
$$

where $\left(\frac{\dot{f}}{f}\right)_{\mathrm{ex,Galpl}} = -\frac{\left(\vec{a}_{\mathrm{p,pl}}-\vec{a}_{\mathrm{s,pl}}\right)\cdot\widehat{n}_{\mathrm{sp}}}{c}$ and $\left(\frac{\dot{f}}{f}\right)_{\mathrm{ex,Galz}} = -\frac{\left(\vec{a}_{\mathrm{p,z}}-\vec{a}_{\mathrm{s,z}}\right)\cdot\widehat{n}_{\mathrm{sp}}}{c}$ as already mentioned. Simplifying the parallel term further with the help of Figs. 2.1 and 2.3:

$$
\begin{aligned}
\left(\frac{\dot{f}}{f}\right)_{\mathrm{ex,Galpl}} &= -\frac{\Big(\vec{a}_{\mathrm{p,pl}} - \vec{a}_{\mathrm{s,pl}}\Big) \cdot \widehat{n}_{\mathrm{sp}}}{c} \\
&= -\frac{1}{c}\left(a_{\mathrm{p,pl}}\, \cos(l+\lambda-\frac{\pi}{2})\widehat{e_x} + a_{\mathrm{p,pl}}\, \sin(l+\lambda-\frac{\pi}{2})\widehat{e_y} - a_{\mathrm{s,pl}}\widehat{e_y}\right)\cdot\widehat{e_r} \\
&= -\frac{1}{c}\left(a_{\mathrm{p,pl}}\, \cos(l+\lambda-\frac{\pi}{2})\widehat{e_x} + a_{\mathrm{p,pl}}\, \sin(l+\lambda-\frac{\pi}{2})\widehat{e_y} - a_{\mathrm{s,pl}}\widehat{e_y}\right) \\
&\qquad \cdot\left(\sin\theta\, \cos\phi\widehat{e_x} + \sin\theta\, \sin\phi\widehat{e_y} + \cos\theta\widehat{e_z}\right) \\
&= -\frac{1}{c}\left(a_{\mathrm{p,pl}}\, \sin(l+\lambda)\, \sin\theta\, \cos\phi - a_{\mathrm{p,pl}}\, \cos(l+\lambda)\, \sin\theta\, \sin\phi - a_{\mathrm{s,pl}}\, \sin\theta\, \sin\phi\right) \\
&= -\frac{1}{c}\left(-a_{\mathrm{p,pl}}\, \sin(l+\lambda)\, \cos b\, \sin l - a_{\mathrm{p,pl}}\, \cos(l+\lambda)\, \cos b\, \cos l - a_{\mathrm{s,pl}}\, \cos b\, \cos l\right) \\
&\qquad [\text{as } \sin\theta = \cos b,\ \cos\phi = -\sin l, \text{ and } \sin\phi = \cos l\,] \\
&= \frac{\cos b}{c}\left(a_{\mathrm{p,pl}}\, \cos\lambda + a_{\mathrm{s,pl}}\, \cos l\right) . \qquad (2.23)
\end{aligned}
$$

To eliminate the unknown angle λ from eq. (2.23), one can use the triangle law as (see Fig. 2.1(b)):

$$
R_{\mathrm{p'}}^2 = R_{\mathrm{s}}^2 + (d\cos b)^2 - 2R_{\mathrm{s}}(d\cos b)\cos l\,, \qquad (2.24a)
$$

$$
R_{\mathrm{s}}^2 = R_{\mathrm{p'}}^2 + (d\cos b)^2 - 2R_{\mathrm{p'}}(d\cos b)\cos\lambda\,. \qquad (2.24b)
$$

From eqs. (2.24a) and (2.24b), one gets

$$\cos\lambda = \frac{R_{\rm s}}{R_{\rm p'}}\left(\frac{d\cos b}{R_{\rm s}} - \cos l\right) . \tag{2.25}$$

Therefore, we can write eq. (2.23) as,

$$\left(\frac{\dot{f}}{f}\right)_{\rm ex,Galpl} = \frac{\cos b}{c}\left\{a_{\rm p,pl}\,\frac{R_{\rm s}}{R_{\rm p'}}\left(\frac{d\cos b}{R_{\rm s}} - \cos l\right) + a_{\rm s,pl}\,\cos l\right\} . \tag{2.26}$$

The perpendicular term can be written as:

$$\begin{aligned}\left(\frac{\dot{f}}{f}\right)_{\rm ex,Galz} &= -\frac{\left(\vec{a}_{\rm p,z} - \vec{a}_{\rm s,z}\right)\cdot\widehat{n}_{\rm sp}}{c}\\ &= -\frac{\vec{a}_{\rm p,z}\cdot\widehat{n}_{\rm sp}}{c} \qquad\qquad [\text{as } \vec{a}_{\rm s,z}\simeq 0]\\ &= \frac{1}{c}\,a_{\rm p,z}\,\sin|b| \, . \end{aligned} \tag{2.27}$$

At the last stage of the above derivation, we have used the fact that $\vec{a}_{\rm p,z}\cdot\widehat{n}_{\rm sp} = -a_{\rm p,z}\sin|b|$ where $a_{\rm p,z}$ is the magnitude of $\vec{a}_{\rm p,z}$ as given by eq. (2.11) and always positive, while b is positive if the pulsar is located above the Galactic disc and negative if it is located below the Galactic disc. This will be clear from Fig. 2.4, which shows the edge-on view of the Galactic plane with two pulsars P1 and P2 above and below the Galactic plane, respectively, and their vertical accelerations as well as unit vectors in the direction from the Sun to the pulsars.

The non-observables appearing in many places in this section are the components of the acceleration of the pulsar parallel and perpendicular to the Galactic plane, $a_{\rm p,pl}$ and $a_{\rm p,z}$ respectively, as well as the component of the acceleration of the Sun parallel to the Galactic plane ($a_{\rm p,pl}$). Different methods to estimate these quantities in terms of observables can be found in section 2.8.

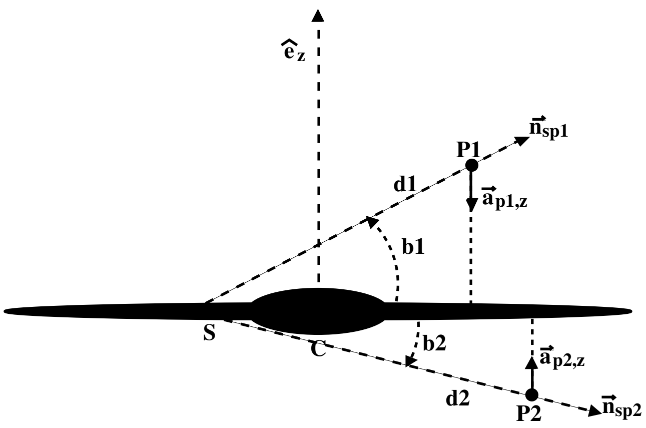

Figure 2.4: Schematic diagram to understand the relative acceleration perpendicular to the Galactic plane (z-acceleration). Two pulsars, P1 at positive z_1, b_1 and P2 at negative z_2, b_2 are shown (z refers to the vertical distance of the pulsar from the Galactic plane and b refers to the Galactic latitude). S is the location of the Sun and C is the Galactic centre.

2.5.2 Derivation of Shklovskii effect

For the sake of completeness, here we re-derive the well known Shklovskii term (the second term in the right hand side of eq. (2.17)):

$$\left(\frac{\dot{f}}{f}\right)_{\text{ex,Shk}} = -\frac{1}{c}(\vec{v}_{\text{p}} - \vec{v}_{\text{s}}) \cdot \frac{d}{dt}(\widehat{n}_{\text{sp}}) \,, \tag{2.28}$$

where $\vec{v}_{\text{p}} - \vec{v}_{\text{s}}$ is the velocity of the pulsar with respect to the Sun. This velocity can be written as:

$$\vec{v}_{\text{p}} - \vec{v}_{\text{s}} = \frac{d}{dt}\,(d\,\widehat{e}_r) = \dot{d}\,\widehat{e}_r + d\,\dot{\widehat{e}}_r = \dot{d}\,\widehat{e}_r + d\,\dot{\theta}\,\widehat{e}_\theta + d\,\dot{\phi}\,\sin\theta\,\widehat{e}_\phi \qquad \text{[used eq. (2.5)]}. \tag{2.29}$$

From Fig. 2.1(a), we can see that $\widehat{n}_{\rm sp} = \widehat{e}_r$, giving $\dot{\widehat{n}}_{\rm sp} = \dot{\widehat{e}}_r$. Using this fact and eqs. (2.5) and (2.29), eq. (2.28) becomes

$$\begin{aligned}
\left(\frac{\dot{f}}{f}\right)_{\rm ex,Shk} &= -\frac{1}{c}\,(\dot{d}\widehat{e}_r + d\,\dot{\theta}\widehat{e}_\theta + d\,\dot{\phi}\,\sin\theta\widehat{e}_\phi)\cdot(\dot{\theta}\widehat{e}_\theta + \dot{\phi}\,\sin\theta\widehat{e}_\phi) \\
&= -\frac{1}{c}\,(d\,\dot{\theta}^2 + d\,\dot{\phi}^2\,\sin^2\theta) \\
&= -\frac{1}{c}\,(d\,{\mu_b}^2 + d\,{\mu_l}^2), \quad [\text{as } \mu_b = -\dot{\theta},\, \mu_l = \dot{\phi}\,\sin\theta] \\
&= -\frac{1}{c}\,d\,\mu_T^2 \qquad\qquad [\text{as } \mu_T = \sqrt{\mu_b^2 + \mu_l^2}\,] \\
&= -\frac{1}{c}\frac{v_T^2}{d}\,. \qquad\qquad [\text{as } \mu_T = v_{\rm T}/d\,]
\end{aligned} \tag{2.30}$$

Eq. (2.30) is generally written as:

$$\left(\frac{\dot{f}}{f}\right)_{\rm ex,Shk} = -2.42925\times10^{-21}\,d_{\rm kpc}\,\mu^2_{T,{\rm mas\,yr^{-1}}}\ \ {\rm s}^{-1}\,, \tag{2.31}$$

where $\mu_{T,{\rm mas\,yr^{-1}}}$ is the total proper motion of the pulsar relative to the Sun, measured in the unit of milliarcsecond per year. For most of the pulsars, this is the largest dynamical contribution and easy to calculate if accurate enough values of the distance and the proper motion of the pulsar are known.

2.6 Analytical expression for the intrinsic second derivative of the frequency

Differentiating eq. (2.15) with respect to time, we get:

$$
\begin{aligned}
\ddot{f}_{\mathrm{int}} =& \frac{\left(\dot{\vec{a}}_{\mathrm{p}} \cdot \widehat{n}_{\mathrm{sp}} + 2\vec{a}_{\mathrm{p}} \cdot \dot{\widehat{n}}_{\mathrm{sp}} + \vec{v}_{\mathrm{p}} \cdot \ddot{\widehat{n}}_{\mathrm{sp}}\right)}{(c + \vec{v}_{\mathrm{s}} \cdot \widehat{n}_{\mathrm{sp}})} f_{\mathrm{obs}} - \frac{(c + \vec{v}_{\mathrm{p}} \cdot \widehat{n}_{\mathrm{sp}})}{(c + \vec{v}_{\mathrm{s}} \cdot \widehat{n}_{\mathrm{sp}})^2} \left(\dot{\vec{a}}_{\mathrm{s}} \cdot \widehat{n}_{\mathrm{sp}} + 2\vec{a}_{\mathrm{s}} \cdot \dot{\widehat{n}}_{\mathrm{sp}} + \vec{v}_{\mathrm{s}} \cdot \ddot{\widehat{n}}_{\mathrm{sp}}\right) f_{\mathrm{obs}} \\
& - 2\frac{\left(\vec{a}_{\mathrm{p}} \cdot \widehat{n}_{\mathrm{sp}} + \vec{v}_{\mathrm{p}} \cdot \dot{\widehat{n}}_{\mathrm{sp}}\right)\left(\vec{a}_{\mathrm{s}} \cdot \widehat{n}_{\mathrm{sp}} + \vec{v}_{\mathrm{s}} \cdot \dot{\widehat{n}}_{\mathrm{sp}}\right)}{(c + \vec{v}_{\mathrm{s}} \cdot \widehat{n}_{\mathrm{sp}})^2} f_{\mathrm{obs}} + 2\frac{(c + \vec{v}_{\mathrm{p}} \cdot \widehat{n}_{\mathrm{sp}})}{(c + \vec{v}_{\mathrm{s}} \cdot \widehat{n}_{\mathrm{sp}})^3} \left(\vec{a}_{\mathrm{s}} \cdot \widehat{n}_{\mathrm{sp}} + \vec{v}_{\mathrm{s}} \cdot \dot{\widehat{n}}_{\mathrm{sp}}\right)^2 f_{\mathrm{obs}} \\
& + 2\frac{\left(\vec{a}_{\mathrm{p}} \cdot \widehat{n}_{\mathrm{sp}} + \vec{v}_{\mathrm{p}} \cdot \dot{\widehat{n}}_{\mathrm{sp}}\right)}{(c + \vec{v}_{\mathrm{s}} \cdot \widehat{n}_{\mathrm{sp}})} \dot{f}_{\mathrm{obs}} - 2\frac{(c + \vec{v}_{\mathrm{p}} \cdot \widehat{n}_{\mathrm{sp}})}{(c + \vec{v}_{\mathrm{s}} \cdot \widehat{n}_{\mathrm{sp}})^2} \left(\vec{a}_{\mathrm{s}} \cdot \widehat{n}_{\mathrm{sp}} + \vec{v}_{\mathrm{s}} \cdot \dot{\widehat{n}}_{\mathrm{sp}}\right) \dot{f}_{\mathrm{obs}} + \frac{(c + \vec{v}_{\mathrm{p}} \cdot \widehat{n}_{\mathrm{sp}})}{(c + \vec{v}_{\mathrm{s}} \cdot \widehat{n}_{\mathrm{sp}})} \ddot{f}_{\mathrm{obs}} \,.
\end{aligned}
\tag{2.32}
$$

Dividing eq. (2.32) by eq. (2.14), we get:

$$
\begin{aligned}
\frac{\ddot{f}_{\mathrm{int}}}{f_{\mathrm{int}}} =& \frac{\left(\dot{\vec{a}}_{\mathrm{p}} \cdot \widehat{n}_{\mathrm{sp}} + 2\vec{a}_{\mathrm{p}} \cdot \dot{\widehat{n}}_{\mathrm{sp}} + \vec{v}_{\mathrm{p}} \cdot \ddot{\widehat{n}}_{\mathrm{sp}}\right)}{(c + \vec{v}_{\mathrm{p}} \cdot \widehat{n}_{\mathrm{sp}})} - \frac{\left(\dot{\vec{a}}_{\mathrm{s}} \cdot \widehat{n}_{\mathrm{sp}} + 2\vec{a}_{\mathrm{s}} \cdot \dot{\widehat{n}}_{\mathrm{sp}} + \vec{v}_{\mathrm{s}} \cdot \ddot{\widehat{n}}_{\mathrm{sp}}\right)}{(c + \vec{v}_{\mathrm{s}} \cdot \widehat{n}_{\mathrm{sp}})} \\
& - 2\frac{\left(\vec{a}_{\mathrm{p}} \cdot \widehat{n}_{\mathrm{sp}} + \vec{v}_{\mathrm{p}} \cdot \dot{\widehat{n}}_{\mathrm{sp}}\right)\left(\vec{a}_{\mathrm{s}} \cdot \widehat{n}_{\mathrm{sp}} + \vec{v}_{\mathrm{s}} \cdot \dot{\widehat{n}}_{\mathrm{sp}}\right)}{(c + \vec{v}_{\mathrm{p}} \cdot \widehat{n}_{\mathrm{sp}})(c + \vec{v}_{\mathrm{s}} \cdot \widehat{n}_{\mathrm{sp}})} + 2\frac{\left(\vec{a}_{\mathrm{s}} \cdot \widehat{n}_{\mathrm{sp}} + \vec{v}_{\mathrm{s}} \cdot \dot{\widehat{n}}_{\mathrm{sp}}\right)^2}{(c + \vec{v}_{\mathrm{s}} \cdot \widehat{n}_{\mathrm{sp}})^2} + 2\frac{\left(\vec{a}_{\mathrm{p}} \cdot \widehat{n}_{\mathrm{sp}} + \vec{v}_{\mathrm{p}} \cdot \dot{\widehat{n}}_{\mathrm{sp}}\right)}{(c + \vec{v}_{\mathrm{p}} \cdot \widehat{n}_{\mathrm{sp}})} \frac{\dot{f}_{\mathrm{obs}}}{f_{\mathrm{obs}}} \\
& - 2\frac{\left(\vec{a}_{\mathrm{s}} \cdot \widehat{n}_{\mathrm{sp}} + \vec{v}_{\mathrm{s}} \cdot \dot{\widehat{n}}_{\mathrm{sp}}\right)}{(c + \vec{v}_{\mathrm{s}} \cdot \widehat{n}_{\mathrm{sp}})} \frac{\dot{f}_{\mathrm{obs}}}{f_{\mathrm{obs}}} + \frac{\ddot{f}_{\mathrm{obs}}}{f_{\mathrm{obs}}} \\
=& \frac{\left(\dot{\vec{a}}_{\mathrm{p}} - \dot{\vec{a}}_{\mathrm{s}}\right) \cdot \widehat{n}_{\mathrm{sp}}}{c} + 2\frac{\left(\vec{a}_{\mathrm{p}} - \vec{a}_{\mathrm{s}}\right) \cdot \dot{\widehat{n}}_{\mathrm{sp}}}{c} + \frac{(\vec{v}_{\mathrm{p}} - \vec{v}_{\mathrm{s}}) \cdot \ddot{\widehat{n}}_{\mathrm{sp}}}{c} \\
& - 2\left(\frac{(\vec{a}_{\mathrm{p}} - \vec{a}_{\mathrm{s}}) \cdot \widehat{n}_{\mathrm{sp}}}{c} + \frac{1}{c}(\vec{v}_{\mathrm{p}} - \vec{v}_{\mathrm{s}}) \cdot \dot{\widehat{n}}_{\mathrm{sp}})\right)\left(\frac{\vec{a}_{\mathrm{s}} \cdot \widehat{n}_{\mathrm{sp}}}{c} + \frac{\vec{v}_{\mathrm{s}} \cdot \dot{\widehat{n}}_{\mathrm{sp}}}{c}\right) \\
& + 2\left(\frac{(\vec{a}_{\mathrm{p}} - \vec{a}_{\mathrm{s}}) \cdot \widehat{n}_{\mathrm{sp}}}{c} + \frac{1}{c}(\vec{v}_{\mathrm{p}} - \vec{v}_{\mathrm{s}}) \cdot \dot{\widehat{n}}_{\mathrm{sp}})\right) \frac{\dot{f}_{\mathrm{obs}}}{f_{\mathrm{obs}}} + \frac{\ddot{f}_{\mathrm{obs}}}{f_{\mathrm{obs}}} \,,
\end{aligned}
\tag{2.33}
$$

where in the second step we have again assumed $1 + \frac{\vec{v}_{\mathrm{s}}.\widehat{n}_{\mathrm{sp}}}{c} \approx 1$ and $1 + \frac{\vec{v}_{\mathrm{p}}.\widehat{n}_{\mathrm{sp}}}{c} \approx 1$. As already mentioned, this assumption also enable us to write $f_{\mathrm{int}} = f_{\mathrm{obs}} = f$. The above equation is simplified further with the help of eq. (2.17) as:

$$
\begin{aligned}
\left(\frac{\ddot{f}}{f}\right)_{\mathrm{int}} =& \frac{\left(\dot{\vec{a}}_{\mathrm{p}} - \dot{\vec{a}}_{\mathrm{s}}\right) \cdot \widehat{n}_{\mathrm{sp}}}{c} + 2\frac{\left(\vec{a}_{\mathrm{p}} - \vec{a}_{\mathrm{s}}\right) \cdot \dot{\widehat{n}}_{\mathrm{sp}}}{c} + \frac{(\vec{v}_{\mathrm{p}} - \vec{v}_{\mathrm{s}}) \cdot \ddot{\widehat{n}}_{\mathrm{sp}}}{c} + 2\left(\frac{\dot{f}}{f}\right)_{\mathrm{ex}} \left(\frac{\vec{a}_{\mathrm{s}} \cdot \widehat{n}_{\mathrm{sp}}}{c} + \frac{\vec{v}_{\mathrm{s}} \cdot \dot{\widehat{n}}_{\mathrm{sp}}}{c}\right) \\
& - 2\left(\frac{\dot{f}}{f}\right)_{\mathrm{ex}} \left(\frac{\dot{f}}{f}\right)_{\mathrm{obs}} + \left(\frac{\ddot{f}}{f}\right)_{\mathrm{obs}} \,,
\end{aligned}
\tag{2.34}
$$

where $\left(\frac{\ddot{f}}{f}\right)_{\rm int} = \frac{\ddot{f}_{\rm int}}{f}$ and $\left(\frac{\ddot{f}}{f}\right)_{\rm obs} = \frac{\ddot{f}_{\rm obs}}{f}$. Defining

$$\left(\frac{\ddot{f}}{f}\right)_{\rm ex} = \left(\frac{\ddot{f}}{f}\right)_{\rm obs} - \left(\frac{\ddot{f}}{f}\right)_{\rm int} \ , \tag{2.35}$$

eq. (2.34) can be written as,

$$\begin{aligned}\left(\frac{\ddot{f}}{f}\right)_{\rm ex} = -\Bigg[& \frac{\left(\dot{\vec{a}}_{\rm p} - \dot{\vec{a}}_{\rm s}\right)\cdot\widehat{n}_{\rm sp}}{c} + 2\frac{\left(\vec{a}_{\rm p} - \vec{a}_{\rm s}\right)\cdot\dot{\widehat{n}}_{\rm sp}}{c} + \frac{(\vec{v}_{\rm p} - \vec{v}_{\rm s})\cdot\ddot{\widehat{n}}_{\rm sp}}{c} + 2\left(\frac{\dot{f}}{f}\right)_{\rm ex}\left(\frac{\vec{a}_{\rm s}\cdot\widehat{n}_{\rm sp}}{c} + \frac{\vec{v}_{\rm s}\cdot\dot{\widehat{n}}_{\rm sp}}{c}\right) \\ & -2\left(\frac{\dot{f}}{f}\right)_{\rm ex}\left(\frac{\dot{f}}{f}\right)_{\rm obs}\Bigg] \ . \end{aligned} \tag{2.36}$$

In eq. (2.36), $\dot{\vec{a}}_{\rm p}$ is the jerk of the pulsar and $\dot{\vec{a}}_{\rm s}$ is the jerk of the Sun. The unit vector $\widehat{n}_{\rm sp}$ and its derivatives can be expressed in terms of other measurable parameters as discussed earlier in section 2.3. Those expressions are used in simplifying various terms of eq. (2.36) in the subsequent subsections. In particular, in section 2.6.1, we derive an expression for the second term $\left(\frac{\left(\vec{a}_{\rm p} - \vec{a}_{\rm s}\right)\cdot\dot{\widehat{n}}_{\rm sp}}{c}\right)$ in terms of measurable parameters. We perform the same task for the third term $\left(\frac{(\vec{v}_{\rm p} - \vec{v}_{\rm s})\cdot\ddot{\widehat{n}}_{\rm sp}}{c}\right)$ in section 2.6.2, for the fourth term $\left(\frac{\vec{a}_{\rm s}\cdot\widehat{n}_{\rm sp}}{c} + \frac{\vec{v}_{\rm s}\cdot\dot{\widehat{n}}_{\rm sp}}{c}\right)$ in section 2.6.3, and then finally for the first term $\left(\frac{\left(\dot{\vec{a}}_{\rm p} - \dot{\vec{a}}_{\rm s}\right)\cdot\widehat{n}_{\rm sp}}{c}\right)$ in section 2.6.4. As the derivation of the first term is the lengthiest, we present it at the end. Using the expressions derived in those subsections, eq. (2.36) can be written as:

for $b > 0$,

$$\begin{aligned}\left(\frac{\ddot{f}}{f}\right)_{\rm ex} = & -\left[\frac{1}{c}\,(\dot{a}_r - a_{\rm T}\mu_T\,\cos\alpha)\right] - \Bigg[2\left(\mu_b\,\frac{\sin b}{c}\,\left\{a_{\rm p,pl}\,\frac{R_{\rm s}}{R_{\rm p'}}\left(\frac{d\cos b}{R_{\rm s}} - \cos l\right) + a_{\rm s,pl}\,\cos l\right\} - \mu_b\,\frac{\cos b}{c}\,a_{\rm p,z}\right. \\ & \left. -\mu_l\,\frac{\sin l}{c}\,\left\{a_{\rm p,pl}\,\frac{R_{\rm s}}{R_{\rm p'}} - a_{\rm s,pl}\right\}\right) + 2\left(\frac{\dot{f}}{f}\right)_{\rm ex}\left(\cos b\,\cos l\,\frac{a_{\rm s,pl}}{c} + \mu_b\,\frac{v_{\rm s,pl}}{c}\,\sin b\,\sin l - \mu_l\,\frac{v_{\rm s,pl}}{c}\,\cos l\right)\Bigg] \\ & - \left[\frac{1}{c}\,\left(\mu_{\rm T}\,a_{\rm T}\,\cos\alpha - 3\,v_r\,{\mu_{\rm T}}^2\right)\right] + \left[2\left(\frac{\dot{f}}{f}\right)_{\rm ex}\left(\frac{\dot{f}}{f}\right)_{\rm obs}\right] \ , \end{aligned} \tag{2.37a}$$

for $b < 0$,

$$\begin{aligned}\left(\frac{\ddot{f}}{f}\right)_{\rm ex} = & -\left[\frac{1}{c}\,(\dot{a}_r - a_{\rm T}\mu_T\,\cos\alpha)\right] - \Bigg[2\left(\mu_b\,\frac{\sin b}{c}\,\left\{a_{\rm p,pl}\,\frac{R_{\rm s}}{R_{\rm p'}}\left(\frac{d\cos b}{R_{\rm s}} - \cos l\right) + a_{\rm s,pl}\,\cos l\right\} + \mu_b\,\frac{\cos b}{c}\,a_{\rm p,z}\right. \\ & \left. -\mu_l\,\frac{\sin l}{c}\,\left\{a_{\rm p,pl}\,\frac{R_{\rm s}}{R_{\rm p'}} - a_{\rm s,pl}\right\}\right) + 2\left(\frac{\dot{f}}{f}\right)_{\rm ex}\left(\cos b\,\cos l\,\frac{a_{\rm s,pl}}{c} + \mu_b\,\frac{v_{\rm s,pl}}{c}\,\sin b\,\sin l - \mu_l\,\frac{v_{\rm s,pl}}{c}\,\cos l\right)\Bigg] \\ & - \left[\frac{1}{c}\,\left(\mu_{\rm T}\,a_{\rm T}\,\cos\alpha - 3\,v_r\,{\mu_{\rm T}}^2\right)\right] + \left[2\left(\frac{\dot{f}}{f}\right)_{\rm ex}\left(\frac{\dot{f}}{f}\right)_{\rm obs}\right] \ . \end{aligned} \tag{2.37b}$$

In eq. (2.37), l is Galactic longitude, b is the Galactic latitude, d is the distance of the pulsar from the Sun, μ_l is the proper motion in l, μ_b is the proper motion in b, μ_{T} is the total transverse proper motion, R_{s} is the Galactocentric distance of the Sun, $R_{\mathrm{p'}}$ is Galactocentric distance of the pulsar projection on the Galactic plane. Additionally, $v_{\mathrm{s,pl}}$, $a_{\mathrm{s,pl}}$, $a_{\mathrm{p,pl}}$, and $a_{\mathrm{p,z}}$ are the components of velocities and accelerations as defined in section 2.4. a_{T} is the transverse component of the relative acceleration of the pulsar with respect to the Sun, and $\dot{a}_r$ is the rate of change of the radial component of the relative acceleration of the pulsar with respect to the Sun, v_r is the radial component of the relative velocity of the pulsar with respect to the Sun, and α is the angle between the transverse components of the relative velocity and the relative acceleration of the pulsar with respect to the Sun.

Eqs. (2.19) and (2.37) will remain the same regardless whether we use the spin frequency (f_{s}) and its derivatives or the orbital frequency (f_{b}) and its derivatives.

However, if the pulsar is in an unmodeled binary, the expressions for $\left(\frac{\dot{f}_{\mathrm{s}}}{f_{\mathrm{s}}}\right)_{\mathrm{ex}}$ and $\left(\frac{\ddot{f}_{\mathrm{s}}}{f_{\mathrm{s}}}\right)_{\mathrm{ex}}$ will contain extra terms due to the line-of-sight component of the orbital acceleration and jerk. There will be additional terms in all of $\left(\frac{\dot{f}_{\mathrm{s}}}{f_{\mathrm{s}}}\right)_{\mathrm{ex}}$, $\left(\frac{\ddot{f}_{\mathrm{s}}}{f_{\mathrm{s}}}\right)_{\mathrm{ex}}$, $\left(\frac{\dot{f}_{\mathrm{b}}}{f_{\mathrm{b}}}\right)_{\mathrm{ex}}$, and $\left(\frac{\ddot{f}_{\mathrm{b}}}{f_{\mathrm{b}}}\right)_{\mathrm{ex}}$ if the pulsar is in a globular cluster. We do not explore these effects in the present thesis, although discuss in brief in section 2.10.

Expressions of $\dot{a}_r$ and a_{T} in terms of observables like l, b, μ_l, μ_b, d, and v_r are derived in the section 2.6.4. Expression of α in terms of these observables is derived in the section 2.6.3. Those expressions are used to obtain numerical values of $\left(\frac{\ddot{f}}{f}\right)_{\mathrm{ex}}$ as will be described in chapter four.

We can now use the values of $\left(\frac{\ddot{f}}{f}\right)_{\mathrm{ex}}$, f, and $\ddot{f}_{\mathrm{obs}}$ to estimate the intrinsic value of the second derivative of the frequency ($\ddot{f}_{\mathrm{int}}$) by the following relation:

$$\ddot{f}_{\mathrm{int}} = f\left[\left(\frac{\ddot{f}}{f}\right)_{\mathrm{obs}} - \left(\frac{\ddot{f}}{f}\right)_{\mathrm{ex}}\right] = \ddot{f}_{\mathrm{obs}} - f\left(\frac{\ddot{f}}{f}\right)_{\mathrm{ex}} . \tag{2.38}$$

2.6.1 Simplifying the second term on the right hand side of eq. (2.36)

Let us now focus on the second term on the right hand side of eq. (2.36):

$$\begin{aligned}
\frac{\left(\vec{a}_{\rm p}-\vec{a}_{\rm s}\right)\cdot\dot{\widehat{n}}_{\rm sp}}{c} =& \frac{\left(\vec{a}_{\rm p}-\vec{a}_{\rm s}\right)\cdot\dot{\widehat{e_r}}}{c}\\
=&\frac{1}{c}\left(\vec{a}_{\rm p,pl}+\vec{a}_{\rm p,z}-\vec{a}_{\rm s,pl}-\vec{a}_{\rm s,z}\right)\cdot\left(\dot{\theta}\widehat{e_\theta}+\dot{\phi}\,\sin\theta\widehat{e_\phi}\right) \qquad \text{[used eq. (2.5)]}\\
=&\frac{1}{c}\left(\vec{a}_{\rm p,pl}-\vec{a}_{\rm s,pl}+\vec{a}_{\rm p,z}-\vec{a}_{\rm s,z}\right)\cdot\left(\dot{\theta}\,\cos\theta\,\cos\phi\widehat{e_x}+\dot{\theta}\,\cos\theta\,\sin\phi\widehat{e_y}-\dot{\theta}\,\sin\theta\widehat{e_z}\right.\\
&\left.-\dot{\phi}\,\sin\theta\,\sin\phi\widehat{e_x}+\dot{\phi}\,\sin\theta\,\cos\phi\widehat{e_y}\right). \qquad \text{[used eqs. (2.3) and (2.4)]}
\end{aligned} \tag{2.39}$$

For the ease of calculation, we perform the multiplication shown in eq. (2.39) by separating the parallel and perpendicular components of the acceleration. When we consider only the parallel component, we get,

$$\begin{aligned}
&\frac{1}{c}\left(\vec{a}_{\rm p,pl}-\vec{a}_{\rm s,pl}\right)\cdot\left(\dot{\theta}\,\cos\theta\,\cos\phi\widehat{e_x}+\dot{\theta}\,\cos\theta\,\sin\phi\widehat{e_y}-\dot{\theta}\,\sin\theta\widehat{e_z}-\dot{\phi}\,\sin\theta\,\sin\phi\widehat{e_x}+\dot{\phi}\,\sin\theta\,\cos\phi\widehat{e_y}\right)\\
=&\frac{1}{c}\left[\left(a_{\rm p,pl}\,\cos(l+\lambda-\frac{\pi}{2})\widehat{e_x}+a_{\rm p,pl}\,\sin(l+\lambda-\frac{\pi}{2})\widehat{e_y}-a_{\rm s,pl}\widehat{e_y}\right)\cdot\left(\dot{\theta}\,\cos\theta\,\cos\phi\widehat{e_x}+\dot{\theta}\,\cos\theta\,\sin\phi\widehat{e_y}\right.\right.\\
&\left.\left.-\dot{\theta}\,\sin\theta\widehat{e_z}-\dot{\phi}\,\sin\theta\,\sin\phi\widehat{e_x}+\dot{\phi}\,\sin\theta\,\cos\phi\widehat{e_y}\right)\right] \qquad \text{[see figs 2.1 and 2.3]}\\
=&\frac{1}{c}\left[-\dot{\theta}\,\sin b\left\{a_{\rm p,pl}\,\cos\lambda+a_{\rm s,pl}\,\cos l\right\}-\dot{\phi}\,\cos b\left\{a_{\rm p,pl}\,\sin\lambda-a_{\rm s,pl}\,\sin l\right\}\right]\\
=&-\frac{\dot{\theta}\,\sin b}{c}\left[a_{\rm p,pl}\,\cos\lambda+a_{\rm s,pl}\,\cos l\right]-\frac{\dot{\phi}\,\cos b}{c}\left[a_{\rm p,pl}\,\frac{R_{\rm s}\,\sin l}{R_{\rm p'}}-a_{\rm s,pl}\,\sin l\right]\\
&\qquad\qquad\qquad\qquad \text{[used } \sin\lambda=\frac{R_{\rm s}\,\sin l}{R_{\rm p'}}\text{, from sine law in } \triangle\text{SP}'\text{C of Fig. 2.1(b)]}\\
=&-\frac{\dot{\theta}\,\sin b}{c}\left[a_{\rm p,pl}\,\frac{R_{\rm s}}{R_{\rm p'}}\left(\frac{d\cos b}{R_{\rm s}}-\cos l\right)+a_{\rm s,pl}\,\cos l\right]-\frac{\dot{\phi}\,\cos b\,\sin l}{c}\left[a_{\rm p,pl}\,\frac{R_{\rm s}}{R_{\rm p'}}-a_{\rm s,pl}\right].
\end{aligned} \tag{2.40}$$

Similarly, when we consider only the perpendicular component, we get,

$$
\begin{aligned}
&\frac{1}{c}\left(\vec{a}_{\mathrm{p,z}}-\vec{a}_{\mathrm{s,z}}\right)\cdot\left(\dot{\theta}\cos\theta\cos\phi\,\widehat{e_x}+\dot{\theta}\cos\theta\sin\phi\,\widehat{e_y}-\dot{\theta}\sin\theta\,\widehat{e_z}-\dot{\phi}\sin\theta\sin\phi\,\widehat{e_x}+\dot{\phi}\sin\theta\cos\phi\,\widehat{e_y}\right)\\
&=\frac{1}{c}\left(\vec{a}_{\mathrm{p,z}}-\vec{a}_{\mathrm{s,z}}\right)\cdot\left(-\dot{\theta}\sin\theta\,\widehat{e_z}\right)\\
&=-\frac{\dot{\theta}\sin\theta}{c}\,\vec{a}_{\mathrm{p,z}}\cdot\widehat{e_z}\qquad[\text{as } a_{\mathrm{s,z}}=0]\\
&=\begin{cases}\frac{\dot{\theta}\cos b}{c}\,a_{\mathrm{p,z}} & \text{if } b>0\ ,\\ \frac{-\dot{\theta}\cos b}{c}\,a_{\mathrm{p,z}} & \text{if } b<0\ .\end{cases}\qquad[\text{used eq. (2.11) and } \sin\theta=\cos b \text{ as discussed in section 2.3}]
\end{aligned}
\tag{2.41}
$$

Using eqs. (2.40) and (2.41), we can re-write eq. (2.39) as:

for $b > 0$,

$$
\begin{aligned}
\frac{\left(\vec{a}_{\mathrm{p}}-\vec{a}_{\mathrm{s}}\right)\cdot\dot{\widehat{n}}_{\mathrm{sp}}}{c}
&=-\frac{\dot{\theta}\sin b}{c}\left[a_{\mathrm{p,pl}}\frac{R_{\mathrm{s}}}{R_{\mathrm{p'}}}\left(\frac{d\cos b}{R_{\mathrm{s}}}-\cos l\right)+a_{\mathrm{s,pl}}\cos l\right]-\frac{\dot{\phi}\cos b\sin l}{c}\left[a_{\mathrm{p,pl}}\frac{R_{\mathrm{s}}}{R_{\mathrm{p'}}}-a_{\mathrm{s,pl}}\right]\\
&\quad+\frac{\dot{\theta}\cos b}{c}a_{\mathrm{p,z}}\\
&=\mu_b\frac{\sin b}{c}\left[a_{\mathrm{p,pl}}\frac{R_{\mathrm{s}}}{R_{\mathrm{p'}}}\left(\frac{d\cos b}{R_{\mathrm{s}}}-\cos l\right)+a_{\mathrm{s,pl}}\cos l\right]-\mu_b\frac{\cos b}{c}a_{\mathrm{p,z}}-\mu_l\frac{\sin l}{c}\left[a_{\mathrm{p,pl}}\frac{R_{\mathrm{s}}}{R_{\mathrm{p'}}}-a_{\mathrm{s,pl}}\right]\ ,
\end{aligned}
\tag{2.42a}
$$

for $b < 0$,

$$
\begin{aligned}
\frac{\left(\vec{a}_{\mathrm{p}}-\vec{a}_{\mathrm{s}}\right)\cdot\dot{\widehat{n}}_{\mathrm{sp}}}{c}
&=-\frac{\dot{\theta}\sin b}{c}\left[a_{\mathrm{p,pl}}\frac{R_{\mathrm{s}}}{R_{\mathrm{p'}}}\left(\frac{d\cos b}{R_{\mathrm{s}}}-\cos l\right)+a_{\mathrm{s,pl}}\cos l\right]-\frac{\dot{\phi}\cos b\sin l}{c}\left[a_{\mathrm{p,pl}}\frac{R_{\mathrm{s}}}{R_{\mathrm{p'}}}-a_{\mathrm{s,pl}}\right]\\
&\quad-\frac{\dot{\theta}\cos b}{c}a_{\mathrm{p,z}}\\
&=\mu_b\frac{\sin b}{c}\left[a_{\mathrm{p,pl}}\frac{R_{\mathrm{s}}}{R_{\mathrm{p'}}}\left(\frac{d\cos b}{R_{\mathrm{s}}}-\cos l\right)+a_{\mathrm{s,pl}}\cos l\right]+\mu_b\frac{\cos b}{c}a_{\mathrm{p,z}}-\mu_l\frac{\sin l}{c}\left[a_{\mathrm{p,pl}}\frac{R_{\mathrm{s}}}{R_{\mathrm{p'}}}-a_{\mathrm{s,pl}}\right]\ .
\end{aligned}
\tag{2.42b}
$$

In the second step of the derivations of both of the eqs. (2.42a) and (2.42b), we have used $\mu_b = -\dot{\theta}$ and $\mu_l = -\dot{\phi}\cos b$ as mentioned in section 2.3.

We have used eq. (2.42) in eq. (2.36) to derive eq. (2.37) of section 2.6.

2.6.2 Simplifying the third term on the right hand side of eq. (2.36)

In this section, we express the third term on the right hand side of eq. (2.36), i.e., $\frac{(\vec{v}_{\rm p}-\vec{v}_{\rm s})\cdot\ddot{\widehat{n}}_{\rm sp}}{c}$ in terms of observable parameters. Using the expressions of $\vec{v}_{\rm p}-\vec{v}_{\rm s}$ from eq. (2.29) and $\ddot{\widehat{n}}_{\rm sp}$ from eq. (2.8), we get,

$$
\begin{aligned}
\frac{(\vec{v}_{\rm p}-\vec{v}_{\rm s})\cdot\ddot{\widehat{n}}_{\rm sp}}{c} =& \frac{1}{c}\left[\dot{d}\,\widehat{e}_r + d\,\dot{\theta}\,\widehat{e}_\theta + d\,\dot{\phi}\,\sin\theta\,\widehat{e}_\phi\right]\cdot\left[\left(\ddot{\theta}-\dot{\phi}^2\,\sin\theta\,\cos\theta\right)\widehat{e}_\theta - \left(\dot{\theta}^2+\dot{\phi}^2\,\sin^2\theta\right)\widehat{e}_r\right.\\
&\left. +\left(2\,\dot{\theta}\,\dot{\phi}\,\cos\theta + \ddot{\phi}\,\sin\theta\right)\widehat{e}_\phi\right]\\
=& \frac{1}{c}\left[d\,\dot{\theta}\,(\ddot{\theta}-\dot{\phi}^2\,\sin\theta\,\cos\theta) - \dot{d}\,(\dot{\theta}^2+\dot{\phi}^2\,\sin^2\theta) + d\,\dot{\phi}\,\sin\theta\,(2\,\dot{\theta}\,\dot{\phi}\,\cos\theta+\ddot{\phi}\,\sin\theta)\right]\\
=& \frac{1}{c}\left[d\,\dot{b}\,\ddot{b} - \dot{d}\,\dot{b}^2 - \dot{d}\,\dot{l}^2\,\cos^2 b - d\,\dot{b}\,\dot{l}^2\,\cos b\,\sin b + d\,\dot{l}\,\cos b\,\ddot{l}\,\cos b\right]\\
&\qquad\qquad [\text{as } \theta = 90^\circ - b,\ \sin\theta=\cos b,\ \cos\theta=\sin b,\ \dot{\theta}=-\dot{b} \text{ and } \dot{\phi}=\dot{l}]\\
=& \frac{1}{c}\left[d\,\dot{b}\,\ddot{b} - \dot{d}\,\dot{b}^2 - \dot{d}\,\dot{l}^2\,\cos^2 b - d\,\dot{b}\,\dot{l}^2\,\cos^2 b\,\tan b + d\,\dot{l}\,\cos b\,\ddot{l}\,\cos b\right]\\
=& \frac{1}{c}\left[d\,\mu_b\,\dot{\mu}_b - \dot{d}\,{\mu_b}^2 - \dot{d}\,{\mu_l}^2 - d\,\mu_b\,{\mu_l}^2\,\tan b + d\,\mu_l\,\ddot{l}\,\cos b\right]\\
&\qquad\qquad [\text{as } \mu_b=\dot{b},\ \dot{\mu}_b=\ddot{b} \text{ and } \mu_l=\dot{\phi}\,\sin\theta=\dot{l}\,\cos b]\\
=& \frac{1}{c}\left[d\,\mu_b\,\dot{\mu}_b - \dot{d}\,{\mu_b}^2 - \dot{d}\,{\mu_l}^2 - d\,\mu_b\,{\mu_l}^2\,\tan b + d\,\mu_l\,\{\dot{\mu}_l+\mu_l\,\mu_b\,\tan b\}\right]\\
&\qquad\qquad [\text{as } \dot{\mu}_l=\ddot{l}\cos b-\dot{l}\sin b\,\dot{b}=\ddot{l}\cos b-\mu_l\tan b\,\mu_b]\\
=& \frac{1}{c}\left[d\,(\mu_b\,\dot{\mu}_b+\mu_l\,\dot{\mu}_l) - \dot{d}\,({\mu_b}^2+{\mu_l}^2)\right]\\
=& \frac{1}{c}\left[d\,\mu_{\rm T}\,\dot{\mu}_{\rm T} - \dot{d}\,{\mu_{\rm T}}^2\right]\ . \qquad [\text{as } \mu_{\rm T}^2=\mu_l^2+\mu_b^2] \qquad (2.43)
\end{aligned}
$$

In eq. (2.43) $\mu_{\rm T}$, d, $\dot{d}=v_r$ are observable parameters, but not $\dot{\mu}_{\rm T}$. So, we need to express $\dot{\mu}_{\rm T}$ in terms of other observables like l, b, μ_l, μ_b, d, and v_r. In order to do so, we start with an alternative expression of the relative velocity:

$$
\vec{v}_{\rm p}-\vec{v}_{\rm s} = \frac{d}{dt}(d\,\widehat{e}_r) = \dot{d}\,\widehat{e}_r + d\,\dot{\widehat{e}}_r = v_r\,\widehat{e}_r + v_{\rm T}\,\widehat{e}_{\rm T,v}\ . \qquad [\text{used eq. (2.10a)}] \qquad (2.44)
$$

Here, v_r is the magnitude of the radial component and v_T is the magnitude of the transverse component of the relative velocity while $\widehat{e}_r$ and $\widehat{e}_{\rm T,v}$ are unit vectors in those directions. Differentiating eq. (2.44) with respect to time, we get the expression of relative acceleration as,

$$\begin{aligned}
\vec{a}_{\mathrm{p}} - \vec{a}_{\mathrm{s}} &= \dot{\vec{v}}_{\mathrm{p}} - \dot{\vec{v}}_{\mathrm{s}} \\
&= \dot{v}_r\, \widehat{e_r} + v_r\, \dot{\widehat{e_r}} + \dot{v}_{\mathrm{T}}\, \widehat{e}_{\mathrm{T,v}} + v_{\mathrm{T}}\, \dot{\widehat{e}}_{\mathrm{T,v}} \\
&= \dot{v}_r\, \widehat{e_r} + \frac{v_r\, v_{\mathrm{T}}}{d} \widehat{e}_{\mathrm{T,v}} + \dot{v}_{\mathrm{T}}\, \widehat{e}_{\mathrm{T,v}} - \frac{{v_{\mathrm{T}}}^2}{d} \widehat{e_r} \qquad \text{[used eqs. (2.10a) and (2.10b)]} \\
&= \left(\dot{v}_r - \frac{{v_{\mathrm{T}}}^2}{d}\right) \widehat{e_r} + \left(\dot{v}_{\mathrm{T}} + \frac{v_r\, v_{\mathrm{T}}}{d}\right) \widehat{e}_{\mathrm{T,v}}\ .
\end{aligned} \tag{2.45}$$

The relative acceleration can also be written as,

$$\vec{a}_{\mathrm{p}} - \vec{a}_{\mathrm{s}} = a_r \widehat{e_r} + a_{\mathrm{T}}\, \widehat{e}_{\mathrm{T,a}}\ , \tag{2.46}$$

where a_r is the magnitude of the radial component and a_T is the magnitude of the transverse component of the relative acceleration while $\widehat{e_r}$ and $\widehat{e}_{\mathrm{T,a}}$ are unit vectors in those directions. The expression for a_{T} in terms of other measurable quantities is derived in the section 2.6.4 (eq. (2.65)).

An important point to note here is the distinction between the directions of the transverse acceleration ($\widehat{e}_{\mathrm{T,a}}$) and the transverse velocity ($\widehat{e}_{\mathrm{T,v}}$). Consider a plane at the pulsar position to which $\widehat{e_r}$ is a normal, i.e., both of the vectors $\widehat{e}_{\mathrm{T,a}}$ and $\widehat{e}_{\mathrm{T,v}}$ lie in that plane. We can compare $\widehat{e}_{\mathrm{T,a}}$ and $\widehat{e}_{\mathrm{T,v}}$ using a set of orthogonal pair of coordinates, ($\widehat{e_l}$, $\widehat{e_b}$), drawn on this plane at the position of the pulsar (see Fig. 2.5). Here $\widehat{e_l}$ is the direction of positive μ_l and $\widehat{e_b}$ is the direction of positive μ_b. Thus the transverse velocity of the pulsar can be decomposed as $\vec{v}_{\mathrm{T}} = v_l \widehat{e_l} + v_b \widehat{e_b}$ with $v_l = d\,\mu_l$ and $v_b = d\,\mu_b$. From Fig. 2.5(b) we can see that, the angle that $\widehat{e}_{\mathrm{T,v}}$ makes with the $\widehat{e_l}$ direction is given by $\alpha_v = \tan^{-1}\left(\frac{v_b}{v_l}\right) = \tan^{-1}\left(\frac{\mu_b}{\mu_l}\right)$, whereas, the angle that $\widehat{e}_{\mathrm{T,a}}$ makes with the $\widehat{e_l}$ direction is given by $\alpha_a = \tan^{-1}\left(\frac{a_{\mathrm{T},b}}{a_{\mathrm{T},l}}\right)$, where $a_{\mathrm{T},l}$ and $a_{\mathrm{T},b}$ are the components of $\vec{a}_{\mathrm{T}}$ along $\widehat{e_l}$ and $\widehat{e_b}$ respectively (refer eqs. (2.54) and (2.56) for their derivation). Hence, as shown in Fig. 2.5(b), the angle (α) between $\widehat{e}_{\mathrm{T,a}}$ and $\widehat{e}_{\mathrm{T,v}}$ is given by the absolute difference of these angles, i.e., $\alpha = |\alpha_a - \alpha_v|$.

To understand the relationship between $\widehat{e}_{\mathrm{T,a}}$ and $\widehat{e}_{\mathrm{T,v}}$, we try to understand the origins of

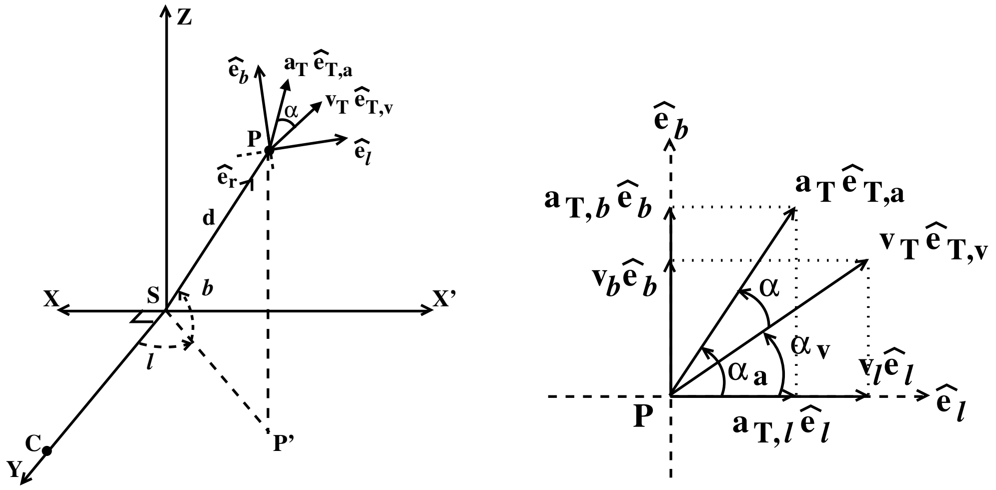

(a) (b)

Figure 2.5: a) A schematic 3D diagram showing the orthogonal coordinate frame $(\widehat{e}_l, \widehat{e}_b)$. b) A schematic planar diagram showing the components of the transverse acceleration and the transverse velocity in the orthogonal coordinate frame $(\widehat{e}_l, \widehat{e}_b)$, centred at the location of the pulsar.

the transverse velocity and acceleration. We have assumed that the gravitational potential of the Galaxy is the only cause of the transverse acceleration. The transverse velocity that we considered till now is based on the observed total proper motion of the pulsar. But this observed transverse velocity is a vector sum of the transverse velocity due to the Galactic potential (in the direction of the transverse acceleration) and an extra transverse velocity term caused by other factors like the initial supernova kick, etc. Hence, we can write,

$$v_{\mathrm{T}}\,\widehat{e}_{\mathrm{T,v}} = v_{\mathrm{T,gal}}\,\widehat{e}_{\mathrm{T,a}} + \vec{v}_{\mathrm{T,ext}}\ , \tag{2.47}$$

where $v_{\mathrm{T,gal}}$ is the magnitude of the transverse velocity due to the Galactic potential, $\widehat{e}_{\mathrm{T,a}}$ is the unit vector in its direction, and $\vec{v}_{\mathrm{T,ext}}$ is the extra transverse velocity term.

So, $\widehat{e}_{\mathrm{T,a}}$ can be written in terms of $\widehat{e}_{\mathrm{T,v}}$ as,

$$\widehat{e}_{\mathrm{T,a}} = \frac{v_{\mathrm{T}}\,\widehat{e}_{\mathrm{T,v}} - \vec{v}_{\mathrm{T,ext}}}{v_{\mathrm{T,gal}}}\ . \tag{2.48}$$

Taking the dot product with $\widehat{e}_{\rm T,v}$ on both sides of eq. (2.47), we get,

$$\begin{aligned} v_{\rm T} &= v_{\rm T,gal}\,\widehat{e}_{\rm T,a}\cdot\widehat{e}_{\rm T,v} + \vec{v}_{\rm T,ex}\cdot\widehat{e}_{\rm T,v}\ , \\ &= v_{\rm T,gal}\ \cos\alpha + \vec{v}_{\rm T,ex}\cdot\widehat{e}_{\rm T,v}\ . \qquad \text{[as } \alpha \text{ is the angle between } \widehat{e}_{\rm T,a} \text{ and } \widehat{e}_{\rm T,v}] \end{aligned} \tag{2.49}$$

Using the expression of $\widehat{e}_{\rm T,a}$ as given by eq. (2.48) in eq. (2.46), we get,

$$\begin{aligned} \vec{a}_{\rm p} - \vec{a}_{\rm s} &= a_r\,\widehat{e}_r + a_{\rm T}\,\frac{v_{\rm T}\,\widehat{e}_{\rm T,v} - \vec{v}_{\rm T,ex}}{v_{\rm T,gal}} \\ &= a_r\,\widehat{e}_r + a_{\rm T}\,\frac{(v_{\rm T,gal}\ \cos\alpha + \vec{v}_{\rm T,ex}\cdot\widehat{e}_{\rm T,v})\,\widehat{e}_{\rm T,v} - \vec{v}_{\rm T,ex}}{v_{\rm T,gal}} \qquad \text{[substituted } v_{\rm T} \text{ from eq. (2.49)]} \\ &= a_r\,\widehat{e}_r + a_{\rm T}\left[\cos\alpha\,\widehat{e}_{\rm T,v} - \frac{\{\vec{v}_{\rm T,ex} - (\vec{v}_{\rm T,ex}\cdot\widehat{e}_{\rm T,v})\,\widehat{e}_{\rm T,v}\}}{v_{\rm T,gal}}\right] \\ &= a_r\,\widehat{e}_r + a_{\rm T}\ \cos\alpha\,\widehat{e}_{\rm T,v} - a_{\rm T}\,\frac{\{\vec{v}_{\rm T,ex} - (\vec{v}_{\rm T,ex}\cdot\widehat{e}_{\rm T,v})\,\widehat{e}_{\rm T,v}\}}{v_{\rm T,gal}}\ . \end{aligned} \tag{2.50}$$

Now, let us define $\vec{\eta} = (\vec{v}_{\rm T,ex} - (\vec{v}_{\rm T,ex}\cdot\widehat{e}_{\rm T,v})\widehat{e}_{\rm T,v})$. We can see that $\vec{\eta}$ is perpendicular to $\widehat{e}_{\rm T,v}$ as $\vec{\eta}\cdot\widehat{e}_{\rm T,v} = \vec{v}_{\rm T,ex}\cdot\widehat{e}_{\rm T,v} - (\vec{v}_{\rm T,ex}\cdot\widehat{e}_{\rm T,v})\,(\widehat{e}_{\rm T,v}\cdot\widehat{e}_{\rm T,v}) = 0$. Hence, the coefficient of $\widehat{e}_{\rm T,v}$ in eq. (2.50) is just $a_{\rm T}\ \cos\alpha$.

Comparing the coefficients of $\widehat{e}_{\rm T,v}$ in eqs. (2.45) and (2.50), we get

$$a_{\rm T}\ \cos\alpha = \left(\dot{v}_{\rm T} + \frac{v_r\,v_{\rm T}}{d}\right)\ . \tag{2.51}$$

This expression would help us write $\dot{\mu}_{\rm T}$ in terms of the other measurable parameters. To do so, we start with differentiating both sides of the expression $\mu_{\rm T} = \frac{v_{\rm T}}{d}$ with respect to time and write

$$\begin{aligned} \dot{\mu}_{\rm T} &= \frac{\dot{v}_{\rm T}}{d} - \frac{v_{\rm T}\,\dot{d}}{d^2} \\ &= \frac{\dot{v}_{\rm T}}{d} - \frac{v_{\rm T}\,v_r}{d^2} \qquad \text{[as } \dot{d} = v_r] \\ &= \frac{1}{d}\left(a_{\rm T}\ \cos\alpha - \frac{v_r\,v_{\rm T}}{d}\right) - \frac{v_{\rm T}\,v_r}{d^2} \qquad \text{[used eq. (2.51)]} \\ &= \frac{a_{\rm T}\ \cos\alpha}{d} - 2\,\frac{v_{\rm T}\,v_r}{d^2} \\ &= \frac{a_{\rm T}\ \cos\alpha}{d} - 2\,\frac{\mu_{\rm T}\,v_r}{d} \qquad \text{[as } \mu_{\rm T} = v_{\rm T}/d]. \end{aligned} \tag{2.52}$$

Using expression of $\dot{\mu}_{\rm T}$ from eq. (2.52) in eq. (2.43), we obtain,

$$\begin{aligned}
\frac{(\vec{v}_{\rm p} - \vec{v}_{\rm s}) \cdot \ddot{\widehat{n}}_{\rm sp}}{c} &= \frac{1}{c} \left[d\, \mu_{\rm T}\, \dot{\mu}_{\rm T} - \dot{d}\, {\mu_{\rm T}}^2 \right] \\
&= \frac{1}{c} \left[d\, \mu_{\rm T} \left(\frac{a_{\rm T}\ \cos\alpha}{d} - 2\, \frac{\mu_{\rm T}\, v_r}{d} \right) - v_r\, {\mu_{\rm T}}^2 \right] \\
&= \frac{1}{c} \left[\mu_{\rm T}\, a_{\rm T}\ \cos\alpha - 3\, v_r\, {\mu_{\rm T}}^2 \right] \, . \qquad (2.53)
\end{aligned}$$

We have used eq. (2.53) in eq. (2.36) to derive eq. (2.37) of section 2.6.

Note that, to find the numerical value of the right hand side of eq. (2.53), we need to know the value of $\alpha = |\alpha_a - \alpha_v|$. For that, we need to know $\alpha_a = \tan^{-1}\left(\frac{a_{{\rm T},b}}{a_{{\rm T},l}}\right)$, and $\alpha_v = \tan^{-1}\left(\frac{\mu_b}{\mu_l}\right)$. α_v is already in terms of observable parameters μ_l and μ_b, but not α_a. So, our next goal is to find expressions for $a_{{\rm T},l}$ and $a_{{\rm T},b}$ in terms of observables or computable parameters. For this purpose we proceed as follows.

From Fig. 2.6(a), we can write expression for $a_{{\rm T},l}$ as,

$$\begin{aligned}
a_{{\rm T},l} &= \vec{a}_{\rm T}\ \cdot \widehat{e_l} = a_{\rm T}\, \widehat{e}_{\rm T,a} \cdot \widehat{e_l} \\
&= (\vec{a}_{\rm p} - \vec{a}_{\rm s} - a_r \widehat{e_r}) \cdot \widehat{e_l} && \text{[used eq. (2.46)]} \\
&= (\vec{a}_{\rm p} - \vec{a}_{\rm s}) \cdot \widehat{e_l} && [\text{as } \widehat{e_r} \perp \widehat{e_l}] \\
&= (\vec{a}_{\rm p,pl} + \vec{a}_{\rm p,z} - \vec{a}_{\rm s,pl} - \vec{a}_{\rm s,z}) \cdot \widehat{e_l} \\
&= \vec{a}_{\rm p,pl} \cdot \widehat{e_l} + \vec{a}_{\rm p,z} \cdot \widehat{e_l} - \vec{a}_{\rm s,pl} \cdot \widehat{e_l} - \vec{a}_{\rm s,z} \cdot \widehat{e_l} \\
&= \vec{a}_{\rm p,pl} \cdot \widehat{e_l} - \vec{a}_{\rm s,pl} \cdot \widehat{e_l} && [\text{as } \widehat{e_z} \perp \widehat{e_l}] \\
&= a_{\rm p,pl}\ \cos(\pi/2 + \lambda) - a_{\rm s,pl} \cos(3\pi/2 - l) && \text{[refer Fig. 2.6(a)]} \\
&= -a_{\rm p,pl}\ \sin\lambda + a_{\rm s,pl}\ \sin l \\
&= -(a_{\rm p,pl}\ \sin\lambda - a_{\rm s,pl}\ \sin l) \, . && (2.54)
\end{aligned}$$

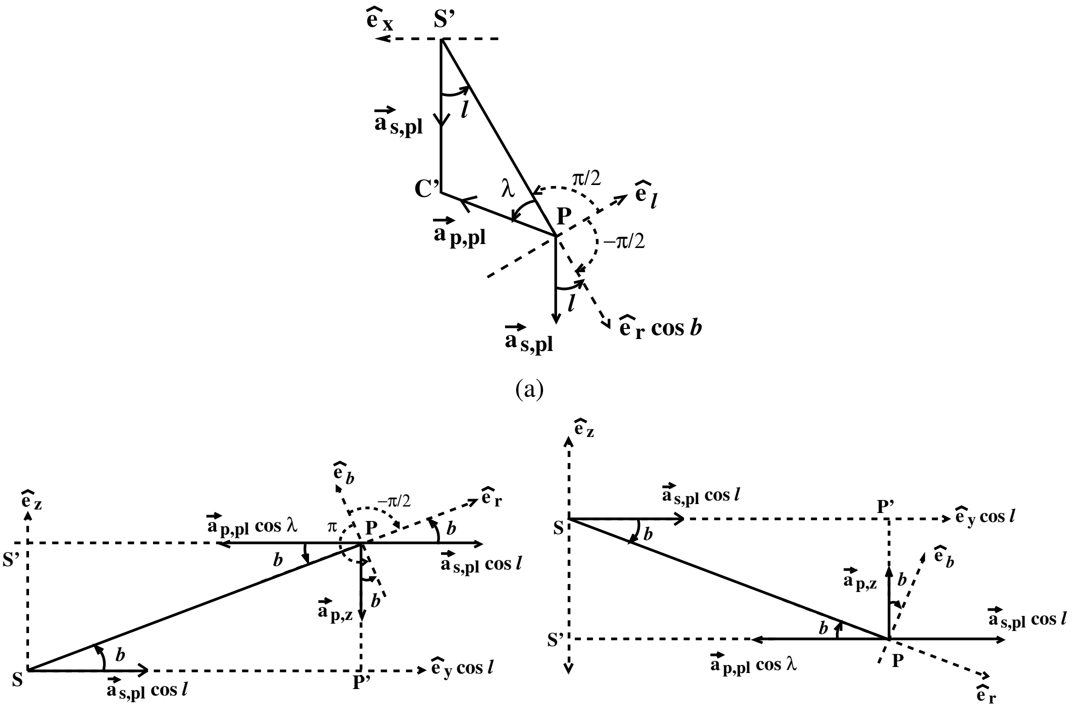

(a)

(b)

(c)

Figure 2.6: A schematic diagram showing the components of Solar and pulsar accelerations, parallel and perpendicular to the Galactic plane. The same cartesian coordinate system as in Fig. 2.1 has been used. (a) The Top panel (subfigure a) shows the top view of the Galactic plane. S′ and C′ are the projections of the Sun (S) and the Galactic centre (C) on the plane containing the pulsar (P) and parallel to the Galactic plane. Various acceleration vectors are shown with arrows. This figure is used to find the accelerations projected along $\widehat{e_l}$ at P. Angles are measured from $\widehat{e_l}$ in the anti-clockwise direction. (b) The bottom-left panel (subfigure b) shows the plane containing the Sun (S), the pulsar (P) and its projection on the Galactic plane (P’) in the edge-on view of the Galactic plane. Various acceleration vectors are shown with arrows. This figure is used to find the accelerations projected along $\widehat{e_b}$ at P. Angles are measured from $\widehat{e_b}$ in the anti-clockwise direction. Here the pulsar is shown above the Galactic plane (positive b). (c) The bottom-right panel (subfigure c) is the same as the ‘subfigure a’ except here the pulsar is shown below the Galactic plane (negative b).

From Figs. 2.6(b) and 2.6(c), we can write expression for $a_{\mathrm{T},b}$ as,

$$\begin{aligned}
a_{\mathrm{T},b} &= \vec{a}_{\mathrm{T}} \cdot \widehat{e_b} = a_{\mathrm{T}}\, \widehat{e}_{\mathrm{T,a}} \cdot \widehat{e_b} \\
&= (\vec{a}_{\mathrm{p}} - \vec{a}_{\mathrm{s}} - a_r \widehat{e_r}) \cdot \widehat{e_b} && \text{[used eq. (2.46)]} \\
&= (\vec{a}_{\mathrm{p}} - \vec{a}_{\mathrm{s}}) \cdot \widehat{e_b} && [\text{as } \widehat{e_r} \perp \widehat{e_b}] \\
&= (\vec{a}_{\mathrm{p,pl}} + \vec{a}_{\mathrm{p,z}} - \vec{a}_{\mathrm{s,pl}} - \vec{a}_{\mathrm{s,z}}) \cdot \widehat{e_b} \\
&= \vec{a}_{\mathrm{p,pl}} \cdot \widehat{e_b} + \vec{a}_{\mathrm{p,z}} \cdot \widehat{e_b} - \vec{a}_{\mathrm{s,pl}} \cdot \widehat{e_b}\, , && [\text{as } \vec{a}_{\mathrm{s,z}} \approx 0]
\end{aligned}$$

for $b > 0$,

$$\begin{aligned}
a_{\mathrm{T},b} &= a_{\mathrm{p,pl}} \cos\lambda \cos(\pi/2 - b) + a_{\mathrm{p,z}} \cos(\pi - b) - a_{\mathrm{s,pl}} \cos l \cos(3\pi/2 - b) \quad \text{[see Fig. 2.6(b)]} \\
&= -a_{\mathrm{p,z}} \cos b + a_{\mathrm{p,pl}} \cos\lambda \sin b + a_{\mathrm{s,pl}} \cos l \sin b \qquad (2.55)
\end{aligned}$$

for $b < 0$,

$$\begin{aligned}
a_{\mathrm{T},b} &= a_{\mathrm{p,pl}} \cos\lambda \cos(\pi/2 - b) + a_{\mathrm{p,z}} \cos b - a_{\mathrm{s,pl}} \cos l \cos(3\pi/2 - b) \quad \text{[see Fig. 2.6(c)]} \\
&= a_{\mathrm{p,z}} \cos b + a_{\mathrm{p,pl}} \cos\lambda \sin b + a_{\mathrm{s,pl}} \cos l \sin b\, . \qquad (2.56)
\end{aligned}$$

In the above derivations, $a_{\mathrm{p,pl}} \cos\lambda$ is the component of $\vec{a}_{\mathrm{p,pl}}$ along PS′. Using the expressions of $a_{\mathrm{T},l}$, and $a_{\mathrm{T},b}$, we calculate α_a, and subsequently, α. We then compute the value of $\cos\alpha$ that appear in eq. (2.37).

2.6.3 Simplifying the fourth term on the right hand side of eq. (2.36)

The fourth term on the right hand side of eq. (2.36) is $2\left(\frac{\dot{f}}{f}\right)_{\mathrm{ex}}\left(\frac{\vec{a}_{\mathrm{s}}\cdot\widehat{n}_{\mathrm{sp}}}{c} + \frac{\vec{v}_{\mathrm{s}}\cdot\dot{\widehat{n}}_{\mathrm{sp}}}{c}\right)$. We need to focus on the part $\left(\frac{\vec{a}_{\mathrm{s}}\cdot\widehat{n}_{\mathrm{sp}}}{c} + \frac{\vec{v}_{\mathrm{s}}\cdot\dot{\widehat{n}}_{\mathrm{sp}}}{c}\right)$, as we already know how to obtain the value of $\left(\frac{\dot{f}}{f}\right)_{\mathrm{ex}}$ (section 2.5).

We first consider $\vec{a}_{\rm s}\cdot\widehat{n}_{\rm sp}$,

$$
\begin{aligned}
\vec{a}_{\rm s}\cdot\widehat{n}_{\rm sp} &= \left(\vec{a}_{\rm s,pl}+\vec{a}_{\rm s,z}\right)\cdot\widehat{n}_{\rm sp}\\
&= \left(a_{\rm s,pl}\,\widehat{e}_{y}\right)\cdot\left(\cos b\,\widehat{n}_{sp'}+\sin b\,\widehat{e}_{z}\right)\quad \text{[as } a_{\rm s,z}\approx 0\text{, and } \widehat{n}_{sp'} \text{ is the unit vector along SP}'\text{ in Fig. 2.1(a)]}\\
&= \left(a_{\rm s,pl}\,\widehat{e}_{y}\right)\cdot\left(\cos b\,\widehat{n}_{sp'}+\sin b\,\widehat{e}_{z}\right)\\
&= a_{\rm s,pl}\cos b\,\widehat{e}_{y}\cdot\widehat{n}_{sp'}\qquad \text{[as } \widehat{e}_{y}\perp\widehat{e}_{z}\text{]}\\
&= \cos b\,\cos l\,a_{\rm s,pl}\,.\qquad \text{[as per Fig. 2.1(a), the angle between } \widehat{n}_{sp'} \text{ and } \widehat{e}_{y} \text{ is } l\text{]}
\end{aligned}
\tag{2.57}
$$

Next we consider $\vec{v}_{\rm s}\cdot\dot{\widehat{n}}_{\rm sp}$,

$$
\begin{aligned}
\vec{v}_{\rm s}\cdot\dot{\widehat{n}}_{\rm sp} &= (\vec{v}_{\rm s,pl}+\vec{v}_{\rm s,z})\cdot(\dot{\theta}\,\widehat{e}_{\theta}+\dot{\phi}\,\sin\theta\,\widehat{e}_{\phi})\qquad \text{[used eq. (2.5) and the fact that } \widehat{n}_{\rm sp}=\widehat{e}_{r};\dot{\widehat{n}}_{\rm sp}=\dot{\widehat{e}}_{r}\text{]}\\
&= (v_{\rm s,pl}\,\widehat{e}_{x}+v_{\rm s,z}\,\widehat{e}_{z})\cdot(\dot{\theta}\,\widehat{e}_{\theta}+\dot{\phi}\,\sin\theta\,\widehat{e}_{\phi})\qquad \text{[as } \vec{v}_{\rm s,pl} \text{ is along } \widehat{e}_{x}\text{, see sec. 2.4]}\\
&= (v_{\rm s,pl}\,\widehat{e}_{x})\cdot(\dot{\theta}\,\widehat{e}_{\theta}+\dot{\phi}\,\sin\theta\,\widehat{e}_{\phi})\qquad \text{[as } v_{\rm s,z}\approx 0\text{]}\\
&= (v_{\rm s,pl}\,\widehat{e}_{x})\cdot(-\mu_{b}\,\widehat{e}_{\theta}+\mu_{l}\,\widehat{e}_{\phi})\qquad \text{[as } \dot{\theta}=-\dot{b}=-\mu_{b},\dot{\phi}\,\sin\theta=\dot{l}\,\cos b=\mu_{l}\text{]}\\
&= (v_{\rm s,pl}\,\widehat{e}_{x})\cdot\{-\mu_{b}\,(\cos\theta\,\cos\phi\,\widehat{e}_{x}+\cos\theta\,\sin\phi\,\widehat{e}_{y}-\sin\theta\,\widehat{e}_{z})+\mu_{l}\,(-\sin\phi\,\widehat{e}_{x}+\cos\phi\,\widehat{e}_{y})\}\\
&\qquad\qquad \text{[used eqs. (2.3) and (2.4)]}\\
&= v_{\rm s,pl}\,(-\mu_{b}\cos\theta\,\cos\phi\,-\mu_{l}\sin\phi)\\
&= \mu_{b}\,v_{\rm s,pl}\,\sin b\,\sin l-\mu_{l}\,v_{\rm s,pl}\,\cos l\,.\\
&\qquad \text{[as } \theta=90^{\circ}-b,\phi=90^{\circ}+l \text{ giving } \cos\theta=\sin b,\sin\phi=\cos l,\cos\phi=-\sin l\text{]}
\end{aligned}
\tag{2.58}
$$

Using eqs. 2.57 and 2.58, we can write

$$
\left(\frac{\vec{a}_{\rm s}\cdot\widehat{n}_{\rm sp}}{c}+\frac{\vec{v}_{\rm s}\cdot\dot{\widehat{n}}_{\rm sp}}{c}\right)=\cos b\,\cos l\,\frac{a_{\rm s,pl}}{c}+\mu_{b}\,\frac{v_{\rm s,pl}}{c}\,\sin b\,\sin l-\mu_{l}\,\frac{v_{\rm s,pl}}{c}\,\cos l\,. \tag{2.59}
$$

We have used eq. (2.59) in eq. (2.36) to derive eq. (2.37) of section 2.5.

2.6.4 Simplifying the first term on the right hand side of eq. (2.36)

Here, we write $\frac{(\dot{\vec{d}}_{\rm p}-\dot{\vec{d}}_{\rm s})\cdot\widehat{n}_{\rm sp}}{c}$ of eq. (2.36) in terms of measurable quantities as follow.

$$
\begin{aligned}
\frac{1}{c}\left(\dot{\vec{d}}_{\rm p}-\dot{\vec{d}}_{\rm s}\right)\cdot\widehat{n}_{\rm sp} &= \frac{1}{c}\left(\frac{d}{dt}(\vec{d}_{\rm p}-\vec{d}_{\rm s})\right)\cdot\widehat{e_r} \\
&= \frac{1}{c}\left(\frac{d}{dt}(a_r\,\widehat{e_r}+a_{\rm T}\,\widehat{e}_{\rm T,a})\right)\cdot\widehat{e_r} \qquad \text{[used eq. (2.46)]} \\
&= \frac{1}{c}\left(\dot{a}_r\,\widehat{e_r}+a_r\,\dot{\widehat{e_r}}+\dot{a}_{\rm T}\,\widehat{e}_{\rm T,a}+a_{\rm T}\,\dot{\widehat{e}}_{\rm T,a}\right)\cdot\widehat{e_r} \\
&= \frac{1}{c}\left(\dot{a}_r\,\widehat{e_r}+a_r\mu_T\,\widehat{e}_{\rm T,v}+\dot{a}_{\rm T}\,\widehat{e}_{\rm T,a}+a_{\rm T}\,\dot{\widehat{e}}_{\rm T,a}\right)\cdot\widehat{e_r} \qquad \text{[used eq. (2.10a)]} \\
&= \frac{1}{c}\left(\dot{a}_r+a_{\rm T}\,\dot{\widehat{e}}_{\rm T,a}\cdot\widehat{e_r}\right)\,. \qquad [\text{as } \widehat{e}_{\rm T,v}\cdot\widehat{e_r}=0,\ \widehat{e}_{\rm T,a}\cdot\widehat{e_r}=0]
\end{aligned}
\tag{2.60}
$$

Let us now focus on the term $\dot{\widehat{e}}_{\rm T,a}\cdot\widehat{e_r}$ in eq. (2.60). Differentiating both sides of eq. (2.48) with respect to time and multiplying by $\widehat{e_r}$ from the right, we get,

$$
\begin{aligned}
\dot{\widehat{e}}_{\rm T,a}\cdot\widehat{e_r} &= \left(\frac{\dot{v}_{\rm T}\,\widehat{e}_{\rm T,v}+v_{\rm T}\,\dot{\widehat{e}}_{\rm T,v}-\dot{\vec{v}}_{\rm T,ex}}{v_{\rm T,gal}}-\frac{v_{\rm T}\,\widehat{e}_{\rm T,v}-\vec{v}_{\rm T,ex}}{{v_{\rm T,gal}}^2}\,\dot{v}_{\rm T,gal}\right)\cdot\widehat{e_r} \\
&= \left(\frac{\dot{v}_{\rm T}\,\widehat{e}_{\rm T,v}+v_{\rm T}\,\dot{\widehat{e}}_{\rm T,v}-\dot{\vec{v}}_{\rm T,ex}}{v_{\rm T,gal}}-\frac{\widehat{e}_{\rm T,a}}{v_{\rm T,gal}}\,\dot{v}_{\rm T,gal}\right)\cdot\widehat{e_r} \qquad \text{[used eq. (2.48)]} \\
&= \frac{(v_{\rm T}\,\dot{\widehat{e}}_{\rm T,v}\cdot\widehat{e_r}-\dot{\vec{v}}_{\rm T,ex}\cdot\widehat{e_r})}{v_{\rm T,gal}} \qquad [\text{as } \widehat{e}_{\rm T,v}\cdot\widehat{e_r}=0,\ \widehat{e}_{\rm T,a}\cdot\widehat{e_r}=0] \\
&= \frac{(-v_{\rm T}\,\mu_{\rm T}\widehat{e_r}\cdot\widehat{e_r}-\dot{\vec{v}}_{\rm T,ex}\cdot\widehat{e_r})}{v_{\rm T,gal}} \qquad \text{[used eq. (2.10b)]} \\
&= \frac{(-v_{\rm T}\,\mu_{\rm T}-\dot{\vec{v}}_{\rm T,ex}\cdot\widehat{e_r})}{v_{\rm T,gal}} \\
&= \frac{\{-(v_{\rm T,gal}\,\cos\alpha+\vec{v}_{\rm T,ex}\cdot\widehat{e}_{\rm T,v})\,\mu_{\rm T}-\dot{\vec{v}}_{\rm T,ex}\cdot\widehat{e_r}\}}{v_{\rm T,gal}} \qquad \text{[used eq. (2.49)]} \\
&= -\cos\alpha\,\mu_{\rm T}-\frac{(\vec{v}_{\rm T,ex}\cdot(\mu_{\rm T}\widehat{e}_{\rm T,v})+\dot{\vec{v}}_{\rm T,ex}\cdot\widehat{e_r})}{v_{\rm T,gal}} \\
&= -\cos\alpha\,\mu_{\rm T}-\frac{(\vec{v}_{\rm T,ex}\cdot\dot{\widehat{e_r}}+\dot{\vec{v}}_{\rm T,ex}\cdot\widehat{e_r})}{v_{\rm T,gal}} \qquad \text{[used eq. (2.10a)]} \\
&= -\cos\alpha\,\mu_{\rm T}-\frac{\frac{d}{dt}(\vec{v}_{\rm T,ex}\cdot\widehat{e_r})}{v_{\rm T,gal}}
\end{aligned}
\tag{2.61}
$$

$$
\begin{aligned}
&= -\cos\alpha\,\mu_{\mathrm{T}} - \frac{\frac{d}{dt}((v_{\mathrm{T}}\,\widehat{e}_{\mathrm{T,v}} - v_{\mathrm{T,gal}}\,\widehat{e}_{\mathrm{T,a}}) \cdot \widehat{e}_r)}{v_{\mathrm{T,gal}}} \qquad \text{[used eq. (2.47)]} \\
&= -\cos\alpha\,\mu_{\mathrm{T}} \;. \qquad [\because \widehat{e}_{\mathrm{T,v}} \cdot \widehat{e}_r = 0,\, \widehat{e}_{\mathrm{T,a}} \cdot \widehat{e}_r = 0] \qquad (2.62)
\end{aligned}
$$

Hence, on substituting the term $\dot{\widehat{e}}_{\mathrm{T,a}} \cdot \widehat{e}_r$ in eq. (2.60) by the final expression of eq. (2.62), we write

$$
\frac{1}{c}\left(\dot{\vec{a}}_{\mathrm{p}} - \dot{\vec{a}}_{\mathrm{s}}\right) \cdot \widehat{n}_{\mathrm{sp}} = \frac{1}{c}\left(\dot{a}_r - a_{\mathrm{T}}\,\mu_{\mathrm{T}}\,\cos\alpha\right)\;. \qquad (2.63)
$$

We now need to derive the expressions for $\dot{a}_r$ and a_{T} in terms of observable parameters like l, b, μ_l, μ_b, d, and v_r as well as calculable quantities like $a_{\mathrm{p,pl}}$, $a_{\mathrm{s,pl}}$, and $a_{\mathrm{p,z}}$. The method of expressing α in terms of observables has been already described in the section 2.6.2.

Eq. (2.46) gives $(\vec{a}_{\mathrm{p}} - \vec{a}_{\mathrm{s}}) \cdot (\vec{a}_{\mathrm{p}} - \vec{a}_{\mathrm{s}}) = a_r^2 + a_{\mathrm{T}}^2$ as $\vec{a}_r$ and $\vec{a}_T$ are perpendicular to each other. So,

$$
\begin{aligned}
a_{\mathrm{T}} &= \left((\vec{a}_{\mathrm{p}} - \vec{a}_{\mathrm{s}}) \cdot (\vec{a}_{\mathrm{p}} - \vec{a}_{\mathrm{s}}) - a_r^2\right)^{1/2} \\
&= \left((\vec{a}_{\mathrm{p}} - \vec{a}_{\mathrm{s}}) \cdot (\vec{a}_{\mathrm{p}} - \vec{a}_{\mathrm{s}}) - ((\vec{a}_{\mathrm{p}} - \vec{a}_{\mathrm{s}}) \cdot \widehat{e}_r)^2\right)^{1/2} \qquad \text{[used eq. (2.46)]} \\
&= \left((\vec{a}_{\mathrm{p,pl}} + \vec{a}_{\mathrm{p,z}} - \vec{a}_{\mathrm{s,pl}} - \vec{a}_{\mathrm{s,z}}) \cdot (\vec{a}_{\mathrm{p,pl}} + \vec{a}_{\mathrm{p,z}} - \vec{a}_{\mathrm{s,pl}} - \vec{a}_{\mathrm{s,z}}) - ((\vec{a}_{\mathrm{p}} - \vec{a}_{\mathrm{s}}) \cdot \widehat{n}_{\mathrm{sp}})^2\right)^{1/2} \\
&= \left((\vec{a}_{\mathrm{p,pl}} - \vec{a}_{\mathrm{s,pl}} + \vec{a}_{\mathrm{p,z}} - \vec{a}_{\mathrm{s,z}}) \cdot (\vec{a}_{\mathrm{p,pl}} - \vec{a}_{\mathrm{s,pl}} + \vec{a}_{\mathrm{p,z}} - \vec{a}_{\mathrm{s,z}}) - ((\vec{a}_{\mathrm{p}} - \vec{a}_{\mathrm{s}}) \cdot \widehat{n}_{\mathrm{sp}})^2\right)^{1/2} \\
&= \left((\vec{a}_{\mathrm{p,pl}} - \vec{a}_{\mathrm{s,pl}}) \cdot (\vec{a}_{\mathrm{p,pl}} - \vec{a}_{\mathrm{s,pl}}) + (\vec{a}_{\mathrm{p,z}} - \vec{a}_{\mathrm{s,z}}) \cdot (\vec{a}_{\mathrm{p,z}} - \vec{a}_{\mathrm{s,z}}) - ((\vec{a}_{\mathrm{p}} - \vec{a}_{\mathrm{s}}) \cdot \widehat{n}_{\mathrm{sp}})^2\right)^{1/2} \\
&\qquad [\text{as } \vec{a}_{\mathrm{p,pl}} \cdot \vec{a}_{\mathrm{p,z}} = \vec{a}_{\mathrm{p,pl}} \cdot \vec{a}_{\mathrm{s,z}} = \vec{a}_{\mathrm{s,pl}} \cdot \vec{a}_{\mathrm{p,z}} = \vec{a}_{\mathrm{s,pl}} \cdot \vec{a}_{\mathrm{s,z}} = 0] \\
&= \left((\vec{a}_{\mathrm{p,pl}} - \vec{a}_{\mathrm{s,pl}}) \cdot (\vec{a}_{\mathrm{p,pl}} - \vec{a}_{\mathrm{s,pl}}) + (\vec{a}_{\mathrm{p,z}} - \vec{a}_{\mathrm{s,z}}) \cdot (\vec{a}_{\mathrm{p,z}} - \vec{a}_{\mathrm{s,z}}) - c^2\left[\left(\frac{\dot{f}}{f}\right)_{\mathrm{ex,Galpl}} + \left(\frac{\dot{f}}{f}\right)_{\mathrm{ex,Galz}}\right]^2\right)^{1/2} \\
&\qquad \text{[used eq. (2.22)]}
\end{aligned}
$$

$$(2.64)$$

$$= \left(a_{\rm p,pl}^2 + a_{\rm s,pl}^2 - 2\, a_{\rm p,pl}\, a_{\rm s,pl}\, \cos(\pi - (l + \lambda)) + a_{\rm p,z}^2 - c^2 \left[\left(\frac{\dot{f}}{f}\right)_{\rm ex,Galpl} + \left(\frac{\dot{f}}{f}\right)_{\rm ex,Galz} \right]^2 \right)^{1/2}$$

[as $a_{\rm s,z} = 0$ and the angle between $\vec{a}_{\rm p,pl}$ and $\vec{a}_{\rm s,pl}$ is $\pi - (l + \lambda)$, see Figs. 2.1(a) and 2.3]

$$= \left(a_{\rm p,pl}^2 + a_{\rm s,pl}^2 + 2\, a_{\rm p,pl}\, a_{\rm s,pl}\, \cos(l + \lambda) + a_{\rm p,z}^2 - c^2 \left[\left(\frac{\dot{f}}{f}\right)_{\rm ex,Galpl} + \left(\frac{\dot{f}}{f}\right)_{\rm ex,Galz} \right]^2 \right)^{1/2} . \qquad (2.65)$$

Among the non-observables in eq. (2.65), the methods to obtain the values of $\left(\frac{\dot{f}}{f}\right)_{\rm ex,Galpl}$ and $\left(\frac{\dot{f}}{f}\right)_{\rm ex,Galz}$ have been discussed in section 2.5.1. In order to find the value of the remaining non-observable λ, we use the sine law in $\triangle$ SP'C of Fig. 2.1 to get,

$$\sin\lambda = \frac{R_{\rm s}\, \sin l}{R_{\rm p'}} . \qquad (2.66)$$

Now we work on the other non-observable in eq. (2.63), i.e., $\dot{a}_r$. Multiplying both sides of eq. (2.46) by $\widehat{e_r}$ from the right, we can write

$$a_r = (\vec{a}_{\rm p} - \vec{a}_{\rm s}) \cdot \widehat{e_r} = (\vec{a}_{\rm p} - \vec{a}_{\rm s}) \cdot \widehat{n}_{\rm sp} . \qquad [as\, \widehat{e}_{\rm T,a} \cdot \widehat{e_r} = 0] \qquad (2.67)$$

Differentiating eq. (2.67) with respect to time, we get

$$\begin{aligned}
\dot{a}_r =& \frac{d}{dt} \left[\left(\vec{a}_{\rm p} - \vec{a}_{\rm s} \right) \cdot \widehat{n}_{\rm sp} \right] \\
=& \frac{d}{dt} \left[\left(\vec{a}_{\rm p,pl} + \vec{a}_{\rm p,z} - \vec{a}_{\rm s,pl} - \vec{a}_{\rm s,z} \right) \cdot \widehat{n}_{\rm sp} \right] \\
=& \frac{d}{dt} \left[\left(\vec{a}_{\rm p,pl} - \vec{a}_{\rm s,pl} \right) \cdot \widehat{n}_{\rm sp} + \vec{a}_{\rm p,z} \cdot \widehat{n}_{\rm sp} \right] \qquad [\text{as } a_{\rm s,z} = 0] \\
=& \frac{d}{dt} \left[- \cos b \left(a_{\rm p,pl}\, \cos\lambda + a_{\rm s,pl}\, \cos l \right) - \left(a_{\rm p,z}\, \sin|b| \right) \right] \qquad [\text{see derivations of eqs. (2.23) and (2.27)}] \\
=& - \frac{d}{dt} \left[\cos b \left(a_{\rm p,pl}\, \cos\lambda + a_{\rm s,pl}\, \cos l \right) + a_{\rm p,z}\, \sin|b| \right] \\
=& - \Big[- \sin b \left(a_{\rm p,pl}\, \cos\lambda + a_{\rm s,pl}\, \cos l \right) \dot{b} + \cos b \left(\dot{a}_{\rm p,pl}\, \cos\lambda - a_{\rm p,pl}\, \sin\lambda\, \dot{\lambda} + \dot{a}_{\rm s,pl}\, \cos l - a_{\rm s,pl}\, \sin l\, \dot{l} \right) \\
& + \dot{a}_{\rm p,z}\, \sin|b| + a_{\rm p,z}\, \cos b\, \dot{b}\, \frac{b}{|b|} \Big] \qquad \left[\text{as } \cos|b| = \cos b, \text{ and } \frac{d}{dt}|b| = \dot{b}\, \frac{b}{|b|} \right] \\
=& \sin b \left(a_{\rm p,pl}\, \cos\lambda + a_{\rm s,pl}\, \cos l \right) \mu_b - \cos b \left(\dot{a}_{\rm p,pl}\, \cos\lambda + \dot{a}_{\rm s,pl}\, \cos l \right) - \dot{a}_{\rm p,z}\, \sin|b| + a_{\rm p,pl}\, \cos b\, \sin\lambda\, \dot{\lambda} \\
& + a_{\rm s,pl}\, \sin l\, \mu_l - a_{\rm p,z}\, \cos b\, \mu_b\, \frac{b}{|b|} . \qquad [\text{as } \mu_l = \dot{l} \cos b;\ \mu_b = \dot{b}] \qquad (2.68)
\end{aligned}$$

The non-observables in eq. (2.68) are λ, $\dot{\lambda}$, $\dot{a}_{\rm p,pl}$, $\dot{a}_{\rm s,pl}$, and $\dot{a}_{\rm p,z}$. The expression for λ is given in eq. (2.66). The time-derivative of this equation leads to an expression of $\dot{\lambda}$ as follows:

$$\cos\lambda\dot{\lambda} = \frac{R_\mathrm{s}\cos l}{R_{\mathrm{p}'}}\dot{l} - \frac{R_\mathrm{s}\sin l}{R_{\mathrm{p}'}^2}\frac{dR_{\mathrm{p}'}}{dt}\,, \tag{2.69}$$

giving

$$\begin{aligned}\dot{\lambda} &= \frac{R_\mathrm{s}\cos l}{\cos\lambda\, R_{\mathrm{p}'}}\dot{l} - \frac{R_\mathrm{s}\sin l}{\cos\lambda\, R_{\mathrm{p}'}^2}\frac{dR_{\mathrm{p}'}}{dt}\\ &= \frac{R_\mathrm{s}\cos l}{\cos\lambda\, R_{\mathrm{p}'}}\frac{\dot{l}\cos b}{\cos b} - \frac{R_\mathrm{s}\sin l}{\cos\lambda\, R_{\mathrm{p}'}^2}\frac{dR_{\mathrm{p}'}}{dt}\\ &= \frac{R_\mathrm{s}\cos l}{\cos\lambda\, R_{\mathrm{p}'}}\frac{\mu_l}{\cos b} - \frac{R_\mathrm{s}\sin l}{\cos\lambda\, R_{\mathrm{p}'}^2}\frac{dR_{\mathrm{p}'}}{dt}\,.\end{aligned} \tag{2.70}$$

The expression for $\frac{dR_{\mathrm{p}'}}{dt}$ in terms of observable quantities is obtained by differentiating both sides of eq. (2.24a) with respect to time as:

$$\begin{aligned}\frac{dR_{\mathrm{p}'}}{dt} &= \frac{1}{R_{\mathrm{p}'}}\left(d\cos^2 b\dot{d} - d^2\cos b\sin b\dot{b} - R_\mathrm{s}\cos b\cos l\dot{d} + R_\mathrm{s}d\sin b\cos l\dot{b} + R_\mathrm{s}d\cos b\sin l\dot{l}\right)\\ &= \frac{1}{R_{\mathrm{p}'}}\left((d\cos^2 b - R_\mathrm{s}\cos b\cos l)v_r + (R_\mathrm{s}d\sin b\cos l - d^2\cos b\sin b)\mu_b + R_\mathrm{s}d\sin l\,\mu_l\right)\,.\end{aligned} \tag{2.71}$$

We use eq. (2.71) in eq. (2.70), and eq. (2.70) in eq. (2.68). We compute the value of a_T using eq. (2.65) and the value of $\dot{a}_r$ using eq. (2.68). However, there are still some non-observable parameter remaining in eq. (2.68) that are $\dot{a}_{\mathrm{p,pl}}$, $\dot{a}_{\mathrm{p,z}}$, and $\dot{a}_{\mathrm{s,pl}}$. A method to obtain the values of these quantities has been described in section 2.9. The numerical values of a_T and $\dot{a}_r$ are then used in eq. (2.63) which is the first term of eq. (2.36).

2.7 Analytical expression for the intrinsic first derivative of the period

As mentioned earlier, in a timing analysis, although the spin frequency and its derivatives are fitted, it is the orbital period and its first derivative that are commonly fitted instead of the orbital frequency and its derivative (unless higher-order derivatives are needed). Thus, having expressions of dynamical terms both in the period and in the frequency domain are useful. In this section, we present the expressions for the dynamical terms contributing to the first derivative of the period.

As $P = \frac{1}{f}$ and $\frac{\dot{P}}{P} = -\frac{\dot{f}}{f}$ where f is the frequency and P is the period (either the spin or the orbital), we can re-write the Doppler shift eqs. (2.14) and (2.17) as,

$$P_{\rm int} = (c + \vec{v}_{\rm s}.\widehat{n}_{\rm sp})(c + \vec{v}_{\rm p}.\widehat{n}_{\rm sp})^{-1} P_{\rm obs} \ , \tag{2.72}$$

where $P_{\rm obs}$ is the observed value of the period and $P_{\rm int}$ is the intrinsic value of the period, and

$$\left(\frac{\dot{P}}{P}\right)_{\rm ex} = \left(\frac{\dot{P}}{P}\right)_{\rm obs} - \left(\frac{\dot{P}}{P}\right)_{\rm int} = \left[\frac{(\vec{a}_s - \vec{a}_p)\cdot\widehat{n}_{\rm sp}}{c} + \frac{1}{c}(\vec{v}_s - \vec{v}_p)\cdot\frac{d}{dt}(\widehat{n}_{\rm sp})\right] \ , \tag{2.73}$$

i.e., the expression of $\left(\frac{\dot{P}}{P}\right)_{\rm ex}$ is negative of that of $\left(\frac{\dot{f}}{f}\right)_{\rm ex}$. In eq. (2.73), $\dot{P}_{\rm obs}$ is the observed value of the first derivative of the period and $\dot{P}_{\rm int}$ is the intrinsic value of the first derivative of the period. With the assumption $P_{\rm obs} \sim P_{\rm int} = P$ (see section 2.5 for the reasoning), we have written $\frac{\dot{P}_{\rm obs}}{P_{\rm obs}} = \frac{\dot{P}_{\rm obs}}{P} = \left(\frac{\dot{P}}{P}\right)_{\rm obs}$ and $\frac{\dot{P}_{\rm int}}{P_{\rm int}} = \frac{\dot{P}_{\rm int}}{P} = \left(\frac{\dot{P}}{P}\right)_{\rm int}$. All the parameters appearing in eqs. (2.72) and (2.73) bear the same meaning as explained earlier.

Similarly, eq. (2.18) changes to,

$$\left(\frac{\dot{P}}{P}\right)_{\rm ex} = \left(\frac{\dot{P}}{P}\right)_{\rm ex,Gal} + \left(\frac{\dot{P}}{P}\right)_{\rm ex,Shk} = \left(\frac{\dot{P}}{P}\right)_{\rm ex,Galpl} + \left(\frac{\dot{P}}{P}\right)_{\rm ex,Galz} + \left(\frac{\dot{P}}{P}\right)_{\rm ex,Shk} \ . \tag{2.74}$$

In eq. (2.74), $\left(\frac{\dot{P}}{P}\right)_{\rm ex,Gal} = \left(\frac{\dot{P}}{P}\right)_{\rm ex,Galpl} + \left(\frac{\dot{P}}{P}\right)_{\rm ex,Galz}$ where $\left(\frac{\dot{P}}{P}\right)_{\rm ex,Galpl}$ and $\left(\frac{\dot{P}}{P}\right)_{\rm ex,Galz}$ are caused respectively, by the parallel and the perpendicular (to the Galactic plane) components of the relative acceleration of the pulsar with respect to the Sun.

Again, because of $\frac{\dot{P}}{P} = -\frac{\dot{f}}{f}$, the expressions for each of the excess terms in eq. (2.74) are the negative of the corresponding terms in the frequency domain. Specifically, from eq. (2.26), we can write,

$$\left(\frac{\dot{P}}{P}\right)_{\text{ex,Galpl}} = -\frac{\cos b}{c}\left\{a_{\text{p,pl}}\,\frac{R_{\text{s}}}{R_{\text{p}'}}\left(\frac{d\cos b}{R_{\text{s}}} - \cos l\right) + a_{\text{s,pl}}\,\cos l\right\}\,, \tag{2.75}$$

from eq. (2.27), we can write,

$$\left(\frac{\dot{P}}{P}\right)_{\text{ex,Galz}} = -\frac{1}{c}\,a_{\text{p,z}}\,\sin|b|\,, \tag{2.76}$$

and from eq. (2.31), we can write,

$$\left(\frac{\dot{P}}{P}\right)_{\text{ex,Shk}} = \frac{1}{c}\,d\mu_T^2 = \frac{1}{c}\frac{v_T^2}{d} = 2.42925\times10^{-21}\,d_{\text{kpc}}\,\mu^2_{T,\text{mas yr}^{-1}}\ \text{s}^{-1}\,. \tag{2.77}$$

Eq. (2.77) is the Shklovskii term in the period domain.

After computing $\left(\frac{\dot{P}}{P}\right)_{\text{ex}}$ in eq. (2.73), one can estimate the value of $\dot{P}_{\text{int}}$ using the relation:

$$\dot{P}_{\text{int}} = P\left[\left(\frac{\dot{P}}{P}\right)_{\text{obs}} - \left(\frac{\dot{P}}{P}\right)_{\text{ex}}\right] = \dot{P}_{\text{obs}} - P\left(\frac{\dot{P}}{P}\right)_{\text{ex}}\,, \tag{2.78}$$

if the values of P and $\dot{P}_{\text{obs}}$ are known.

The fractional dynamical terms shown in eq. (2.74) can be converted to the absolute dynamical terms as:

$$\dot{P}_{\text{Galpl}} = P\left(\frac{\dot{P}}{P}\right)_{\text{ex,Galpl}}\,, \tag{2.79a}$$

$$\dot{P}_{\text{Galz}} = P\left(\frac{\dot{P}}{P}\right)_{\text{ex,Galz}}\,, \tag{2.79b}$$

$$\dot{P}_{\text{Gal}} = P\left(\frac{\dot{P}}{P}\right)_{\text{ex,Gal}} = \dot{P}_{\text{Galpl}} + \dot{P}_{\text{Galz}}\,, \tag{2.79c}$$

$$\dot{P}_{\text{Shk}} = P\left(\frac{\dot{P}}{P}\right)_{\text{ex,Shk}}\,, \tag{2.79d}$$

$$\dot{P}_{\text{int}} = \dot{P}_{\text{obs}} - \dot{P}_{\text{Gal}} - \dot{P}_{\text{Shk}}\,. \tag{2.79e}$$

We have not shown the expressions of the excess terms in the second derivatives of the periods, as usually, the second or higher-order derivatives are fitted in the frequency domain. If needed, one can convert the intrinsic value of the second derivative of the frequency to the intrinsic value of the second derivative of the period using the relation $\ddot{P} = 2\frac{\dot{f}^2}{f^3} - \frac{\ddot{f}}{f^2}$.

2.8 Finding the parallel and perpendicular components of accelerations

We have seen that the final expressions for the 'excess' or the dynamical terms both for the first and the second derivative of the frequency (eqs. (2.19) and (2.37)) contain the components of acceleration of the pulsar parallel and perpendicular to the Galactic plane ($a_{\rm p,pl}$ and $a_{\rm p,z}$ respectively), as well as the acceleration of the Sun parallel to the Galactic plane ($a_{\rm s,pl}$). In this section, we describe the methods to obtain numerical values of $a_{\rm p,pl}$, $a_{\rm p,z}$, and $a_{\rm s,pl}$.

Conventionally, people adopt different approximations to find the values of $a_{\rm p,pl}$, $a_{\rm p,z}$, and $a_{\rm s,pl}$. As these approximations are still in practice, we first discuss these and point out their limitations in section 2.8.1. Then in section 2.8.2, we discuss a method to overcome these limitations using a model of the gravitational potential of the Galaxy. Finally, in sections 2.10 and 2.11, we discuss extra contributions in $\vec{a}_{\rm p}$ that might arise in special situations.

2.8.1 Finding the parallel and perpendicular components of accelerations: traditional methods

Here, we discuss the traditional methods to find the values of $a_{\rm s,pl}$ and $a_{\rm p,pl}$ in section 2.8.1.1 and then the method to find the value of $a_{\rm p,z}$ in section 2.8.1.2. For both of the cases, we also discuss the excess terms in the first derivative of the period (or the frequency).

2.8.1.1 Components of the accelerations parallel to the Galactic plane and their contributions to the excess term

We continue to use the labeling and nomenclature shown in Figs. 2.1 and 2.3 for reference in this section. As the Milky Way is in a stable configuration, $a_{\mathrm{s,pl}}$ and $a_{\mathrm{p,pl}}$ in can be identified with the magnitude of the equilibrium centripetal accelerations at S and P respectively of Fig. 2.3. Similarly, the equilibrium centripetal acceleration at P' can be denoted by $\vec{a}_{\mathrm{p',pl}}$ whose magnitude is $a_{\mathrm{p',pl}}$. So, we can write:

$$a_{\mathrm{s,pl}} = \frac{v_{\mathrm{s}}^2}{R_{\mathrm{s}}} , \tag{2.80a}$$

$$a_{\mathrm{p,pl}} = \frac{v_{\mathrm{p}}^2}{R_{\mathrm{p}}} , \tag{2.80b}$$

$$a_{\mathrm{p',pl}} = \frac{v_{\mathrm{p'}}^2}{R_{p'}} = \frac{v_{\mathrm{p'}}^2}{R_{\mathrm{p}}} , \tag{2.80c}$$

where v_{s} is the Galactic rotational speed at the location of the Sun, v_{p} is the Galactic rotational speed at P, and $v_{\mathrm{p'}}$ is the Galactic rotational speed at P′. We also know that $R_p = R_{p'}$.

One can find the value of $a_{\mathrm{s,pl}}$ from eq. (2.80a) with known values of v_{s} and R_{s}. It is of wide practise to use $v_{\mathrm{s}} = 240 \pm 8\,\mathrm{km\,s^{-1}}$ and $R_{\mathrm{s}} = 8.34 \pm 0.16\,\mathrm{kpc}$ (Reid et al., 2014; Matthews et al., 2016).

From the above equations, it is obvious that the magnitude of $\vec{a}_{\mathrm{p',pl}}$ is constant at a fixed value of R_{p}, but its direction depends on the value of l as it is always directed towards C. Similarly, $\vec{a}_{\mathrm{p,pl}}$ is always directed towards C′. Neglecting the height (perpendicular to the Galactic plane) dependence of the Galactic rotation curve, one usually assumes $v_{\mathrm{p}} = v_{\mathrm{p'}}$ giving $a_{\mathrm{p,pl}} = a_{\mathrm{p',pl}}$. Using these approximations, we can write eqs. (2.26) and (2.75) as,

$$\left(\frac{\dot{P}}{P}\right)_{\mathrm{ex,Galpl}} = -\left(\frac{\dot{f}}{f}\right)_{\mathrm{ex,Galpl}} = -\frac{\cos b}{c}\left\{\frac{v_{\mathrm{p'}}^2}{R_{\mathrm{p'}}}\frac{R_{\mathrm{s}}}{R_{\mathrm{p'}}}\left(\frac{d\cos b}{R_{\mathrm{s}}} - \cos l\right) + \frac{v_{\mathrm{s}}^2}{R_{\mathrm{s}}}\cos l\right\} . \tag{2.81}$$

Eq. (2.81) can be simplified as,

$$\left(\frac{\dot{P}}{P}\right)_{\text{ex,Galpl}} = -\left(\frac{\dot{f}}{f}\right)_{\text{ex,Galpl}} = -\frac{1}{c}\frac{v_{\text{s}}^2}{R_{\text{s}}}\left(\cos l + \frac{v_{\text{p}'}^2}{v_{\text{s}}^2}\,\frac{\beta}{(\sin^2 l + \beta^2)}\right)\cos b\,, \tag{2.82}$$

where $\beta = \frac{d\cos b}{R_{\text{s}}} - \cos l$ and $\frac{R_{\text{p}'}^2}{R_{\text{s}}^2} = \sin^2 l + \beta^2$. The second expression can be derived by rewriting eq. (2.24a) as

$$\begin{aligned}
\frac{R_{\text{p}'}^2}{R_{\text{s}}^2} &= 1 + \frac{(d\cos b)^2}{R_{\text{s}}^2} - 2\frac{d\cos b}{R_{\text{s}}}\cos l \\
&= 1 + \left(\frac{d\cos b}{R_{\text{s}}} - \cos l\right)^2 - \cos^2 l \qquad \text{[completed the square]} \\
&= \sin^2 l + \left(\frac{d\cos b}{R_{\text{s}}} - \cos l\right)^2 \\
&= \sin^2 l + \beta^2 \qquad \left[\text{defining}\,\beta = \frac{d\cos b}{R_{\text{s}}} - \cos l\right]
\end{aligned} \tag{2.83}$$

It is obvious that the sign of $\left(\frac{\dot{P}}{P}\right)_{\text{ex,Galpl}}$ depends on the values of l, b, d as well as on the form of the Galactic rotation curve. Eq. (2.82) is the expression of $\left(\frac{\dot{P}}{P}\right)_{\text{ex,Galpl}}$ provided the assumption $v_{\text{p}'} = v_{\text{p}}$ holds valid.

As the majority of known pulsars are located near the solar system ($R_{\text{p}} \sim R_{\text{s}}$), it is a common practice to use a linear form for the Galactic rotation curve, as:

$$v_{\text{p}'} = v_{\text{s}} + \left.\frac{dv}{dR}\right|_{R=R_{\text{s}}}\left(R_{\text{p}} - R_{\text{s}}\right) = v_{\text{s}}\left(1 - b_0\,\frac{R_{\text{p}} - R_{\text{s}}}{R_{\text{s}}}\right)\,, \tag{2.84}$$

where $b_0 = -\left.\frac{R_{\text{s}}}{v_{\text{s}}}\frac{dv}{dR}\right|_{R=R_{\text{s}}}$ is known as the 'slope parameter'. Damour & Taylor (1991) used eq. (2.84) with a negligibly small value of $b_0 = 0.00 \pm 0.03$, i.e., $v_{\text{p}'} \simeq v_{\text{s}}$ and eq. (2.82) with $\cos b = 1$ ($b \simeq 0°$) to obtain

$$\left(\frac{\dot{P}}{P}\right)_{\text{ex,Galpl,b=0}} = -\left(\frac{\dot{f}}{f}\right)_{\text{ex,Galpl,b=0}} = -\frac{1}{c}\frac{v_{\text{s}}^2}{R_{\text{s}}}\left(\cos l + \frac{\beta}{(\sin^2 l + \beta^2)}\right)\,. \tag{2.85}$$

If we remove the assumption $\cos b = 1$, but keep $v_{\text{p}'} \simeq v_{\text{s}}$, we can write,

$$\left(\frac{\dot{P}}{P}\right)_{\text{ex,Galpl}} = -\left(\frac{\dot{f}}{f}\right)_{\text{ex,Galpl}} = -\frac{1}{c}\frac{v_{\text{s}}^2}{R_{\text{s}}}\left(\cos l + \frac{\beta}{(\sin^2 l + \beta^2)}\right)\cos b\,. \tag{2.86}$$

Often, people simply use eq. (2.86) with recently estimated values of the parameters, e.g., $R_{\rm s} = 8.34 \pm 0.16\,{\rm kpc}$ and $v_{\rm s} = 240 \pm 8\,{\rm km\ s^{-1}}$ (Reid et al., 2014; Matthews et al., 2016). However, Reid et al. (2014) also obtained $\frac{dv}{dR}\big|_{R=R_{\rm s}} = -0.2 \pm 0.4$ km s^{-1} kpc^{-1}, i.e., $b_0 \neq 0$. So it would be more logical to use eq. (2.84) with these updated values of the parameters to calculate $v_{\rm p'}$ and then use that value in eq. (2.82) to estimate $\left(\frac{\dot{P}}{P}\right)_{\rm ex,Galpl}$.

Nonetheless, eq. (2.84) is not valid for pulsars with $R_{\rm p} < 4$ kpc where the Galactic rotation curve is not linear at all (Crosta et al., 2020). In such a case one can replace eq. (2.84) by a more realistic rotation curve, say the one returned by 'galpy' (Bovy, 2015)[2] . The value of $v_{\rm p'}$ from that rotation curve can be used in eq. (2.82) to estimate the value of $\left(\frac{\dot{P}}{P}\right)_{\rm ex,Galpl}$.

However, for high-latitude pulsars, the assumption of $v_{\rm p} = v_{\rm p'}$ (or $a_{\rm p,pl} = a_{\rm p',pl}$) resulting in eq. (2.82) should not be used, and one should rather find a better way to estimate $\left(\frac{\dot{P}}{P}\right)_{\rm ex,Galpl}$ or $\left(\frac{\dot{f}}{f}\right)_{\rm ex,Galpl}$, which we discuss in section 2.8.2.

2.8.1.2 Components of the accelerations perpendicular to the Galactic plane and their contributions to the excess term

We already know (eqs. (2.27) and (2.76)) that

$$\left(\frac{\dot{P}}{P}\right)_{\rm ex,Galz} = -\left(\frac{\dot{f}}{f}\right)_{\rm ex,Galz} = -\frac{1}{c}\, a_{\rm p,z} \sin|b| \,. \tag{2.87}$$

There have been many efforts to evaluate this perpendicular component of the acceleration, commonly known as K_z, due to the gravitational field of the Galaxy. In these traditional approaches, one usually first determines the densities of different components of the Galaxy using observed positions, velocities, numbers and luminosities of different types of stars (mainly K-giants), and then solves Poisson's equation for each component to find the value of K_z (Holmberg & Flynn, 2000, and references therein). Such works are usually done for 'local' stars, i.e., for stars very close to the Sun. Nice & Taylor (1995) used

---

[2] 'galpy' is a python package publicly available at https://github.com/jobovy/galpy. It contains the model of the gravitational potential of the Galaxy, which we have decided to use and will discuss later in details.

one such work (Kuijken & Gilmore, 1989) when they were studying PSR J2019+2425 ($R_p \simeq 7.92$ kpc, $z \simeq -0.13$ kpc) and PSR J2322+2057 ($R_p \simeq 8.47$ kpc, $z \simeq -0.61$ kpc), as both of these pulsars are close enough to the Sun. The analytical expression for $a_{\rm p,z}/c$ (or K_z/c) used by Nice & Taylor (1995) can be written (with the direction of the vectors for better clarity) as:

$$\frac{a_{\rm p,z}}{c} = 1.08101 \times 10^{-19} \left[0.58 + \frac{1.25}{(z_{\rm kpc}^2 + 0.0324)^{1/2}} \right] |z_{\rm kpc}| \;\; {\rm s}^{-1} \, , \tag{2.88}$$

where $z_{\rm kpc}$ is the vertical height of the pulsar in the unit of kpc and the relation $z = d \, \sin b$ leads to $z_{\rm kpc} = d_{\rm kpc} \, \sin b$ where $d_{\rm kpc}$ is the distance of the pulsar from the Sun in the unit of kpc.

Afterwards, this expression has been used for other pulsars, even for the ones that are not that close to the Sun. However, Lazaridis et al. (2009) and Desvignes et al. (2016) used revised values of K_z given by Holmberg & Flynn (2004). The z-dependence of K_z is shown in the Figure 8 of Holmberg & Flynn (2004), which Lazaridis et al. (2009) fitted as

$$a_{\rm p,z} = 0.30857 \, (2.27|z_{\rm kpc}| + 3.68(1.0 - e^{(-4.31|z_{\rm kpc}|)})) \;\; {\rm km\,s^{-2}pc^{-1}} \, . \tag{2.89}$$

We fit the same data with a different functional form as:

$$\begin{aligned} \frac{a_{\rm p,z}}{c} &= 1.08101 \times 10^{-19} \left[0.47 + \frac{1.56}{(z_{\rm kpc}^2 + 0.1673)^{1/2}} + \frac{0.01}{(z_{\rm kpc}^2 + 0.0318)^{3/2}} \right] |z_{\rm kpc}| \;\; {\rm s}^{-1} \qquad \text{for } |z_{kpc}| \leq 1.5 \\ &= 1.08101 \times 10^{-19} \left[0.54 + \frac{1.43}{(z_{\rm kpc}^2 + 0.0467)^{1/2}} \right] |z_{\rm kpc}| \;\; {\rm s}^{-1} \qquad \text{for } |z_{kpc}| > 1.5 \, . \end{aligned} \tag{2.90}$$

In both the eqs. (2.88) and (2.90), the multiplicative factor 1.08101×10^{-19} arises to convert km^2 s^{-2} pc$^{-1}/c$ to the unit of s^{-1}.

In the left panel of Fig 2.7, we show our fit, i.e., eq. (2.90) with a dotted line and the earlier fit by Lazaridis et al. (2009), i.e., eq. (2.89) with a dashed line with the data of Holmberg

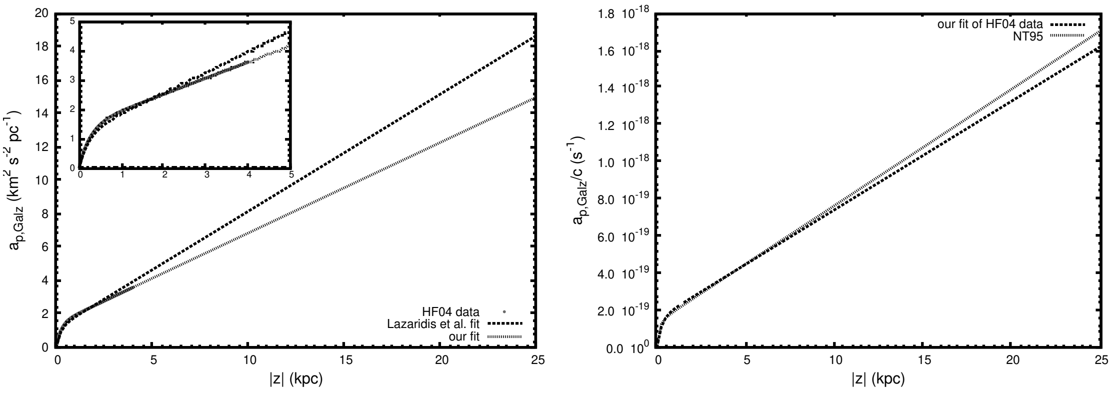

(a)

(b)

Figure 2.7: The vertical acceleration due to the gravitational potential of the Galaxy. In both of the panels, the absolute value of the vertical height in kpc ($|z_{\rm kpc}|$) is shown along the abscissa. The left panel (panel-a) compares our fit (the dotted line) as in eq. (2.90), and the fit by Lazaridis et al. (2009) (the dashed line) as in eq. (2.89) with the data of Holmberg & Flynn (2004) (dark circles plotted upto $|z_{\rm kpc}| \sim 5$). We also show a zoomed in (upto $|z_{\rm kpc}| = 5$) plot in the inset. The mixed unit along the ordinate that represents $a_{\rm p,z}$ should be noted. A multiplicative factor of 3.24078×10^{-11} will convert this into the SI unit m s^{-2}. The right panel (panel-b) compares our fit (eq. (2.90), the dashed line) with the expression given by Nice & Taylor (1995) (eq. (2.88), the dotted line). A multiplicative factor of $3.24078 \times 10^{-11}/c = 1.08101 \times 10^{-19}$ has been used to obtain the values of $a_{\rm p,z}/c$ in s^{-1}.

& Flynn (2004) (dark circles plotted upto $|z_{\rm kpc}| \sim 5$). We also show a zoomed in (upto $|z_{\rm kpc}| = 5$) plot in the inset. The discrepancy between the two fits for $|z| > 5$ kpc is clearly visible. Moreover, even at low values of $|z|$, i.e., for $|z| < 1.5$ kpc, our fit matches the data better than the fit by Lazaridis et al. (2009). In the right panel of Fig 2.7, we compare eqs. (2.88) and (2.90). It is clear that for upto $|z| \sim 10$ kpc, both of these equations give almost the same results. However, even Holmberg & Flynn (2004) used only the stars close to the Sun. So, it will not be accurate enough to even use eq. (2.90) for pulsars with $R_{\rm p}$ significantly different than $R_{\rm s}$ and/or very high values of $|z|$. In such cases, it would be preferable to adopt a better method to calculate the value of $a_{\rm p,z}/c$. More recently, Bovy & Rix (2013, figure 17) gave a $K_z(R)$ law for stars in somewhat larger range of the Galactocentric radius (R), i.e., between 5 to 9 kpc, but keeping $|z| = 1.1$ kpc. So, even this work is not suitable to use for pulsars in any arbitrary locations in the Galaxy, and we decide to use the gravitational potential of the Galaxy provided by galpy to resolve this issue.

Intuitively, at a very high value of $|z|$, a pulsar would experience less gravitational force, hence $a_{\rm p,z}/c$ should start decreasing with the increase of $|z|$ after a certain value of $|z|$. Both eqs. (2.88) and (2.90) fail to hint for this trend. The realistic potential used for the Galaxy in galpy reveals this feature.

2.8.2 Finding the parallel and perpendicular components of accelerations: a new method based on a model of the gravitational potential of the Galaxy

If we write the gravitational potential of the Galaxy as $\Phi_{\rm MW}(R,z)$, where R is the Galactocentric cylindrical radius and z is the height along the z-axis taken perpendicular to the Galactic plane, then $\vec{a}_{\rm p} = -\vec{\nabla}\Phi_{\rm MW}(R_{\rm p},z) = -\vec{\nabla}\Phi_{\rm MW}(R_{\rm p'},z)$ and $\vec{a}_{\rm s} = -\vec{\nabla}\Phi_{\rm MW}(R_{\rm s},z)$. Also, as $\Phi_{\rm MW}(R,z)$ is an attractive potential, it is a negative quantity, $\frac{\partial \Phi_{\rm MW}(R,z)}{\partial R}$ is always positive, and $\frac{\partial \Phi_{\mathrm{MW}}(R,z)}{\partial z}$ is positive for positive z and negative for negative z. On the other hand, $a_{\mathrm{p,pl}}$, $a_{\mathrm{p,z}}$, and $a_{\mathrm{s,pl}}$ are always positive as these are the magnitudes of the vectors $\vec{a}_{\mathrm{p,pl}}$, $\vec{a}_{\mathrm{p,z}}$, and $\vec{a}_{\mathrm{s,pl}}$ respectively.

With these definitions, we get,

$$a_{\mathrm{p,pl}} = \left| \left. \frac{\partial \Phi_{\mathrm{MW}}(R,z)}{\partial R} \right|_{R=R_{\mathrm{p}}} \right| = \left. \frac{\partial \Phi_{\mathrm{MW}}(R,z)}{\partial R} \right|_{R=R_{\mathrm{p}}} , \tag{2.91}$$

$$a_{\mathrm{s,pl}} = \left| \left. \frac{\partial \Phi_{\mathrm{MW}}(R,z)}{\partial R} \right|_{R=R_{\mathrm{s}}} \right| = \left. \frac{\partial \Phi_{\mathrm{MW}}(R,z)}{\partial R} \right|_{R=R_{\mathrm{p}}} , \tag{2.92}$$

and

$$\begin{aligned} a_{\mathrm{p,z}} &= \left| \left. \frac{\partial \Phi_{\mathrm{MW}}(R,z)}{\partial z} \right|_{R=R_{\mathrm{p}}} \right| \\ &= \begin{cases} \left. \frac{\partial \Phi_{\mathrm{MW}}(R,z)}{\partial z} \right|_{R=R_{\mathrm{p}}} & \text{if } z > 0 \\ - \left. \frac{\partial \Phi_{\mathrm{MW}}(R,z)}{\partial z} \right|_{R=R_{\mathrm{p}}} & \text{if } z < 0 \, . \end{cases} \end{aligned} \tag{2.93}$$

The publicly available package ‘galpy’ (Bovy, 2011) has a wide collection of models for $\Phi_{\mathrm{MW}}(R,z)$ and any of those can be used to estimate the values of $a_{\mathrm{p,pl}}$, $a_{\mathrm{p,z}}$ and $a_{\mathrm{s,pl}}$ using the known values of R and z and the above equations. One such potential is a combination of three potentials, a Miyamoto-Nagai disc potential (Miyamoto & Nagai, 1975), a spherical power-law density with an exponential cut-off to model the potential of the Galactic bulge, and a Navarro-Frenk-White potential (Navarro et al., 1997) for the dark matter halo. The resulting potential $\Phi_{\mathrm{MW}}(R,z)$ is known as `MWPotential2014` in galpy. However, this default potential does not include the super-massive black hole at the Galactic centre. It is suggested to include the effect of the supermassive black hole by adding a Kepler potential in the form of `KeplerPotential` with a proper choice of the mass of the black hole (e.g., $4 \times 10^{6}\,\mathrm{M}_{\odot}$) to the original `MWPotential2014`. This new potential can be called `MWPotential2014BH`. In this thesis, we mainly work with these two potentials.

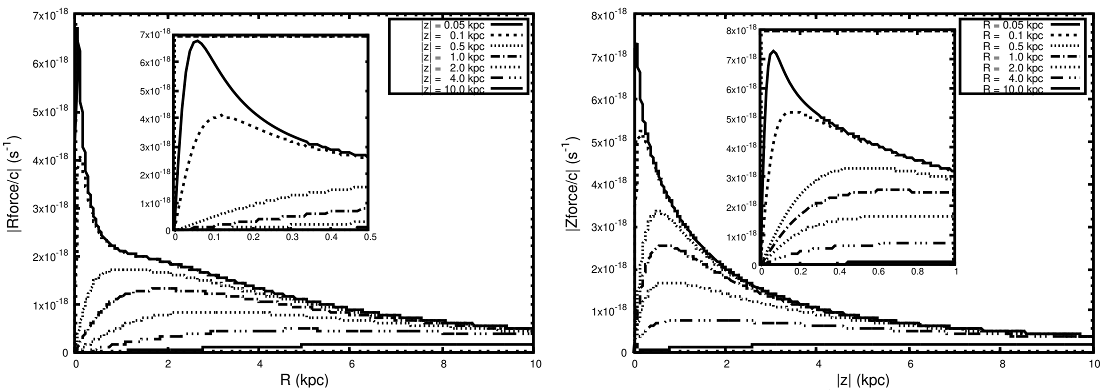

(a) (b)

Figure 2.8: The left panel shows the variation of |`Rforce`|/c with R for different fixed values of $|z|$. The inset shows the low R region zoomed in. The right panel shows the variation of |`zforce`|/c with $|z|$ for different fixed values of R. The inset shows the low $|z|$ region zoomed in. For both of the panels, galpy's default potential for the Galaxy without the central super-massive black-hole `MWPotential2014` has been used.

In galpy, two useful functions are `Rforce` $= -\frac{\partial \Phi_{\rm MW}(R,z)}{\partial R}$ and `zforce` $= -\frac{\partial \Phi_{\rm MW}(R,z)}{\partial z}$. With these definitions, `Rforce` is always negative and `zforce` is negative for positive z and positive for negative z. Then eqs. (2.91) and (2.92) give $a_{\rm p,pl} = -$`Rforce` at the location of the pulsar and $a_{\rm p,pl} = -$`Rforce` at the location of the Sun. Similarly, eq. (2.92) give $a_{\rm p,z} = -$`zforce` at the location of the pulsar if the pulsar is above the Galactic plane ($z > 0$) or $a_{\rm p,z} =$ `zforce` at the location of the pulsar if the pulsar is below the Galactic plane ($z < 0$). For the sake of simplicity, one can write $a_{\rm p,pl} =$ |`Rforce`| and $a_{\rm p,z} =$ |`zforce`|. We now explore the preperties of |`Rforce`| and |`zforce`| with `MWPotential2014`.

By plotting |`Rforce`|/c against R for different fixed values of $|z|$ (the left panel of Fig. 2.8), we find that it first increases and then decreases with the increase of R. The slope of the curve is steeper at smaller $|z|$ in both the rising and the falling sides. For any fixed $|z|$, the rise is much steeper than the fall. |`Rforce`|/c reaches its peak value at $R < 1$ kpc unless $|z| > 1$ kpc. The value of |`Rforce`|/c is larger at smaller values of $|z|$ for any particular value of R. This difference is maximum near the peak value. At large R, curves are almost flat.

Similarly, we plot |`zforce`|/c against $|z|$ for different fixed values of R in the right panel of Fig. 2.8. We find that it first increases and then decreases with the increase of $|z|$. The slope of the curve is steeper at smaller R in both the rising and the falling sides. For each R, the rise is steeper than the fall. $|$`zforce`$|/c$ reaches its peak value at $|z| < 0.5$ kpc. The value of $|$`zforce`$|/c$ is larger at lower values of R for any particular value of $|z|$. This difference is maximum near the peak value. At large $|z|$, curves are almost flat. Comparison between Fig. 2.7 and Fig. 2.8(b) shows a clear difference between the conventional and galpy produced values and $|z|$ dependence of $a_{\rm p,z}/c$.

It should be noted that, the value of $\left(\frac{\dot{P}}{P}\right)_{\rm ex,Galz}$ or $\left(\frac{\dot{f}}{f}\right)_{\rm ex,Galz}$ depends not only on $a_{\rm p,z}$, i.e., $|$`zforce`$|$, but also on $\sin|b|$ (eqs. (2.27) and (2.76)). So, at very low values of $|b|$, the absolute value of $\left(\frac{\dot{P}}{P}\right)_{\rm ex,Galz}$ or $\left(\frac{\dot{f}}{f}\right)_{\rm ex,Galz}$ is small even if $a_{\rm p,z}$ is high (possible at very low values of R). Similarly, eqs. (2.26) and (2.75) show that the value $\left(\frac{\dot{P}}{P}\right)_{\rm ex,Galpl}$ or $\left(\frac{\dot{f}}{f}\right)_{\rm ex,Galpl}$ depends not only on $a_{\rm p,pl}$ but also on $a_{\rm s,pl}$, $\cos l$, and $\cos\lambda$.

We have already mentioned that galpy has the option of using the Galactic potential without or with the black hole. However, the addition of the black hole does not make much change, varying both R and z over the range of $0.01 - 10.0$ kpc, we find that both the ratio of the $|$`Rforce`$|$ with the black hole to that without the black hole and the ratio of the $|$`zforce`$|$ with the black hole to that without the black hole remains less than 1.36. However, as expected, these ratios can be large at very small values of R and $|z|$. As an example, at $R = z = 0.001$ kpc, both of these ratios become 4.81. However, in the region so close to the Galactic centre, there will be additional sources of acceleration of the pulsars, e.g., molecular gases (especially in the central molecular zone in l ranging from -0.7° to 1.7°, and b ranging from -0.2° to 0.2°), nearby stars, etc. These effects will depend on the exact location of the pulsar.

As expected, near the sun, the values of $a_{\rm p,z}/c$ returned by various methods are very close. As an example, for $z = 0.5$ kpc, $R = 8$ kpc, the values of $a_{\rm p,z}/c$ as obtained using various fits of K_z data, i.e., eqs. (2.88), (2.89) and (2.90) are -1.58×10^{-19} s^{-1}, -1.46×10^{-19} s^{-1}, and -1.60×10^{-19} s^{-1} respectively, while the value of `zforce`$/c$ with `MWPotential2014` is -1.63×10^{-19} s^{-1}.

As galpy works best in its natural units where all distances are in the units of R_s and velocities are in the unit of v_s, one needs to perform proper unit conversions to use galpy functions. Another important point to remember is the fact that the default values of the parameters in galpy are $R_\mathrm{s} = 8.0$ kpc and $v_\mathrm{s} = 220$ km s^{-1} (defined under names 'ro' and 'vo' respectively in a file '\$home/.galpyrc'), which have been used to fit various observational data (Bovy, 2015, section 3.5). These values agree with the recent conclusion by Camarillo et al. (2018) that the best choice is $R_\mathrm{s} = 8.0 \pm 0.17$ kpc and $v_\mathrm{s} = 220 \pm 7$ km s^{-1} (both 1σ errors). One can in principle change these parameters by editing the file '\$home/.galpyrc', but in such a case one must re-fit other parameters of the potential `MWPotential2014` too as explained in Bovy (2015).

2.9 Finding the parallel and perpendicular components of jerks

In the derivation of eq. (2.68), we have seen that the terms $\dot{a}_\mathrm{p,pl}$, $\dot{a}_\mathrm{p,z}$, and $\dot{a}_\mathrm{s,pl}$ appear when we take time derivatives of $a_\mathrm{p,pl}$, $a_\mathrm{p,z}$, and $a_\mathrm{s,pl}$, respectively. So,

$$\begin{aligned}\dot{a}_\mathrm{p,pl} &= \frac{d}{dt}\left(a_\mathrm{p,pl}(R,z)\right)\Big|_{(R=R_\mathrm{p})} \\ &= \left(\frac{\partial}{\partial R}a_\mathrm{p,pl}(R,z)\frac{dR}{dt} + \frac{\partial}{\partial z}a_\mathrm{p,pl}(R,z)\frac{dz}{dt}\right)_{(R=R_\mathrm{p})} \\ &= \left(\frac{\partial^2\Phi_{MW}(R,z)}{\partial R^2}\frac{dR}{dt} + \frac{\partial^2\Phi_{MW}(R,z)}{\partial z\partial R}\frac{dz}{dt}\right)_{(R=R_\mathrm{p})} \qquad \text{[used eq. (2.91)]} \qquad (2.94)\end{aligned}$$

$$\begin{aligned}\dot{a}_{\mathrm{s,pl}} &= \frac{d}{dt}\left(a_{\mathrm{s,pl}}(R,z)\right)\Big|_{(R=R_{\mathrm{s}})}\\ &= \left(\frac{\partial}{\partial R}a_{\mathrm{s,pl}}(R,z)\frac{dR}{dt}+\frac{\partial}{\partial z}a_{\mathrm{s,pl}}(R,z)\frac{dz}{dt}\right)_{(R=R_{\mathrm{s}})}\\ &= \left(\frac{\partial^2\Phi_{MW}(R,z)}{\partial R^2}\frac{dR}{dt}+\frac{\partial^2\Phi_{MW}(R,z)}{\partial z\partial R}\frac{dz}{dt}\right)_{(R=R_{\mathrm{s}})} \qquad \text{[used eq. (2.92)]} \end{aligned} \tag{2.95}$$

$$\begin{aligned}\dot{a}_{\mathrm{p,z}} &= \frac{d}{dt}\left(a_{\mathrm{p,z}}(R,z)\right)\Big|_{(R=R_{\mathrm{p}})}\\ &= \left(\frac{\partial}{\partial R}a_{\mathrm{p,z}}(R,z)\frac{dR}{dt}+\frac{\partial}{\partial z}a_{\mathrm{p,z}}(R,z)\frac{dz}{dt}\right)\Big|_{(R=R_{\mathrm{p}})}\\ &= \begin{cases}\left(\frac{\partial^2\Phi_{MW}(R,z)}{\partial R\partial z}\frac{dR}{dt}+\frac{\partial^2\Phi_{MW}(R,z)}{\partial z^2}\frac{dz}{dt}\right)\Big|_{(R=R_{\mathrm{p}})} & \text{if } z>0\text{; see eq. (2.93)}\\ -\left(\frac{\partial^2\Phi_{MW}(R,z)}{\partial R\partial z}\frac{dR}{dt}+\frac{\partial^2\Phi_{MW}(R,z)}{\partial z^2}\frac{dz}{dt}\right)\Big|_{(R=R_{\mathrm{p}})} & \text{if } z<0\text{; see eq. (2.93)}\end{cases}\end{aligned} \tag{2.96}$$

and we have assumed $\dot{a}_{\mathrm{s,z}} = 0$.

For above eqs. (2.94), (2.95), and (2.96), we can use eq. (2.71) for the expression of $\frac{dR}{dt}\Big|_{R=R_{\mathrm{p}}}$, and for the expression of $\frac{dz}{dt}$, we differentiate eq. (2.1) with respect to time to get,

$$\frac{dz}{dt} = \dot{d}\sin b + d\cos b\,\dot{b} = v_r\sin b + \mu_b d\cos b\,. \qquad [\text{As } \mu_b = \dot{b}\text{, and } v_r = \dot{d}\,)] \tag{2.97}$$

One can evaluate the partial derivatives of $\Phi_{MW}(R,z)$ as appeared in eqs. (2.94), (2.95), and (2.96) in various ways. One option is to use galpy that provides models of the potential of the Galaxy as well as these derivatives. More specifically, functions ‘evaluateR2derivs’, ‘evaluatez2derivs’, and ‘evaluateRzderivs’ in galpy evaluate $\frac{\partial^2\Phi_{MW}(R,z)}{\partial R^2}$, $\frac{\partial^2\Phi_{MW}(R,z)}{\partial z^2}$, and $\frac{\partial^2\Phi_{MW}(R,z)}{\partial R\partial z}$ respectively.

2.10 Additional dynamical contributions when the pulsar is located in a globular cluster

In the regions where the local gravitational potential is large enough, there will be extra dynamical effects. Globular clusters are the best examples of such regions. For a pulsar located in a globular cluster, there will be two additional terms, the first is the acceleration ($\vec{a}_{\rm p,gc}$) of the pulsar due to the overall potential of the cluster and the second one is the acceleration ($\vec{a}_{\rm p,stars}$) of the pulsar due to the gravitational potential of one or more very close by stars in the same cluster (Blandford et al., 1987; Phinney, 1992, 1993). $\vec{a}_{\rm p,stars}$ is usually very small (Phinney, 1992; Prager et al., 2017) and its effect is likely to be perceptible only in the higher-order derivatives of the frequency (Freire et al., 2017). $\vec{a}_{\rm p,gc}$ depends not only on the location of the pulsar inside the globular cluster but also on the mass distribution of the cluster. One needs to evaluate this term with a well measured location of the pulsar and a good model for the host globular cluster as recently done by Freire et al. (2017) for pulsars in 47 Tucanae and by Prager et al. (2017) for pulsars in Terzan 5.

Moreover, one needs to use the high precision proper motions of the pulsars measured through timing analysis to estimate $\left(\frac{\dot{P}}{P}\right)_{\rm ex,Shk}$ or $\left(\frac{\dot{f}}{f}\right)_{\rm ex,Shk}$, as the overall proper motion of the cluster as seen by optical astrometric instruments like *Hipparcos* or *Gaia* would be different than the proper motions of the pulsars (Freire et al., 2017) in that cluster.

It should be noted that the higher-order (time derivative) dynamical effects involving jounces, crackles, pops, etc., are also likely to be significant inside a globular cluster as the gradient of the gravitational potential changes rapidly with the spatial coordinates and a slight movement of the pulsar from one position to another, yields a change in its acceleration. Moreover, in such dense stellar environments, the probability of close fly-bys causing a change in the acceleration of the pulsar is also high.

Finally, if a pulsar is close to the centre of the cluster and orbits around the centre (or a massive object at the centre), and this orbital motion is unmodeled, then the pulsar will experience another extra effect due to the line-of-sight component of the orbital acceleration, which we discuss in section 2.11. By modeling this effect, Perera et al. (2017) concluded the existence of an intermediate-mass black hole at the centre of the globular cluster NGC 6624.

2.11 Additional dynamical contribution from the orbital motion

We have seen that the dynamical parameter of a pulsar due to the gravitational potential of the Galaxy affects the first and the second derivatives of the frequency in a similar manner regardless of whether it is the spin frequency or the orbital frequency. However, if the pulsar is a member of an unmodeled binary (usually in a very wide orbit, so that a good timing solution can be obtained even without fitting for binary parameters), there would be an additional term due to the line-of-sight component of the orbital acceleration of the pulsar:

$$\left(\frac{\dot{P}_{\rm s}}{P_{\rm s}}\right)_{\rm ex,orbit} = -\left(\frac{\dot{f}_{\rm s}}{f_{\rm s}}\right)_{\rm ex,orbit} = \frac{1}{c}\widehat{n}_{\rm sp}\cdot\vec{a}_{\rm p,orbit} = \frac{1}{c}a_{\rm p_{l,orbit}} \;. \qquad (2.98)$$

Higher-order derivatives that depend on the line-of-sight component of the orbital jerk, jounce, crackle, pop, etc., might also be significant, depending on the properties of the binary. Joshi and Rasio (1997) gave the simple expression:

$$\left.\frac{1}{P_{\rm s}}\frac{d^k\,P_{\rm s}}{dt^k}\right|_{\rm ex,orbit} = \frac{1}{c}\frac{d^{k-1}\,a_{\rm p_{l,orbit}}}{dt^{k-1}}\;, \qquad k \geq 2\;. \qquad (2.99)$$

The values of $a_{\rm p_{l,orbit}}$ and its derivatives depend on the properties of the binary not known a priori, e.g., the masses of the components, the size of the orbit, the eccentricity, the orientation of the orbit, etc. However, it is possible to constrain the allowed ranges of the parameters using the values of $\left.\frac{1}{P_{\rm s}}\frac{d^k\,P_{\rm s}}{dt^k}\right|_{\rm ex,orbit}$. The expressions for the line of sight acceleration, jerk, jounce, and crackle, due to the orbital motion are given in Bagchi et al. (2013) and Bassa et al. (2016). The expression for the line of sight pop due to the orbital motion has been given for the first time in chapter 1 of this thesis.

2.12 Summary

The measured values of the first and the second derivatives of the frequency ($\dot{f}_{\rm obs}$ and $\ddot{f}_{\rm obs}$ respectively) of a pulsar differ from the intrinsic values ($\dot{f}_{\rm int}$ and $\ddot{f}_{\rm int}$ respectively) due to its velocity, acceleration, and jerk. These derivatives can be either of the spin frequency or of the orbital frequency. In this chapter, we provide expressions for $\dot{f}_{\rm int}$ and $\ddot{f}_{\rm int}$ in terms of other measurable parameters with the assumption that the gravitational potential of the Galaxy is the only cause of the acceleration and jerk of the pulsar. When we discuss the first derivative, we do so both in the frequency and in the period domain as the first derivative of the orbital period is fitted in a timing analysis, not the first derivative of the orbital frequency.

We have also discussed the limitations of earlier approaches to find the values of $\dot{f}_{\rm int}$ and proposed a new method to do so. Our method is very timely, as the recent advancement of technology is leading to discoveries of many distant pulsars that are being followed by precise timing analysis, and for these distant pulsars, earlier approximations are invalid.

Note that, although our work is not the first one studying dynamical contributions in the second derivative of the frequency of a pulsar, this is the first time an accurate analytical expression is given (see Liu et al. (2018) and references therein for earlier approximated approaches to this issue). We have also presented detailed mathematical derivations which might be useful for further exploration of the dynamics of pulsars in the Galaxy.

It should be noted that, $\dot{f}_{\rm int}$ and $\ddot{f}_{\rm int}$ as given in eqs. (2.20) and (2.38) are the values of the first and second time-derivatives of the frequency after eliminating contributions from the velocity of the pulsar and its acceleration and jerk due to the gravitational potential of the

Galaxy. There might be additional case-specific dynamical contributions, some of which have been discussed in brief.

So, although we call these 'intrinsic', they might not be the true intrinsic values. If the presence of additional dynamical terms is confirmed, then the value of the second derivative of the frequency obtained after eliminating the effects due to the velocity, acceleration and jerk of the pulsar due to the Galactic potential, as given in eq. (2.38) should be rather called the 'residual' value or $\ddot{f}_{\rm res}$. The same is true for the first derivative.

Bibliography

Bagchi, M., Lorimer, D. R., Wolfe, S., 2013. On the detectability of eccentric binary pulsars. MNRAS. 432, 1303-1314. https://doi.org/10.1093/mnras/stt559.

Bassa, C. G., Janssen, G. H., Stappers, B. W., Tauris, T. M., & Wevers, T., 2016. A millisecond pulsar in an extremely wide binary system. MNRAS. 460, 2207-2222. https://doi.org/10.1093/mnras/stw1134.

Blandford, R. D., Romani, R. W., & Applegate, J. H., 1987. Timing a millisecond pulsar in a globular cluster. MNRAS. 225, 51P. https://doi.org/10.1093/mnras/225.1.51P.

Bovy, J., 2011. Dynamical Inference in the Milky Way. PhD Thesis, New York University.

Bovy, J., & Rix, H. W., 2013. A Direct Dynamical Measurement of the Milky Way's Disk Surface Density Profile, Disk Scale Length, and Dark Matter Profile at 4 kpc < R < 9 kpc . ApJ. 779, 115. https://doi.org/10.1088/0004-637X/779/2/115.

Bovy, J., 2015. galpy: A python Library for Galactic Dynamics. ApJS. 216, 29-55. https://doi.org/10.1088/0067-0049/216/2/29.

Camarillo, T., Dredger, P., & Ratra, B., 2018. Median statistics estimate of the galactic rotational velocity. Ap&SS. 363, 268. https://doi.org/10.1007/s10509-018-3486-8.

Coles, W., Hobbs, G., Champion, D. J., Manchester, R. N., & Verbiest, J. P. W., 2011. Pulsar timing analysis in the presence of correlated noise. MNRAS. 418, 561. https://doi.org/10.1111/j.1365-2966.2011.19505.x.

Crosta, M., Giammaria, M., Lattanzi, M. G., Poggio, E., 2020. On testing CDM and geometry-driven Milky Way rotation curve models with Gaia DR2. MNRAS. 496, 2107. https://doi.org/10.1093/mnras/staa1511.

Damour, T., & Taylor, J. H., 1991. On the Orbital Period Change of the Binary Pulsar PSR 1913+16. ApJ. 366, 501. https://doi.org/10.1086/169585.

Desvignes, G., Caballero, R. N., Lentati, L., Verbiest, J. P. W., Champion, D. J., et al., 2016. High-precision timing of 42 millisecond pulsars with the European Pulsar Timing Array. MNRAS. 458, 3341. https://doi.org/10.1093/mnras/stw483.

Freire, P. C. C., Ridolfi, A., Kramer, M., Jordan, C., Manchester, R. N. et al., 2017. Long-term observations of the pulsars in 47 Tucanae - II. Proper motions, accelerations and jerks. MNRAS. 471, 857-876. https://doi.org/10.1093/mnras/stx1533.

Holmberg, J., & Flynn, C., 2000. The local density of matter mapped by Hipparcos. MNRAS. 313, 209. https://doi.org/10.1046/j.1365-8711.2000.02905.x.

Holmberg, J., & Flynn, C, 2004. The local surface density of disc matter mapped by Hipparcos. MNRAS. 352, 440. https://doi.org/10.1111/j.1365-2966.2004.07931.x.

Joshi, K. J., Rasio, F. A., 1997. Distant Companions and Planets around Millisecond Pulsars. ApJ. 479, 948-959. https://doi.org/10.1086/303916.

Kuijken, K., & Gilmore, G., 1989. The mass distribution in the galactic disc -II. Determination of the surface mass density of the galactic disc near the Sun. MNRAS. 239, 605. https://doi.org/10.1093/mnras/239.2.605.

Lazaridis, K., Wex, N., Jessner, A., Kramer, M., Stappers, B. W. et al., 2009. Generic tests of the existence of the gravitational dipole radiation and the variation of the gravitational constant. MNRAS. 400, 805. https://doi.org/10.1111/j.1365-2966.2009.15481.x.

Liu, X. J., Bassa, C. G., Stappers, B. W., 2018. High-precision pulsar timing and spin frequency second derivatives. MNRAS. 478, 2359-2367. https://doi.org/10.1093/mnras/sty1202.

Matthews, A. M., Nice, D. J., Fonseca, E., Arzoumanian, Z., Crowter, K. et al., 2016. The NANOGrav Nine-year Data Set: Astrometric Measurements of 37 Millisecond Pulsars. ApJ. 818, 92. https://doi.org/10.3847/0004-637X/818/1/92.

Miyamoto, M., & Nagai, R., 1975. Three-dimensional models for the distribution of mass in galaxies. PASJ. 27, 533. https://ui.adsabs.harvard.edu/abs/1975PASJ...27..533M/abstract.

Navarro, J. F., Frenk, C. S., & White, S. D. M., 1997. A Universal Density Profile from Hierarchical Clustering. ApJ. 490, 493. https://doi.org/10.1086/304888.

Nice, D. J., & Taylor, J. H., 1995. PSR J2019+2425 and PSR J2322+2057 and the Proper Motions of Millisecond Pulsars. ApJ. 441, 429. https://doi.org/10.1086/175367.

Pathak, D., Bagchi, M., 2018. Dynamical Effects in the Observed Rate of Change of the Orbital and the Spin Periods of Radio Pulsars: Improvement in the Method of Estimation and Its Implications. ApJ. 868, 123-136. https://doi.org/10.3847/1538-4357/aae9d9.

Perera, B. B. P., Stappers, B. W., Lyne, A. G., et al. 2017. Evidence for an intermediate-mass black hole in the globular cluster NGC 6624. MNRAS. 468, 2114. https://doi.org/10.1093/mnras/stx501.

Perryman, M. A. C., & Schulze-Hartung, T., 2011. The barycentric motion of exoplanet host stars. Tests of solar spin-orbit coupling. A & A. 525A, 65. https://doi.org/10.1051/0004-6361/201015668.

Phinney, E. S., 1992. Pulsars as probes of newtonian dynamical systems. RSPTA. 341, 39. https://doi.org/10.1098/rsta.1992.0084.

Phinney, E. S., 1993. Pulsars as Probes of Globular Cluster Dynamics. ASPC. 50, 141. https://ui.adsabs.harvard.edu/abs/1993ASPC...50..141P/abstract.

Prager, B. J. et al., 2017. Using Long-term Millisecond Pulsar Timing to Obtain Physical Characteristics of the Bulge Globular Cluster Terzan 5. ApJ. 845, 148-171. https://doi.org/10.3847/1538-4357/aa7ed7.

Reardon, D. J., Hobbs, G., Coles, W., Levin, Y., Keith, M. J., et al. 2016. Timing analysis for 20 millisecond pulsars in the Parkes Pulsar Timing Array. MNRAS. 455, 1751. https://doi.org/10.1093/mnras/stv2395.

Reid, M. J.et al., 2014. Trigonometric Parallaxes of High Mass Star Forming Regions: The Structure and Kinematics of the Milky Way. ApJ. 783, 130-144. https://doi.org/10.1088/0004-637X/783/2/130.

Schönrich, R., Binney, J., Dehnen, W., 2010. Local kinematics and the local standard of rest. MNRAS. 403, 1829-1833. https://doi.org/10.1111/j.1365-2966.2010.16253.x.

Shannon, R. M., & Cordes, J. M., 2010. Assessing the Role of Spin Noise in the Precision Timing of Millisecond Pulsars. ApJ. 725, 1607. https://doi.org/10.1088/0004-637X/725/2/1607.

Shklovskii, I. S., 1970. Possible Causes of the Secular Increase in Pulsar Periods. Soviet Astronomy. 13, 562. https://ui.adsabs.harvard.edu/abs/1970SvA....13..562S/abstract.

Xu, M. H., Wang, G. L., Zhao, M., 2012. The solar acceleration obtained by VLBI observations. A&A, 544A, 135. https://doi.org/10.1051/0004-6361/201219593.

Chapter 3

Dynamical Effects in First Derivative of Period (Spin and Orbital): Methods of Estimation and Introduction to GalDynPsr

3.1 Introduction

We have seen in the previous chapter that the observed values of the rate of change of the orbital and the spin periods (or frequencies) of pulsars are affected by different dynamical parameters, for example, the line-of-sight acceleration and the proper motion of the pulsar relative to the Sun. We have presented analytical expressions for the fractional excess or dynamical terms $(\dot{P}/P)_{\rm ex}$ that involves various components of the accelerations and the velocities. We discussed methods to estimate those excess terms, both in the traditional way and in a new way proposed by us. We have pointed out the limitations of existing methods and argued the need for improved methods. In this chapter, we demonstrate the applications of all these methods for a few pulsars and point out the differences between results obtained in various methods.

We have created a package 'GalDynPsr' for this purpose. We discuss salient features of GalDynPsr with some examples and the potential roles it can play while interpreting the results of precise timing experiments. In fact, GalDynPsr has been already used by Archibald et al. (2018) to place the best ever limit of the non-violation of the universality of free fall. GalDynPsr can be used in many other similarly important studies, some of which we discuss in this chapter.

Various symbols used in this chapter, i.e., l, b, d, z, μ_α, μ_δ, R_p, R_s, $v_{\rm s}(= v_{\rm s,pl})$, $a_{\rm s,pl}$, $a_{\rm p,pl}$, $a_{\rm p,z}$, etc. bear the same meaning as in chapter 2. We use $P_{\rm s}$ for the spin period and $P_{\rm b}$ for the orbital period. As usual, a dot over any of these parameters represents the first time-derivative.

In section 3.2, we introduce GalDynPsr and describe its various modules. In section 3.3, we demonstrate the usage of GalDynPsr and compare the results obtained from the various models of GalDynPsr. In section 3.4, we discuss some of the potential applications of the package. In section 3.5, we summarize the results of this chapter.

3.2 Improvements in the methods of estimation of dynamical effects: introduction to GalDynPsr

In this section, we discuss our package GalDynPsr that can estimate various dynamical terms more accurately than conventional methods. GalDynPsr depends on the publicly available package 'galpy' (Bovy, 2015) for the model of the gravitational potential of the Galaxy. As mentioned in Chapter 2 (section 2.8.2), we use the potential model `MWPotential2014` that does not incorporate the contribution of the central black hole and `MWPotential2014BH` that incorporates the contribution of the central black hole, in the form of `KeplerPotential` added to the original `MWPotential2014`. It should be noted that GalDynPsr does not calculate special dynamical terms, e.g., the one arising due to a local potential, the one due to an unmodeled orbital motion, etc.

GalDynPsr computes the fractional excess terms $\left(\frac{\dot{P}}{P}\right)_{\rm ex}$ which are the same regardless of whether we are working with the spin period and its derivative or with the orbital period and its derivative. However, as the absolute dynamical terms are calculated by multiplying these fractional excess terms by values of the periods as shown in eqs. (2.79), the absolute dynamical terms are different for the spin period and the orbital period. That is why when we report the value of an absolute dynamical term, we either use the subscript 'b' to imply 'orbital' or the subscript 's' to imply 'spin'. The same notation is used when we report the intrinsic or the observed values of the period derivatives.

Various models presently available in GalDynPsr are listed in Table 3.1. Some of the models (A, B, C, D) follow the conventional approaches as discussed in sections 2.8.1.1 and 2.8.1.2, which would be fine for nearby (within 1 kpc distance from the Sun) pulsars. Model-L estimates the values of $a_{\rm p,pl}/c$, $a_{\rm s,pl}/c$ and $a_{\rm p,z}/c$ using galpy. There are some semi-conventional models (G, I, K), where instead of eq. (2.84), GalDynPsr calculates $v_{\rm p'}$ using the rotation curve returned by galpy, and uses this value of $v_{\rm p'}$ in eq. (2.82) to estimate the value of $\left(\frac{\dot{P}}{P}\right)_{\rm ex,Galpl}$. However, at high $|z|$ values $v_{\rm p} \neq v_{\rm p'}$ and eq. (2.82) is not valid (see the derivation of eq. (2.82) in section 2.8.1.1). So this method of calculating $\left(\frac{\dot{P}}{P}\right)_{\rm ex,Galpl}$ is also inaccurate for high $|z|$ pulsars. GalDynPsr also has a few mixed models (E, F, H, J), where either one of $\left(\frac{\dot{P}}{P}\right)_{\rm ex,Galpl}$ or $\left(\frac{\dot{P}}{P}\right)_{\rm ex,Galz}$ is calculated using a conventional method and the other one by using galpy. Each model involving galpy has two sub-classes, denoted by 'a' and 'b'. An 'a' in the name of the model means that the model uses `MWPotential2014` from galpy, while a 'b' in the name of the model means that the model uses `MWPotential2014BH` from galpy. GalDynPsr can also calculate $\left(\frac{\dot{P}}{P}\right)_{\rm ex,Shk}$ if the proper motion of the pulsar is known. It also has the option of calculating the dynamical terms for pulsars in globular clusters using the cluster parameters provided in a file made using the catalogue by W. Harris (Harris , 1996, 2010 edition available at `http://physwww.physics.mcmaster.ca/~harris/mwgc.dat`) and assuming those to be the values of the parameters of the pulsar itself. GaldynPsr has two versions, one is a standalone script (GaldynPsrScript, available at `https://github.com/pathakdhruv/GalDynPsrScript_py3`) where inputs are to be given as command line arguments. The second version of GalDynPsr is designed to be usable as a library (importable module) by other python programs which would provide the values of the parameters needed. The second version is available at `https://github.com/pathakdhruv/GalDynPsr`, and can even be installed using the `pip3` command of python. This version is also available at `http://doi.org/10.5281/zenodo.1461551.` Both of these versions can return the values of the fractional and the absolute dynamical terms for any model. The first version is more useful when the user wants to estimate the dynamical terms for a single pulsar, and the second version is more useful when the user wants to use these results as a part of bigger calculations or simulations. Details of usage (including a number of examples) are available in the package documentation. One needs basic python libraries, like 'scipy', 'numpy', 'astropy', and 'galpy' to be installed in the system to use GalDynPsr.

GalDynPsr returns uncertainties in dynamical terms except when it uses globular cluster parameters from the Harris catalogue or when it uses galpy. It performs standard error propagation calculations using user provided values of the uncertainties in l, b, d, μ_α, and μ_δ. GalDynPsr also reads the uncertainties in $R_{\rm s}$, $v_{\rm s}$, and $\frac{dv}{dR}\Big|_{R=R_{\rm s}}$ (or b_0, see eq. (2.84)) from a parameter file 'parameters.in' provided with the package. The user can change the values in this file if they wish.

3.3 Demonstration of GalDynPsr

First, to check the efficiency of GalDynPsr, we confirm that it agrees with the results available in the literature when we use models involving conventional methods. As an

Table 3.1: Models available in GalDynPsr. The columns from the left to the right are the name of the model, the method of estimating $\left(\frac{\dot{P}}{P}\right)_{\rm ex,Galpl}$, and the method of estimating $\left(\frac{\dot{P}}{P}\right)_{\rm ex,Galz}$. Each model involving galpy has two options: (a) without the super-massive black hole (BH) and (b) with the BH. For each of the models, users have the freedom to change the values of the parameters involved (see text for details).

	Method of calculating $\left(\frac{\dot{P}}{P}\right)_{\rm ex,Galpl}$	Method of calculating $\left(\frac{\dot{P}}{P}\right)_{\rm ex,Galz}$
Model-A	eq. (2.86)	eq. (2.88)
Model-B	eq. (2.86)	eq. (2.90)
Model-C	eqs. (2.24a, 2.84, 2.82)	eq. (2.88)
Model-D	eqs. (2.24a, 2.84, 2.82)	eq. (2.90)
Model-Ea	eq. (2.86)	‘zforce’ in galpy (without BH)
Model-Eb	eq. (2.86)	‘zforce’ in galpy (with BH)
Model-Fa	eqs. (2.24a, 2.84, 2.82)	‘zforce’ in galpy (without BH)
Model-Fb	eqs. (2.24a, 2.84, 2.82)	‘zforce’ in galpy (with BH)
Model-Ga	$v_{\rm p'}/v_{\rm s}$ ‘galpy’ (without BH) + eq. (2.82)	eq. (2.88)
Model-Gb	$v_{\rm p'}/v_{\rm s}$ ‘galpy’ (with BH) + eq. (2.82)	eq. (2.88)
Model-Ha	‘Rforce’ in ‘galpy’ (without BH)	eq. (2.88)
Model-Hb	‘Rforce’ in ‘galpy’ (with BH)	eq. (2.88)
Model-Ia	$v_{\rm p'}/v_{\rm s}$ galpy (without BH) + eq. (2.82)	eq. (2.90)
Model-Ib	$v_{\rm p'}/v_{\rm s}$ galpy (without BH) + eq. (2.82)	eq. (2.90)
Model-Ja	‘Rforce’ in galpy (without BH)	eq. (2.90)
Model-Jb	‘Rforce’ in galpy (with BH)	eq. (2.90)
Model-Ka	$v_{\rm p'}/v_{\rm s}$ galpy (without BH) + eq. (2.82)	‘zforce’ in galpy (without BH)
Model-Kb	$v_{\rm p'}/v_{\rm s}$ galpy (with BH) + eq. (2.82)	‘zforce’ in galpy (with BH)
Model-La	‘Rforce’ in galpy (without BH)	‘zforce’ in galpy (without BH)
Model-Lb	‘Rforce’ in galpy (with BH)	‘zforce’ in galpy (with BH)

example, Prager et al. (2017) reported $(\vec{a}_{\rm p} - \vec{a}_{\rm s}) \cdot \widehat{n}_{\rm sp} = 5.1 \times 10^{-10}$ m s^{-2} using $l = 3.8°$, $b = 1.7°$, and $d = 5.9$ kpc for Terzan 5 ($R_{\rm s} = 8.34$ kpc, $v_{\rm s} = 240$ km s^{-1}). This value matches with the value returned by model-A of GalDynPsr if we use the same values of $R_{\rm s}$, $v_{\rm s}$, d, l, and b. Model-A in GalDynPsr represents the traditional approach taken by Prager et al. (2017). However, they used a more recently measured value of d, which is smaller than the value quoted in the Harris catalogue, i.e., $d = 6.9$ kpc. We also obtain $\dot{P}_{\rm b,Gal} = -0.008 \times 10^{-12}$ ss^{-1} for PSR B1913+16 using the latest parameters reported by Deller et al. (2018) in both model-B and model-La. This value matches with the value reported by them. As this pulsar is located at a low $|z|$ value, i.e., at $z = 0.15$ kpc and $R_{\rm p} = 6.21$ kpc, the conventional method is sufficient. We also find that the difference between the values of $\dot{P}_{\rm b,Gal}$ obtained in models B and La is 7×10^{-17} ss^{-1} (calculated using the best values of the parameters and ignoring the errors). This difference is ignorable in the context of the present-day accuracy of $\dot{P}_{\rm b,obs} = -2.423 \pm 0.001 \times 10^{-12}$ s s^{-1}, but will be of importance when the precision of $\dot{P}_{\rm b,obs}$ measurement will improve by two or more orders and the use of model-La will make more sense.

In Table 3.2, we report values of various fractional dynamical terms estimated for four sample pulsars (the only ones for which Desvignes et al. (2016) could measure $\dot{P}_{\rm b,obs}$, see their table 16) and two most pulsar populated globular clusters, Terzan 5 and 47 Tucanae, using different models of GalDynPsr. The reason behind the choice of pulsars was to be able to compare with existing estimates of dynamical terms. The parameters for the globular clusters are taken from the Harris catalogue (Harris , 1996, 2010 edition, for globular clusters). For the pulsars, l and b values are calculated using the `SkyCoord` module of astropy from the reported values of the right ascension and the declination in tables 3, 4, and 8 of Desvignes et al. (2016). The values of μ_α and μ_δ are taken from the same tables. The values of d are taken from table 16 of Desvignes et al. (2016). For the sake of simplicity, we do not report uncertainties in the table, although used while running GalDynPsr. Moreover, we display the values of the dynamical terms up to the fourth decimal place, just to compare between models. In reality, these values are precise only up to the second decimal place as the uncertainties in the values of d appear in the second decimal place in Desvignes et al. (2016). We have used $R_\mathrm{s} = 8.00 \pm 0.17$ kpc and $v_\mathrm{s} = 220 \pm 7\ \mathrm{km\,s^{-1}}$, which are used in galpy (without the uncertainties) to fit the parameters of the Galactic potential to agree with observations. Our main findings are summarized below.

1. We have already discussed in section 2.8.2 that the addition of the black hole does not affect much in the values of the `Rforce` and `zforce`, and as a result, does not affect much in the values of the dynamical terms. This fact is clear from the closeness of the results obtained with model-La and model-Lb in Table 3.2. We still keep both of the options available in GalDynPsr. However, we prefer model-Lb, which is physically more realistic.

2. Our model-B is the closest to the method used by Desvignes et al. (2016). However, we still see some discrepancies. The main reason is the fact that we used $R_\mathrm{s} = 8.0 \pm 0.17$ kpc and $v_\mathrm{s} = 220 \pm 7\ \mathrm{km\,s^{-1}}$ (Camarillo et al. , 2018) while Desvignes et al. (2016) used $R_\mathrm{s} = 8.34$ kpc and $v_\mathrm{s} = 240\ \mathrm{km\,s^{-1}}$. Using the later set of values of R_s and v_s, we obtained similar values for $\left(\frac{\dot{P}}{P}\right)_{\mathrm{ex,Galpl}}$, i.e., $3.30 \times 10^{-20}\ \mathrm{s^{-1}}$, $5.48 \times 10^{-20}\ \mathrm{s^{-1}}$, $2.99 \times 10^{-20}\ \mathrm{s^{-1}}$, and $10.50 \times 10^{-20}\ \mathrm{s^{-1}}$ for pulsars J0613-0200, J0751+1807, J1012+5307, and J1909−3744 respectively. However, the use of this set of values of R_s and v_s produces little (in the third decimal places) difference in the values of $\left(\frac{\dot{P}}{P}\right)_{\mathrm{ex,Galz}}$ than those reported in Table 3.2. We do not recommend the use of model-B as it uses the traditional approach with drawbacks that have been discussed in Chapter 2.

3. Our preferred model-Lb gives significantly different values of both $\left(\frac{\dot{P}}{P}\right)_{\mathrm{ex,Galpl}}$ and $\left(\frac{\dot{P}}{P}\right)_{\mathrm{ex,Galz}}$ from the values quoted in Desvignes et al. (2016) for PSR J1012−5307, as this pulsar has a moderately high value of $|z|$. This happens because at high values of $|z|$ the assumption $v_{\mathrm{p}'} = v_\mathrm{p}$ used to derive eq. (2.81) for $\left(\frac{\dot{P}}{P}\right)_{\mathrm{ex,Galpl}}$ is invalid. Similarly, at high values of $|z|$, neither of the fits shown in eqs. (2.88) and (2.90) is

a true measure of $a_{\rm p,z}$ that appears in the expression of $\left(\frac{\dot{P}}{P}\right)_{\rm ex,Galz}$.

For PSR J1909−3744, the values of $\left(\frac{\dot{P}}{P}\right)_{\rm ex,Galz}$ as obtained by our model-Lb and reported by Desvignes et al. (2016) are significantly different, because for this pulsar, R_p is significantly smaller than R_s as well as $|z|$ is not too small. This happens because the fits for $a_{\rm p,z}$ as given in eqs. (2.88) and (2.90) used the data only for the stars located near the Sun.

For PSR J0613−0200 and PSR J0751+1807, model-Lb gives the values for $\left(\frac{\dot{P}}{P}\right)_{\rm ex,Galz}$ are not much different than the ones reported by Desvignes et al. (2016). The reason is the fact that for both of these pulsars $R_p \sim R_s$ and $|z|$ is not too high. Moreover, the low $|z|$ value of PSR J0613−0200 makes the value of $\left(\frac{\dot{P}}{P}\right)_{\rm ex,Galpl}$ as obtained by model-Lb to be very close to the one reported by Desvignes et al. (2016). On the other hand, a larger value of $|z|$ for PSR J0751+1807 produces a somewhat larger disagreement between the value of $\left(\frac{\dot{P}}{P}\right)_{\rm ex,Galpl}$ as obtained by model-Lb with the one reported by Desvignes et al. (2016).

4. When $R_{\rm p} << R_{\rm s}$, `zforce` gives significantly different results than other methods. This is the case for Terzan 5, where $R_{\rm p} = 1.21$ kpc. Models involving eq. (2.88) give $\left(\frac{\dot{P}}{P}\right)_{\rm ex,Galz} = -0.34 \times 10^{-20}\,{\rm s}^{-1}$, models involving eq. (2.90) give $\left(\frac{\dot{P}}{P}\right)_{\rm ex,Galz} = -0.28 \times 10^{-20}\,{\rm s}^{-1}$, but models involving `zforce` give $\left(\frac{\dot{P}}{P}\right)_{\rm ex,Galz} = -4.65 \times 10^{-20}\,{\rm s}^{-1}$. The discrepancies between different methods of calculating $\left(\frac{\dot{P}}{P}\right)_{\rm ex,Galz}$ are not so severe for any other examples chosen, as none of those have $R_{\rm p}$ so small.

   In such a case ($R_p << R_{\rm s}$), traditional methods also fail to give a correct value of $\left(\frac{\dot{P}}{P}\right)_{\rm ex,Galpl}$. This happens because when $R_{\rm p} \neq R_{\rm s}$, the use of a Galactic rotation curve as given in eq. (2.84) is incorrect. Again, we can take Terzan 5 as an example, and see that $\left(\frac{\dot{P}}{P}\right)_{\rm ex,Galpl} = 322.29 \times 10^{-20}\,{\rm s}^{-1}$ for models involving eq. (2.86), and as expected, the substitution of the perfect flat rotation curve of Damour & Taylor (1991) by the rotation curve of Reid et al. (2014), i.e., the use of the models involving eqs. (2.24a), (2.84), and (2.82) does not make much difference, gives

$\left(\frac{\dot{P}}{P}\right)_{\rm ex,Galpl} = 327.08 \times 10^{-20}\,{\rm s}^{-1}$. On the other hand, instead of eq. (2.84), if we use the rotation curve from galpy in eq. (2.82), we get a significantly different value, i.e., $\left(\frac{\dot{P}}{P}\right)_{\rm ex,Galpl} = 119.78 \times 10^{-20}\,{\rm s}^{-1}$ (with the black hole as the theoretical value of the Galactic rotation curve depends on the chosen potential), even though one still uses the approximation $v_{\rm p'} = v_{\rm p}$. The use of `Rforce` option of galpy accounts for the height dependence and hence improves the accuracy further. It gives $\left(\frac{\dot{P}}{P}\right)_{\rm ex,Galpl} = 113.08 \times 10^{-20}\,{\rm s}^{-1}$.

The above-mentioned points establish the fact that for a pulsar with $R_{\rm p} << R_{\rm s}$, one must abandon conventional methods to calculate the dynamical terms and opt for a more modern method like model-La or model-Lb provided in GalDynPsr.

5. The role of a high value of $|z|$ in these dynamical terms will be clear from a comparison between PSR J0613−0200 and PSR J1012+5307. These two pulsars have almost the same value of $R_{\rm p}$, i.e. 8.67 kpc and 8.69 kpc respectively, but somewhat different values of $|z|$, 0.13 kpc and 0.89 kpc respectively. We see a larger difference between the value of $\left(\frac{\dot{P}}{P}\right)_{\rm ex,Galz}$ obtained using `zforce` and that obtained using conventional methods for PSR J1012+5307 which has larger $|z|$. Similarly, this pulsar shows a larger disagreement in the values of $\left(\frac{\dot{P}_{\rm b}}{P_{\rm b}}\right)_{\rm ex,Galpl}$ obtained using `Rforce` and that obtained using conventional methods.

6. In addition to the comparison between models as demonstrated in Table 3.2, we have also explored the difference between the fractional dynamical contributions from the Galactic potential, i.e., $\left(\frac{\dot{P}_{\rm b}}{P_{\rm b}}\right)_{\rm ex,Gal}$ as returned by the full conventional method (model-A) and the full galpy based model (model-La) over the full range of l and b for different values of d. The difference increases with the increase of d, and when $d \geq 1$ kpc, the absolute value of the difference becomes greater than 2×10^{-20} s^{-1} for most of the $l - b$ phase space. As the value of $\left(\frac{\dot{P}_{\rm b}}{P_{\rm b}}\right)_{\rm ex,Gal}$ is usually in the order of 10^{-20} s^{-1} (see Table 3.2 for some examples), we can conclude that the accuracy of the model can impact the result if $d \geq 1$ kpc.

7. GalDynPsr does not return uncertainties in the fractional dynamical terms when it uses models involving galpy, because galpy does not return uncertainties. However, because of the modular structure of GalDynPsr, one can estimate uncertainties by employing Monte-Carlo simulation. As an example, for PSR J0613−0200, model-Lb returns $\left(\frac{\dot{P}}{P}\right)_{\rm ex,Galpl} = 4.00 \times 10^{-20}\ {\rm s}^{-1}$ and $\left(\frac{\dot{P}}{P}\right)_{\rm ex,Galz} = -9.29 \times 10^{-21}\ {\rm s}^{-1}$ using the values of l, b, and d as given in Table 3.2. We then simulated 50000 instances of l, b, and d following a Gaussian distribution. For l and b, as usual, we converted the mean values and uncertainties in the right ascension and the declination from table 3 of Desvignes et al. (2016) using the `SkyCoord` module of the astropy package. The mean value and the uncertainty in d are taken from table 16 of Desvignes et al. (2016). We then randomly chose one value each from the distributions of l, b, and d, and calculated the fractional dynamical terms using model-Lb for each of such 50000 cases. We then calculated the mean and the standard deviation of these 50000 values of $\left(\frac{\dot{P}}{P}\right)_{\rm ex,Galpl}$ and $\left(\frac{\dot{P}}{P}\right)_{\rm ex,Galz}$. In this manner, we found $\left(\frac{\dot{P}}{P}\right)_{\rm ex,Galpl} = (4.00 \pm 0.41) \times 10^{-20}\ {\rm s}^{-1}$ and $\left(\frac{\dot{P}}{P}\right)_{\rm ex,Galz} = -(9.29 \pm 0.63) \times 10^{-21}\ {\rm s}^{-1}$ respectively.

8. $\left(\frac{\dot{P}}{P}\right)_{\rm ex,Shk}$ is usually order of magnitude larger than $\left(\frac{\dot{P}}{P}\right)_{\rm ex,Gal} = \left(\frac{\dot{P}}{P}\right)_{\rm ex,Galpl} + \left(\frac{\dot{P}}{P}\right)_{\rm ex,Galz}$.

3.4 Applicability of GalDynPsr

GalDynPsr has the potential to be used in various studies involving precise timing of pulsars, we mention some of them below.

In section 3.3, we have seen that depending on the location of a pulsar, conventional methods can give wrong values of the dynamical terms leading to wrong values of $\left(\frac{\dot{P}}{P}\right)_{\rm ex,Gal}$. If this $\left(\frac{\dot{P}}{P}\right)_{\rm ex,Gal}$ is comparable to $\left(\frac{\dot{P}}{P}\right)_{\rm ex,Shk}$, which is usually larger, this will lead to a wrong value of $\dot{P}_{\rm b,int}$ or $\dot{P}_{\rm s,int}$. It is expected that the improved timing precision with SKA1-Mid (Shao et al., 2014) will reveal higher order post-Newtonian terms, at least for relativistic pulsars like the double pulsar or neutron star−black hole binaries (if discovered). VLBI

Table 3.2: Comparison of the values of the fractional dynamical terms estimated using different methods for the pulsars mentioned in table 16 of Desvignes et al. (2016) as well as for the two most pulsar populated globular clusters, Terzan 5 and 47 Tucanae. The parameters for the globular clusters are taken from the Harris catalogue. For the 4 pulsars, l, b values are calculated using the `SkyCoord` module of astropy from the reported values of the right ascension and the declination in tables 3, 4, and 8 of Desvignes et al. (2016). The values of μ_α and μ_δ can be found in the same tables. The values of d are taken from table 16 of Desvignes et al. (2016). For the sake of simplicity, we do not report uncertainties here, although used while running GalDynPsr. Moreover, we display many significant digits for the sake of comparison between models. We have used $R_{\rm s} = 8.00 \pm 0.17$ kpc and $v_{\rm s} = 220 \pm 7$ km s^{-1}, that are used in galpy to fit the parameters of the Galactic potential to agree with the observational data.

Pulsars/Cluster		PSR J0613−0200	PSR J0751+1807	PSR J1012+5307	PSR J1909−3744	Ter5	47Tuc
l (deg)		210.4131	202.7297	160.3471	359.7308	3.84	305.89
b (deg)		−9.3049	21.0858	50.8578	−19.5958	1.69	−44.89
d (kpc)		0.78	1.07	1.15	1.15	6.9	4.5
μ_α (mas yr^{-1})		1.822	−2.73	2.609	−9.519	–	–
μ_δ (mas yr^{-1})		−10.355	−13.4	−25.482	−35.775	–	–
$\left(\frac{\dot{P}_{\rm b}}{P_{\rm b}}\right)_{\rm obs}$ (in 10^{-20} s^{-1})		46.3538	-153.9432	116.7604	379.6512	–	–
$\left(\frac{\dot{P}_{\rm s}}{P_{\rm s}}\right)_{\rm obs}$ (in 10^{-20} s^{-1})		313.2142	223.8549	325.8774	475.8964	–	–
z (kpc)		−0.13	0.38	0.89	−0.39	0.20	−3.18
$R_{\rm p}$ (kpc)		8.67	8.93	8.69	6.92	1.21	6.65
$\left(\frac{\dot{P}}{P}\right)_{\rm ex,Shk}$ (in 10^{-20} s^{-1})		20.9463	48.6102	183.3013	382.8569	–	–
	Values of $\left(\frac{\dot{P}}{P}\right)_{\rm ex,Galpl}$ (in 10^{-20} s^{-1}) for different models:						
A, B, Ea, Eb	eq. (2.86)	3.0142	4.9912	2.7298	9.6504	322.2856	-14.5856
C, D, Fa, Fb	eqs. (2.24a, 2.84, 2.82)	3.0786	5.0778	2.7750	9.7908	327.0843	-14.5547
Ga, Ia, Ka	$v_{\rm p'}/v_{\rm s}$ galpy (without BH) + eq. (2.82)	3.9031	6.1821	3.3532	11.5438	119.6713	-14.1771
Gb, Ib, Kb	$v_{\rm p'}/v_{\rm s}$ galpy (with BH) + eq. (2.82)	3.9010	6.1800	3.3517	11.5482	119.7851	-14.1764
Ha, Ja, La	‘Rforce’ in galpy (without BH)	4.0004	6.8354	5.0696	9.9521	112.9790	-18.6831
Hb, Jb, Lb	‘Rforce’ in galpy (with BH)	4.0007	6.8359	5.0699	9.9530	113.0853	-18.6838
table 16 of Desvignes et al. (2016)		3.28	5.50	3.01	10.49	–	–
	Values of $\left(\frac{\dot{P}}{P}\right)_{\rm ex,Galz}$ (in 10^{-20} s^{-1}) for different models:						
A, C, Ga Gb, Ha, Hb	eq. (2.88)	-1.3815	-5.2721	-14.6102	-4.9177	-0.3361	-23.5742
B, D, Ia Ib, Ja, Jb	eq. (2.90)	-1.1081	-5.0601	-15.5418	-4.7219	-0.2835	-23.9731
Ea, Fa, Ka, La	‘zforce’ in galpy (without BH)	-0.9291	-4.0218	-12.6005	-6.9854	-4.6468	-26.7781
Eb, Fb, Kb, Lb	‘zforce’ in galpy (with BH)	-0.9291	-4.0218	-12.6007	-6.9855	-4.6474	-26.7792
table 16 of Desvignes et al. (2016)		−1.28	−4.57	−14.55	−8.24	–	–

using SKA1 (Paragi et al., 2015) will also give better parallaxes, i.e., better distance estimates as well as better proper motion measurements leading to accurate estimation of $\left(\frac{\dot{P}}{P}\right)_{\rm ex,Shk}$. This will be useful only if accompanied by accurate estimates of $\left(\frac{\dot{P}}{P}\right)_{\rm ex,Gal}$, and GalDynPsr can play a crucial role in this. We discuss some potential areas where precise values of $\dot{P}_{\rm b,int}$ or $\dot{P}_{\rm s,int}$ will be very important.

One such area would be the tests of theories of gravity. Although the most accepted gravity theory, the general relativity (GR) has passed all the tests so far, it is expected to get better limits on various alternative theories of gravity in the future, especially in the strong-field regime with more precise timing solutions of pulsars. The most obvious test will be the detection of a deviation of the value of $\dot{P}_{\rm b,int}$ from that expected from GR. We have already mentioned that for a clean binary system, the emission of the gravitational waves is responsible for $\dot{P}_{\rm b,int}$ and GR allows only quadrupolar gravitational waves. The rate of change of the orbital period due to the emission of the quadrupolar gravitational waves ($\dot{P}^{Q}_{\rm b,GW}$) depends on the values of the orbital period, the orbital eccentricity, the mass of the pulsar and the mass of the companion (see eq. (1.28)). Thus, under GR, $\dot{P}_{\rm b,int} = \dot{P}^{Q}_{\rm b,GW}$. However, there are various theories of gravity that allow other multipoles (Bagchi & Torres , 2014, and references therein). The dipolar gravitational waves, if exist, become the most significant source of radiation and hence the largest contributing factor in the value of $\dot{P}_{\rm b,int}$. One can place limits on the parameter of the gravity theory by equating $\dot{P}_{\rm b,int} = \dot{P}^{D}_{\rm b,GW} + \dot{P}^{Q}_{\rm b,GW}$ (neglecting other poles of the gravitational wave emission) where $\dot{P}^{D}_{\rm b,GW}$ is the rate of change of the orbital period due to the emission of the dipolar gravitational waves. Additionally, if the value of the gravitational constant G changes with time, that will also lead to a change in the orbital period, and the rate of change of the orbital period becomes $\dot{P}_{\rm b,int} = \dot{P}^{D}_{\rm b,GW} + \dot{P}^{Q}_{\rm b,GW} + \dot{P}^{\dot{G}}_{\rm b}$, where $\dot{P}^{\dot{G}}_{\rm b}$ is the rate of change of the orbital period due to the change in the value of G. The expressions for different terms in the above equation depend on various parameters, including the orbital period, the masses, the orbital eccentricity, the 'sensitivity' of the objects etc. These expressions can be found in various literature, one example being Bagchi & Torres (2014). If one can calculate the value of $\dot{P}^{Q}_{\rm b,GW}$ from the knowledge of relevant parameters, then it will be possible to obtain a value of $\dot{P}^{D}_{\rm b,GW} + \dot{P}^{\dot{G}}_{\rm b}$. Recently, Zhu et al. (2019) placed a limit on both $\dot{G}/G$ and κ_D (a characteristic parameter of the gravity theory allowing the dipolar gravitational wave emission). As such limits depend crucially on the value of $\dot{P}_{\rm b,int}$, one needs to estimate and eliminate the dynamical terms as accurately as possible. GalDynPsr will help in performing this task better, especially if such tests are done in the future with pulsars at high $|z|$ or at low $R_{\rm p}$ where conventional methods fail.

Another test of GR is the test of the Strong Equivalence Principle (SEP), which is one of the main features of GR but is usually violated in alternative theories. One important aspect of SEP is the universality of the free fall (UFF). The violation of UFF in the case of a binary system can be parametrized by a dimensional parameter $|\Delta|$ that quantifies the differential acceleration between the members (of different constituents) of the freely falling binary. Damour & Schäfer (1991) showed that the UFF violation can manifest into a 'forced' eccentricity that depends on the value of $|\Delta|$, the masses of the members of the binary, the orbital period of the binary, and the projection of the Galactic acceleration vector at the location of the pulsar onto the orbital plane, i.e., $a_{\rm p,Gal,proj}$. Eqs. (1.35) and (1.36) in Chapter 1 of this thesis described the expressions for the 'forced' eccentricity and $|\Delta|$. This $a_{\rm p,Gal,proj}$ is related to $\vec{a}_{\rm p,Gal}$ with a multiplicative function that depends on the orientation of the orbit where $\vec{a}_{\rm p,Gal} = \vec{a}_{\rm p,pl} + \vec{a}_{\rm p,z}$. The measurement of the signature of this 'forced' eccentricity in the timing solution of a wide-orbit low-eccentricity binary pulsar with a low-mass white-dwarf companion helps in placing an upper limit on $|\Delta|$ (Stairs et al., 2005; Gonzalez et al., 2016; Zhu et al., 2019). In such efforts, GalDynPsr can also be used to estimate the value of $a_{\rm p,Gal}$, which might be more precise than conventional methods, depending on the location of the pulsar in the Galaxy. In fact, GalDynPsr has been already used by Archibald et al. (2018) to place the best ever limit of the non-violation of the strong equivalence principle using the pulsar PSR J0337+1715 in a triple system.

Even within the framework of GR, i.e., for the binaries for which $\dot{P}^{D}_{\rm b,GW}$ and $\dot{P}^{\dot{G}}_{\rm b}$ can be ignored and SEP test is not possible, e.g., for double neutron star binaries, a wrong estimate of $\dot{P}_{\rm b,int}$ will have detrimental consequences like erroneous estimates of the masses of the pulsar and the companion, especially when one excludes the most accurately measurable post-Keplerian parameter, i.e., the rate of the periastron advance, which is affected by the Lense-Thirring effect that depends on the unknown values of the moment of inertia, the orientation of spin axis, etc. (Bagchi, 2018, and references therein). To avoid such consequences, one should use GalDynPsr, especially if the pulsar is located far from the Sun where the conventional methods are inaccurate.

Similarly, there are many cases where it is very important to estimate the values of $\dot{P}_{\rm s,int}$ as precise as possible. One such case is to understand the emission of the continuous gravitational waves from pulsars due to their rotationally induced quadrupole moments. The value of $\dot{P}_{\rm s,int}$ is needed to calculate the 'spin-down' limit of the strain (h_0^{sd}) of the gravitational waves emitted at a frequency of $f_{\rm gw} = 2 f_{\rm s}$. The expression for h_0^{sd} is derived under the assumption that the total spin-down energy is being lost only in the form of the gravitational waves, and the expression is $h_0^{sd} = [2.5(G\ I_{\rm s}\ |\dot{f}_{\rm s,int}|)/(c^3\ d^2\ f_{\rm s})]^{0.5}$ where G is the gravitational constant, $I_{\rm s}$ is the moment of inertia of the pulsar along its spin axis. In reality, especially in the cases of rotation powered radio pulsars, only a fraction η of the spin-down energy is converted to the gravitational energy, and $h_0 = \eta^{0.5}\, h_0^{sd}$. As $\eta < 1$ giving $h_0 < h_0^{sd}$, one can confirm the detection of gravitational waves or can place an upper limit on the value of h_0 only when the detection sensitivity reaches below h_0^{sd}. Although the last science run (O1) of the advanced-LIGO-Virgo did not detect any continuous gravitational waves, it has placed the best so far 95% upper limit of h_0, i.e., h_0^{95} for a number of pulsars and for eight of those, $h_0^{95} < h^{sd}$ (Abbott et al., 2017). It is expected that in the future, the detector sensitivity will surpass the spin-down limit for more pulsars, especially for the pulsars with large values of h_0^{sd}. The ongoing and future pulsar surveys and follow-up timing will provide more pulsars with $f_{\rm gw}$ in the LIGO range as well as large enough values of h_0^{sd}. GalDynPsr will help us calculate the values of h_0^{sd} by providing precise values of $\dot{f}_{\rm s,int}$ for non-globular cluster pulsars, especially if the pulsars are located in the regions where conventional methods to estimate and eliminate the dynamical effects fail.

Another application of the precisely estimated value of $\dot{P}_{\rm s,int}$ is in the study of the pulsar 'deathline' (Guillemot et al., 2016, and references therein), i.e., in the effort to understand the radio emission mechanism. Pulsars close to the 'deathline' have small values of the rate of loss of the spin down energy[1] $\dot{E}_{\rm rot} = 4\pi^2 I_{\rm s} \dot{P}_{\rm s,int}/P_{\rm s}$. A larger population of low $\dot{E}_{\rm rot}$ pulsars will improve our understanding of the 'deathline' better. On the other hand, a larger population will increase the probability of some of such pulsars having large enough values of $|\dot{P}_{\rm s,Gal}|$ located in the regions where the use of the conventional methods give inaccurate values of $\dot{P}_{\rm s,Gal}$ resulting in inaccurate values of $\dot{P}_{\rm s,int}$ and $\dot{E}_{\rm rot}$.

GaldynPsr can be useful even when the timing solution is not good enough, especially when the distance measurements are not as accurate as desired. In such cases, one can use the expression $\dot{P}_{\rm b,obs} - \dot{P}_{\rm b,Gal} - \dot{P}^{Q}_{\rm b,GW} = \dot{P}_{\rm b,Shk}$ to obtain the value of $\dot{P}_{\rm b,Shk}$ if at least some of the post-Keplerian parameters are measured to give sufficiently accurate values of the masses of the pulsar and the companion and hence a theoretical value of $\dot{P}^{Q}_{\rm b,GW}$, neglecting the manifestation of non-quadrupolar gravitational wave emission (if exists). One can extract the value of the distance from the value of $\dot{P}_{\rm b,Shk}$ if the proper motion is known. The value of the distance obtained in such a manner can be compared with other distance estimates (if available). Discrepancies between the values of distances estimated in different methods have the potential to reveal inaccuracies either in the timing solution or in the methods of distance estimation, or the presence of additional effects.

Finally, although we have confined our discussions to rotation powered pulsars only, GaldynPsr can be used to estimate the value of $\left(\frac{\dot{P}}{P}\right)_{\rm ex}$ for any object in the Galaxy provided their distance, location, and the proper motion are known.

---

[1] The pulsar 'deathline' is a hypothetical line in the $P_{\rm s} - \dot{P}_{\rm s,int}$ plane defining a maximum potential drop above which the radio emission turns off (Chen & Ruderman, 1993). This line is very close and almost parallel to the $\dot{E}_{\rm rot} = 10^{-30}$ erg s^{-1} line (Ng et al., 2015).

3.5 Summary

The values of the rate of change of the period (either the spin or the orbital) measured through pulsar timing analysis are affected by the dynamics of the pulsars. In this chapter, we presented GalDynPsr, a python package that evaluates different dynamical terms following the traditional as well as an improved method based on the model of the Galactic potential provided in the package galpy. GalDynPsr is publicly available and open for contributions.

With a number of examples, we demonstrated how for some pulsars, the new method can result in significantly different values of the dynamical terms in comparison to those obtained by conventional methods. We also explained the physical reasons for the new method to be more accurate.

We emphasise the fact that although the existing approximate methods are often sufficient for the present-day accuracy of timing solutions, one should be careful as this accuracy is getting improved for a number of millisecond pulsars owing to the pulsar timing array efforts. In particular, the improved method to estimate dynamical effects will be essential for pulsars far away from the solar system (either horizontally, vertically, or both) with precise timing solutions. Even for other pulsars, as the timing accuracy improves, one should opt for a more accurate estimation of dynamical effects. We recommend the use of model Lb, which calculates $a_{\rm p,pl}/c$ and $a_{\rm p,z}/c$ directly using galpy.

Bibliography

Abbott, B. P., Abbott, R., Abbott, T. D., Abernathy, M. R., Acernese, F. et al. 2017. First Search for Gravitational Waves from Known Pulsars with Advanced LIGO. ApJ. 839, 12. https://doi.org/10.3847/1538-4357/aa677f.

Archibald, A. M., Gusinskaia, N. V., Hessels, J. W. T., Deller, A. T., Kaplan, D. L., et al. 2018. Universality of free fall from the orbital motion of a pulsar in a stellar triple system. Nature. 559, 73. https://doi.org/10.1038/s41586-018-0265-1.

Bagchi, M., 2018. Prospects of Constraining the Dense Matter Equation of State from Timing Analysis of Pulsars in Double Neutron Star Binaries: The Cases of PSR J0737−3039A and PSR J1757−1854. Universe. 4, 36. https://doi.org/10.3390/universe4020036.

Bagchi, M., & Torres, M., 2014. In what sense a neutron star-black hole binary is the holy grail for testing gravity? JCAP. 08, 055. https://doi.org/10.1088/1475-7516/2014/08/055.

Bovy, J., 2015. galpy: A python Library for Galactic Dynamics. ApJS. 216, 29-55. https://doi.org/10.1088/0067-0049/216/2/29.

Camarillo, T., Dredger, P., & Ratra, B., 2018. Median statistics estimate of the galactic rotational velocity. Ap&SS. 363, 268. https://doi.org/10.1007/s10509-018-3486-8.

Chen, K., & Ruderman, M., 1993. Pulsar Death Lines and Death Valley. ApJ. 402, 264. https://doi.org/10.1086/172129.

Damour, T., & Schäfer, G., 1991. New tests of the strong equivalence principle using binary-pulsar data. PhRvL. 66, 2549. https://doi.org/10.1103/PhysRevLett.66.2549.

Damour, T., & Taylor, J. H., 1991. On the Orbital Period Change of the Binary Pulsar PSR 1913+16. ApJ. 366, 501. https://doi.org/10.1086/169585.

Deller, A. T., Weisberg, J. M., Nice, D. J., & Chatterjee, S., 2018. ApJ. A VLBI Distance and Transverse Velocity for PSR B1913+16. 862, 139. https://doi.org/10.3847/1538-4357/aacf95.

Desvignes, G., Caballero, R. N., Lentati, L., Verbiest, J. P. W., Champion, D. J., et al., 2016. High-precision timing of 42 millisecond pulsars with the European Pulsar Timing Array. MNRAS. 458, 3341. https://doi.org/10.1093/mnras/stw483.

Gonzalez, M. E., Stairs, I. H., Ferdman, R. D., Freire, P. C. C., Nice, D. J. et al., 2011. High-precision Timing of Five Millisecond Pulsars: Space Velocities, Binary Evolution, and Equivalence Principles. ApJ. 743, 102. https://doi.org/10.1088/0004-637X/743/2/102.

Guillemot, L., Smith, D. A., Laffon, H., Janssen, G. H., Cognard, I. et al., 2016. The gamma-ray millisecond pulsar deathline, revisited. New velocity and distance measurements. A&A. 587, A109. https://doi.org/10.1051/0004-6361/201527847.

Harris, W. E., 1996. A Catalog of Parameters for Globular Clusters in the Milky Way. AJ. 112, 1487. https://doi.org/10.1086/118116.

Ng, C., Champion, D. J., Bailes, M., Barr, E. D., Bates, S. D. et al., 2015. The High Time Resolution Universe Pulsar Survey - XII. Galactic plane acceleration search and the discovery of 60 pulsars. MNRAS. 450, 2922. https://doi.org/10.1093/mnras/stv753.

Paragi, Z., Godfrey, L., Reynolds, C., Rioja, M. J., Deller, A. et al., 2015. Very Long Baseline Interferometry with the SKA. Proceedings of Advancing Astrophysics with the Square Kilometre Array (AASKA14) 143. https://doi.org/10.22323/1.215.0143.

Prager, B. J. Ransom, S., Freire, P. et al., 2017. Using Long-term Millisecond Pulsar Timing to Obtain Physical Characteristics of the Bulge Globular Cluster Terzan 5. ApJ. 845, 148-171. https://doi.org/10.3847/1538-4357/aa7ed7.

Reid, M. J., Menten, K. M., Brunthaler, A., Zheng, X. W., Dame, T. M. et al., 2014. Trigonometric Parallaxes of High Mass Star Forming Regions: The Structure and Kinematics of the Milky Way. ApJ. 783, 130. https://doi.org/10.1088/0004-637X/783/2/130.

Shao, L., Stairs, I. H., Antoniadis, J. et al., 2014. Proceedings of Science, Advancing Astrophysics with the Square Kilometre Array (AASKA14). https://10.22323/1.215.0042 doi.org/.

Stairs, I. H., Faulkner, A. J., Lyne, A. G., Kramer, M., Lorimer, D. R. et al., 2005. Discovery of Three Wide-Orbit Binary Pulsars: Implications for Binary Evolution and Equivalence Principles. ApJ. 632, 1060. https://doi.org/10.1086/432526.

Zhu, W. W., Desvignes, G., Wex, N., Caballero, R. N., Champion, D. J. et al., 2019. Tests of gravitational symmetries with pulsar binary J1713+0747. MNRAS. 482, 3249. https://doi.org/10.1093/mnras/sty2905.

Chapter 4

Dynamical Effects in Second Derivative of Frequency (Spin and Orbital): Methods of Estimation and Introduction to GalDynPsrFreq

4.1 Introduction

We have already mentioned the fact that instead of the second derivatives of periods (both of the spin and the orbital), one often fits for the second derivatives of frequencies while doing a timing analysis. That is why in Chapter 2, we discussed the dynamical terms affecting the second derivative of the spin and orbital frequencies of radio pulsars.

Looking at previous works, we find that some interesting results by modeling the higher-order time derivatives of spin frequencies have come up in the past few years. One example is the revelation of millisecond pulsars PSRs J1024−0719 and J1823-3021A being members of very wide orbit binaries (Guillemot et al., 2016; Kaplan et al., 2016; Bassa et al., 2016; Perera et al., 2017). Although for the second pulsar, which is located in the globular cluster NGC 6624, there is some controversy on the conclusion of the mass modeling of the cluster (Gieles et al., 2016), the binary nature of the pulsar is still unchallenged. Liu et al. (2018) also provided approximate analytical derivations for the dynamical effects on the first and second derivatives of the pulsar spin frequency.

We have already derived complete analytical expressions for all dynamical terms in chapter 2 and provided a way to calculate their individual contribution to the measured second derivative of the frequency without any numerical fitting. However, given the difficulty in the measurement of the second derivative of the spin frequency, the usefulness of these expressions may come into question. In version 1.63 of the ATNF catalogue (Manchester et al., 2005), there are only 434 pulsars in the Galactic field for which measured values of the second derivative of the spin frequency have been reported out of a total of 2634 of such pulsars. Moreover, this parameter has not been fitted in the timing solutions of any of the pulsars in the second data release of the International Pulsar Timing Array (IPTA) (Perera et al., 2019).

These facts do not make the study of dynamical contributions in the second derivative of the frequency irrelevant. Liu et al. (2019) suggested that the timing solutions would be more accurate if this parameter is fitted for at least some of the IPTA pulsars (e.g., PSRs J1024−0719, J1939+2134, J0621+1002, J1022+1001, and B1821−24A). Moreover, in the future, the square kilometre array (SKA) will detect many millisecond pulsars. The simulations by Keane et al. (2014) showed that SKA1-MID would detect about 9000 normal pulsars and about 1400 millisecond pulsars while the numbers for SKA1-LOW were about 7000 normal pulsars and about 900 millisecond pulsars. Out of this large number of new pulsars, some will have measurably large values of the second derivative of the spin frequency.

One difficulty of measuring the second derivative of the spin frequency is the fact that there are other factors that might induce a wrong value in this parameter, some examples are the variation of the dispersion measure (DM) with time, the red noise in the timing data etc. However, there are ongoing efforts to understand and model these effects, as an example, the Indian Pulsar Timing Array can measure the variation of DM accurate up to the fourth decimal place (Krishnakumar et al., 2021). There are many efforts to model the red noise in pulsar timing data too. The implementation of these results and models in the timing analysis will reduce the uncertainty in the measurement of the second derivative of the spin frequency. With a larger sample of measured values of this parameter, a good model to decouple the dynamical terms from the intrinsic term will help in better understanding of pulsar properties like the braking index etc. The additional advantage is that this same formalism can be applied to decouple the dynamical terms from the intrinsic term in the second derivative of the orbital frequency.

We have created a python-package ‘GalDynPsrFreq’ based on our formalism, that is, it can be used to extract dynamical contributions to the first and the second time-derivatives of the frequencies and also obtain their intrinsic values.

In this chapter, we describe the numerical works done in order to estimate the contributions of dynamical terms to the second derivative of the frequency, both spin and orbital, of pulsars. In section 4.2 particularly, we present the numerical exploration to understand the relative importance of these dynamical terms in the cases of both synthetic as well as real pulsars. In section 4.3, we present an introduction to our python package ‘GalDynPsrFreq’. In section 4.4, we present some applications of GalDynPsrFreq in correcting the dynamical effects from the second derivatives of the frequencies. In particular, first, we discuss the properties of PSR J1024−0719, then we investigate how dynamical terms can affect the measured values of the braking index and finally we explore the contributions from the dynamical terms to the second derivative of orbital frequencies. In section 4.5, we describe the details of the simulation techniques adopted to generate the pulsar parameters based on observed values from the ATNF pulsar catalogue. In section 4.6, we present the summary of the work.

4.2 Numerical exploration to understand relative importance of various terms in the expression of $\left(\frac{\ddot{f}}{f}\right)_{\text{ex}}$

In chapter 2, we presented an expression for the fractional excess dynamical term for the second derivative of the frequency, i.e., $\left(\frac{\ddot{f}}{f}\right)_{\text{ex}}$ in eq. (2.37) in terms of observable parameters (e.g., l, b, d, μ_l, μ_b, etc) as well as computable parameters like $a_{\text{s,pl}}$, $a_{\text{p,pl}}$, $a_{\text{s,z}}$, $\dot{a}_r$, α, etc.

Among various terms in eq. (2.37), the last square bracket term contains the excess dynamical term for the first derivative of the frequency $\left(\frac{\dot{f}}{f}\right)_{\text{ex}}$ as well as the observed first derivative of the frequency and the frequency. So, this term can be converted to the period domain and easily computed using GalDynPsr if all the relevant parameters like the coordinates, the distance, the proper motion, the period and the period derivative of the pulsar are known. Our new package GalDynPsrFreq computes this term directly in the frequency domain within the framework of our new model (model Lb, as discussed in Chapter3) to compute various acceleration terms. GalDynPsrFreq also computes other terms in eq. (2.37), including the jerk terms. The computation of the jerk terms is in harmony with the method of calculation of the acceleration terms, i.e., both use the same model for the Galactic potential available in galpy.

However, most of the terms in eq. (2.37) contain parameters that might not be easily measurable, especially the first square bracket term. So, it is worth investigating the relative significance of various terms within the square brackets in eq. (2.37) to decide whether any one of those can be ignored. As there are not many pulsars with all relevant parameters (appearing in the first three square bracket terms) known, we decided to perform simulations, where a simulated pulsar is essentially a set of synthetic values of various parameters, each of which is taken from values simulated following chosen distributions. The details of our simulations and their results are described next.

4.2.1 Pulsar population in the Galactic field

We use 'PsrPopPy' (Bates et al., 2014), a python based population synthesis package to generate a population of pulsars in the Galactic field. Note that, PsrPopPy generates a set of synthetic pulsars with simulated values of various parameters, e.g., the spin period, the distance, the coordinates, etc. It also uses the NE2001 model of Galactic electron density (Cordes and Lazio, 2002, 2003) to obtain values of the Dispersion Measure (DM) that is needed to check whether the pulsar would be detected by a specific pulsar survey. PsrPopPy does not put any constraint on the distances of the pulsars, so in some cases, it returns such a high distance that in that direction, the maximum DM in NE2001 model (DM_∞, see Cordes and Lazio (2002) for details) is attained even at a smaller value of the distance ($d_{\rm max,ne2001}$). The values of DM returned by PsrPopPy are not accurate in such cases, and it is better to remove such pulsars from further study.

The default distribution functions for various parameters are set in such a way that after taking care of selection biases, the parameters of the underlying population of normal pulsars agree well with the observed sample (Ridley & Lorimer, 2010). These distribution functions as well as the values of the underlying model parameters have been displayed in Table 4.1. Among various known pulsar surveys, the Parkes Multibeam Pulsar Survey (Manchester et al., 2001), henceforth PMPS, has been modeled most rigorously in PsrPopPy and hence in this thesis, we use only PMPS. Our simulation procedure and the following analysis are described below.

In version 1.63 of the ATNF[1] pulsar catalogue (Manchester et al., 2005), there are 1085 normal pulsars (spin period > 30 ms) that are detected by PMPS, with well defined distance values, obtained from their DM values using the NE2001 model of electron density.

This set excludes pulsars in globular clusters and both Large and Small Magellanic Clouds as in these cases, there will be extra dynamical effects due to the local gravitational po-

---

[1] http://www.atnf.csiro.au/research/pulsar/psrcat/

tentials. We used this number (1085) as the target number for detection in PsrPopPy with default settings, i.e., the best model parameters, and survey set to PMPS. We found that a population of 124310 pulsars is generated in order to detect 1085 cases by that survey. However, 180 synthetic pulsars had to be discarded as they had $d > d_{\mathrm{max,ne2001}}$. From the remaining ones, we excluded 15 cases with spin period less than 30 ms. In this way, we were left with a set of 124115 synthetic normal pulsars.

Similarly, there are 29 millisecond pulsars (spin period $<$ 30 ms), as per the ATNF catalogue, that are detected by the PMPS, and have well-defined NE2001 model-based distance values. Using this number as the target number for detection in PsrPopPy, with survey set to PMPS and the spin period set to follow a log-normal distribution with the mean as 1.45 and the standard deviation as 0.36, and all other distributions as the best model of PsrPopPy, we generated a population of 5338 pulsars. Here, we first tried a log-normal distribution with the mean as 1.5 and the standard deviation as 0.58 as suggested by Lorimer et al. (2015). However, then we changed the values of the mean and the standard deviation a bit to ensure that, a) the minimum value of the simulated spin periods (1.518 ms) does not go below the minimum observed value of the spin period (1.396 ms) as reported in the ATNF catalogue and b) the range of the simulated values of the spin periods remains as constrained as possible so that we have a substantial number of simulated values of the spin period being less than 30 ms. Note that, the best fit distributions of other parameters were obtained for normal pulsars (Faucher-Giguère & Kaspi, 2006; Ridley & Lorimer, 2010). Although there would be some differences in the distributions of various parameters for the populations of the normal and the millisecond pulsars, it has been observed that moderately good statistical agreement between the synthetic and the real millisecond pulsar populations could be found by using the distributions given by Faucher-Giguère & Kaspi (2006) and Ridley & Lorimer (2010) except the one for the spin period (Lorimer et al., 2015; Lorimer , 2013; Lorimer et al., 2006). In the present work, we use this approach, as the main aim of the paper is not to study the population properties of millisecond pulsars.

Table 4.1: The input parameters for simulating pulsar populations using PsrPopPy for both normal pulsars as well as millisecond pulsars are listed.

Parameter	Normal Pulsar	Millisecond Pulsar
Pulse period distribution (mean, standard deviation)	log-normal (2.7, -0.34)	log-normal (1.45, 0.36)
Luminosity distribution (mean, standard deviation)	log-normal (-1.1, 0.9)	log-normal (-1.1, 0.9)
Electron density model	NE2001	NE2001
Radial distance distribution model	as given by Lorimer et al. (2006)	as given by Lorimer et al. (2006)
z value distribution (scale in kpc)	exponential (0.33)	exponential (0.33)
Spectral index distribution (mean, standard deviation)	normal (-1.6, 0.35)	normal (-1.6, 0.35)

Out of these 5338 synthetic pulsars, seven had $d > d_{\rm max,ne2001}$. We excluded these cases and got 5331 simulated pulsars. Out of these, we further excluded the cases with spin period greater than 30 ms and worked with the remaining 2791 synthetic millisecond pulsars.

From the population models generated by PsrPopPy, we extracted the values of the Galactic longitude (l), the Galactic latitude (b), the spin period ($P_{\rm s}$), and the distance (d) based on NE2001 model in order to use in our calculations. We converted the values of the spin period to that of the spin frequency ($f_{\rm s}$). For the parameters that are not available in PsrPopPy, e.g., the proper motion in the Galactic longitude (μ_l), the proper motion in the Galactic latitude (μ_b), the observed value of the time-derivative of the spin frequency ($\dot{f}_{\rm s,obs}$), and the observed value of the second time-derivative of the spin frequency ($\ddot{f}_{\rm s,obs}$), we generated synthetic values based on the distribution followed by the values of each of these parameters given in the ATNF catalogue, independently.

For this, we fitted the values of the parameter reported in the ATNF catalogue with an Empirical Cumulative Distribution Function (ECDF) and then used the inverse CDF technique to generate the required number of synthetic values following the same ECDF. We followed the same procedure whenever we fitted the parameters from the ATNF catalogue.

We performed this task separately for the normal and millisecond pulsars, i.e., generated 124115 synthetic sets of parameters based on the distributions followed by the values of the parameters for the normal pulsars and generated 2791 synthetic sets of parameters based on the distributions followed by the values of the parameters for the millisecond pulsars. This technique is described in detail in section 4.5 where we have demonstrated the generation of synthetic millisecond pulsar parameters as an example. We followed the same approach for generating such synthetic parameters for normal pulsars too.

As most of the binary pulsars are millisecond pulsars, we additionally generated 2791 synthetic values of the orbital frequency (f_{b}), the observed value of the first time-derivative of the orbital frequency ($\dot{f}_{\mathrm{b,obs}}$), and the observed value of the second time-derivative of the orbital frequency ($\ddot{f}_{\mathrm{b,obs}}$) for millisecond pulsars. The underlying assumption here is that these parameters by themselves are not affected much by selection effects unlike the parameters like the spin period, the coordinates and the distance of the pulsar. For radial velocity, we took a uniform distribution between -200 and 200 km/s, same as the range used by Liu et al. (2018).

We calculated all square bracket terms of eq. (2.37) separately as well as the sum of the first three square bracket terms, which we call the 'combined' term. Each term can have positive or negative values depending on the values of the parameters. However, the absolute value or the magnitude of these terms are more useful for comparison.

We summarize these results in the histograms of Fig. 4.1 for synthetic millisecond pulsars and Fig. 4.2 for synthetic normal pulsars. Additionally, Table 4.2 contains the statistical summary for the synthetic millisecond pulsars while Table 4.3 contains the statistical summary for the synthetic normal pulsars. From these, it is clear that all of the first three square bracket terms contribute 'almost' equally to the observed value of the second derivative of the frequency.

We next aimed to compare the combined term with the remaining one, i.e., the fourth square bracket term of eq. (2.37). We can see from eq. (2.37) that the fourth square bracket term contains a factor $\left(\frac{\dot{f}}{f}\right)_{\rm obs}$, i.e., the ratio of the observed frequency derivative and the frequency. The spin frequency and its derivative and the orbital frequency and its derivative are physically different entities. We can measure the values of the spin frequency and its derivative even for isolated pulsars. Moreover, the magnitudes of these parameters and the sign of the derivatives are usually different. The spin frequency derivative is intrinsically a result of the slow down of the pulsar spin as it loses its rotational kinetic energy in the form of the electromagnetic energy and hence expected to be negative while the orbital frequency derivative is intrinsically a result of the shrinkage of the orbit due to the emission of the gravitational waves and hence expected to be positive. Although the dynamics affect the values of both the spin frequency derivative and the orbital frequency derivative, it alters the sign very rarely. Hence, the ratio of the observed frequency derivative and the frequency, and consequently, the entire fourth square bracket term will be different for the case when we consider the spin frequency and its derivative as compared to when we consider the orbital frequency and its derivative.

We first calculated the values of the fourth square bracket using the spin frequency and its derivative for both the millisecond pulsar and the normal pulsar populations. Then, for the millisecond pulsar population, we calculated the value of this term using the orbital frequency and its derivative. Figs. 4.1 and 4.2 as well as tables 4.2 and 4.3 contain results for the fourth square bracket term too. We did not calculate this term using the orbital frequency and its derivative for the normal pulsar population, as most of the real normal pulsars are isolated, and the orbital frequency and its first derivative for the handful of normal pulsars do not bear the characteristic of the population. To be more specific, the ATNF catalogue (version 1.63) reports total 255 millisecond pulsars in the Galactic field; out of which 189 have the value of the orbital frequency reported and 30 have the value of the orbital frequency derivative measured. On the other hand, out of 2353 normal pulsars in the Galactic field, only 48 have the value of the orbital frequency reported and only 9 have the value of the orbital frequency derivative measured. Also, this fourth square bracket term is a part of the excess contribution (due to dynamics) to the second derivative of the orbital frequency as expressed in eq. (2.37), and so far no second derivative of orbital frequency has ever been measured for any normal pulsar. On the other hand, these parameters are measurable for millisecond pulsars as they are more stable and their precise timing is possible. We notice that,

- The median of the absolute value of the combined term for millisecond pulsars is within about an order of magnitude of the absolute value of their fourth square bracket term for the orbital frequency.
- The median of the absolute value of the combined term for millisecond pulsars is within about two orders of magnitude of the absolute value of their fourth square bracket term for the spin frequency. Note that, due to their extreme stability, millisecond pulsars are timed better, so the second derivative of the spin frequency of millisecond pulsars are likely to be measured more accurately than those for the normal pulsars.
- The median of the absolute value of the combined term for normal pulsars is within about an order of magnitude of the absolute value of their fourth square bracket term for the spin frequency.

From the above results, we conclude that it is wise to retain all of the terms in eq. (2.37) when accurate values are aimed for.

In order to assess whether our result could be affected by our choice of the Galactic electron density model, i.e., the use of the NE2001 model instead of the YMW16 (Yao et al., 2017) model, we explored both the models, though we report only the results based on the NE2001 model.

To perform simulation based on the YMW16 model, we used PsrPopPy2[2]. The use of different electron density models did not alter our conclusions, as over such a large number

---

[2] `https://github.com/devanshkv/PsrPopPy2`

Table 4.2: The top section of the table shows the statistical summary of all the square bracket terms appearing in eq. (2.37) for the simulated millisecond pulsars. We compare the absolute values of all the terms here. The middle section of the table shows the comparison of absolute values of the combined and the fourth square bracket (spin) terms for the 140 real millisecond pulsars in ATNF catalogue for which all relevant parameters to calculate $\left(\frac{\dot{f}}{f}\right)_{\rm ex}$, for the spin frequency and its derivative, are available. The bottom section of the table shows the comparison of absolute values of the combined and the fourth square bracket (orbital) terms for the 31 millisecond pulsars in the ATNF catalogue for which all relevant parameters to calculate $\left(\frac{\dot{f}}{f}\right)_{\rm ex}$, for the orbital frequency and its derivative, are available.

Simulated Millisecond Pulsars				
Term	Minimum (s^{-2})	Mean (s^{-2})	Median (s^{-2})	Maximum (s^{-2})
First Square Bracket Term	3.49×10^{-37}	2.34×10^{-33}	1.15×10^{-33}	5.80×10^{-32}
Second Square Bracket Term	4.51×10^{-37}	1.71×10^{-33}	6.54×10^{-34}	3.48×10^{-32}
Third Square Bracket Term	3.78×10^{-37}	1.34×10^{-32}	2.20×10^{-33}	5.90×10^{-31}
Combined Term	2.38×10^{-37}	1.38×10^{-32}	2.53×10^{-33}	5.77×10^{-31}
Fourth Square Bracket Term (spin)	1.23×10^{-38}	6.32×10^{-34}	3.89×10^{-35}	2.60×10^{-31}
Fourth Square Bracket Term (orbital)	1.17×10^{-39}	1.84×10^{-29}	3.40×10^{-33}	1.12×10^{-26}
Real Millisecond Pulsars (spin)				
Combined Term	9.51×10^{-37}	8.95×10^{-33}	1.36×10^{-33}	2.36×10^{-31}
Fourth Square Bracket Term (spin)	7.01×10^{-39}	1.34×10^{-35}	2.23×10^{-36}	5.98×10^{-34}
Real Millisecond Pulsars (orbital)				
Combined Term	1.16×10^{-34}	1.23×10^{-32}	2.53×10^{-33}	2.36×10^{-31}
Fourth Square Bracket Term (orbital)	1.62×10^{-38}	1.39×10^{-32}	1.21×10^{-35}	1.85×10^{-31}

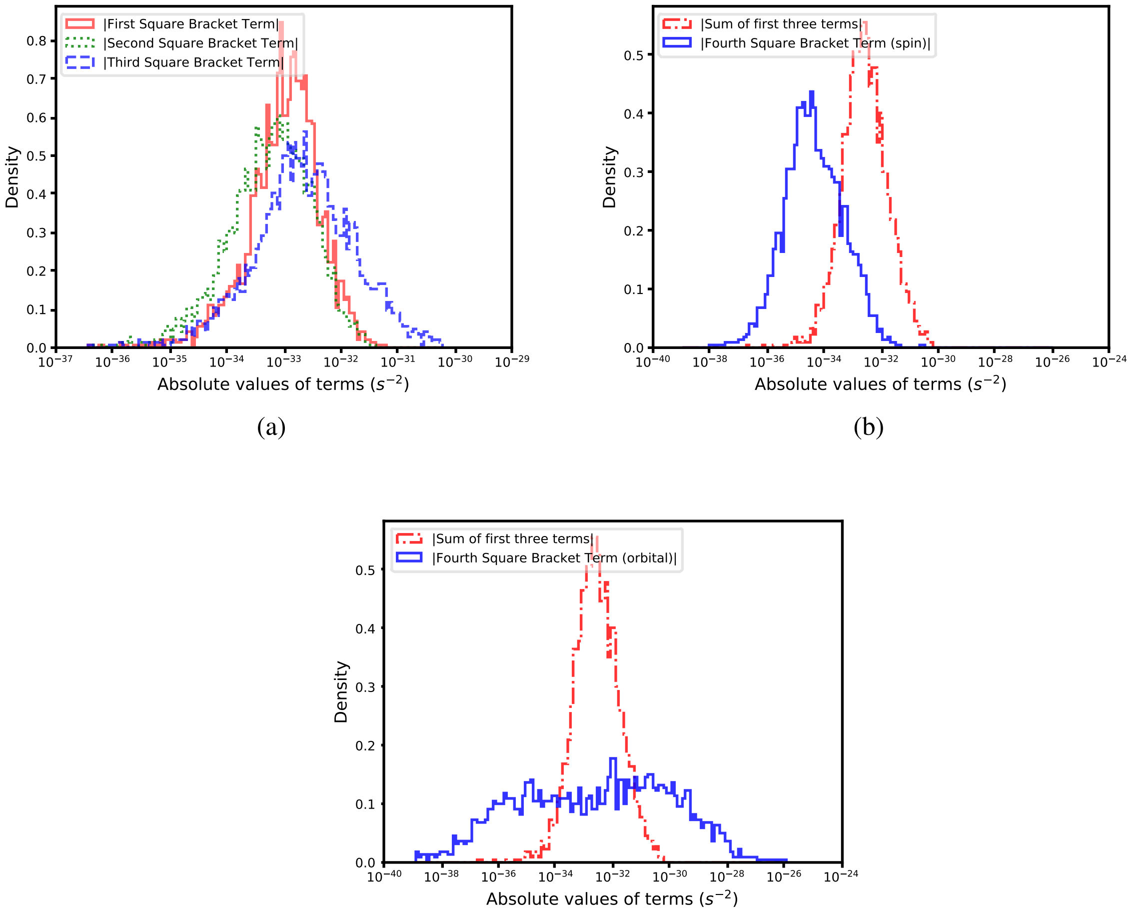

(a)

(b)

(c)

Figure 4.1: Density distribution of the absolute values of various square bracket terms in eq. (2.37) for simulated millisecond pulsars. The subplots are as follow: a) comparison of line histograms for the first square bracket term, the second square bracket term, and the third square bracket term, b) comparison of line histograms for the sum of the first three terms and the fourth square bracket term using the spin frequency and its derivatives, and c) comparison of line histograms for the sum of the first three terms and the fourth square bracket term using the orbital frequency and its derivatives.

Table 4.3: The top section of the table shows the statistical summary of all the square bracket terms appearing in eq. (2.37) for the simulated normal pulsars. We compare the absolute values of all the terms here. The bottom section of the table shows the comparison of absolute values of the combined and the fourth square bracket (spin) terms for the 238 real normal pulsars in the ATNF catalogue for which all relevant parameters to calculate $\left(\frac{\dot{f}}{f}\right)_{\mathrm{ex}}$, for the spin frequency and its derivative, are available.

Simulated Normal Pulsars				
Term	Minimum (s^{-2})	Mean (s^{-2})	Median (s^{-2})	Maximum (s^{-2})
First Square Bracket Term	6.22×10^{-39}	4.54×10^{-33}	1.98×10^{-33}	3.57×10^{-31}
Second Square Bracket Term	2.29×10^{-39}	3.83×10^{-33}	1.36×10^{-33}	4.36×10^{-31}
Third Square Bracket Term	2.68×10^{-38}	5.57×10^{-32}	9.38×10^{-33}	6.73×10^{-30}
Combined Term	1.01×10^{-37}	5.59×10^{-32}	9.62×10^{-33}	7.07×10^{-30}
Fourth Square Bracket Term (spin)	1.57×10^{-39}	5.16×10^{-29}	4.33×10^{-32}	1.97×10^{-25}
Real Normal Pulsars				
Combined Term	1.17×10^{-35}	3.68×10^{-32}	5.19×10^{-33}	1.65×10^{-30}
Fourth Square Bracket Term (spin)	1.12×10^{-37}	1.85×10^{-30}	1.47×10^{-32}	2.32×10^{-28}

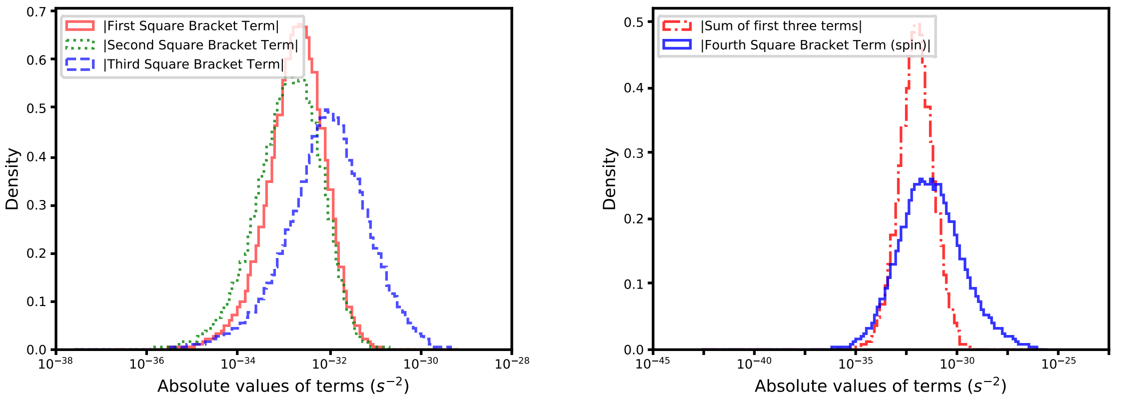

(a)

(b)

Figure 4.2: Density distribution of the absolute values of various square bracket terms in eq. (2.37) for the simulated normal pulsars. The subplots are as follow: a) comparison of line histograms for the first square bracket term, the second square bracket term, and the third square bracket term, and b) comparison of line histograms for the sum of the first three terms and the fourth square bracket term using the spin frequency and its derivatives.

of samples, they provide almost the same statistics. Particularly, for MSPs (Table 4.2), using the NE2001 model, the median of the combined term, the fourth square bracket spin term, and the fourth square bracket orbital term are 2.53×10^{-33}, 3.89×10^{-35}, and 3.40×10^{-33} s^{-2} respectively while for the YMW16 model, these terms are 2.72×10^{-33}, 3.79×10^{-35}, and 3.48×10^{-33} s^{-2}. For normal pulsars (Table 4.3) the median of the combined term and the fourth square bracket spin term are 9.62×10^{-33} and 4.33×10^{-32} s^{-2} respectively while for the YMW16 model, these terms are 9.51×10^{-33} and 4.22×10^{-32} s^{-2}. Other statistics also do not differ much.

It should also be noted that even though YMW16 is newer, it is not necessarily better than NE2001. In some directions, YMW16 is better, but in some other directions, NE2001 is better. The following examples substantiate this claim. (i) For PSR J0034−0721, YMW16 agrees better with the independent distance measurement. For this pulsar, YMW16 distance, NE2001 distance, and the independent distance values are 1.00, 0.39, and 1.03 kpc respectively. (ii) For PSR J0751+1807, NE2001 agrees better with the independent distance measurement. For this pulsar, YMW16 distance, NE2001 distance and the independent distance values are 0.43, 1.15, and 1.11 kpc respectively. (iii) Both the models are poor (i.e., they disagree with the independent distance measurement) for PSR J2337+6151. For this pulsar, YMW16 distance, NE2001 distance, and the independent distance values are 2.08, 3.15, and 0.70 kpc respectively. (iv) Both of the models are good (i.e., they agree with the independent distance measurement) for PSR J1833−0827. For this pulsar, YMW16 distance, NE2001 distance, and the independent distance values are 4.38, 4.66, 4.50 kpc respectively. There are more examples in each of these categories. We have decided to keep only NE2001 results in this study as it will ease the comparison with older literature.

For the sake of comparison, we also computed the values of various terms of eq. (2.37) for real pulsars. The ATNF catalogue (version 1.63) has 378 pulsars for which all relevant parameters to calculate the value of $\left(\frac{\dot{f}}{f}\right)_{\rm ex}$, appearing in the fourth square bracket of eq.

(2.37) for the spin frequency and its derivative, are available. Out of these 378 pulsars, 140 are millisecond pulsars and the rest 238 are normal pulsars[3]. For these pulsars, all parameters required to calculate the first three square bracket terms are also known, except v_r that appears in the first and the third square bracket terms. So, we needed to choose reasonable values for v_r, one such value is 50 km/s (Liu et al., 2019). However, for two millisecond pulsars, PSRs J1024−0719 and J1903+0327, the values of v_r are known to be 185 km/s and 42 km/s respectively (Liu et al., 2018), and these values were used. We performed our calculations separately for both the sets- normal and millisecond pulsars.

For millisecond pulsars, we found the maximum difference between the absolute value of the combined and the fourth term for PSR J0437−4715, values being 2.36×10^{-31} s^{-2} and 1.55×10^{-34} s^{-2} respectively. Whereas we found the minimum difference between the absolute value of the combined and the fourth term for PSR J1902−5105, values being 9.51×10^{-37} s^{-2} and 1.12×10^{-36} s^{-2} respectively.

Similarly, for the normal pulsars, we found the maximum difference between the absolute value of the combined and the fourth term for PSR J1808−2024, values being 2.26×10^{-34} s^{-2} and 2.32×10^{-28} s^{-2} respectively. Whereas we found the minimum difference between the absolute value of the combined and the fourth term for PSR J2055+2209, values being 5.42×10^{-34} s^{-2} and 5.50×10^{-34} s^{-2} respectively.

Additionally, we report the statistical summary of the absolute values of the combined and the fourth square bracket term for the real millisecond pulsars in Table 4.2 and the real normal pulsars in Table 4.3. We see that the median of the absolute values of the combined term is within three orders of magnitude of the median of the absolute values of the fourth square bracket term for both millisecond as well as normal pulsars.

We have also found that, for 63.03% of the normal pulsars, the absolute value of the fourth square bracket term is larger than the absolute value of the combined term. Further,

---

[3] Note that earlier we mentioned that ATNF catalogue reports 2353 normal and 255 millisecond pulsars. However, not for all of those, all the parameters needed to compute the dynamical terms have been reported, hence, here we are working with less number of pulsars.

31.33% of this particular set of pulsars (or 19.75% of the total normal pulsar population) have the absolute value of the fourth square bracket term larger than the absolute value of the combined term by more than one order of magnitude. In the case of the 140 millisecond pulsars, only 2 of them had the absolute value of the fourth square bracket term greater than the absolute value of the combined term. Furthermore, for 95.71% of the millisecond pulsars, the absolute value of the combined term was found to be larger than the absolute value of the fourth square bracket term by more than one order of magnitude. These facts again support our conclusion that the first three terms should not be ignored.

To complete our exploration with real pulsars, we find that the ATNF catalogue (version 1.63) has 31 millisecond pulsars for which all relevant parameters to calculate $\left(\frac{\dot{f}}{f}\right)_{\text{ex}}$ for the orbital frequency and its derivative are available. For these pulsars too, all parameters required to calculate the first three square bracket terms are also known, except v_r, and we choose the same values of v_r as discussed above. We found the maximum difference between the absolute value of the combined and the fourth term for PSR J0437−4715, values being 2.36×10^{-31} s^{-2} and 1.17×10^{-34} s^{-2} respectively. Whereas we found the minimum difference between the absolute value of the combined and the fourth term for PSR J1949+3106, values being 1.16×10^{-34} s^{-2} and 2.29×10^{-37} s^{-2} respectively.

We report the statistical summary of the absolute values of the combined and the fourth square bracket term for the orbital frequency for these real millisecond pulsars in the bottom part of Table 4.2. We see that the median of the absolute values of the combined term is within three orders of magnitude of the absolute values of the fourth square bracket term. We have also found that, for only 16.13% pulsars, the magnitude of the fourth square bracket term is larger than the magnitude of the combined term. Further, 40% of this particular set of pulsars (or 6.45% of the total population) have the magnitude of the fourth square bracket term larger than the magnitude of the combined term by more than one order of magnitude. These facts again support our conclusion that the first three terms should not be ignored, even when we are concerned with the dynamical effects in the second derivative of the orbital frequency.

We also investigated the impact of the value of v_r in the absolute value of the combined term. It should be noted that the fourth term is independent of v_r. Here we excluded the pulsars with known values of v_r, i.e., PSRs J1024−0719 and J1903+0327. We performed our calculations for the remaining real pulsars, 238 normal pulsars and 138 millisecond pulsars separately, for which all relevant parameters to calculate $\left(\frac{\dot{f}}{f}\right)_{\rm ex}$ for the spin frequency and its derivative are available. We also performed calculations for the set of 31 millisecond pulsars for which all relevant parameters to calculate $\left(\frac{\dot{f}}{f}\right)_{\rm ex}$ for the orbital frequency and its derivative are available. We chose some specific values of v_r, i.e., -200, -100, -50, 0, 50, 100, and 200 km/s (Liu et al., 2018). We identified the maximum (*max*) and minimum (*min*) values of the absolute value of the combined term and calculated the percentage difference as $100 \times (max - min)/max$, for each pulsar.

We found that among the set of normal pulsars, the variation of the combined term with v_r was maximum for PSR J1741−2054 (percentage difference of 99.99% with *max* at $v_r = -200$ km/s and *min* at $v_r = 0$ km/s) and minimum for PSR J1741−0840 (percentage difference of 86.46% with *max* at $v_r = 200$ km/s and *min* at $v_r = -200$ km/s). For the set of millisecond pulsars where we worked with the spin frequency and its derivatives, the variation with v_r was maximum for PSR J1902−5105 (percentage difference of 99.97% with *max* at $v_r = 200$ km/s and *min* at $v_r = 50$ km/s) and minimum for PSR J1747−4036 (percentage difference of 6.93% with *max* at $v_r = 200$ km/s and *min* at $v_r = -200$ km/s). For the set of millisecond pulsars where we worked with the orbital frequency and its derivatives, the variation with v_r was maximum for PSR J1723−2837 (percentage difference of 99.90% with *max* at $v_r = 200$ km/s and *min* at $v_r = 0$ km/s) and minimum for PSR J2055+3829 (percentage difference of 88.94% with *max* at $v_r = -200$ km/s and *min* at $v_r = 0$ km/s). From all these, it is evident that depending upon other parameters, the value of the combined term might be very sensitive to the value of v_r, and hence the measurement of the value of v_r is desirable to estimate the effect of the dynamics in the second derivative of the frequency accurately.

However, measuring the radial velocity of a radio pulsar is a challenging task. The best way is to measure the radial velocity of the companion star of a binary pulsar using optical spectroscopy. This has been done so far only for five binary pulsars (see the references in the caption of table 2 of Liu et al. (2018)). It should be noted that this radial velocity is a combination of the radial velocity component of the orbital motion of the companion around the centre of mass of the binary and the radial velocity of the binary system (i.e., the centre of mass of the binary) in the Galaxy. For very wide binaries (e.g., PSR J1024−0719), the orbital part can be ignored as done by Bassa et al. (2016). For binaries with shorter orbits, careful modeling is needed to decouple the orbital (periodical) part of the radial velocity from the radial velocity of the system with respect to the local standard of rest.

It is obvious that the above method cannot be applied to the isolated pulsars. Helfand & Tademaru (1977) first suggested a solution that the apparent motion of slow pulsars towards the Galactic disk as obtained from the measured proper motion might be the result of unaccounted radial velocity. They suggested that such a motion might give a hint of moderately large radial velocity. However, a part of this motion might arise due to the perpendicular component of the acceleration of the pulsar due to the Galactic potential (as we have discussed earlier, the perpendicular component of the pulsar acceleration due to the gravitational potential is directed towards the Galactic plane). Sun & Han (2004) found this significant. However, Hobbs et al. (2005) found this effect to be rarely significant. This method has not been pursued much by pulsar astronomers but might be worth exploring in the future.

Another potential method is to fit for a radial velocity when the transverse velocity is known to find an association of young pulsars with nearby supernova remnants (Chmyreva et al., 2017).

4.2.2 Pulsar population near the Galactic centre

In chapter 3, we saw that at low values of R and z, both $|\frac{\partial\Phi}{\partial R}|$ and $|\frac{\partial\Phi}{\partial z}|$ peak, and here Φ is the gravitational potential of the Galaxy, R is the Galactocentric cylindrical radius, and z is the vertical height from the Galactic disc. Moreover, the slopes of the $|\frac{\partial\Phi}{\partial R}|$ vs R and $|\frac{\partial\Phi}{\partial R}|$ vs z curves are steepest near the peak. As $-\frac{\partial\Phi}{\partial R}$ and $-\frac{\partial\Phi}{\partial z}$ provide the acceleration of the pulsars parallel and perpendicular to the Galactic disc, we expect that the magnitudes of both of the acceleration and the jerk would be large for pulsars located in this region, which corresponds to the region close to the Galactic centre. Unfortunately, no such pulsar is known at present in this region, so we decided to work on a synthetic set of pulsars.

Like section 4.2.1, here too, we separately studied the millisecond pulsar population and the normal pulsar population, and we took a uniform distribution between -200 and 200 km/s, for v_r both of the populations. We constrained our simulations to the cases with l varying uniformly between 0 and 5 degrees as well as between 355 and 360 degrees, b varying uniformly between -5 and 5 degrees, and d varying uniformly between 7.8 and 8.2 kpc. Note that this region is somewhat large, extending up to a distance of 1.02 kpc from the Galactic centre. There is one real pulsar in this region, PSR J1746-2856 at a distance of 0.432 kpc from the Galactic centre. So, this is not the exact 'Galactic centre region', which is defined to be the region within a few parsecs around the Galactic centre. However, we choose this larger region to have a larger sample of synthetic pulsars. Our aim is to understand the effect of the gravitational potential induced dynamics on the observed values of frequency derivatives in this region in comparison to those in the outer regions of the Galaxy.

For these parameters, we generated the same number of cases (124115) corresponding to the normal pulsar population as those generated in the earlier subsection, so that we could use the same sample of $f_{\rm s}$ as obtained from PsrPopPy earlier. Similarly, we generated the same number of cases (2791) corresponding to the millisecond pulsar population and used the corresponding sample of $f_{\rm s}$ as obtained from PsrPopPy earlier.

Table 4.4: Statistical summary of all the square bracket terms appearing in eq. (2.37) for the simulated millisecond pulsars near the Galactic centre. We compare the absolute values of all the terms here.

Term	Minimum (s^{-2})	Mean (s^{-2})	Median (s^{-2})	Maximum (s^{-2})
First Square Bracket Term	4.49×10^{-36}	5.23×10^{-32}	1.96×10^{-32}	4.69×10^{-30}
Second Square Bracket Term	1.23×10^{-35}	1.17×10^{-32}	6.65×10^{-33}	1.58×10^{-31}
Third Square Bracket Term	5.12×10^{-37}	1.50×10^{-32}	3.67×10^{-33}	6.39×10^{-31}
Combined Term	1.69×10^{-35}	5.79×10^{-32}	2.15×10^{-32}	4.69×10^{-30}
Fourth Square Bracket Term (spin)	5.43×10^{-40}	5.16×10^{-34}	4.00×10^{-35}	1.65×10^{-31}
Fourth Square Bracket Term (orbital)	7.00×10^{-40}	2.02×10^{-29}	3.17×10^{-33}	1.89×10^{-26}

For the rest of the parameters (μ_l, μ_b, $\dot{f}_{\mathrm{s,obs}}$, $\ddot{f}_{\mathrm{s,obs}}$, f_{b}, $\dot{f}_{\mathrm{b,obs}}$, and $\ddot{f}_{\mathrm{b,obs}}$) we used the same distributions as generated in section 4.2.1 for the millisecond pulsars. Similarly, for the normal pulsars, we used the same distributions generated in section 4.2.1 for the remaining corresponding parameters (μ_l, μ_b, $\dot{f}_{\mathrm{s,obs}}$ and, $\ddot{f}_{\mathrm{s,obs}}$). The underlying assumption here is that the population of pulsars near the Galactic centre is not way too different than the overall disk population. This assumption might not be perfectly valid, however our only aim was to obtain a qualitative comparison between various terms in eq. (2.37).

Similar to section 4.2.1, here also, we calculate all square bracket terms of eq. (2.37) separately. We summarize these results in the histograms of Fig. 4.3 for millisecond pulsars and Fig. 4.4 for normal pulsars. Additionally, Table 4.4 contains the statistical summary for the synthetic millisecond pulsars while Table 4.5 contains the statistical summary for the synthetic normal pulsars.

Comparing the values reported in tables 4.2 and 4.4 for the millisecond pulsars, and the values reported in tables 4.3 and 4.5 for the normal pulsars, we see that the median values of the absolute values of the first three square bracket terms are about one order of magnitude larger for the pulsar population near the Galactic centre than the general population. For the fourth square bracket term, we get almost the same median values for the two populations as expected, as in the fourth square bracket term, the dynamics dependent $\left(\frac{\dot{f}}{f}\right)_{\mathrm{ex}}$ is multiplied by $\left(\frac{\dot{f}}{f}\right)_{\mathrm{obs}}$ which have been simulated with the help of the observed values of

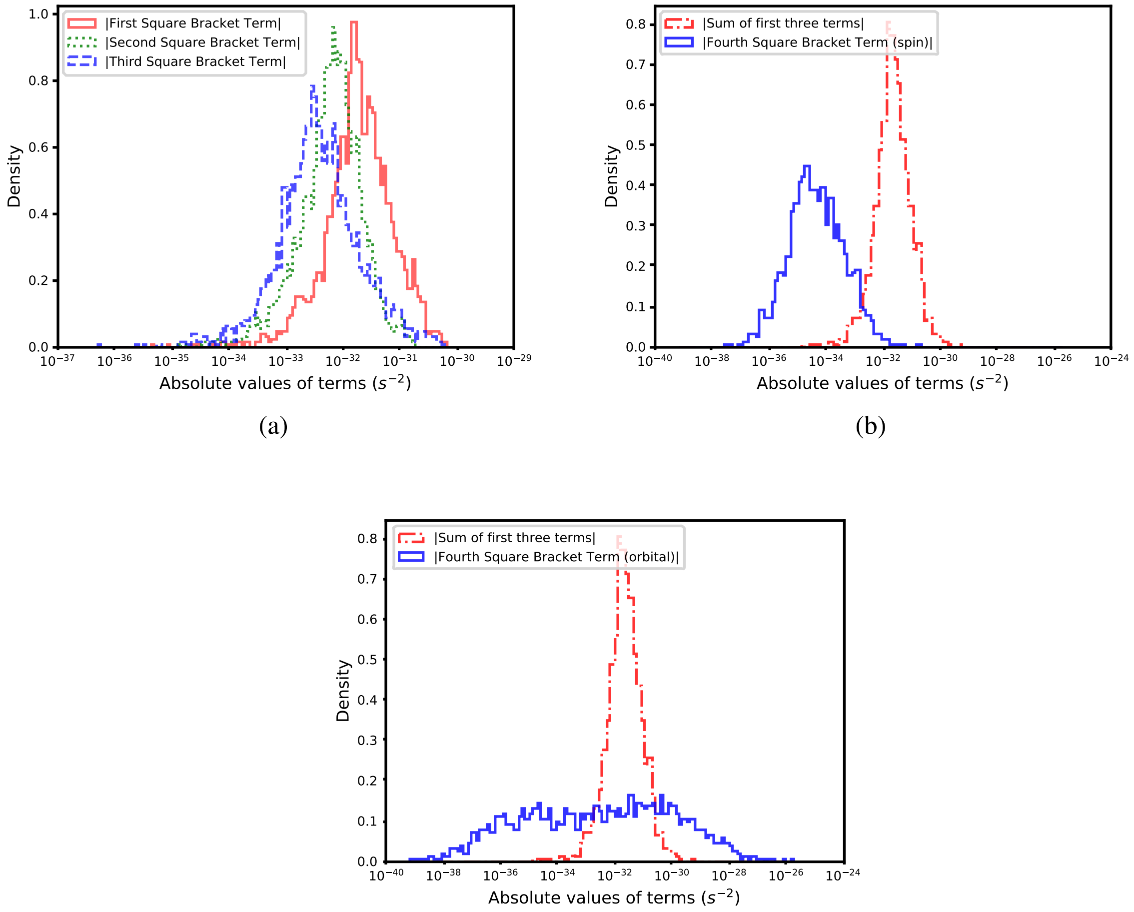

(a)

(b)

(c)

Figure 4.3: Density distribution of the absolute values of various square bracket terms in eq. (2.37) for simulated millisecond pulsars near the Galactic centre. The subplots are as follow: a) comparison of line histograms for the first square bracket term, the second square bracket term, and the third square bracket term, b) comparison of line histograms for the sum of the first three terms and the fourth square bracket term using the spin frequency and its derivatives, and c) comparison of line histograms for the sum of the first three terms and the fourth square bracket term using the orbital frequency and its derivatives.

Table 4.5: Statistical summary of all the square bracket terms appearing in eq. (2.37) for the simulated normal pulsars near the Galactic centre. We compare the absolute values of all the terms here.

Term	Minimum (s^{-2})	Mean (s^{-2})	Median (s^{-2})	Maximum (s^{-2})
First Square Bracket Term	1.11×10^{-36}	9.97×10^{-32}	3.06×10^{-32}	2.29×10^{-28}
Second Square Bracket Term	3.53×10^{-38}	2.38×10^{-32}	1.39×10^{-32}	8.33×10^{-31}
Third Square Bracket Term	6.17×10^{-38}	5.72×10^{-32}	1.09×10^{-32}	7.70×10^{-30}
Combined Term	2.74×10^{-37}	1.29×10^{-31}	3.75×10^{-32}	2.28×10^{-28}
Fourth Square Bracket Term (spin)	1.28×10^{-39}	4.10×10^{-29}	3.94×10^{-32}	1.78×10^{-25}

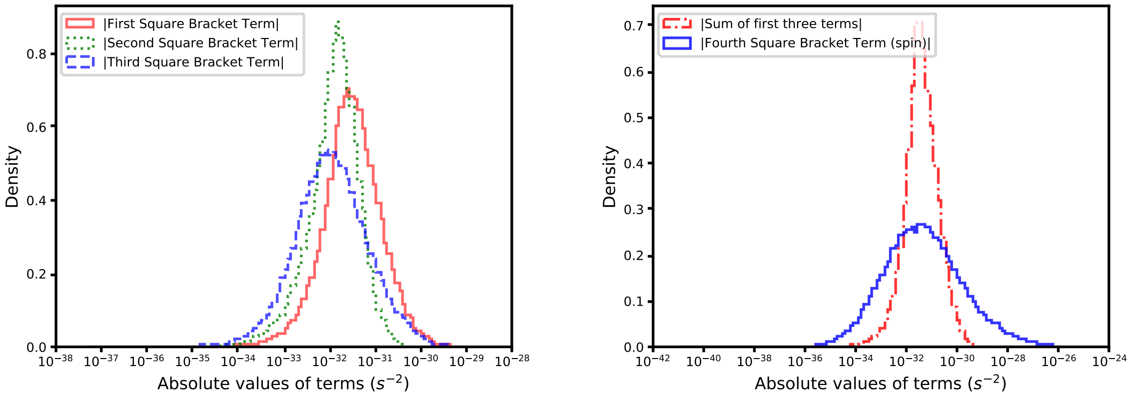

(a)

(b)

Figure 4.4: Density distribution of the absolute values of various square bracket terms in eq. (2.37) for the simulated normal pulsars near the Galactic centre. The subplots are as follow: a) comparison of line histograms for the first square bracket term, the second square bracket term, and the third square bracket term, and b) comparison of line histograms for the sum of the first three terms and the fourth square bracket term using the spin frequency and its derivatives.

the field pulsars.

From the above-mentioned facts, we conclude that the measured values (through timing analysis) of the second derivative of the spin or orbital frequency of a pulsar near the Galactic centre would likely be contaminated by the dynamical terms by a larger amount than the pulsars away from the Galactic centre, especially if the distributions of frequencies and its derivatives are not drastically different.

It should be noted that, although our formalism can be used for pulsars close to the Galactic centre, it is not very accurate there, as the gravitational pulls of nearby stars on the pulsars are likely to be significant. Nevertheless, if any pulsar close to the Galactic centre is discovered in the near future, our expressions can be used to obtain a first-order correction.

4.3 Introduction to GalDynPsrFreq

We have created a python-package GalDynPsrFreq that estimates the dynamical terms in the measured values of the first and the second time derivatives of the frequency. This frequency can be either the spin or the orbital. It can even eliminate these dynamical terms and directly give the intrinsic values of the frequency derivatives.

It is known that the accelerations and jerks of pulsars depend on the gravitational potential of the Galaxy. GalDynPsrFreq uses ‘galpy’ based potentials `MWPotential2014` and `MWPotential2014BH` that have been discussed in Chapter 3. The user has the freedom to choose one of these two models. It is clear that to use GalDynPsrFreq, one needs to install galpy first. Additionally, basic python libraries ‘scipy’, ‘numpy’, and ‘astropy’ are needed.

GalDynPsrFreq is designed to be usable as a library (importable module) by other python programs which would provide the values of the parameters needed. It is available at `https://github.com/pathakdhruv/GalDynPsrFreq` and can be even installed using the `pip3` command of python. This version is also available at `http://doi.org/10.5281/zenodo.4603803`. The details of the usage and the description of various modules of GalDynPsrFreq with a number of examples are available in the package documentation.

The user needs to provide observable pulsar parameters like the Galactic longitude, l, in degrees, the Galactic latitude, b, in degrees, the distance of the pulsar from the solar system barycenter, d, in kpc, the proper motion in the Galactic longitude, μ_l, in mas/yr, the proper motion in the Galactic latitude, μ_b, in mas/yr, the radial component of the relative velocity, v_r, of the pulsar with respect to the solar system barycenter in km/s, the frequency, f, in Hz, the observed frequency derivative, $\dot{f}_{\rm obs}$, in s^{-2}, and the observed frequency second derivative, $\ddot{f}_{\rm obs}$, in s^{-3}. The frequency and its derivatives can be either the spin or the orbital.

GalDynPsrFreq does not return uncertainties in the results, because the models of the Galactic potential given in galpy do not return uncertainties. However, since ours is a modular package, if a Galactic potential model along with uncertainties becomes available in the future, it can be easily included in this package. Then, modules to calculate the uncertainties in the dynamical terms can be incorporated using standard error propagation techniques. Presently, uncertainties can be calculated by evaluating the same parameter several times, and then by estimating the mean and standard deviation of all of these values. In the following sections, we report the results mostly using `MWPotential2014BH` as the model potential of the Galaxy.

4.4 Applications

In this section, we discuss some practical applications of our formalism of correcting dynamical effects in the second derivative of frequencies and explore whether parameters that depend on the second derivative can be affected significantly by the dynamics.

4.4.1 Properties of PSR J1024−0719

As mentioned previously, Kaplan et al. (2016) and Bassa et al. (2016) showed that PSR J1024−0719 is a wide-orbit binary pulsar. Its orbit is so wide that a good timing solution could be obtained even without fitting for orbital parameters. However, for this pulsar, after eliminating the contributions of the velocity, acceleration and jerk due to the Galactic potential from the measured first and second time derivative of the spin frequency, additional dynamical effects due to the orbital motion would remain and hence, after using eqs. (2.20) and (2.38), what we obtain should be better called 'residual' (subscript 'res') instead of 'intrinsic' values of the frequency derivatives. Kaplan et al. (2016) reported derivatives of spin periods instead of spin frequencies and used the values of $\dot{P}_{\mathrm{s,res}}$ and $\ddot{P}_{\mathrm{s,obs}}$ to put some constraints on the orbit of the pulsar. They did not correct for the dynamical effects in the second derivative as they correctly guessed that it would be very small. Indeed, we see that $\ddot{P}_{\mathrm{s,res}} = 1.10 \times 10^{-31}\ \mathrm{s}^{-1}$ while $\ddot{P}_{\mathrm{s,obs}} = 1.1 \times 10^{-31}\ \mathrm{s}^{-1}$ as reported by Kaplan et al. (2016). Thus, for this particular pulsar, the contribution of the acceleration and jerk due to the gravitational potential of the Galaxy to the measured second derivative of the spin frequency is negligible. However, this might not be the case always, as we will explore in the next subsection. It is to be noted that we obtain $\dot{P}_{\mathrm{s,res}} = -3.89 \times 10^{-20}\ \mathrm{ss}^{-1}$ while Kaplan et al. (2016) had $\dot{P}_{\mathrm{s,res}} = -3.96 \times 10^{-20}\ \mathrm{ss}^{-1}$.

4.4.2 Intrinsic spin frequency second derivative and the braking index

Instead of exploring the effect of the dynamical terms in the second derivative of the spin frequency alone, we decided to concentrate on the braking index n which is associated with the basic emission model of rotation powered pulsars. As explained in Chapter 1 of the present thesis (in section 1.2), the expression for n can be written as:

$$n = \frac{\ddot{f}_{\rm s,int}\, f_{\rm s}}{\dot{f}^2_{\rm s,int}} \, . \tag{4.1}$$

We have also mentioned in section 1.8 the fact that although the value of n is expected to be three under the perfect dipole model, the measured values often differ largely.

Here we first investigated whether those anomalous values of n are affected by the dynamics or there are other physical reasons intrinsic to the pulsars. Hobbs et al. (2004) reported measurements of n for 374 pulsars. They found that the reported values of n for a number of pulsars lie in the range -2.6×10^8 to 2.5×10^8. These large deviations from the expected value 3 cannot be due to the timing noise as they had taken care of it by whitening the timing residuals. Although they calculated the values of n using the measured values of the spin frequency and its derivatives instead of their intrinsic values, it is unlikely that the dynamical effects would change the value of n from 3 to 10^8. Therefore, for pulsars having such large values of n, the conclusion of Hobbs et al. (2004) that the measured values of the second derivative of the spin frequency of the pulsars do not represent just the braking due to magnetic dipole radiation, seems valid. However, we explored whether for the pulsars with measured $|n| < 10$, dynamical terms play a significant role to shift the values from 3. Using the values of l, b, $f_{\rm s}$, $\dot{f}_{\rm s,obs}$, and $\ddot{f}_{\rm s,obs}$ directly from Hobbs et al. (2004), d, calculated using NE2001 model (Cordes and Lazio, 2002, 2003) based on the DM values given in Hobbs et al. (2004), and μ_l and μ_b, calculated using the values of RA, DEC and corresponding proper motion values given in Hobbs et al. (2004), we calculated values of $\dot{f}_{\rm int}$ and $\ddot{f}_{\rm int}$. We took a nominal $v_r = 50$ km/s, like Liu et al. (2019). For all these pulsars, we didn't see any significant change by correcting for the dynamical terms. We repeated the above calculations for $v_r = 0$ km/s and $v_r = -100$ km/s without any significant difference. Hence, we conclude that even for these pulsars, there are physical reasons for n to differ from 3. Recently, Dang et al. (2020) reported measurements of n for 73 pulsars. Out of these, they reported braking index values to be less than 10 for only two pulsars, namely, PSR J0157+6212 ($n = 4.8$) and PSR J1743-3150 ($n = 6.5$). Using the values of d, $f_{\rm s}$, $\dot{f}_{\rm s,obs}$, and $\ddot{f}_{\rm s,obs}$ directly from Dang et al. (2020), l, b, μ_l, and μ_b, from the values of RA and DEC and corresponding proper motion values given in Dang et al. (2020), we found only a small change in the braking index value of PSR J0157+6212 ($n = 5.0$) and a little higher change in PSR J1743-3150 ($n = 8.3$), but still, in no case, n gets closer to 3.

Now the question that arises is whether it is even possible for the dynamical effects to be large enough to alter the value of n significantly. To answer this question, we performed calculations on simulated millisecond pulsars. We concentrated only on millisecond pulsars, as these are more stable than normal pulsars, so less likely to have glitches, red timing noises, etc., that might make the observed value of n deviate from 3 (Dang et al., 2020). We aimed whether we could get a sufficient number of millisecond pulsars for which n is close to three (theoretically expected), i.e., $2.5 < n < 3.5$, and $n_{\rm obs} < 0$ or $n_{\rm obs} > 6$, i.e., $n_{\rm obs}$ is substantially different from n due to dynamical effects. Here, $n_{\rm obs}$ means the value of the braking index we get by using the observed values of the spin frequency and its derivatives, and n is the true braking index that we get after eliminating the dynamical contributions from the frequency derivatives. We used the same simulation approach as described in section 4.2.1. We did not find any case where $2.5 < n < 3.5$, but $n_{\rm obs} < 0$ or $n_{\rm obs} > 6$. We even performed the investigation over a larger number of synthetic pulsars (10000 instead of 2791 as in section 4.2.1), still did not find any favourable case. We then generated 10000 pulsars near the Galactic centre where the distributions of various parameters are the same as in section 4.2.2. But still, no favourable case was found.

However, it is possible that there might exist unique pulsars whose parameters are missed by the standard representation of the population (generated by ‘PsrPopPy’), and have $2.5 < n < 3.5$, and $n_{\rm obs} < 0$ or $n_{\rm obs} > 6$. To take care of this possibility, we adopted a different approach to simulate parameters for a synthetic set of millisecond pulsars. We explored two populations of millisecond pulsars, one in the Galactic field and the other in the near-Galactic centre region, by using two approaches to simulate l, b, and d. For the first population, we just fitted the distribution from the ATNF catalogue for the millisecond pulsars (excluding the ones in globular clusters, the Large Magellanic Cloud, and the Small Magellanic Cloud), i.e., we fitted the 142 values of a parameter, say, l reported in the ATNF catalogue with an Empirical Cumulative Distribution Function (ECDF) and then used the inverse CDF technique to generate 10000 synthetic values following the same ECDF [4]. For the second population, we used the approach as described in section 4.2.2. For both the populations, we generated 10000 values of these parameters. For μ_l and μ_b too, we simulated 10000 values based on the distribution of values in the ATNF catalogue for the millisecond pulsars. We also generated 10000 values of v_r distributed uniformly between -200 to 200 km/s. However, for $f_{\rm s}$, $\dot{f}_{\rm s,obs}$, and $\ddot{f}_{\rm s,obs}$, we needed to take a closer look at the ATNF catalogue values, again excluding the ones in globular clusters, the Large Magellanic Cloud, and the Small Magellanic Cloud.

We found that the range of $f_{\rm s}$ spans from 34.657 Hz to 641.928 Hz for millisecond pulsars. We divided this range into three equal parts and generated 10000 uniformly distributed values for each subrange. For $\dot{f}_{\rm s,obs}$, the values span in the range of -1.0×10^{-13} s^{-2} and -1.0×10^{-17} s^{-2} for millisecond pulsars. We divided this range into four parts with each part spanning over one order of magnitude and generated uniform distributions of 10000 values for each subrange. Since the ATNF catalogue only gives eight measurements of the $\ddot{f}_{\rm s,obs}$ for millisecond pulsars, we decided to extend the ranges. More specifically, the values of $\ddot{f}_{\rm s,obs}$ for these 8 millisecond pulsars lie in the ranges of -1.0×10^{-24} s^{-3} to -1.0×10^{-28} s^{-3} and 1.0×10^{-27} s^{-3} to 1.0×10^{-25} s^{-3}, whereas, by fitting these values with a distribution function and generating a synthetic values, we found that $\ddot{f}_{\rm s,obs}$ vary between -1.0×10^{-24} s^{-3} to -1.0×10^{-30} s^{-3} and 1.0×10^{-30} s^{-3} to 1.0×10^{-24} s^{-3}. We used these two sets and divided each set into 6 subranges, each of which span over one order of magnitude and generated uniform distributions of 10000 values for each subrange.

In this way, we got 3 subranges of $f_{\rm s}$, 4 subranges of $\dot{f}_{\rm s,obs}$, and 12 subranges of $\ddot{f}_{\rm s,obs}$, each

---

[4] See section 4.5 for the details of this procedure.

having 10000 uniformly generated values. For the braking index calculations, we chose one subrange corresponding to each of these three parameters, in addition to the 10000 values generated for the parameters l, b, d, μ_l, μ_b, and v_r each. These 10000 values for each parameter constitute the 10000 synthetic millisecond pulsars, concentrated in a specific subrange of the multi-dimensional parameter space, out of the total 144 ($3\times4\times12$) of such subranges. We computed the values of n and $n_{\rm obs}$ for all 10000 synthetic pulsars in each subrange and selected the favourable cases. In this approach, we implicitly assumed that the total number of millisecond pulsars over the full parameter space is much larger than 10000, which might not be very realistic. However, our quest here was to find unique combinations of parameters that could give large differences between the observed and intrinsic values of the braking index.

The number of favourable cases for different combinations of $f_{\rm s}$, $\dot{f}_{\rm s,obs}$, and $\ddot{f}_{\rm s,obs}$ subranges are summarized in Table 4.6. We display six examples from each set (pulsars in the field and pulsars near the Galactic centre) in Table 4.7, such that three of the Galactic field pulsars represent largest differences in n and $n_{\rm obs}$ when $n_{\rm obs} > 6$ (Pulsar1$_{\rm GF}$, Pulsar2$_{\rm GF}$, and Pulsar3$_{\rm GF}$) and the other three when $n_{\rm obs} < 0$ (Pulsar4$_{\rm GF}$, Pulsar5$_{\rm GF}$, and Pulsar6$_{\rm GF}$). We also display six examples of the near-Galactic centre pulsars in Table 4.7, such that three of them represent largest differences in n and $n_{\rm obs}$ when $n_{\rm obs} > 6$ (Pulsar1$_{\rm GC}$, Pulsar2$_{\rm GC}$, and Pulsar3$_{\rm GC}$) and the other three when $n_{\rm obs} < 0$ (Pulsar4$_{\rm GC}$, Pulsar5$_{\rm GC}$, and Pulsar6$_{\rm GC}$). It should be noted that, even if we get large values of $n_{\rm obs}$ for pulsars near the Galactic centre, those values are never as large as 10^8 as reported for a number of field pulsars by Hobbs et al. (2004).

We also see that the difference between the observed and intrinsic values of $\ddot{f}_{\rm s}$ are much larger than that for $\dot{f}_{\rm s}$ and the ratio of the observed and intrinsic values of braking index depends on both of these ratios as $n_{\rm obs}/n = \left(\dot{f}_{\rm s,int}/\dot{f}_{\rm s,obs}\right)^2 \cdot \left(\ddot{f}_{\rm s,obs}/\ddot{f}_{\rm s,int}\right)$. This emphasizes the fact that if one wants to use the value of the second derivative of the spin frequency to get better insight into the properties of the pulsar, it is better to correct for the dynamical terms as accurately as possible, as this parameter can be affected significantly by the dynamics.

Moreover, the difference in the results of the simulated millisecond pulsars in the Galactic field and those near the Galactic centre in tables 4.6 and 4.7 are noticeable. For the pulsars near the Galactic centre, a considerably larger number of favourable cases are generated and there is also a larger change in the values of the braking index. In summary, these simulations establish the fact that it is possible that the dynamical terms change the value of n significantly from three, especially near the Galactic centre. However, the possibility of having such a system is not very high as it needs a very unique combination of various parameters.

Note that, there is nothing very special about these pulsars. They are not located in special places in the Galaxy where the acceleration and/or the jerk due to the gravitational potential is very high. They also do not have anomalously large proper motions. In fact, there are many pulsars with such large differences between the values of n_{obs} and n. However, in most of such cases, the values of n differ largely from three. One example is the real millisecond pulsar PSR J1824−2452 that has $n_{\mathrm{obs}} = -326.22$ and $n = -504.86$ (we calculated and eliminated the dynamical effects using the values of the relevant parameters given in Hobbs et al. (2004)).

Table 4.6: Number of favourable cases where $2.5 < n < 3.5$, and $n_{\rm obs} < 0$ or $n_{\rm obs} > 6$, for various ranges of $f_{\rm s}$, $\dot{f}_{\rm s,obs}$, and $\ddot{f}_{\rm s,obs}$ values. The fourth column displays the number of favourable cases for pulsars in the Galactic field, whereas, the fifth column displays the number of favourable cases for pulsars near the Galactic centre. We display $f_{\rm s}$ rounded off to 2 decimal places. Each row represents one simulation run of 10000 simulated millisecond pulsars.

$f_{\rm s}$ range (Hz)	$\dot{f}_{\rm s,obs}$ range ($\rm s^{-2}$)	$\ddot{f}_{\rm s,obs}$ range ($\rm s^{-3}$)	Favourable Cases (Galactic Field)	Favourable Cases (Near Galactic Centre)
34.66 to 273.08	-10^{-13} to -10^{-14}	10^{-29} to 10^{-28}	3	7
		10^{-30} to 10^{-29}	1	5
		-10^{-28} to -10^{-29}	1	9
		-10^{-29} to -10^{-30}	10	51
	-10^{-14} to -10^{-15}	10^{-29} to 10^{-28}	0	3
		10^{-30} to 10^{-29}	19	56
		-10^{-28} to -10^{-29}	0	1
		-10^{-29} to -10^{-30}	13	48
	-10^{-15} to -10^{-16}	-10^{-29} to -10^{-30}	0	1
273.08 to 439.50	-10^{-13} to -10^{-14}	10^{-28} to 10^{-27}	0	2
		10^{-29} to 10^{-28}	7	25
		10^{-30} to 10^{-29}	7	16
		-10^{-27} to -10^{-28}	1	0
		-10^{-28} to -10^{-29}	10	31
		-10^{-29} to -10^{-30}	53	162
	-10^{-14} to -10^{-15}	10^{-29} to 10^{-28}	0	1
		10^{-30} to 10^{-29}	13	29
		-10^{-28} to -10^{-29}	0	3
		-10^{-29} to -10^{-30}	19	27
	-10^{-15} to -10^{-16}	10^{-30} to 10^{-29}	0	2

Continued on the next page

(continued from the previous page)

f_s range	$\dot{f}_{s,obs}$ range	$\ddot{f}_{s,obs}$ range	Favourable Cases	Favourable Case
439.50 to 641.93	-10^{-13} to -10^{-14}	10^{-28} to 10^{-27}	0	1
		10^{-29} to 10^{-28}	11	40
		10^{-30} to 10^{-29}	19	13
		-10^{-27} to -10^{-28}	0	1
		-10^{-28} to -10^{-29}	9	40
		-10^{-29} to -10^{-30}	64	249
	-10^{-14} to -10^{-15}	10^{-29} to 10^{-28}	0	1
		10^{-30} to 10^{-29}	16	18
		-10^{-28} to -10^{-29}	0	2
		-10^{-29} to -10^{-30}	8	10

Table 4.7: Parameters for simulated millisecond pulsars with $2.5 < n < 3.5$, and $n_{\rm obs} < 0$ or $n_{\rm obs} > 6$. Here, l is the Galactic longitude, b is the Galactic latitude, d is the distance between the pulsar and the Solar system barycentre, μ_l is proper motion in l, μ_b is the proper motion in b, $f_{\rm s}$ is the spin frequency, v_r is the radial velocity, $R_{\rm p}$ is the Galactocentric cylindrical distance of the pulsar, z is the vertical coordinate of the pulsar, $d_{\rm GC}$ is the distance between the pulsar and the Galactic centre, $\dot{f}_{\rm s,obs}$ is the observed (simulated) value of the first derivative of the spin frequency, $\dot{f}_{\rm s,int}$ is the intrinsic value of the first derivative of the spin frequency, $\ddot{f}_{\rm s,obs}$ is the observed (simulated) value of the second derivative of the spin frequency, $\ddot{f}_{\rm s,int}$ is the intrinsic value of the second derivative of the spin frequency, $n_{\rm obs}$ is the braking index based on the observed values of the spin frequency derivatives, and n is the braking index based on the intrinsic values of the spin frequency derivatives. The top half displays the parameters of simulated millisecond pulsars in the Galactic field (represented by the subscript 'GF'). Pulsar1$_{\rm GF}$, Pulsar2$_{\rm GF}$, and Pulsar3$_{\rm GF}$ represent the largest differences in n and $n_{\rm obs}$ when $n_{\rm obs} > 6$ whereas Pulsar4$_{\rm GF}$, Pulsar5$_{\rm GF}$, and Pulsar6$_{\rm GF}$ represent the largest differences in n and $n_{\rm obs}$ when $n_{\rm obs} < 0$. The bottom half displays the parameters of simulated millisecond pulsars near the Galactic centre (represented by the subscript 'GC'). Pulsar1$_{\rm GC}$, Pulsar2$_{\rm GC}$, and Pulsar3$_{\rm GC}$ represent the largest differences in n and $n_{\rm obs}$ when $n_{\rm obs} > 6$ whereas Pulsar4$_{\rm GC}$, Pulsar5$_{\rm GC}$, and Pulsar6$_{\rm GC}$ represent the largest differences in n and $n_{\rm obs}$ when $n_{\rm obs} < 0$. We display the results till the second decimal place.

Galactic Field pulsars						
Parameters	Pulsar1$_{\rm GF}$	Pulsar2$_{\rm GF}$	Pulsar3$_{\rm GF}$	Pulsar4$_{GF}$	Pulsar5$_{\rm GF}$	Pulsar6$_{\rm GF}$
l (deg)	37.94	61.77	319.51	111.40	338.79	27.47
b (deg)	19.15	-40.68	2.90	30.70	-21.22	-39.13
d (kpc)	1.15	0.63	0.62	1.42	0.77	0.73
μ_l (mas/yr)	18.18	-7.92	-12.80	17.64	7.82	-19.53
μ_b (mas/yr)	5.27	1.55	10.42	6.11	-31.79	3.18
v_r (km/s)	122.99	147.92	112.89	-140.45	-84.09	-130.41
$f_{\rm s}$ (Hz)	465.52	453.92	486.18	306.79	136.23	380.92
$\dot{f}_{\rm s,obs}$ ($\times 10^{-15}$ s^{-2})	-4.61	-2.15	-4.38	-1.48	-1.43	-4.08
$\ddot{f}_{\rm s,obs}$ ($\times 10^{-30}$ s^{-3})	5.83	1.28	4.00	-3.79	-2.52	-4.90

continued on the next page

(continued from the previous page)

Parameters	Pulsar1$_{\rm GF}$	Pulsar2$_{\rm GF}$	Pulsar3$_{\rm GF}$	Pulsar4$_{GF}$	Pulsar5$_{\rm GF}$	Pulsar6$_{\rm GF}$
$R_{\rm p}$ (kpc)	7.17	7.78	7.54	8.52	7.33	7.50
z (kpc)	0.38	-0.41	0.03	0.73	-0.28	-0.46
$d_{\rm GC}$ (kpc)	7.18	7.80	7.54	8.55	7.34	7.52
$\dot{f}_{\rm s,int}$ ($\times10^{-15}$ s^{-2})	-4.17	-2.16	-4.18	-1.15	-1.16	-3.85
$\ddot{f}_{\rm s,int}$ ($\times10^{-32}$ s^{-3})	12.32	3.58	11.82	1.33	3.35	12.25
$n_{\rm obs}$	127.72	125.76	101.32	-530.67	-168.71	-112.20
n	3.31	3.47	3.29	3.10	3.42	3.14
$\frac{(\dot{f}_{\rm s,int}-\dot{f}_{\rm s,obs})\times100}{\dot{f}_{\rm s,obs}}$	-9.65	0.56	-4.67	-22.48	-19.06	-5.53
$\frac{(\ddot{f}_{\rm s,int}-\ddot{f}_{\rm s,obs})\times100}{\ddot{f}_{\rm s,obs}}$	-97.89	-97.21	-97.05	-100.35	-101.33	-102.50

Near Galactic Centre pulsars

Parameters	Pulsar1$_{\rm GC}$	Pulsar2$_{\rm GC}$	Pulsar3$_{\rm GC}$	Pulsar4$_{\rm GC}$	Pulsar5$_{\rm GC}$	Pulsar6$_{\rm GC}$
l (deg)	358.30	3.83	359.32	356.68	0.23	358.99
b (deg)	-3.54	-3.59	4.50	-0.11	-3.45	0.82
d (kpc)	7.99	8.08	8.09	8.09	7.81	7.99
μ_l (mas/yr)	-0.55	-0.90	5.82	-6.91	-6.77	27.44
μ_b (mas/yr)	-1.28	-0.37	2.48	0.19	6.81	-5.87
v_r (km/s)	116.97	40.36	139.56	-180.66	-152.08	-99.60
$f_{\rm s}$ (Hz)	407.56	288.69	419.49	218.05	544.35	286.99

continued on the next page

(continued from the previous page)

Parameters	Pulsar1$_{\rm GC}$	Pulsar2$_{\rm GC}$	Pulsar3$_{\rm GC}$	Pulsar4$_{\rm GC}$	Pulsar5$_{\rm GC}$	Pulsar6$_{\rm GC}$
$\dot{f}_{\rm s,obs}$ ($\times 10^{-15}$ s^{-2})	-0.62	-0.58	-3.26	-0.52	-7.73	-9.38
$\ddot{f}_{\rm s,obs}$ ($\times 10^{-30}$ s^{-3})	7.91	1.16	7.72	-8.86	-31.51	-56.54
$R_{\rm p}$ (kpc)	0.24	0.54	0.12	0.47	0.21	0.14
z (kpc)	-0.49	-0.51	0.64	-0.02	-0.47	0.11
$d_{\rm GC}$ (kpc)	0.55	0.74	0.65	0.47	0.51	0.18
$\dot{f}_{\rm s,int}$ ($\times 10^{-15}$ s^{-2})	-0.93	-0.90	-3.43	-0.58	-6.72	-5.14
$\ddot{f}_{\rm s,int}$ ($\times 10^{-32}$ s^{-3})	0.61	0.93	8.24	0.47	26.40	27.38
$n_{\rm obs}$	8508.29	980.51	304.36	-7230.42	-286.94	-184.45
n	2.84	3.34	2.93	3.08	3.18	2.97
$\frac{(\dot{f}_{\rm s,int}-\dot{f}_{\rm s,obs})\times 100}{\dot{f}_{\rm s,obs}}$	51.71	53.63	5.24	12.02	-13.07	-45.16
$\frac{(\ddot{f}_{\rm s,int}-\ddot{f}_{\rm s,obs})\times 100}{\ddot{f}_{\rm s,obs}}$	-99.92	-99.20	-98.93	-100.05	-100.84	-100.48

In Table 4.7, the results are reported without any uncertainties. The main reason is the fact that the model of the gravitational potential we use (borrowed from galpy) does not return any uncertainties in the values of the accelerations and jerks. The lack of error estimation does not alter the conclusions as these are simulated pulsars anyway. If one wants to apply our formalism for a real pulsar for which uncertainties of all relevant observed parameters are known, then they can use a simulation technique. To demonstrate this technique, we took three Galactic field pulsars from Table 4.7, namely, $\mathrm{Pulsar1_{GF}}$, $\mathrm{Pulsar2_{GF}}$, and $\mathrm{Pulsar3_{GF}}$. For each pulsar, we simulated 10000 values for each of the input parameters (l, b, d, μ_l, μ_b, v_r, f_s, $\dot{f}_{\mathrm{s,obs}}$, $\ddot{f}_{\mathrm{s,obs}}$) following normal distributions. The values reported in Table 4.7 are taken as the mean and 5% of those as the standard deviation of these normal distributions. A set of values of the parameters taken from the newly simulated values form a new simulated pulsar, i.e., there are 10000 simulated pulsars corresponding to each of the aforementioned three pulsars (simulated) of Table 4.7.

We computed the values of the dynamical terms for each of those pulsars and found values of $\dot{f}_{\mathrm{s,int}}$, $\ddot{f}_{\mathrm{s,int}}$, and n. We then calculated the mean and the standard deviations for these results as well as the simulated values for the input parameters. These values are reported in Table 4.8. Note that the mean and the standard deviations of the simulated values of the input parameters differ slightly from the original values reported in Table 4.7.

However, it will be more accurate if a model of the Galactic potential that provides the uncertainties in the acceleration and jerk terms, is employed. If any such potential model is available in the future, then it will not be difficult to adopt the standard error propagation technique on our analytical expressions and the following codes.

Table 4.8: Demonstration of calculation of uncertainties in the values of $\dot{f}_{\rm s,int}$, $\ddot{f}_{\rm s,int}$, and n using a simulation technique for three pulsars of Table 4.7.

Parameters	Pulsar1$_{\rm GF}$	Pulsar2$_{\rm GF}$	Pulsar3$_{\rm GF}$
l (deg)	37.93 ± 1.90	61.83 ± 3.11	319.84 ± 16.08
b (deg)	19.14 ± 0.96	-40.69 ± 2.03	2.90 ± 0.14
d (kpc)	1.15 ± 0.06	0.63 ± 0.03	0.62 ± 0.03
μ_l (mas/yr)	18.19 ± 0.91	-7.93 ± 0.39	-12.80 ± 0.64
μ_b (mas/yr)	5.27 ± 0.26	1.55 ± 0.08	10.41 ± 0.52
v_r (km/s)	122.94 ± 6.16	147.93 ± 7.45	112.90 ± 5.67
$f_{\rm s}$ (Hz)	465.56 ± 23.40	453.77 ± 22.89	486.64 ± 24.59
$\dot{f}_{\rm s,obs}$ ($\times 10^{-15}$ s^{-2})	-4.61 ± 0.23	-2.15 ± 0.11	-4.38 ± 0.22
$\ddot{f}_{\rm s,obs}$ ($\times 10^{-30}$ s^{-3})	5.83 ± 0.30	1.28 ± 0.06	4.0 ± 0.20
$\dot{f}_{\rm s,int}$ ($\times 10^{-15}$ s^{-2})	-4.16 ± 0.24	-2.16 ± 0.11	-4.18 ± 0.22
$\ddot{f}_{\rm s,int}$ ($\times 10^{-31}$ s^{-3})	1.06 ± 6.79	0.30 ± 1.50	1.37 ± 4.30
$n_{\rm obs}$	128.72 ± 15.94	126.64 ± 15.60	102.02 ± 12.75
n	2.12 ± 18.66	2.62 ± 14.69	3.51 ± 12.12

4.4.3 Exploring the cases with the measured second derivative of the orbital frequency

In this section, we study dynamical contributions in the observed values of the second derivative of the orbital frequency, $\ddot{f}_{\rm b,obs}$. We find eight pulsars with reported values of $\ddot{f}_{\rm b,obs}$ in the ATNF catalogue - PSRs J0023+0923, J1048+2339, J1731−1847, J2339−0533, J0024−7204J, J0024−7204V, J0024−7204O, and J0024−7204W, and two additional pulsars whose $\ddot{f}_{\rm b,obs}$ value is not reported in the ATNF catalogue - PSRs J1723−2837 (Crawford et al., 2013), and J2051−0827 (Shaifullah et al., 2016). All these ten pulsars are millisecond pulsars.

Among these pulsars, five are black-widows, which are PSRs J0023+0923 (Arzoumanian et al., 2018), J0024−7204J (Freire et al., 2017), J0024−7204O (Freire et al., 2017), J1731−1847 (Ng et al., 2014), and J2051−0827 (Shaifullah et al., 2016) and four are Red-Backs, which are PSRs J0024−7204W (Ridolfi et al., 2016), J1048+2339 (Deneva et al., 2016), J1723−2837 (Crawford et al., 2013), and J2339−0533 (Pletsch and Clark, 2015)[5]. Additionally, pulsars PSRs J0024−7204J, J0024−7204V, J0024−7204O, and J0024−7204W, belong to the Globular Cluster 47 Tucanae (Freire et al., 2017; Ridolfi et al., 2016).

We calculated the intrinsic values of the first and second derivatives of the orbital frequency, $\dot{f}_{\rm b,int}$ and $\ddot{f}_{\rm b,int}$ respectively, for these pulsars. We took the parameters as given in the ATNF catalogue except a few cases as mentioned below. The $f_{\rm b}$, $\dot{f}_{\rm b,obs}$, and $\ddot{f}_{\rm b,obs}$ values for PSR J0023+0923 were taken from Arzoumanian et al. (2018). The $\ddot{f}_{\rm b,obs}$ value for PSR J1723−2837 was taken from Crawford et al. (2013), and for PSR J2051−0827 was taken from Shaifullah et al. (2016). The proper motion values for PSR J0024−7204V

---

[5] Both black widow and redback pulsars are binary millisecond pulsars with small values of the orbital period (~ 0.5 day), where the strong wind from the pulsar keeps on evaporating the companion. Black widows are identified by companions of mass of around 0.05 $M_\odot$ while redbacks are identified by companions of mass of around 0.2 $M_\odot$. Higher derivatives of the orbital frequencies of these systems are affected by the pulsar wind and intra-binary matter. However, to understand the contributions of these, one will first need to subtract the external dynamical effects, e.g., the effect of the gravitational potential of the Galaxy, etc.

were taken from Ridolfi et al. (2016). For all of the pulsars, we used independent distance estimates if available, otherwise NE2001 based distance. We took a nominal value for v_r as 50 km/s for all cases. We found that for all the cases, there is no perceptible difference between $\dot{f}_{\rm b,obs}$ and $\dot{f}_{\rm b,int}$ values, and $\ddot{f}_{\rm b,obs}$ and $\ddot{f}_{\rm b,int}$ values. It should be noted that, for pulsars in globular clusters, additional correction is needed to account for the cluster potential.

However, it is not wise to make any strong conclusion based on such a small number of pulsars with measurements of the second derivatives of the orbital frequency. We again used the simulated millisecond pulsar population generated in section 4.2.1, to study the dynamical contributions in $\ddot{f}_{\rm b,obs}$. Here, we aimed if we could get a sufficient number of millisecond pulsars for which the values of $\ddot{f}_{\rm b,obs}$ and $\ddot{f}_{\rm b,int}$ differ at least in the first decimal place but we could not find such a case for this set of synthetic millisecond pulsars.

Even when we performed the investigation over a larger number of synthetic pulsars (10000 instead of 2791 as in section 4.2.1), we did not find any favourable case. We also generated 10000 pulsars near the Galactic centre where the distributions of various parameters are the same as in section 4.2.2. But we still could not find any favourable case.

Consequently, we adopted a different approach to simulate parameters for a synthetic set of millisecond pulsars. Similar to the approach used in section 4.4.2, in order to explore two populations of millisecond pulsars, one in the Galactic field and the other in the near Galactic centre region, we used two approaches to simulate l, b, and d. For the first population, we just fitted the distribution from the ATNF catalogue for the millisecond pulsars (excluding the ones in the globular clusters, the Large Magellanic Cloud, and the Small Magellanic Cloud), and for the second population, we used the approach as described in section 4.2.2. For both the populations, we generated 10000 values of these parameters. For μ_l and μ_b too, we simulated 10000 values based on the distribution of values in the ATNF catalogue for the millisecond pulsars. We also generated 10000 values of v_r distributed uniformly between -200 to 200 km/s.

For $\dot{f}_{\rm b,obs}$ and $\ddot{f}_{\rm b,obs}$, we generated uniform distributions in subranges, and the logic of selection of the subranges is described as follows. From the ATNF catalogue, we see that the observed values of $\dot{f}_{\rm b,obs}$ lie in the ranges of -1.0×10^{-17} s^{-2} to -1.0×10^{-25} s^{-2} and 1.0×10^{-25} s^{-2} to 1.0×10^{-17} s^{-2}. We divided each set into subranges that span over one order of magnitude and generated 10000 uniformly distributed values for each subrange. Since the ATNF catalogue only gives four measurements of the $\ddot{f}_{\rm b,obs}$ for millisecond pulsars, we decided to extend its range. More specifically, the values of $\ddot{f}_{\rm s,obs}$ for these four millisecond pulsars lie in the ranges of -1.0×10^{-26} s^{-3} to -1.0×10^{-27} s^{-3} and 1.0×10^{-28} s^{-3} to 1.0×10^{-26} s^{-3}, while, by fitting these values with a distribution function and generating synthetic values in section 4.2.1, we found that $\ddot{f}_{\rm b,obs}$ vary between -1.0×10^{-25} s^{-3} to -1.0×10^{-30} s^{-3} and 1.0×10^{-30} s^{-3} to 1.0×10^{-25} s^{-3}. We used these two sets and divided each set into 5 subranges each of which span over one order of magnitude and generated uniform distributions of 10000 values for each subrange.

In this way, we got 16 subranges of $\dot{f}_{\rm b,obs}$, and 10 subranges of $\ddot{f}_{\rm b,obs}$, each having 10000 uniformly generated values. Similar to the technique used for simulation and calculation in section 4.4.2, we chose one subrange corresponding to $\dot{f}_{\rm b,obs}$ and $\ddot{f}_{\rm b,obs}$ each, in addition to the 10000 values generated for the parameters l, b, d, μ_l, μ_b, and v_r each. These 10000 values for each parameter constitute the 10000 synthetic millisecond pulsars, concentrated in the specific subrange in the multi-dimensional parameter space, out of the total 160 (16×10) such subranges. We computed the values of $\dot{f}_{\rm b,int}$ and $\ddot{f}_{\rm b,int}$ for all 10000 synthetic pulsars in each subrange and selected the favourable cases. In this approach, we implicitly assumed that the total number of millisecond pulsars over the full parameter space is much larger than 10000, which is a bit over-estimation. However, our quest here is to find unique combinations of parameters that can give large differences between the observed and intrinsic values of the second derivative of the orbital period.

Since we did not get any favourable result, we then used uniform distributions for μ_l

and μ_b too. As per the ATNF catalogue, for millisecond pulsars, μ_l varies between -52.8 mas/yr and 74.485 mas/yr, and μ_b varies between -103 mas/yr and 120.820 mas/yr. We generated 10000 uniformly distributed values between these maximum and minimum values of μ_l and μ_b, respectively. However, we did not get any favourable case, not even for near-Galactic centre pulsars. We then checked the maximum and minimum values of μ_l and μ_b from the ATNF catalogue for the set of all the pulsars and found that μ_l varies between -336.73 mas/yr and 193.8 mas/yr, and μ_b varies between -314.1 mas/yr and 176 mas/yr. We then generated 10000 uniformly distributed values between these maximum and minimum values of μ_l and μ_b, respectively. We found only one favourable case among the simulated Galactic field pulsars but multiple for the simulated near-Galactic centre pulsars. All of these pulsars have large values of $|\mu_l|$ and $|\mu_b|$, and consequently of μ_{T} leading to very high values of $V_{\mathrm{T}} = d\,\mu_{\mathrm{T}}$. Such unrealistically high values of V_{T} make us conclude that it is very unlikely that the second derivative of the orbital period would be contaminated by the dynamical terms. We still display these simulated pulsars as we are exploring the effect of various terms.

The number of favourable cases (where $\ddot{f}_{\mathrm{b,obs}}$ and $\ddot{f}_{\mathrm{b,int}}$ values differ at least in the first decimal place) for different subranges of $\dot{f}_{\mathrm{b,obs}}$ and $\ddot{f}_{\mathrm{b,obs}}$ are summarized in Table 4.9 for both the sets, i.e., the simulated Galactic field pulsars as well as the simulated near-Galactic centre pulsars. There was no favourable case (either in the Galactic field or near the Galactic centre) in various subranges of $\dot{f}_{\mathrm{b,obs}}$ and $\ddot{f}_{\mathrm{b,obs}}$, other than the ones reported in Table 4.9. The subranges where we found favourable cases are marked as subrange (i), (ii), (iii), and (iv). From Table 4.9, it is evident that the number of favourable cases significantly increase when we consider simulated pulsars near the Galactic centre.

We display the one favourable case from the simulated Galactic field pulsar and five examples from the set of favourable simulated near-Galactic centre pulsars in Table 4.10 with maximum percentage change in $\ddot{f}_{\mathrm{b,obs}}$. These six pulsars belong to various subranges of 4.9, except the subrange (i). Note that for the Galactic field pulsar and one of the

Table 4.9: Number of favourable simulated millisecond pulsars in the Galactic field as well as near the Galactic centre where $\ddot{f}_{\rm b,obs}$ and $\ddot{f}_{\rm b,int}$ values differ at least in the first decimal place, for various ranges of $\dot{f}_{\rm b,obs}$, and $\ddot{f}_{\rm b,obs}$ values. One row represents single simulation run of 10000 millisecond pulsars. These entries represent the simulation runs when -336.73 < μ_l < 193.8 mas/yr and -314.1 < μ_b < 176 mas/yr. The third column shows the number of the favourable cases for the Galactic field pulsars, and the fourth column shows the number of the favourable cases for the pulsars near the Galactic centre.

subrange no.	$\dot{f}_{\rm b,obs}$ range ($\rm s^{-2}$)	$\ddot{f}_{\rm b,obs}$ range ($\rm s^{-3}$)	Favourable Cases (Galactic Field)	Favourable Cases (Near Galactic Centre)
(i)	-10^{-17} to -10^{-18}	-10^{-29} to -10^{-30}	0	6
(ii)	-10^{-17} to -10^{-18}	10^{-30} to 10^{-29}	0	10
(iii)	10^{-18} to 10^{-17}	-10^{-29} to -10^{-30}	0	6
(iv)	10^{-18} to 10^{-17}	10^{-30} to 10^{-29}	1	4

near-Galactic centre pulsar (Pulsar2$_{\rm GC}$), the values of $\dot{f}_{\rm b,obs}$ and $\dot{f}_{\rm b,int}$ differ in the second decimal place, although when rounded off, the first decimal place shows the difference.

4.5 Details of simulation techniques adopted to generate parameters of millisecond pulsars

As mentioned earlier, for millisecond pulsars, we needed to generate a synthetic set of parameters from their observed distributions reported in version 1.63 of the ATNF catalogue. The number of pulsars with the measured values of a particular parameter is much less than the number of synthetic values we wanted. To ensure that the parameter for the synthetic and the real pulsars follow the same distribution, we first fitted an Empirical Cumulative Distribution Function (ECDF) to the real distribution and then used the inverse CDF technique to generate the intended number of synthetic values following the same ECDF. We performed this task using the in-built functions in the ‘R’ statistical package such as ‘ecdf()’, which calculates the ECDF of given data, and ‘approxfun()’, which is an interpolation function. Using the function generated by ‘approxfun()’, we simulated the required number of pulsars. Below we show a sample code to perform this procedure,

Table 4.10: Parameters for simulated millisecond pulsars with $\ddot{f}_{\rm b,int}$ being different from $\ddot{f}_{\rm b,obs}$ at least in the first decimal place. Meanings of l, b, d, μ_l, μ_b, v_r, $R_{\rm p}$, z, and $d_{\rm GC}$ are explained in the caption of Table 4.7. Additionally, $\mu_{\rm Tot}$ is the total transverse proper motion, $f_{\rm b}$ is the orbital frequency, $\dot{f}_{\rm b,obs}$ is the observed (simulated) value of the first derivative of the orbital frequency, $\dot{f}_{\rm b,int}$ is the intrinsic value of the first derivative of the orbital frequency, $\ddot{f}_{\rm b,obs}$ is the observed (simulated) value of the second derivative of the orbital frequency, and $\ddot{f}_{\rm b,int}$ is the intrinsic value of the second derivative of the orbital frequency. We also report which subrange of Table 4.9 these pulsars belong to. The second column displays the parameters of the one favourable simulated Galactic field pulsar (represented by Pulsar$_{\rm GF}$), whereas, columns 3, 4, 5, 6, and 7, display the parameters of the favourable simulated pulsars near the Galactic centre (represented by the subscript ‘GC’). We display the results till the second decimal place.

Parameters	Pulsar$_{\rm GF}$	Pulsar1$_{\rm GC}$	Pulsar2$_{\rm GC}$	Pulsar3$_{\rm GC}$	Pulsar4$_{\rm GC}$	Pulsar5$_{\rm GC}$
l (deg)	317.85	355.92	2.24	3.97	357.33	0.39
b (deg)	-43.66	2.80	4.48	-4.20	0.52	-3.12
d (kpc)	7.61	8.19	7.98	7.88	7.82	7.87
$d_{\rm GC}$ (kpc)	7.52	0.72	0.70	0.81	0.42	0.45
μ_l (mas/yr)	-335.29	-336.10	-266.69	-266.29	-288.00	-336.07
μ_b (mas/yr)	-304.39	-228.82	-254.38	-290.02	-298.10	-271.67
$\mu_{\rm Tot}$ (mas/yr)	452.85	406.60	368.55	393.73	414.50	432.14
v_r (km/s)	30.77	-187.18	122.58	-23.85	160.44	35.67
$f_{\rm b}$ ($\times 10^{-5}$ Hz)	3.68	9.51	0.71	11.79	4.05	0.12
$\dot{f}_{\rm b,obs}$ ($\times 10^{-18}$ s^{-2})	8.15	-8.63	9.80	-9.89	9.24	8.53
$\ddot{f}_{\rm b,obs}$ ($\times 10^{-30}$ s^{-3})	2.50	1.01	-1.15	1.60	2.00	-2.45
subrange of Table 4.9	(iv)	(ii)	(iii)	(ii)	(iv)	(iii)
$R_{\rm p}$ (kpc)	5.39	0.60	0.32	0.57	0.41	0.15
z (kpc)	-5.25	0.40	0.62	-0.58	0.07	-0.43
$\dot{f}_{\rm b,int}$ ($\times 10^{-18}$ s^{-2})	8.29	-8.31	9.82	-9.54	9.38	8.54
$\ddot{f}_{\rm b,int}$ ($\times 10^{-30}$ s^{-3})	2.56	0.95	-1.10	1.54	2.06	-2.39
$\frac{(\dot{f}_{\rm b,int}-\dot{f}_{\rm b,obs})\times 100}{\dot{f}_{\rm b,obs}}$	1.71	-3.63	0.19	-3.54	1.43	0.05
$\frac{(\ddot{f}_{\rm b,int}-\ddot{f}_{\rm b,obs})\times 100}{\ddot{f}_{\rm b,obs}}$	2.47	-5.57	-4.48	-3.66	3.00	-2.49

where 10000 values are being generated from the ecdf created from the data stored in the first column of the inputdatafile.txt, and those simulated values are being stored in another file called outputdatafile.txt.

```
» N=10000
» d1 <- read.table("datafile.txt")
» par <- d1[,1]
» spar <- sort(par)
» y1 <- ecdf(spar)
» fy <- y1(spar)
» qf <- approxfun(fy,spar,rule=2)
» n=0
» while (n < N){
» val <- qf(runif(1,0,1))
» if(val < max(par) && val > min(par)){
» z <- as.data.frame(val)
» write.table(z,file="outputdatafile.txt",append = TRUE, sep =
" ", dec = ".", row.names=FALSE, col.names=FALSE)
» n <- n+1}
» }
```

The parameters for which we use this technique are l, b, d, μ_l, μ_b, f_s, $\dot{f}_\mathrm{s,obs}$, $\ddot{f}_\mathrm{s,obs}$, f_b, $\dot{f}_\mathrm{b,obs}$, and $\ddot{f}_\mathrm{b,obs}$. It should be noted that, since binary parameters are not reported for all millisecond pulsars, we did the above procedures for two sets of real millisecond pulsars. The first set consisted of the millisecond pulsars for which all relevant spin parameters are known and the second set consisted of the millisecond pulsars for which all relevant orbital parameters are known.

Comparisons between the histograms of the values of various parameters for real pulsars with those of the synthetic ones are demonstrated in Figs. 4.5 and 4.6. We see good agreements between the two sets for all of the parameters.

Moreover, for each case, we also fit analytical functions to the ECDFs that might be used for future simulations. In Figs. 4.7 and 4.8, we show the ECDFs of the catalogued parameters (black circles) and the corresponding fitted analytical functions (magenta line). The analytical functions fitted for the ECDFs are given next.

A) For millisecond pulsars for which we study the spin period and its derivatives:

For l,

$$f(x) = a_1 + b_1 x + c_1 x^2 + d_1 x^3 + e_1 x^4 + f_1 x^5 + g_1 x^6 + h_1 x^7 + i_1 x^{0.5}, \tag{4.2}$$

where x is l in degrees, $a_1 = -0.0529731$, $b_1 = -0.0177131$, $c_1 = 4.90899 \times 10^{-4}$, $d_1 = -6.36035 \times 10^{-6}$, $e_1 = 4.21318 \times 10^{-8}$, $f_1 = -1.50626 \times 10^{-10}$, $g_1 = 2.76759 \times 10^{-13}$, $h_1 = -2.04602 \times 10^{-16}$, and $i_1 = 0.0824625$.

For b,

$$f(x) = a_1 + b_1 x + c_1 x^3 + d_1 \tan^{-1}(e_1 x + f_1), \tag{4.3}$$

where x is b in degrees, $a_1 = 0.503818$, $b_1 = 5.94973 \times 10^{-3}$, $c_1 = -3.82843 \times 10^{-7}$, $d_1 = 0.13707$, $e_1 = 0.177927$, and $f_1 = 0.0123772$.

For d,

$$f(x) = \begin{cases} a_1 + b_1 x + c_1 x^2 + d_1 x^3 + e_1 x^4 + f_1 x^5 + g_1 x^6 + h_1 \cos(i_1 x + j_1) & \text{for } 0.16 \le x < 6.52 \\ a_2 + b_2 x + c_2 x^2 & \text{for } 6.52 \le x \le 9.57, \end{cases} \tag{4.4}$$

where x is d in kpc, $a_1 = -0.183758$, $b_1 = 0.727475$, $c_1 = 1.882$, $d_1 = -1.38698$, $e_1 = 0.330001$, $f_1 = -0.0325109$, $g_1 = 0.00114405$, $h_1 = 1.33382$, $i_1 = 1.03336$, $j_1 = 1.3714$, $a_2 = 0.880219$, $b_2 = 0.0241095$, and $c_2 = -0.00121142$.

For μ_l,

$$f(x) = a_1 + b_1 x + c_1 x^3 + d_1 x^4 + e_1 x^5 + f_1 x^6 + g_1 \tan^{-1}(h_1 x + i_1), \tag{4.5}$$

where x is μ_l in mas/yr, $a_1 = 0.50758$, $b_1 = -4.95419 \times 10^{-3}$, $c_1 = 1.28996 \times 10^{-6}$, $d_1 = -3.36161 \times 10^{-9}$, $e_1 = -1.6026 \times 10^{-10}$, $f_1 = -8.5719 \times 10^{-13}$, $g_1 = 0.447531$, $h_1 = 0.117067$, and $i_1 = 0.132973$.

For μ_b,

$$f(x) = \begin{cases} a_1 + b_1 \tan^{-1}(c_1 x + d_1) & \text{for } -103.0 \leq x < -10.88 \\ a_2 + b_2 x + c_2 x^2 + d_2 x^3 + e_2 x^4 + f_2 x^5 + g_2 x^6 + h_2 \tan^{-1}(i_2 x + j_2) & \text{for } -10.88 \leq x < 33.0 \\ a_3 + b_3 \tan^{-1}(c_3 x + d_3) & \text{for } 33.0 \leq x \leq 120.82, \end{cases} \tag{4.6}$$

where x is μ_b in mas/yr, $a_1 = 0.0599331$, $b_1 = 0.0338245$, $c_1 = 0.104666$, $d_1 = 1.57861$, $a_2 = 0.45342$, $b_2 = -4.69699 \times 10^{-3}$, $c_2 = 5.24825 \times 10^{-5}$, $d_2 = 5.8858 \times 10^{-7}$, $e_2 = -9.48048 \times 10^{-9}$, $f_2 = -2.87306 \times 10^{-11}$, $g_2 = 4.54409 \times 10^{-13}$, $h_2 = 0.433273$, $i_2 = 0.149375$, $j_2 = 0.0493088$, $a_3 = -0.232011$, $b_3 = 0.789204$, $c_3 = 0.751781$, and $d_3 = -7.03388$.

For f_s,

$$f(x) = a_1 + b_1 x + c_1 x^3 + d_1 x^4 + e_1 x^5 + f_1 x^6 + g_1 x^7 + h_1 \ln(i_1 x + j_1), \tag{4.7}$$

where x is f_s in Hz, $a_1 = -2.43949$, $b_1 = -0.0106382$, $c_1 = 3.17806 \times 10^{-7}$, $d_1 = -1.42841 \times 10^{-9}$, $e_1 = 2.74707 \times 10^{-12}$, $f_1 = -2.5095 \times 10^{-15}$, $g_1 = 8.92214 \times 10^{-19}$, $h_1 = 0.853209$, $i_1 = 0.429942$, and $j_1 = 11.9449$.

For $\dot{f}_s$,

$$f(x) = \begin{cases} a_1 + b_1 x + c_1 \tan^{-1}(d_1 x + e_1) & \text{for } -4.331143 \times 10^{-14} \leq x < -2.805 \times 10^{-15} \\ a_2 + b_2 x + c_2 x^3 + d_2 x^4 + e_2 x^5 + f_2 x^6 + g_2 \tan^{-1}(h_2 x + i_2) & \\ & \text{for x} - 2.805 \times 10^{-15} \leq x \leq 8.001 \times 10^{-19}, \end{cases} \tag{4.8}$$

where x is $\dot{f}_s$ in s^{-2}, $a_1 = 0.125467$, $b_1 = 2.43942 \times 10^{11}$, $c_1 = -0.0729254$, $d_1 = -5.59244 \times 10^{14}$, $e_1 = -1.81661$, $a_2 = 0.739498$, $b_2 = 4.24045 \times 10^{13}$, $c_2 = -6.67543 \times 10^{41}$, $d_2 = -6.0641 \times 10^{55}$, $e_2 = -1.98126 \times 10^{69}$, $f_2 = -2.13864 \times 10^{82}$, $g_2 = 0.341357$, $h_2 = 2.89221 \times 10^{15}$, and $i_2 = 1.03125$.

For $\ddot{f}_s$,

$$f(x) = \begin{cases} a_1 + b_1 x & \text{for } -1.8 \times 10^{-25} \leq x < -1.04 \times 10^{-25} \\ a_2 + b_2 x & \text{for } -1.04 \times 10^{-25} \leq x < -3.5 \times 10^{-27} \\ a_3 + b_3 x & \text{for } -3.5 \times 10^{-27} \leq x < -5.9 \times 10^{-28} \\ a_4 + b_4 x & \text{for } -5.9 \times 10^{-28} \leq x < 8. \times 10^{-27} \\ a_5 + b_5 x & \text{for } \quad 8. \times 10^{-27} \leq x < 2.8 \times 10^{-26} \\ a_6 + b_6 x & \text{for } \quad 2.8 \times 10^{-26} \leq x < 5.5 \times 10^{-26} \\ a_7 + b_7 x & \text{for } \quad 5.5 \times 10^{-26} \leq x \leq 6.1001 \times 10^{-26}, \end{cases} \tag{4.9}$$

where x is $\ddot{f}_s$ in s^{-3}, $a_1 = 0.421053$, $b_1 = 1.64474 \times 10^{24}$, $a_2 = 0.379353$, $b_2 = 1.24378 \times 10^{24}$, $a_3 = 0.525344$, $b_3 = 4.29553 \times 10^{25}$, $a_4 = 0.508586$, $b_4 = 1.45518 \times 10^{25}$, $a_5 = 0.575$, $b_5 = 6.25 \times 10^{24}$, $a_6 = 0.62037$, $b_6 = 4.62963 \times 10^{24}$, $a_7 = -0.270833$, and $b_7 = 2.08333 \times 10^{25}$.

B) For millisecond pulsars for which we study the orbital period and its derivatives:

For l,

$$f(x) = a_1 + b_1 x + c_1 x^2 + d_1 x^3 + e_1 x^4 + f_1 x^5 + g_1 x^6 + h_1 x^7 + i_1 x^{0.5}, \tag{4.10}$$

where x is l in degrees, $a_1 = -0.0485927$, $b_1 = -0.0218928$, $c_1 = 6.77443 \times 10^{-4}$, $d_1 = -9.25316 \times 10^{-6}$, $e_1 = 6.36726 \times 10^{-8}$, $f_1 = -2.3393 \times 10^{-10}$, $g_1 = 4.3803 \times 10^{-13}$, $h_1 = -3.28094 \times 10^{-16}$, and $i_1 = 0.0776432$.

For b,

$$f(x) = a_1 + b_1 x + c_1 x^2 + d_1 x^3 + e_1 x^4 + f_1 x^5 + g_1 x^6 + h_1 x^7 + i_1 \tan^{-1}(j_1 x + k_1), \tag{4.11}$$

where x is b in degrees, $a_1 = 0.477823$, $b_1 = 0.0117684$, $c_1 = 4.71953 \times 10^{-5}$, $d_1 = -3.83345 \times 10^{-6}$, $e_1 = -2.09694 \times 10^{-8}$, $f_1 = 8.93978 \times 10^{-10}$, $g_1 = 2.55224 \times 10^{-12}$, $h_1 = -7.85373 \times 10^{-14}$, $i_1 = 0.0833227$, $j_1 = 0.412748$, and $k_1 = 0.151804$.

For d,

$$f(x) = \begin{cases} a_1 + b_1 x + c_1 x^2 + d_1 x^3 + e_1 x^4 + f_1 x^5 & \text{for } 0.16 \leq x < 0.70 \\ a_2 \tan^{-1}(b_2 x + c_2) & \text{for } 0.70 \leq x \leq 10.37, \end{cases} \tag{4.12}$$

where x is d in kpc, $a_1 = 0.24179$, $b_1 = -4.01779$, $c_1 = 24.8668$, $d_1 = -69.7158$, $e_1 = 91.1958$, $f_1 = -44.6237$, $a_2 = 0.703997$, $b_2 = 0.738592$, and $c_2 = -0.319079$.

For μ_l,

$$f(x) = a_1 + b_1 x + c_1 x^2 + d_1 x^3 + e_1 x^4 + f_1 x^5 + g_1 x^6 + h_1 x^7 + i_1 \tan^{-1}(j_1 x + k_1), \tag{4.13}$$

where x is μ_l in mas/yr, $a_1 = 0.505004$, $b_1 = -6.6135 \times 10^{-3}$, $c_1 = 4.72798 \times 10^{-6}$, $d_1 = 2.22105 \times 10^{-6}$, $e_1 = -5.01809 \times 10^{-9}$, $f_1 = -4.64163 \times 10^{-10}$, $g_1 = 8.91905 \times 10^{-13}$, $h_1 = 3.29716 \times 10^{-14}$, $i_1 = 0.474632$, $j_1 = 0.113521$, and $k_1 = 0.130561$.

For μ_b,

$$f(x) = \begin{cases} a_1 + b_1 \tan^{-1}(c_1 x + d_1) & \text{for } -103.0 \leq x < -10.88 \\ a_2 + b_2 x + c_2 x^2 + d_2 x^3 + e_2 x^4 + f_2 x^5 + h_2 x^7 + i_2 \tan^{-1}(j_2 x + k_2) & \text{for } -10.88 \leq x < 24.0 \\ a_3 + b_3 \tan^{-1}(c_3 x + d_3) & \text{for } 24.0 \leq x \leq 120.82, \end{cases} \tag{4.14}$$

where x is μ_b in mas/yr, $a_1 = 0.0599331$, $b_1 = 0.0338245$, $c_1 = 0.104666$, $d_1 = 1.57861$, $a_2 = 0.463032$, $b_2 = -5.72758 \times 10^3$, $c_2 = 2.28548 \times 10^5$, $d_2 = 1.34693 \times 10^{-6}$, $e_2 = -2.16677 \times 10^{-9}$, $f_2 = -1.6908 \times 10^{-10}$, $h_2 = 7.06577 \times 10^{-15}$, $i_2 = 0.447546$, $j_2 = 0.14614$, $k_2 = 0.0217994$, $a_3 = -0.232011$, $b_3 = 0.789204$, $c_3 = 0.751781$, and $d_3 = -7.03388$.

For f_b,

$$f(x) = \begin{cases} a_1 + b_1 x + c_1 x^3 & \text{for } 1.730 \times 10^{-28} \leq x < 1.513 \times 10^{-7} \\ a_2 + b_2 x + c_2 x^2 + d_2 x^3 + e_2 x^4 + f_2 x^5 + g_2 x^6 + h_2 x^7 + i_2 x^{0.5} & \text{for } 1.513 \times 10^{-7} \leq x \leq 1.778 \times 10^{-4}, \end{cases} \tag{4.15}$$

where x is f_b in Hz, $a_1 = 1.95698 \times 10^{-3}$, $b_1 = 2.09868 \times 10^5$, $c_1 = 1.81457 \times 10^{19}$, $a_2 = -0.103612$, $b_2 = -1.24620 \times 10^5$, $c_2 = 2.79517 \times 10^9$, $d_2 = -5.17979 \times 10^{13}$, $e_2 = 5.90848 \times 10^{17}$, $f_2 = -3.92399 \times 10^{21}$, $g_2 = 1.38707 \times 10^{25}$, $h_2 = -2.01098 \times 10^{28}$, and $i_2 = 566.13$.

For $\dot{f}_b$,

$$f(x) = \begin{cases} a_1 + b_1 x & \text{for } -8.3 \times 10^{-18} \leq x < -4.4 \times 10^{-19} \\ a_2 + b_2 x + c_2 \tan^{-1}(d_2 x + e_2) & \text{for } -4.4 \times 10^{-19} \leq x < -2.96 \times 10^{-23} \\ a_3 + b_3 x & \text{for } -2.96 \times 10^{-23} \leq x < -5.0 \times 10^{-24} \\ a_4 + b_4 \tan^{-1}(c_4 x + d_4) & \text{for } -5.0 \times 10^{-24} \leq x < 1.13 \times 10^{-22} \\ a_5 + b_5 x & \text{for } 1.13 \times 10^{-22} \leq x < 1.82 \times 10^{-22} \\ a_6 + b_6 x + c_6 x^2 & \text{for } 1.82 \times 10^{-22} \leq x < 2.15 \times 10^{-20} \\ a_7 + b_7 x + c_7 x^2 + d_7 \tan^{-1}(e_7 x + f_7) & \text{for } 2.15 \times 10^{-20} \leq x \leq 1.9763 \times 10^{-18}, \end{cases} \tag{4.16}$$

where x is $\dot{f}_b$ in s^{-2}, $a_1 = 0.0708958$, $b_1 = 4.38712 \times 10^{15}$, $a_2 = 0.176865$, $b_2 = 5.69998 \times 10^{16}$, $c_2 = 0.0543125$, $d_2 = 5.08556 \times 10^{19}$, $e_2 = 0.618662$, $a_3 = 0.336052$, $b_3 = 4.35315 \times 10^{21}$, $a_4 = 0.417954$, $b_4 = 0.113064$, $c_4 = 3.71689 \times 10^{23}$, $d_4 = -0.433861$, $a_5 = 0.5761$, $b_5 = 1.48633 \times 10^{20}$, $a_6 = 0.602375$, $b_6 = 4.68001 \times 10^{18}$, $c_6 = 5.04 \times 10^{37}$, $a_7 = 0.787153$, $b_7 = 2.43602 \times 10^{16}$, $c_7 = 1.74204 \times 10^{34}$, $d_7 = 0.0645722$, $e_7 = 1.28703 \times 10^{19}$, and $f_7 = -1.64509$.

For $\ddot{f}_b$,

$$f(x) = \begin{cases} a_1 + b_1 x & \text{for } -1.6 \times 10^{-26} \leq x < -5. \times 10^{-27} \\ a_2 + b_2 x & \text{for } -5. \times 10^{-27} \leq x < 2.4 \times 10^{-28} \\ a_3 + b_3 x & \text{for } 2.4 \times 10^{-28} \leq x \leq 1.77 \times 10^{-26}, \end{cases} \tag{4.17}$$

where x is $\ddot{f}_b$ in s^{-3}, $a_1 = 0.613636$, $b_1 = 2.27273 \times 10^{25}$, $a_2 = 0.73855$, $b_2 = 4.77099 \times 10^{25}$, $a_3 = 0.746564$, and $b_3 = 1.43184 \times 10^{25}$.

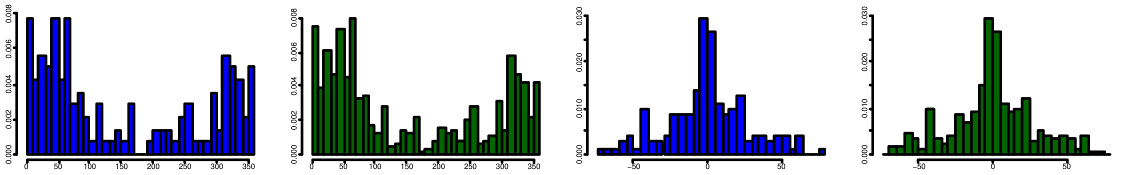

(a) distribution of l in deg (real)

(b) distribution of l in deg (synthetic)

(c) distribution of b in deg (real)

(d) distribution of b in deg (synthetic)

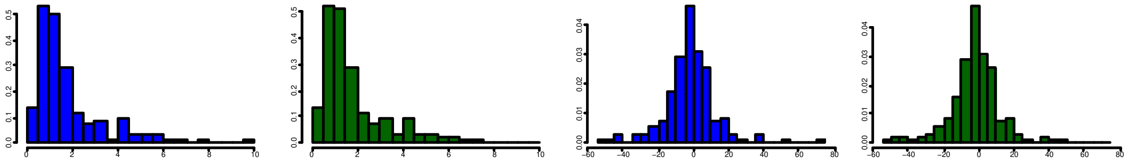

(e) distribution of d in kpc (real)

(f) distribution of d in kpc (synthetic)

(g) distribution of μ_l in mas/yr (real)

(h) distribution of μ_l in mas/yr (synthetic)

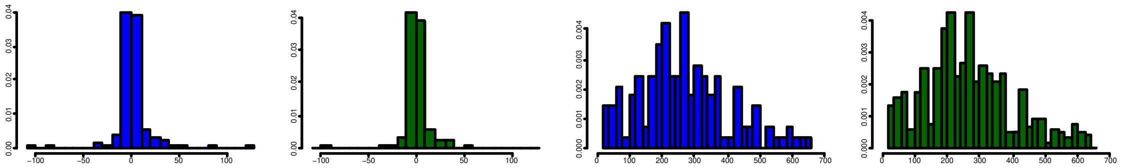

(i) distribution of μ_b in mas/yr (real)

(j) distribution of μ_b in mas/yr (synthetic)

(k) distribution of f_s in Hz (real)

(l) distribution of f_s in Hz (synthetic)

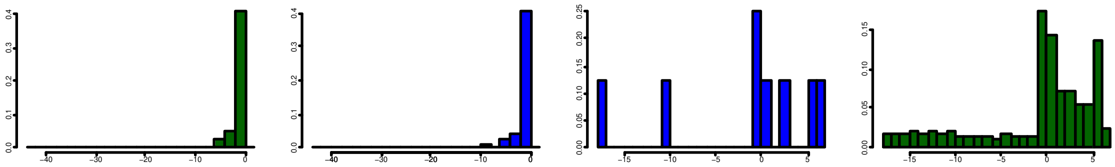

(m) distribution of $\dot{f}_s$ in 10^{-15} s^{-2} (real)

(n) distribution of $\dot{f}_s$ in 10^{-15} s^{-2} (synthetic)

(o) distribution of $\ddot{f}_s$ in 10^{-26} s^{-3} (real)

(p) distribution of $\ddot{f}_s$ in 10^{-26} s^{-3} (synthetic)

Figure 4.5: Comparison of the observed and simulated density distributions of parameters of millisecond pulsars in the Galactic field for which we study the spin frequency and its derivatives.

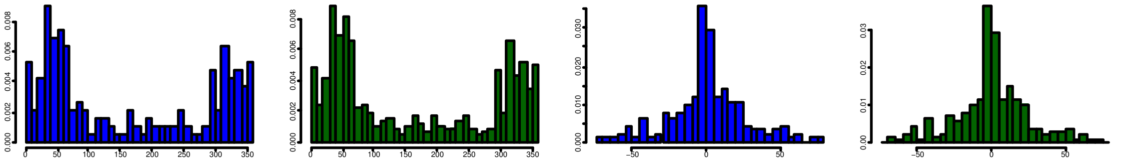

(a) distribution of l in deg (real)

(b) distribution of l in deg (synthetic)

(c) distribution of b in deg (real)

(d) distribution of b in deg (synthetic)

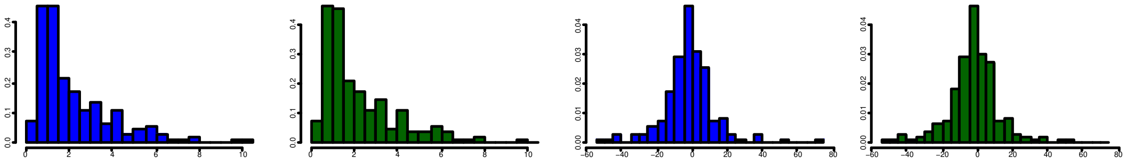

(e) distribution of d in kpc (real)

(f) distribution of d in kpc (synthetic)

(g) distribution of μ_l in mas/yr (real)

(h) distribution of μ_l in mas/yr (synthetic)

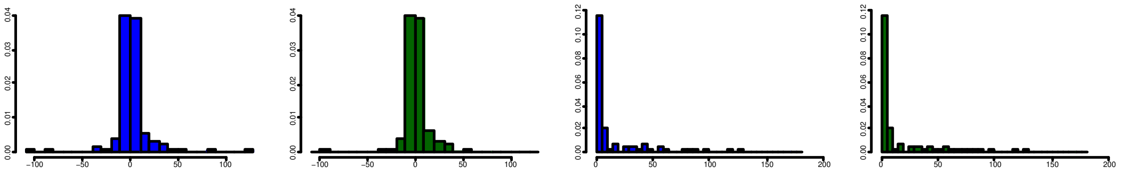

(i) distribution of μ_b in mas/yr (real)

(j) distribution of μ_b in mas/yr(synthetic)

(k) distribution of f_b in 10^{-6} Hz (real)

(l) distribution of f_b in 10^{-6} Hz (synthetic)

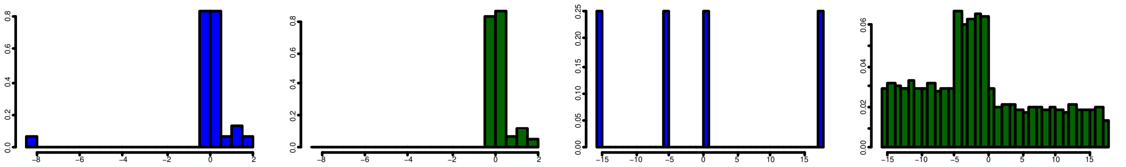

(m) distribution of $\dot{f}_b$ in 10^{-18} s^{-2} (real)

(n) distribution of $\dot{f}_b$ in 10^{-18} s^{-2} (synthetic)

(o) distribution of $\ddot{f}_b$ in 10^{-27} s^{-3} (real)

(p) distribution of $\ddot{f}_b$ in 10^{-27} s^{-3} (synthetic)

Figure 4.6: Comparison of the observed and simulated density distributions of parameters of millisecond pulsars in the Galactic field for which we study the orbital frequency and its derivatives.

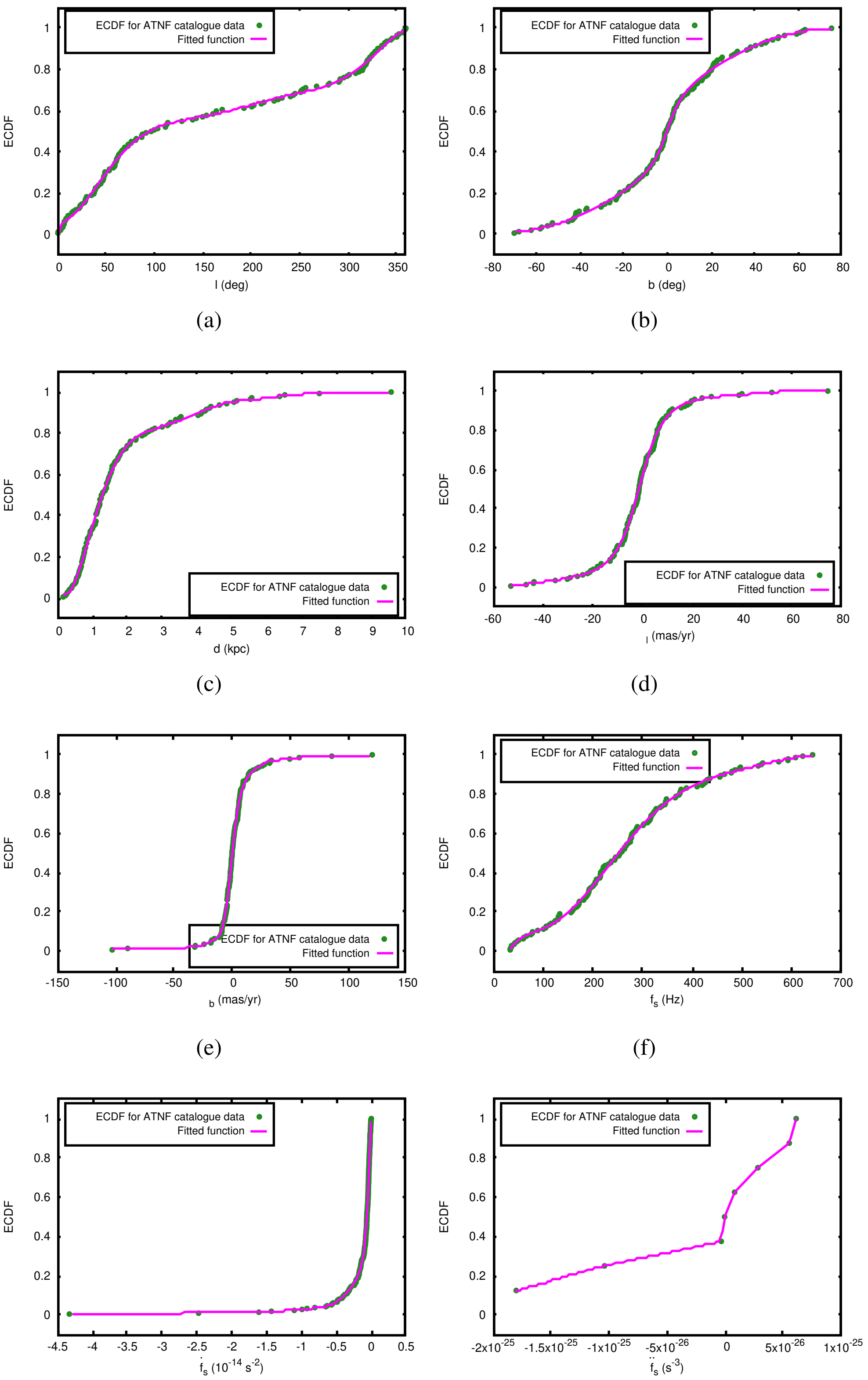

(a) (b) (c) (d) (e) (f) (g) (h)

Figure 4.7: Plots showing the Empirical Cumulative Distribution Functions of various parameters of millisecond pulsars as reported in the ATNF catalogue along with corresponding fitted functions for (a) l,(b) b, (c) d, (d) μ_l, (e) μ_b, (f) f_s, (g) $\dot{f}_{s,\mathrm{obs}}$, and (h) $\ddot{f}_{s,\mathrm{obs}}$. This is for the case when we study the spin frequency and its derivatives.

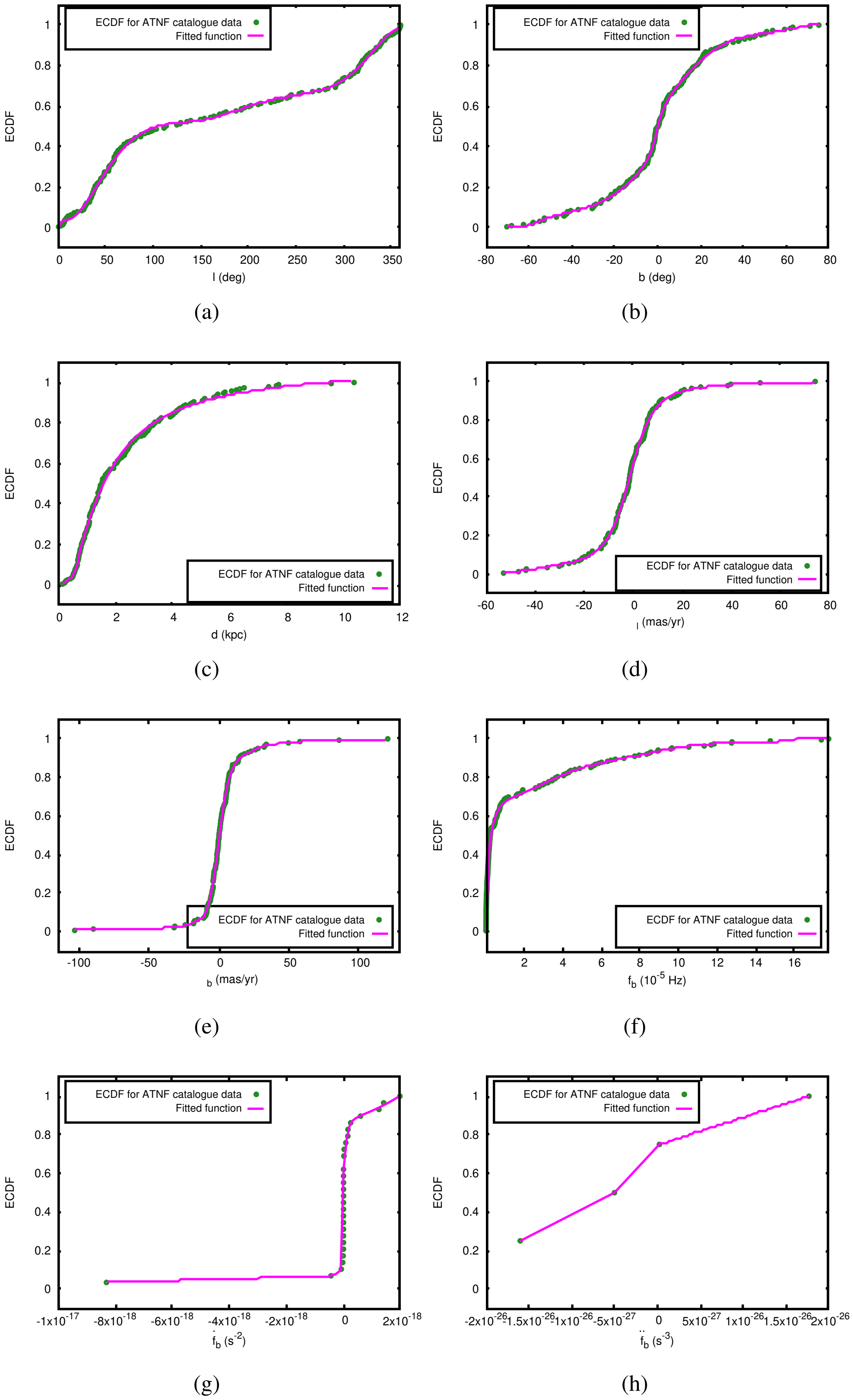

(a) (b)

(c) (d)

(e) (f)

(g) (h)

Figure 4.8: Plots showing the Empirical Cumulative Distribution Functions of various parameters of millisecond pulsars as reported in the ATNF catalogue along with corresponding fitted functions for (a) l,(b) b, (c) d, (d) μ_l, (e) μ_b, (f) f_s, (g) $\dot{f}_{\mathrm{b,obs}}$, and (h) $\ddot{f}_{\mathrm{b,obs}}$. This is for the case when we study the orbital frequency and its derivatives.

4.6 Summary

As the expression of $\left(\frac{\ddot{f}}{f}\right)_{\rm ex}$ in eq. (2.37) is quite long, consisting of multiple terms, which by themselves are not very simple, we first explored whether any one or more of the terms can be ignored. Our simulations established the fact that all terms are of nearly equal importance, and should be kept. We also found that the total dynamical contribution would be much larger for pulsars located near the Galactic centre, so when such pulsars will be discovered and timed, one should not forget to correct for dynamical contributions from the first and second derivatives of the frequencies. However, we emphasize that the values reported in this work for the Galactic centre are not very accurate, as the gravitational potential of the Galaxy in that region is not very well modeled. If such a model is available in the future, one can easily implement that in a code based on our analytical expressions.

We have created a python package GalDynPsrFreq that estimates the contribution of the dynamical terms to the measured values of the first and the second time derivatives of the frequency. Using GalDynPsrFreq, we investigated potential cases where the dynamical contributions might lead to confusing results if not accounted for. As our expression is valid for the second derivatives of the spin frequency as well as the second derivatives of the orbital frequency, we studied both. We paid special attention to the pulsars with reported values of the braking index being different from 3 (Hobbs et al., 2004; Dang et al., 2020). Although for these real pulsars, we did not see any significant contribution of the dynamical terms to the value of the braking index, our simulations resulted in a few such cases. We also saw that it is very unlikely to have the second derivative of the orbital frequency contaminated by the dynamical terms.

We have reported the values of the dynamical terms contributing to the second derivative of frequencies without any uncertainties, as we calculated the accelerations and jerks of pulsars using a model of the Galactic potential that does not report errors. The lack of error estimation does not alter the conclusions of this work, because, first, most of the results we report are for simulated pulsars, second, dynamical effects are not that large for the second derivative of the frequencies for the real pulsars we have. However, we have seen that these effects will be large for pulsars near the Galactic centre. For such pulsars, it will be necessary to have an improved model of the Galactic potential including uncertainties on various parameters. In that case, it will not be difficult to adopt the standard error propagation technique on our analytical expressions which are the main results of the present thesis. Presently, if needed, one can use a simulation technique to find the uncertainties. We have demonstrated the use of such a technique.

Bibliography

Arzoumanian, Z. et al., 2018. The NANOGrav 11-year Data Set: High-precision Timing of 45 Millisecond Pulsars. ApJS. 235, 37-77. https://doi.org/10.3847/1538-4365/aab5b0.

Bassa, C. G., Janssen, G. H., Stappers, B. W., Tauris, T. M., & Wevers, T., 2016. A millisecond pulsar in an extremely wide binary system. MNRAS. 460, 2207-2222. https://doi.org/10.1093/mnras/stw1134.

Bates, S. D., Lorimer, D. R., Rane, A., Swiggum, A., 2014. PSRPOPPy: an open-source package for pulsar population simulations. MNRAS. 439, 2893-2902. https://doi.org/10.1093/mnras/stu157.

Chmyreva, E., Beskin, G. & Dyachenko, V., 2017. A Search for Isolated Stellar-Mass Black Hole Candidates Based on Pulsar Kinematics. Stars: from Collapse to Collapse, ASP Conference Series. 510, 317. http://aspbooks.org/publications/510/317.pdf.

Cordes, J. M., Lazio, T. J. W., 2002. NE2001. I. A New Model for the Galactic Distribution of Free Electrons and its Fluctuations. preprint(arXiv:astro-ph/0207156).

Cordes, J. M., Lazio, T. J. W., 2003. NE2001. II. Using Radio Propagation Data to Construct a Model for the Galactic Distribution of Free Electrons. preprint(arXiv:astro-ph/0301598).

Crawford, F. et al., 2013. PSR J1723−2837: An Eclipsing Binary Radio Millisecond Pulsar. ApJ. 776, 20-31. https://doi.org/10.1088/0004-637X/776/1/20.

Dang, S. J. et al., 2020. Results of 12 Years of Pulsar Timing at Nanshan . I. ApJ. 896, 140-160. https://doi.org/10.3847/1538-4357/ab9082.

Deneva, J. S. et al., 2016. Multiwavelength Observations of the Redback Millisecond Pulsar J1048+2339. ApJ. 823, 105-118. https://doi.org/10.3847/0004-637X/823/2/105.

Freire, P. C. C., Ridolfi, A., Kramer, M., Jordan, C., Manchester, R. N. et al., 2017. Long-term observations of the pulsars in 47 Tucanae - II. Proper motions, accelerations and jerks. MNRAS. 471, 857-876. https://doi.org/10.1093/mnras/stx1533.

Faucher-Giguère, Claude-André & Kaspi, V. M., 2006. Birth and Evolution of Isolated Radio Pulsars. ApJ. 643, 332-355. https://doi.org/10.1086/501516.

Gieles, M. et al., 2018. Mass models of NGC 6624 without an intermediate-mass black hole. MNRAS. 473, 4832-4839. https://doi.org/10.1093/mnras/stx2694.

Guillemot, L. et al., 2016. The gamma-ray millisecond pulsar deathline, revisited. New velocity and distance measurements. A&A. 587, 109-120. https://doi.org/10.1051/0004-6361/201527847.

Helfand, D. J. & Tademaru, E., 1977. Pulsar velocity observations: correlations, interpretations, and discussion. MNRAS. 216, 842-851. https://doi.org/10.1086/155529.

Hobbs, G., Lyne, A. G., Kramer, M., Martin, C. E., Jordan, C., 2004. Long-term timing observations of 374 pulsars. MNRAS. 353, 1311-1344. https://doi.org/10.1111/j.1365-2966.2004.08157.x.

Hobbs, G., Lorimer, D. R., Lyne, A. G. & Kramer, M., 2005. A statistical study of 233 pulsar proper motions. MNRAS. 360, 974-992. https://doi.org/10.1111/j.1365-2966.2005.09087.x.

Kaplan, D. L., et al., 2016. PSR J1024−0719: A Millisecond Pulsar in an Unusual Long-period Orbit. ApJ. 826, 86-96. https://doi.org/10.3847/0004-637X/826/1/86.

Keane, E. et al., 2014. A Cosmic Census of Radio Pulsars with the SKA. Proceedings of Science, Advancing Astrophysics with the Square Kilometre Array (AASKA14). 040. http://pos.sissa.it/cgi-bin/reader/conf.cgi?confid=215.

Krishnakumar, M. A., Manoharan, P. K., Joshi, B. C., Girgaonkar, R., Desai, S. et al., 2021. High precision measurements of interstellar dispersion measure with the upgraded GMRT. A&A. 651, A5. https://doi.org/10.1051/0004-6361/202140340.

Liu, X. J., Bassa, C. G., Stappers, B. W., 2018. High-precision pulsar timing and spin frequency second derivatives. MNRAS. 478, 2359-2367. https://doi.org/10.1093/mnras/sty1202.

Liu, X. J., Keith, M. J., Bassa, C. G., Stappers, B. W., 2019. Correlated timing noise and high-precision pulsar timing: measuring frequency second derivatives as an example. MNRAS. 488, 2190-2201. https://doi.org/10.1093/mnras/stz1801.

Lorimer, D. R., Faulkner, A. J., Lyne, A. G., Manchester, R. N., Kramer, M. et al., 2006. The Parkes Multibeam Pulsar Survey-VI. Discovery and timing of 142 pulsars and a Galactic population analysis. MNRAS. 372, 777-800. https://doi.org/10.1111/j.1365-2966.2006.10887.x.

Lorimer, D. R., 2013. The Galactic Millisecond Pulsar Population. Proceedings of the International Astronomical Union. 291, 237-242. https://doi.org/10.1017/S1743921312023769.

Lorimer, D. R., Esposito, P., Manchester, R. N., Possenti, A., Lyne, A. G. et al., 2015. The Parkes multibeam pulsar survey - VII. Timing of four millisecond pulsars and the underlying spin-period distribution of the Galactic millisecond pulsar population. MNRAS. 450, 2185-2194. https://doi.org/10.1093/mnras/stv804.

Manchester, R. N., Hobbs, G. B., Teoh, A., Hobbs, M., 2005. The Australia Telescope National Facility Pulsar Catalogue. AJ. 129, 1993-2006. Online version http://www.atnf.csiro.au/people/pulsar/psrcat/. https://doi.org/10.1086/428488.

Manchester, R. N. et al., 2001. The Parkes multi-beam pulsar survey - I. Observing and data analysis systems, discovery and timing of 100 pulsars. MNRAS. 328, 17-35. https://doi.org/10.1046/j.1365-8711.2001.04751.x.

Ng, C. et al., 2014. The High Time Resolution Universe pulsar survey - X. Discovery of four millisecond pulsars and updated timing solutions of a further 12. MNRAS. 439, 1865-1883. https://doi.org/10.1093/mnras/stu067.

Perera, B. B. P. et al., 2017. Evidence for an intermediate-mass black hole in the globular cluster NGC 6624. MNRAS. 468, 2114-2127. https://doi.org/10.1093/mnras/stx501.

Perera, B. B. P., DeCesar, M. E., Demorest, P. B., Kerr, M., Lentati, L. et al., 2019. The International Pulsar Timing Array: second data release. MNRAS. 490, 4666. https://doi.org/10.1093/mnras/stz2857.

Pletsch, H. J., Clark, C. J., 2015. Gamma-Ray Timing of Redback PSR J2339−0533: Hints for Gravitational Quadrupole Moment Changes. ApJ. 807, 18-26. https://doi.org/10.1088/0004-637X/807/1/18.

Ridley, J. P., Lorimer, D. R., 2010. Isolated pulsar spin evolution on the diagram. MNRAS. 404. 1081-1088. https://doi.org/10.1111/j.1365-2966.2010.16342.x.

Ridolfi, A. et al., 2016. Long-term observations of the pulsars in 47 Tucanae - I. A study of four elusive binary systems. MNRAS. 462, 2918-2933. https://doi.org/10.1093/mnras/stw1850.

Sun, X. H. & Han, J. L., 2004. Pulsar motions in our Galaxy. MNRAS. 350, 232-242. https://doi.org/10.1111/j.1365-2966.2004.07640.x.

Shaifullah, G. et al., 2016. 21 year timing of the black-widow pulsar J2051−0827. MNRAS. 462, 1029-1038. https://doi.org/10.1093/mnras/stw1737.

Yao, J. M., Manchester, R. N., Wang, N., 2017. A New Electron-density Model for Estimation of Pulsar and FRB Distances. ApJ. 835, 29-60. https://doi.org/10.3847/1538-4357/835/1/29.

Chapter 5

Conclusion

We have seen that it is important to do correction for the dynamical terms in the first as well as in the second derivatives of the spin frequency, as they can drastically affect the braking index values, which might lead to inaccurate conclusions on the true physics behind the spin-down of such pulsars. Similarly, the dynamical terms can impact the values of the first and second derivatives of orbital frequencies of binary pulsars significantly that might have consequences in applications of these measurements in the study of gravitational physics.

Previous studies on estimation of the dynamical terms have resorted to approximate methods that fail to provide an accurate picture of the intrinsic frequency derivatives (either the spin or the orbital) of all the pulsars spread across the Galactic field. They might have been sufficient to estimate parameters for some pulsars for the accuracy of the timing solutions existing in the past. However, improvements in the timing precision demand improvements in methods of estimation of dynamical terms.

In the present thesis, we have provided a formalism to calculate analytical expressions of the dynamical terms in the first and the second derivatives of the frequency with the assumption that the gravitational potential of the Galaxy is the only cause of the acceleration and the jerk of the pulsar. These expressions involve various measurable parameters and are equally valid for the spin and the orbital frequencies.

We have created two python packages, ‘GalDynPsr’ and ‘GalDynPsrFreq’, both of which are publicly available. ‘GalDynPsr’ evaluates the contribution of dynamical effect-terms to the first derivative of the period following the traditional as well as improved methods based on a model of the Galactic potential provided in a public package called ‘galpy’. GalDynPsrFreq estimates the dynamical terms in the measured values of the first and the second derivatives of the frequency, based on the improved model, as investigations with GalDynPsr already established the superiority of this model over the conventional ones.

It should also be noted that even after eliminating the dynamical contributions from the observed derivatives of the frequencies, there might exist additional external contributions due to the error while modeling the time-dependent change in the dispersion measure (Prager et al., 2017). So, care should be taken regarding this. Additionally, for a pulsar very close to the Galactic centre, extra contributions due to the nearby stars or the potential of the nuclear cluster (if the pulsar is in such a cluster) will be significant. So care should be taken to extract these effects in addition to other effects calculable by GalDynPsr or GalDynPsrFreq. Similarly, for pulsars in globular clusters, the cluster potential is to be modeled out of GalDynPsr or GalDynPsrFreq.

Since galpy as well as GalDynPsr and GalDynPsrFreq are being improved continuously, potential users are requested to check for new versions on the source repositories of these packages. It is important to note that the model of the Galactic potential as done in galpy is not the only one, many different models exist in the literature, e.g., McMillan (2017); Pouliasis et al. (2017), etc. The modular structures of GalDynPsr and GalDynPsrFreq make sure that the interested users can incorporate new models without much difficulty.

The work presented in this thesis has potential applications in probing the structural properties of pulsars as well as in studies of fundamental physics. In fact, Archibald et al. (2018) used GalDynPsr when they placed the best ever limit of the non-violation of the universality of free fall using data of the pulsar PSR J0337+1715, which is a part of a three-body system. Moreover, using GalDynPsrFreq, one can get more accurate measurements of the values of the braking index that are gateways to study the structural properties of pulsars by being indicators of the true spin-down nature of pulsars. With both GalDynPsr and GalDynPsrFreq, we can get intrinsic values of the derivatives of the orbital period or frequency, which can be used in tests of gravity theories and measurements of masses of both components of binary pulsars. We can also obtain intrinsic spin frequency derivatives, which can be used in calculating the spin-down limit of the amplitude of the strain of continuous gravitational waves. This can be helpful in constraining continuous gravitational waves from rotationally deformed pulsars.

Bibliography

Archibald, A. M., Gusinskaia, N. V., Hessels, J. W. T., Deller, A. T., Kaplan, D. L., et al. 2018. Universality of free fall from the orbital motion of a pulsar in a stellar triple system. Nature. 559, 73. https://doi.org/10.1038/s41586-018-0265-1.

McMillan, P. J., 2017. The mass distribution and gravitational potential of the Milky Way. MNRAS. 465, 76. https://doi.org/10.1093/mnras/stw2759.

Pouliasis, E., Di Matteo, P., & Haywood, M., 2017. A Milky Way with a massive, centrally concentrated thick disc: new Galactic mass models for orbit computations. A&A. 598A, 66. https://doi.org/10.1051/0004-6361/201527346.

Prager, B. J. et al., 2017. Using Long-term Millisecond Pulsar Timing to Obtain Physical Characteristics of the Bulge Globular Cluster Terzan 5. ApJ. 845, 148-171. https://doi.org/10.3847/1538-4357/aa7ed7.